UNIVERSITY OF SOUTHAMPTON

FACULTY OF ENGINEERING AND THE ENVIRONMENT

Airbus Noise Technology Centre

Aircraft Noise Installation Effects

by

Timothy James Heffernon

Thesis for the degree of Doctor of Philosophy

September 2017

UNIVERSITY OF SOUTHAMPTON

ABSTRACT

FACULTY OF ENGINEERING AND THE ENVIRONMENT
Airbus Noise Technology Centre

Doctor of Philosophy

AIRCRAFT NOISE INSTALLATION EFFECTS

by Timothy James Heffernon

Airframe noise is currently of a comparable level to engine noise for an aircraft on approach with high-lift devices and landing gears deployed. The landing gears are a large contributor to the overall airframe noise in this situation. Main landing gears are typically installed beneath a lifting wing. The wing surfaces act as scattering surfaces for the noise generated by these landing gears, and the non-uniform flow around the wing affects both the propagation and strength of the noise. This thesis focuses on investigating the propagation and scattering of installed landing gear noise sources.

Boundary element methods are capable of computing acoustic scattering by large and complex geometries, such as a complete aircraft geometry. However, due to their use of Green's functions, flow effects can only be approximated. As a result, the refraction of acoustic waves due to a non-uniform flow is not accounted for. A uniform flow formulation based on a Lorentz-type transform is typically employed with boundary element methods. The effect of neglecting refraction on the propagation and scattering of landing gear noise sources is determined in this thesis. Investigations are conducted using computational aeroacoustic methods that solve the linearised Euler equations, which account for the refraction of acoustic waves due to non-uniform flow.

Using computational aeroacoustic methods, the effect of non-uniform flow due to circulation on the acoustic scattering is quantified as the difference in acoustic scattering over uniform and non-uniform base flows. These investigations are conducted using both single frequency and broadband monopole sources, and both single-element and multi-element airfoils. Increasing the angle of attack, increasing the Mach number, and deploying flaps all increase the circulation around the airfoil. The effect of varying these parameters is investigated systematically. It

is shown that for a source in the approximate position of a landing gear with flow conditions similar to that of an airliner on approach, the largest difference observed is at single frequencies for an airfoil configuration with a deployed flap. Otherwise, the differences are small, and in some cases so small that they can be considered negligible. It is shown that moving the source to a position above the airfoil and using a higher Mach number gives a larger difference, although this is not representative of a landing gear source.

A new method is proposed to generate a broadband input signal for use with a computational aeroacoustic solver that gives a specified power spectral density at a given radial distance from a monopole source. A signal that is equal in power across a specified range of frequencies is generated using this method. The effect on the frequency content of the scattered noise from a broadband source installed beneath a lifting wing is investigated using this generated signal. It is shown for a single-element airfoil that the major contributor to the obtained power spectral density is the distance of the source from the airfoil. Varying the angle of attack and Mach number has only a small additional effect on the power spectral density. It is then shown that flap and slat deployment has a larger effect on the computed power spectral density due to the additional reflective surfaces.

Existing boundary element method formulations that estimate uniform and non-uniform flow effects are evaluated for their suitability for landing gear noise scattering predictions. It is shown that the uniform flow formulation is more suitable due to a simplifying assumption made in the derivation of the non-uniform flow formulation. An existing realistic landing gear noise model is coupled with a three-dimensional acoustic boundary element method solver. The landing gear noise model applies scaling laws to directional databases for isolated landing gear components in order to estimate the total far-field noise. The implemented coupling methodology is used to compute the sound pressure level on a ground plane beneath a realistic scattering aircraft geometry. The geometrical effect of flap deployment is investigated using sources of constant strength for each configuration. It is shown that the effect of flap deployment is to increase the sound pressure level directly below and in the region immediately surrounding the aircraft. The effect of source strength reduction due to circulation around a lifting wing is then included in the predictions. This results in a large decrease in the predicted sound pressure level on the ground plane with flap deployment.

Contents

List of Figures vii

List of Tables xiii

Declaration of Authorship xv

Acknowledgements xvii

Nomenclature xix

1 Introduction 1
- 1.1 Motivation and Aims . . . 1
- 1.2 Original Contributions . . . 6
- 1.3 Thesis Structure . . . 7

2 Aeroacoustics and Aircraft Noise 9
- 2.1 Introduction . . . 9
- 2.2 Computational Methods . . . 10
  - 2.2.1 Modelling of Noise for a Computational Approach . . . 10
  - 2.2.2 Far-Field Noise Estimation . . . 11
  - 2.2.3 Noise Generation . . . 12
  - 2.2.4 Noise Propagation and Computational Aeroacoustic Methods 14
  - 2.2.5 Hybrid Method Examples . . . 16
  - 2.2.6 Near-Field Propagation Examples . . . 17
  - 2.2.7 Boundary Element Methods for Aeroacoustics . . . 19
  - 2.2.8 Accelerated BEM Solution Methods . . . 24
  - 2.2.9 Examples of the Boundary Element Method for Aeroacoustics 26
- 2.3 Landing Gear Noise . . . 29
- 2.4 Landing Gear Installation Effects . . . 32
- 2.5 Discussion and Summary . . . 34

3 Mathematical Preliminaries 37
- 3.1 Introduction . . . 37
- 3.2 Overview of Employed Solvers and Codes . . . 38
- 3.3 Boundary Element Methods . . . 40
  - 3.3.1 The Helmholtz Equation, Boundary Conditions, Fundamental Solution, and Acoustic Source . . . 40
  - 3.3.2 Overview and Validation of Employed Solvers . . . 42

3.3.3 Flow Approximation Methods . . . 46
3.3.3.1 Uniform Flow . . . 46
3.3.3.2 Non-Uniform Potential Flow . . . 48
3.4 Potential Flow Solver . . . 50
3.4.1 Panel Method . . . 50
3.4.2 Validation of Panel Method Solver . . . 52
3.5 Linearised Euler Equations . . . 55
3.5.1 Derivation and Acoustic Source . . . 55
3.5.2 Solution by the Finite Difference Method and Boundary Conditions . . . 57
3.5.3 Monopole Parameter Study . . . 57
3.5.4 Validation of Solver for Scattering Problems . . . 62
3.6 Computational Costs of the Solvers . . . 63
3.7 Summary . . . 66

4 The Scattering of a Single Frequency Source by an Airfoil 69
4.1 Introduction . . . 69
4.2 Model Description . . . 71
4.3 Computational Grids . . . 73
4.4 Base Flows . . . 76
4.5 The Effect of Circulation on the Scattering of a Single Frequency Source . . . 78
4.5.1 Varying Angle of Attack and Mach Number . . . 81
4.5.2 Varying Flap Configuration . . . 89
4.6 A Discussion on Accuracy . . . 91
4.7 The Effect of a Higher Mach Number . . . 95
4.8 The Effect of an Alternative Source Location . . . 97
4.9 Quantification of the 2-D Assumption . . . 101
4.10 Evaluation of Boundary Element Method Flow Approximations . . 103
4.10.1 Single Element Airfoil . . . 109
4.10.2 Airfoil With Flap . . . 111
4.11 Summary . . . 113

5 The Scattering of a Broadband Source by an Airfoil 117
5.1 Introduction . . . 117
5.2 The Generation and Testing of a Broadband Signal . . . 118
5.3 The Creation of a Modified Input Signal for the Correct Power Spectral Density . . . 123
5.4 Model Description and Computational Grids . . . 125
5.5 The Effect of Circulation on Sound Pressure Level . . . 126
5.5.1 Varying Angle of Attack and Mach Number . . . 128
5.5.2 Varying Flap and Slat Configuration . . . 130
5.6 Frequency Analysis of the Scattered Source . . . 133
5.6.1 Single Element Airfoil . . . 134
5.6.2 Multi-Element High-Lift Airfoil . . . 137
5.7 Comparison to the Scattering of a Single Frequency Source . . . 139
5.8 Summary . . . 144

6 The Scattering of Single Frequency Sources by an Aircraft 147
6.1 Introduction . . . 147
6.2 Model Description . . . 148
6.3 Geometry and Computational Meshes . . . 150
6.4 Landing Gear Noise Source Model . . . 154
6.5 Sound Pressure Level on the Ground and the Effect of Flap Deployment . . . 159
6.5.1 Constant Strength Sources . . . 160
6.5.2 Source Strength Reduction for Installed Main Landing Gear 163
6.6 The Effect of Alternative Locations for the Main Landing Gear Source . . . 164
6.7 Summary . . . 168

7 Conclusion 171
7.1 Summary of Results . . . 171
7.1.1 The Effect of Non-Uniform Flow on the Scattering of Landing Gear Noise Sources . . . 171
7.1.2 Quantification of the 2-D Assumption . . . 173
7.1.3 The Effect of an Alternative Source Location and Higher Mach Numbers . . . 174
7.1.4 The Frequency Content of Broadband Sources Scattered by a Lifting Wing . . . 175
7.1.5 The Evaluation of BEM Flow Approximations for Landing Gear Noise Scattering Problems . . . 176
7.1.6 Coupling a Landing Gear Noise Source Model with a 3-D BEM Solver . . . 177
7.2 Future Work . . . 178
7.2.1 Experimental Validation of Computational Methods . . . 179
7.2.2 Improving the Landing Gear Noise Source Model Coupling . 179
7.2.3 Time-Domain BEM . . . 180

Appendix 181
A LEE Simulation Data . . . 181
B BEM Simulation Data . . . 191
C Guidance for *SotonLGAP* Subroutine to Generate *ACTIPOLE* Input Files . . . 197
D Additional 2-D LEE Simulation Examples . . . 201

References 215

List of Figures

1.1 Aircraft noise certification reference points. 2
1.2 The relative contribution of landing gear noise to the overall noise for an Airbus A320. 3
1.3 The contribution of circulation to the non-uniform flow around a lifting wing. 4
1.4 The refraction of acoustic waves from a point source beneath a lifting wing due to the streamwise flow velocity gradient in this region. 5

2.1 Landing gear noise spectra obtained from experiments on a full-scale Boeing 737 two-wheel main landing gear at various Mach numbers, in both clean and fully dressed configurations. 31

3.1 Cylinder/sphere geometry with source and observer positions. . . . 43
3.2 Comparison of SPL (dB) between an analytical solution and the numerical solution, evaluated at a radius of 10 m centred on the cylinder. 44
3.3 Comparison of SPL (dB) between an analytical solution and the numerical solution, evaluated at a radius of 10 m centred on the sphere. 45
3.4 Acoustic pressure (Pa) for the scattering of a monopole at 325 Hz at a distance of 5 m from the centre of a sphere of radius 1 m in 3-D. 45
3.5 Validation of panel solver. NACA 0012 airfoil, $\alpha = 5°$, $M_\infty = 0.2$. . 54
3.6 Validation of panel solver. RA16SC1 airfoil with flap 20°, $\alpha = 0°$, $M_\infty = 0.2$. 54
3.7 Mach number magnitude and streamlines, RA16SC1 airfoil with flap 20°, $\alpha = 0°$, $M_\infty = 0.2$. 55
3.8 Percentage error of p_{rms} against the analytical solution for various values of R. 61
3.9 Acoustic pressure (Pa) for the scattering of a monopole at 325 Hz at a distance of 5 m from the centre of a circular cylinder of radius 1 m in 2-D. 63
3.10 Comparison of SPL (dB) between an analytical solution and the numerical solution, evaluated at a radius of 10 m centred on the cylinder centre. 64
3.11 Percentage error of p_{rms} against the analytical solution. 64

4.1 Airfoil geometries. 71

4.2 RA16SC1 airfoil with flap 40° plus slat, with source and observer locations. 72
4.3 Monopole forcing region and local grid refinement for each frequency. 75
4.4 RA16SC1 with flap 40° plus slat, mesh topology and details. 76
4.5 Mach number magnitude and streamlines, RA16SC1 airfoil with flap 40° plus slat, $\alpha = 0°$, $M_\infty = 0.2$. 77
4.6 Region of flow tangential to the airfoil surface in an otherwise uniform flow. 78
4.7 Acoustic pressure (Pa) for the scattering of a monopole at 500 Hz by a NACA 0012 airfoil in a non-uniform $M_\infty = 0.2$ flow at $\alpha = 5°$. 79
4.8 Acoustic pressure (Pa) for the scattering of a monopole at 500 Hz by an RA16SC1 airfoil with flap 40° in a non-uniform $M_\infty = 0.2$ flow at $\alpha = 0°$. 80
4.9 SPL contour (dB) for the scattered source over a non-uniform flow at observer angles $0° \leq \theta \leq 180°$, NACA 0012 airfoil, varying α, $M_\infty = 0.2$. 82
4.10 Contour of $\mathrm{SPL}_{\text{non-uniform}} - \mathrm{SPL}_{\text{uniform}}$ (dB) for the scattered source at observer angles $0° \leq \theta \leq 180°$, NACA 0012 airfoil, varying α, $M_\infty = 0.2$. 83
4.11 Difference in SPL between non-uniform and uniform base flows across various frequencies, NACA 0012, varying α, $M_\infty = 0.2$. . . . 84
4.12 Mach number magnitude and streamlines showing the difference between non-uniform and uniform flows. NACA 0012 airfoil, varying α, $M_\infty = 0.2$. 85
4.13 SPL contour (dB) for the scattered source over a non-uniform flow at observer angles $0° \leq \theta \leq 180°$, NACA 0012 airfoil, varying M_∞, $\alpha = 5°$. 87
4.14 Difference in SPL between non-uniform and uniform base flows across various frequencies, NACA 0012, varying M_∞, $\alpha = 5°$. 88
4.15 Difference in SPL between non-uniform and uniform base flows across various frequencies, RA16SC1, varying flap configuration, $M_\infty = 0.2$, $\alpha = 0°$. 90
4.16 Mach number magnitude and streamlines showing the difference between non-uniform and uniform flows. RA16SC1 airfoil, varying configuration, $\alpha = 0°$, $M_\infty = 0.2$. 91
4.17 SPL (dB). RA16SC1 with flap 40°, 500 Hz, $\alpha = 0°$, $M_\infty = 0.2$. . . . 92
4.18 The difference in SPL (dB) between uniform and non-uniform flows at the $\theta = 90°$ observer. NACA 0012 airfoil, $M_\infty = 0.2$, varying α. . 94
4.19 SPL (dB). NACA 0012, 250 Hz, $\alpha = 3°$, $M_\infty = 0.6$. 97
4.20 NACA 0012 airfoil, with source location above the airfoil, and observer locations. 98
4.21 SPL (dB). NACA 0012, 250 Hz, $\alpha = 3°$, varying M_∞. 99
4.22 Acoustic pressure (Pa), NACA 0012, 250 Hz, $\alpha = 3°$, $M_\infty = 0.6$. . . 101
4.23 Isocontours of acoustic pressure, ±8.4 Pa. NACA 0012, $\alpha = 4°$, $M_\infty = 0.2$, non-uniform flow, source at 250 Hz. 104

4.24 Comparison of 3-D BEM and LEE results. SPL (dB) for the scattering of a monopole at 250 Hz by a NACA 0012 airfoil at $\alpha = 4°$ and $M_\infty = 0.2$. 104
4.25 Comparison between the difference in SPL over non-uniform and uniform base flows in 2-D and 3-D. NACA 0012, $\alpha = 4°$, $M_\infty = 0.2$, source at 250 Hz. 105
4.26 Acoustic pressure (Pa) for the two BEM flow approximations, NACA 0012, 250 Hz, $\alpha = 5°$, $M_\infty = 0.2$. 107
4.27 SPL (dB) showing a comparison of BEM solutions for the NACA 0012 airfoil at 250 Hz. 107
4.28 SPL (dB) showing a comparison of BEM solutions against LEE solutions without flow for observers in the range $0° \leq \theta \leq 180°$. . . 109
4.29 NACA 0012 airfoil, varying M_∞, $\alpha = 5°$. 110
4.30 NACA 0012 airfoil, varying α, $M_\infty = 0.2$. 111
4.31 RA16SC1 airfoil, varying configuration, $M_\infty = 0.2$, $\alpha = 0°$. 112

5.1 Segment of generated time series. 120
5.2 One-sided PSD of the generated time series. 120
5.3 PDF of the generated time series. 121
5.4 Autocorrelation of the generated time series. 121
5.5 PSD (dB/Hz) at a radius of 5 m for a broadband monopole in the free-field without flow using the original input signal. 122
5.6 PSD (dB/Hz) at a radius of 5 m for a broadband monopole in the free-field without flow using the modified input signal. 124
5.7 Segment of received pressure signal. 125
5.8 Autocorrelation of received pressure signal. 125
5.9 Acoustic pressure (Pa) for the scattering of a broadband monopole by a NACA 0012 airfoil in a non-uniform $M_\infty = 0.2$ flow at $\alpha = 5°$. 127
5.10 Acoustic pressure (Pa) for the scattering of a broadband monopole by an RA16SC1 airfoil with flap 40° plus slat in a non-uniform $M_\infty = 0.2$ flow at $\alpha = 0°$. 128
5.11 Difference in acoustic scattering (dB) between non-uniform and uniform base flows. Scattering of a broadband monopole by a NACA 0012 airfoil at $M_\infty = 0.2$ and varying α. 129
5.12 Difference in acoustic scattering (dB) between non-uniform and uniform base flows. Scattering of a broadband monopole by a NACA 0012 airfoil at $\alpha = 5°$ and varying M_∞. 130
5.13 SPL (dB) for the scattering of a broadband monopole by an RA16SC1 geometry with varying configuration, $M_\infty = 0.2$, $\alpha = 0°$, non-uniform flow. 131
5.14 Difference in acoustic scattering (dB) between non-uniform and uniform base flows. Scattering of a broadband monopole by an RA16SC1 airfoil at $\alpha = 0°$, $M_\infty = 0.2$, and varying configuration. . 132
5.15 PSD (dB/Hz) at the $\theta = 90°$ observer for the scattering of a broadband monopole by a NACA 0012 airfoil with varying α, $M_\infty = 0.2$, non-uniform flow. 134

5.16 PSD (dB/Hz) at the $\theta = 90°$ observer for the scattering of a broadband monopole by a NACA 0012 airfoil with varying M_∞, $\alpha = 5°$, non-uniform flow. 136
5.17 PSD contour (dB/Hz) of the scattered signal over a non-uniform flow at observer angles $0° \leq \theta \leq 180°$, NACA 0012 airfoil, $M_\infty = 0.2$, $\alpha = 5°$. 137
5.18 PSD (dB/Hz) at the $\theta = 90°$ observer for the scattering of a broadband monopole by an RA16SC1 airfoil with varying configuration, $\alpha = 0°$, $M_\infty = 0.2$, non-uniform flow. 138
5.19 PSD contour (dB/Hz) of the scattered signal over a non-uniform flow at observer angles $0° \leq \theta \leq 180°$, RA16SC1 airfoil with flap 20°, $M_\infty = 0.2$, $\alpha = 0°$. 139
5.20 PSD contour (dB/Hz) of the scattered signal over a non-uniform flow at observer angles $0° \leq \theta \leq 180°$, RA16SC1 airfoil with flap 40°, $M_\infty = 0.2$, $\alpha = 0°$. 140
5.21 PSD contour (dB/Hz) of the scattered signal over a non-uniform flow at observer angles $0° \leq \theta \leq 180°$, RA16SC1 airfoil with flap 40° plus slat, $M_\infty = 0.2$, $\alpha = 0°$. 140
5.22 Comparison of the SPL (dB) obtained from the broadband and single frequency simulations at 250Hz. 143

6.1 The size and location of the ground plane in relation to the runway at the approach reference point. 149
6.2 Airbus A320-style geometry with CFM56 engine nacelles, showing monopole source locations. 152
6.3 Mesh detail of the 500 Hz mesh with flaps deployed, showing the starboard nacelle, pylon, and lower wing surface. 153
6.4 Mesh detail of the 500 Hz mesh with flaps deployed, showing the starboard pylon, lower wing surface, and flaps. 153
6.5 SPL (dB), directivities from *SotonLGAP* in the streamwise direction. A320 MLG without installation effect. 156
6.6 SPL (dB), directivities from *SotonLGAP* in the streamwise direction. A320 NLG without installation effect. 157
6.7 Standard deviation (dB) of the directivity at each frequency for the A320 MLG and NLG directivity estimates from *SotonLGAP*. 159
6.8 Acoustic pressure (Pa) of the starboard MLG on the aircraft surface. Flaps deployed, source strengths without installation effect. 160
6.9 Sound pressure level (dB) of the starboard MLG on the ground plane. MLG source strengths without installation effect. 161
6.10 Sound pressure level (dB) of the NLG on the ground plane. 162
6.11 Sound pressure level (dB) of all landing gears on the ground plane. MLG source strengths without installation effect. 162
6.12 Sound pressure level (dB) of all landing gears on the ground plane. MLG source strengths with installation effect. 164
6.13 Alternative starboard MLG source locations. 165

6.14 Acoustic pressure (Pa) of the starboard MLG at 500 Hz on the aircraft surface. Flaps deployed, source strength without installation effect. 166
6.15 SPL (dB) on the ground plane for the starboard MLG at 500 Hz with flaps deployed. Source strength without installation effect. . . 167

A.1 Grid topology, circular cylinder. 182
A.2 Grid topology, NACA 0012 airfoil. 182
A.3 Grid topology, RA16SC1 airfoil. 183
A.4 Grid topology, RA16SC1 airfoil with flap 20°. 183
A.5 Grid topology, RA16SC1 airfoil with flap 40°. 184
A.6 Grid topology, RA16SC1 airfoil with flap 40° plus slat. 184
B.1 Reference images used for the construction of the A320-style geometry. 192
B.2 Creating the A320-style fuselage surface using *Larosterna Sumo*. . . 193
C.1 Source location for *ACTIPOLE*. 60 % of the overall gear length beneath the pressure surface of the wing. 198
C.2 Example contents of the *ACTIPOLE* observer position file `ACTIPOLE_observer_locations.txt` for a 2-D grid. 198
C.3 Example of observers specified in *SotonLGAP* to generate landing gear sources for *ACTIPOLE*. 199
D.1 Non-uniform base flow Mach number magnitude and streamlines, NACA 0012 airfoil, $\alpha = 5°$, $M_\infty = 0.2$. 201
D.2 Non-uniform base flow Mach number magnitude and streamlines, RA16SC1 airfoil, $\alpha = 0°$, $M_\infty = 0.2$. 201
D.3 Non-uniform base flow Mach number magnitude and streamlines, RA16SC1 airfoil with flap 20°, $\alpha = 0°$, $M_\infty = 0.2$. 202
D.4 Non-uniform base flow Mach number magnitude and streamlines, RA16SC1 airfoil with flap 40°, $\alpha = 0°$, $M_\infty = 0.2$. 202
D.5 Acoustic pressure (Pa), NACA 0012, $\alpha = 5°$, 125 Hz. 203
D.6 Acoustic pressure (Pa), NACA 0012, $\alpha = 5°$, 250 Hz. 204
D.7 Acoustic pressure (Pa), NACA 0012, $\alpha = 5°$, 500 Hz. 205
D.8 Acoustic pressure (Pa), RA16SC1, $\alpha = 0°$, 125 Hz. 206
D.9 Acoustic pressure (Pa), RA16SC1, $\alpha = 0°$, 250 Hz. 207
D.10 Acoustic pressure (Pa), RA16SC1, $\alpha = 0°$, 500 Hz. 208
D.11 Acoustic pressure (Pa), NACA 0012, $\alpha = 3°$, 250 Hz. 209
D.11 Acoustic pressure (Pa), NACA 0012, $\alpha = 3°$, 250 Hz (continued). . . 210
D.12 Acoustic pressure (Pa), NACA 0012, $\alpha = 5°$, broadband. 211
D.13 Acoustic pressure (Pa), RA16SC1, $\alpha = 0°$, broadband. 212
D.13 Acoustic pressure (Pa), RA16SC1, $\alpha = 0°$, broadband (continued). . 213

List of Tables

2.1 Effect of non-uniform flow on simple sources using LEE. 18
2.2 BEM flow formulations. 23
2.3 Computational complexity of the BEM and its accelerated methods. 25
2.4 Computation of aircraft noise using BEM. 27

3.1 Overview of employed solvers and codes. 40
3.2 Overview of employed BEM solvers. 43
3.3 Source radii, and average and maximum percentage error in p_{rms} against the analytical solution across all observers. 61

4.1 Required source radius R for each frequency given a maximum Mach number of $M_\infty = 0.3$. 74
4.2 Convective amplification for a monopole in a uniform free-stream at $M_\infty = 0.2$. 94
4.3 Average absolute percentage error in p_{rms}, denoted by ψ, for observers in the range $0° \leq \theta \leq 180°$. BEM vs LEE, without flow. . . 108

5.1 The relationship at the $\theta = 90°$ observer between the acoustic wavelength λ and the distance d between the source and the airfoil surface in the y-direction. NACA 0012 airfoil, $d = 2.235\,\text{m}$. 136

6.1 Values of mean SPL at 1 m for the A320 MLG with installation effect. 163

A.1 2-D LEE scattering validation simulation. 181
A.2 Details of 2-D LEE airfoil grids. 181
A.3 2-D LEE single frequency simulations. 185
A.4 2-D LEE single frequency simulations with a higher Mach number. . 188
A.5 2-D LEE single frequency simulations with an alternative source location. 189
A.6 3-D LEE single frequency simulations. 189
A.7 2-D LEE broadband simulations. 189
B.1 3-D BEM scattering validation simulation. 191
B.2 3-D BEM airfoil simulation. 191
B.3 Details of 2-D boundary meshes for the BEM and panel solvers. . . 192
B.4 Details of 3-D A320 boundary element meshes. 194
B.5 3-D BEM aircraft simulations. 194
B.6 3-D BEM aircraft simulations with alternative source positions. . . 195
B.7 Airbus A320 MLG geometry input for *SotonLGAP*. 195
B.8 Airbus A320 NLG geometry input for *SotonLGAP*. 196

B.9 Mean values of SPL and equivalent source strengths for A320 MLG and NLG from *SotonLGAP* estimate without installation effect. . . 196
B.10 Mean values of SPL and equivalent source strengths for A320 MLG from *SotonLGAP* estimate with installation effect. 196
C.1 Additional variables in *SotonLGAP* input file `input.xls` that control *ACTIPOLE* output. 197

Declaration of Authorship

I, Timothy James Heffernon, declare that the thesis entitled *Aircraft Noise Installation Effects* and the work presented in the thesis are both my own, and have been generated by me as the result of my own original research. I confirm that:

- This work was done wholly or mainly while in candidature for a research degree at this University;
- Where any part of this thesis has previously been submitted for a degree or any other qualification at this University or any other institution, this has been clearly stated;
- Where I have consulted the published work of others, this is always clearly attributed;
- Where I have quoted from the work of others, the source is always given. With the exception of such quotations, this thesis is entirely my own work;
- I have acknowledged all main sources of help;
- Where the thesis is based on work done by myself jointly with others, I have made clear exactly what was done by others and what I have contributed myself;
- Parts of this work have been published by the author, as listed in Section 1.2.

Signed:.....

Date:.....

Acknowledgements

Firstly, I would like to thank my supervisors Doctor David Angland, Professor Xin Zhang, and Doctor Malcolm Smith, for all of their support and guidance during my work on this thesis.

I am very grateful to Airbus for providing funding and support for this work through the Airbus Noise Technology Centre. Thanks must go to Ahmed Bennani at IMACS, École Polytechnique, for all of his advice regarding the *ACTIPOLE* solver. I also acknowledge the use of the IRIDIS High Performance Computing Facility, and associated support services at the University of Southampton, in the completion of this work.

Thanks must go to my colleagues James, Ryu, Mike, Fernando, Ravish, and Sylvain, for their support, all of the interesting discussions, and helping make my time at the University of Southampton so enjoyable.

I would like to thank my parents Dennis and June, whose unwavering belief in me and support in every possible way has helped to get me to where I am today.

Finally, I would like to thank Sarah, who has been by my side throughout my work on this thesis, and who has been a never-ending source of support, motivation, and encouragement. Time for our next adventure together.

Nomenclature

Symbols

a	airfoil chord length	m
C_L	coefficient of lift	
C_p	coefficient of pressure	
c	speed of sound	$\mathrm{m\,s^{-1}}$
D	number of samples in a signal	
d	distance between the source and the airfoil surface in the y-direction	m
d_c	component diameter	m
E	number of elements in a multi-element airfoil	
$\mathcal{F}$	Fourier transform	
F	monopole forcing region function	
f	acoustic frequency	Hz
G	Green's function	
H	Fourier transformed broadband input signal	
$H_n^{(1)}$	Hankel function of the first kind of order n	
i	complex unit	
k	acoustic wavenumber	$\mathrm{rad\,m^{-1}}$
L	segment length for Welch's method	

l_c	component length	m
M	Mach number	
$N_{i,j}$	normal influence coefficient	
$\mathbf{n}$	normal vector	
n	normal	
P	number of surface panels	
p	pressure	Pa
Q	monopole source strength	
R	distributed monopole source radius	m
r	distance between two points	m
$\mathbf{S}$	monopole source function	
S	surface	
s	number of standard deviations in Gaussian source distribution radius	
T	Taylor-transformed time	s
$T_{i,j}$	tangential influence coefficient	
t	time	s
$\mathbf{u}$	velocity vector	$\mathrm{m\,s^{-1}}$
V	velocity magnitude	$\mathrm{m\,s^{-1}}$
$\mathbf{v}$	velocity vector	$\mathrm{m\,s^{-1}}$
$\mathbf{X}$	Taylor-transformed position vector	m
$\mathbf{x}$	position vector	m
$\mathbf{y}$	position vector	m
Z	Fourier transformed received broadband signal	

Greek Symbols

α	angle of attack	deg
β	monopole forcing region parameter	
γ	potential flow vortex strength	
Δt	time step	s
δ	delta function	
ϵ	monopole amplitude parameter	
ζ	received broadband signal	
η	broadband input signal	
θ	observer angle	deg
κ	modified acoustic wavenumber	$\mathrm{rad\,m^{-1}}$
λ	acoustic wavelength	m
Ξ	transfer function	
ξ	impulse response	
ρ	density	$\mathrm{kg\,m^{-3}}$
σ	potential flow source strength	
Φ_a	time-dependent acoustic potential	$\mathrm{m^2\,s^{-1}}$
ϕ_a	time-harmonic acoustic potential	$\mathrm{m^2\,s^{-1}}$
ϕ_f	flow potential	$\mathrm{m^2\,s^{-1}}$
φ	phase angle	rad
χ	ratio of wavelength to source radius	
ω	angular frequency	$\mathrm{rad\,s^{-1}}$
ψ	average absolute percentage error in p_{rms}	

Subscripts

ref	reference
rms	root mean square
s	monopole source
t	tangential component
0	mean flow variable
∞	free-stream

Superscripts

d	disturbance
I	incident
S	scattered
$'$	acoustic variable
$*$	non-dimensional variable
$\sim$	Lorentz-transformed variable
$\wedge$	Taylor-transformed variable
$-$	Taylor-transformed Helmholtz variable
$\vee$	unit vector
∞	free-stream

Abbreviations

1-D	One-Dimensional
2-D	Two-Dimensional
3-D	Three-Dimensional
ACA	Adaptive Cross Approximation
AIAA	American Institute of Aeronautics and Astronautics
APE	Acoustic Perturbation Equations

BEM	Boundary Element Method	
BIE	Boundary Integral Equation	
CAA	Computational Aeroacoustics	
CFD	Computational Fluid Dynamics	
CFL	Courant-Friedrichs-Lewy	
DES	Detached Eddy Simulation	
DFT	Discrete Fourier Transform	
DGM	Discontinuous Galerkin Method	
DNS	Direct Numerical Simulation	
DRM	Dual-Reciprocity Method	
EASA	European Aviation Safety Agency	
EPNL	Effective Perceived Noise Level	EPNdB
ESM	Equivalent Source Method	
FDM	Finite Difference Method	
FEE	Full Euler Equations	
FEM	Finite Element Method	
FMM	Fast Multipole Method	
FWH	Ffowcs Williams and Hawkings	
GTF	Gradient Term Filtering	
GTM	Gradient Term Modification	
GTS	Gradient Term Suppression	
LBM	Lattice Boltzmann Method	
LDDRK	Low-Dissipation and low-Dispersion Runge-Kutta	
LEE	Linearised Euler Equations	
LES	Large Eddy Simulation	

MLG	Main Landing Gear	
NLG	Nose Landing Gear	
OASPL	Overall Sound Pressure Level	dB
PDE	Partial Differential Equation	
PDF	Probability Density Function	
pFFT	Precorrected Fast Fourier Transform	
PML	Perfectly Matched Layer	
PPW	Points Per Wavelength	
PSD	Power Spectral Density	
RANS	Reynolds-Averaged Navier-Stokes	
RMS	Root Mean Square	
SGS	Sub Grid Scale	
SNGR	Stochastic Noise Generation and Radiation	
SPL	Sound Pressure Level	dB
SST	Source Simulation Technique	
URANS	Unsteady Reynolds-Averaged Navier-Stokes	

Chapter 1

Introduction

1.1 Motivation and Aims

Noise emissions from aircraft are a nuisance to communities in the vicinity of airports. Exposure to aircraft noise has been linked to various non-auditory health effects. These include annoyance, sleep disturbance, hypertension and cardiovascular disease, and impairment of cognitive performance in children [1]. Increasingly stringent noise regulations are being enforced in an effort to reduce the environmental impact of the aviation industry on communities living and working near to airports.

Each aircraft type must undergo noise certification. There are three reference points for aircraft noise certification where noise levels are measured: approach, lateral/sideline, and flyover/cutback [2]. These are illustrated in Figure 1.1. The metric used to quantify the noise level for certification at each reference point is the effective perceived noise level (EPNL) measured in units of EPNdB, as set out by the International Civil Aviation Organization [3]. This measure takes into account the spectral content and duration of the noise from an aircraft passing a given point. Each aircraft type must have an EPNL below a given limit at each reference point to gain certification. This limit varies with aircraft takeoff weight and number of engines [4]. The European Commission has set a target to reduce the EPNL for aircraft by 65 % by the year 2050 relative to a new aircraft in 2000 [5]. It is therefore important to understand both how aircraft noise is generated, and how this noise propagates to the far-field.

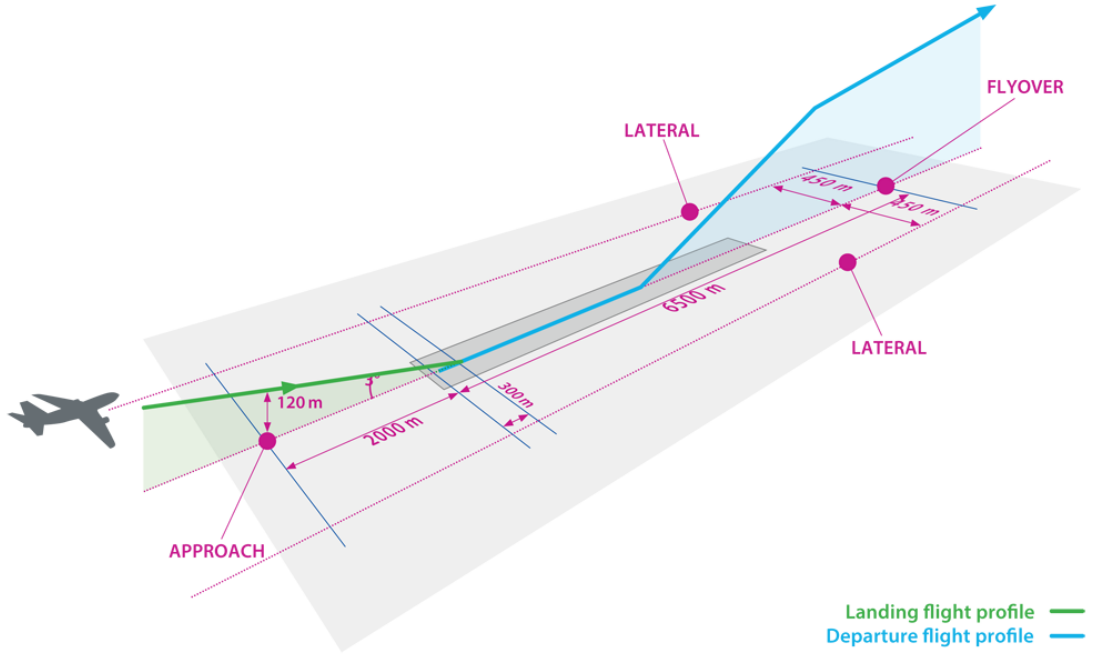

Figure 1.1: Aircraft noise certification reference points. Copyright EASA, reproduced with permission from [2].

The noise from an aircraft can be categorised as being one of two types: engine noise or airframe noise. Turbofan engines featuring a bypass design were introduced in the 1970s, primarily to improve fuel consumption. However, a beneficial consequence of the new design was a reduction in noise from the engines [6]. Further increases in the engine bypass ratio over the subsequent decades, along with research into engine noise, has led to further large reductions in noise from engines. The extent of this ongoing reduction in engine noise is such that airframe noise is now comparable to engine noise on approach [6].

At the approach reference point, an aircraft will have flaps, slats, and landing gears deployed. These are all major sources of airframe noise, and lead to a large contribution from the airframe to the overall perceived noise. Merino-Martínez *et al.* [7] conducted an analysis of landing gear noise during approach using functional beamforming. Data were acquired from seven Airbus A320 flyovers. Figure 1.2a shows a beamforming source plot example for an A320 flyover. The dominant noise sources can be seen to be the nose landing gear, and a combination of the main landing gears and flaps. The authors noted that due to the proximity of the main landing gears to the flaps, and the interaction of the wakes from the main landing gears with the deployed flaps, it was difficult to separate the individual contribution of the main landing gears using the current experimental setup. Figure 1.2b shows the relative contribution of the nose landing gear to the total noise

for an Airbus A320 in the form of boxplots. The boxplot for the nose landing gear was created by extracting the maximum value of the overall sound pressure level (OASPL) in the nose landing gear region for each flyover. The nose landing gear region is shown by the black box in Figure 1.2a. It can be seen in Figure 1.2b that the average OASPL of the nose landing gear is approximately 4 dB lower than the average total OASPL. This highlights that landing gear noise is a significant contributor to the overall noise.

In order to better understand the noise generating mechanism of each of the component parts of an aircraft, the parts are investigated in isolation using experimental or computational methods. However, in doing so, the effects of installing a noise source in proximity to an aircraft airframe are not observed. Installation effects can drastically alter the observed far-field noise. This can be due to the scattering of the source by the airframe, or local flow variations around the airframe altering the strength of the source or how it propagates to the far-field.

The focus of this thesis is on the installation effects of landing gears beneath a lifting wing. The non-uniform flow around a lifting wing can be decomposed into circulation and a uniform free-stream, as illustrated in Figure 1.3. The Kutta condition states that the strength of the circulation must ensure that the non-uniform flow leaves the trailing edge of the wing smoothly. This implies that the rear stagnation point is located at the trailing edge of the wing. The strength of

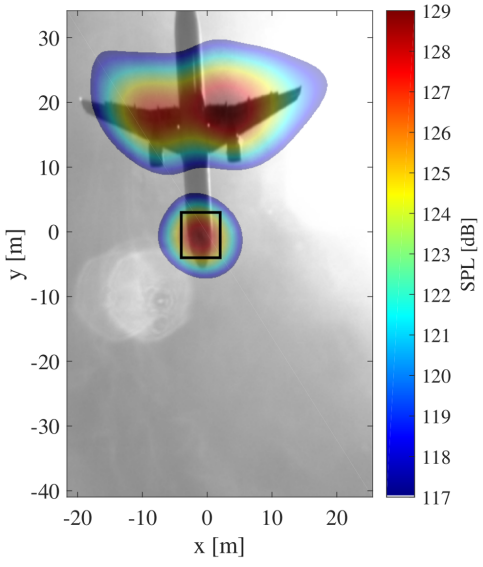

(a) Beamforming source plot example.

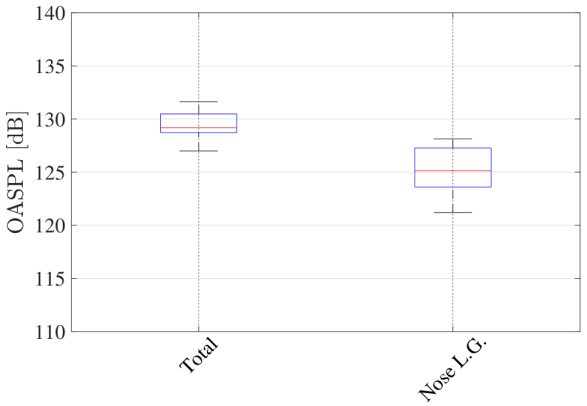

(b) Boxplots of the measured total OASPL and the OASPL of the nose landing gear. The whiskers represent the most extreme data points.

Figure 1.2: The relative contribution of landing gear noise to the overall noise for an Airbus A320. Copyright AIAA, reproduced with permission from [7].

the circulation is therefore unique for a given angle of attack and Mach number. Due to the circulation, the flow velocity beneath the airfoil is reduced compared to the free-stream. This reduces the strength of the noise generated by a landing gear installed in this region of flow [8].

Velocity gradients exist in the non-uniform flow around the wing due to circulation. These velocity gradients cause the refraction of acoustic waves as the waves propagate through the non-uniform flow. Figure 1.4a shows an example streamwise velocity gradient typical of that found beneath a lifting wing. The effect of this velocity gradient on the propagation of acoustic waves from a point source in the upstream and downstream directions is illustrated in Figure 1.4b. It is one of the aims of this thesis to quantify the extent of this effect on landing gear noise sources at Mach numbers representative of a commercial airliner on approach. The main landing gears of commercial aircraft are typically located beneath the wing, and are deployed when the aircraft is on approach. Flaps and slats are also typically deployed when an aircraft is on approach. These not only increase the circulation around the wing, but alter the reflective underside of the scattering wing surface. It is another aim of this thesis to investigate the effect of flap and slat deployment on the scattered sound.

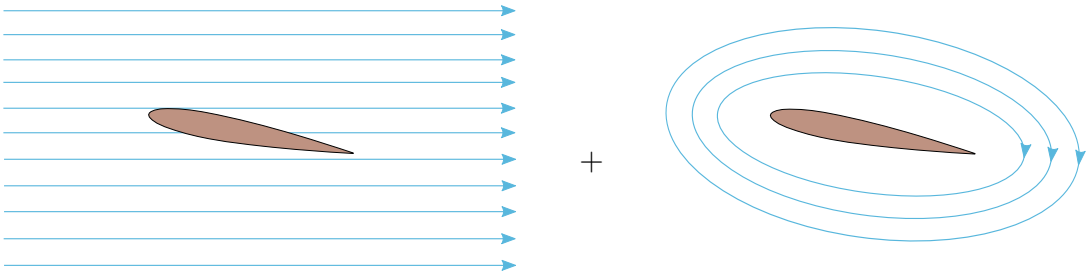

(a) Uniform flow.

(b) Circulation.

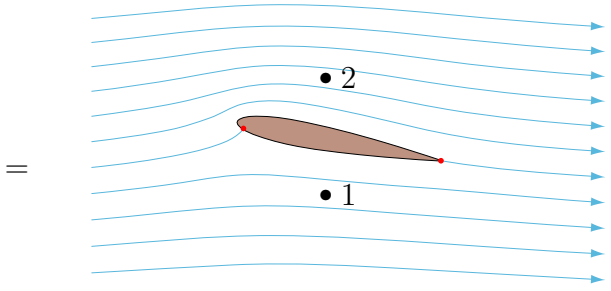

(c) Non-uniform flow.

Figure 1.3: The contribution of circulation to the non-uniform flow around a lifting wing. The velocity at point 1 < the free-stream velocity, and the velocity at point 2 > the free-stream velocity.

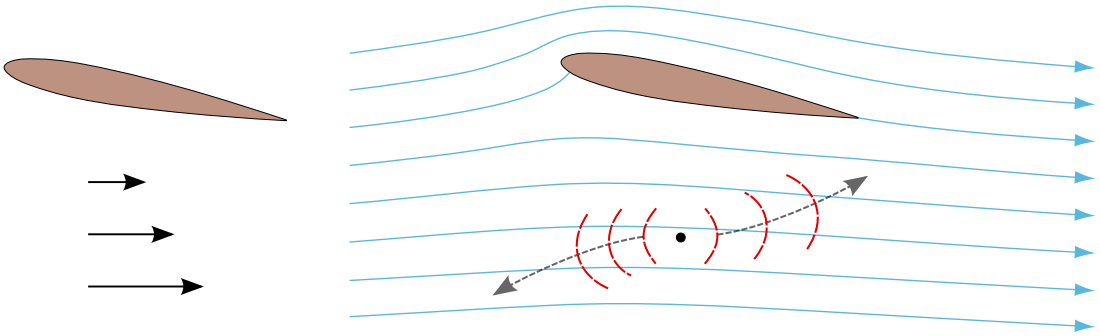

(a) Velocity gradient.

(b) Acoustic waves from a point source.

Figure 1.4: The refraction of acoustic waves from a point source beneath a lifting wing due to the streamwise flow velocity gradient in this region.

Simple acoustic sources are used throughout the current work to represent idealised landing gear noise sources, and so the emphasis is on noise propagation rather than generation. A high-order solver for the linearised Euler equations (LEE) is used to compute the scattered sound field around various isolated airfoil configurations. The LEE are able to represent the refraction effects of a non-uniform flow on the sound field. The boundary element method (BEM) is an alternative to solving the LEE that allows the computation of acoustic scattering by large and complex geometries. However, due to the use of Green's functions in the BEM, flow effects can only be approximated. As a consequence, refraction effects are not accounted for by the available BEM flow formulations. It is an aim of this thesis to assess two available BEM flow formulations for their suitability for landing gear noise scattering problems. The final aim is to couple an existing realistic landing gear noise source model with a BEM solver, and use sources generated using this method to investigate the scattering of landing gear noise by a complete aircraft geometry.

The aims of this thesis are summarised as follows:

- To quantify the effect of non-uniform flow due to circulation around a lifting wing on the scattering of landing gear noise sources.
- To investigate the effect of flap and slat deployment on the scattered sound.
- To evaluate existing BEM flow formulations for their suitability to model landing gear noise installation effects.
- To couple a realistic landing gear noise source model with a BEM solver, and use this model to investigate the scattering of landing gear noise by a complete aircraft geometry.

1.2 Original Contributions

The original contributions of this thesis are as follows:

- The effect of non-uniform flow due to circulation around a lifting wing on the acoustic scattering of installed harmonic simple sources has been investigated computationally. The circulation was varied by varying the angle of attack and Mach number of a single-element airfoil, and flap configuration of a multi-element airfoil. The effect of the non-uniform flow was quantified as the difference in acoustic scattering over uniform and non-uniform base flows.

- Existing uniform and non-uniform flow BEM approximation methods were evaluated for their suitability to model the scattering of landing gear noise. The accuracy of each method is determined through comparison with an equivalent LEE solution, under the assumption that the LEE solution is correct.

- A new method has been proposed to generate a modified broadband input signal for a LEE solver that gives a prescribed power spectral density (PSD) at a given distance from a simple source. An existing method was used to generate the original broadband input signal, but it was seen in free-field simulations that the PSD at the observer radius was not the same as that of the original input signal.

- The modified broadband input signal was used to computationally investigate the effect of non-uniform flow due to circulation around a lifting wing on the acoustic scattering of an installed broadband simple source.

- A frequency analysis of the scattered field produced by the installed broadband source was conducted to determine the effect of both flow and airfoil shape on the PSD computed at various observers.

- A method to couple a landing gear noise source model with a BEM solver has been proposed. The method was used to investigate the scattering of installed simple sources in the approximate positions of landing gear by a full aircraft geometry. The sound pressure level (SPL) was computed on a ground plane at the approach reference point, and the effect of flap deployment was investigated.

A proof-of-concept study for the investigations detailed in Chapter 4 was presented at the 21st AIAA/CEAS Aeroacoustics Conference [9]. A journal paper has been

submitted to the *Journal of Computational Acoustics* [10], which details the new method presented in Chapter 5 for the specification of a broadband monopole with a target spectrum for computational aeroacoustics applications.

1.3 Thesis Structure

A review of the relevant literature is presented in Chapter 2, including a discussion on its influence on the work in this thesis.

The governing equations for acoustics under the influence of flow that are used throughout this thesis are detailed in Chapter 3, along with the numerical methods used for their solution. This also includes validations of all acoustic solvers for scattering problems, and the implementation and validation of a two-dimensional (2-D) panel solver for potential flow around an airfoil.

Investigations into the scattering of a harmonic source by an airfoil are presented in Chapter 4. The effect of non-uniform flow due to circulation around the lifting wing on the scattering was investigated using a LEE solver. The effect of varying the angle of attack and Mach number on the scattering was studied using a single-element airfoil, and the effect of flap deployment was studied using a multi-element airfoil. The effect of a higher Mach number and an alternative source location is also presented. These investigations were conducted using 2-D simulations due to computational cost. Additional three-dimensional (3-D) simulations were also conducted in order to determine if the 2-D results were representative of what would be observed if the investigations were conducted using 3-D simulations. Under the assumption that the 2-D LEE results were correct, the uniform and non-uniform flow BEM approximation methods were evaluated against the LEE solutions.

The extension of the single frequency LEE investigations to the scattering of a broadband source by an airfoil is presented in Chapter 5. A suitable broadband input signal was generated using an existing method from the literature. However, initial simulations showed that the observed PSD at a distance from the source was different from that of the input signal. The reason for this is explained, and a new method to generate a modified input signal that gives the desired PSD at the observer radius is presented. This modified signal was used to determine the effect of non-uniform flow due to circulation around the lifting wing on the acoustic scattering. A frequency analysis of the scattered source was conducted.

This also allowed the comparison of the results at discrete frequencies from the broadband simulations with the equivalent single frequency simulations from the previous chapter.

The scattering of single frequency sources by a complete aircraft geometry was investigated using a BEM solver, and this is presented in Chapter 6. Modelling assumptions were made based on the conclusions from the previous investigations into scattering by an isolated airfoil. A new method is proposed to couple a landing gear noise source model with the acoustic solver in order to give realistic values for the computed SPL. The effect of flap deployment on the SPL on the ground at the approach reference point was investigated. The effect of varying the positions of the single frequency sources in relation to the scattering body was also investigated.

Finally, a summary of the results of this thesis and a discussion on possible future work is given in Chapter 7.

Chapter 2

Aeroacoustics and Aircraft Noise

2.1 Introduction

The topic of aircraft noise is currently an active area of research. Computational and experimental aeroacoustic methods are being used to investigate the generation and propagation of noise from engines, airframe, and internal aircraft systems such as air conditioning. Airframe noise is generated from separated and turbulent flows interacting with the airframe [11]. Turbofan engine noise is generated from turbulent flow over fans/compressors/turbines, fuel combustion, and jet mixing [4]. Propeller engine noise is generated from steady blade loading and blade thickness, or from turbulent flow passing over the blades [12]. In all cases, the generated noise must propagate through non-uniform flow to reach the far-field. It is the propagation of airframe noise, specifically landing gear, that is the focus of this thesis.

A review of the relevant literature is presented in this chapter. Section 2.2 presents an overview of computational methods used in the field of aeroacoustics. The generation, propagation, and radiation of noise to the far-field using domain-based methods is presented first, including examples of the application of the methods. An alternative approach to computing the propagation of noise using the BEM is then presented, along with flow approximation methods, and methods for accelerating a BEM solver. Examples of applications of the BEM to aeroacoustic problems are included. An overview of the generation and characteristics of landing gear noise is given in Section 2.3. Section 2.4 provides an overview of the installation effects of landing gear. Finally, a discussion of the presented literature and its influence on the work in this thesis is given in Section 2.5.

2.2 Computational Methods

2.2.1 Modelling of Noise for a Computational Approach

The generation of noise from an airframe or engine, and its subsequent propagation to the far-field, can be divided into three regions for computation [11]:

Region 1 Generation of noise.

Region 2 Propagation and scattering of noise in the near-field.

Region 3 Radiation of scattered noise to the far-field.

In Region 1, the turbulent flow and acoustics are strongly coupled. They influence each other and cannot be separated. In Region 2, the turbulence is low and the flow and acoustics are only weakly coupled. The non-uniform flow influences the acoustic propagation without feedback, and the acoustic propagation may be subject to strong refraction effects [13]. Scattering effects from aircraft surfaces may also be included in this region. In Region 3, the acoustics propagate to the far-field. Depending upon the frame of reference for the observers, this may be over a uniform flow with weak coupling, or a stationary media.

The Navier-Stokes equations fully describe all of the aeroacoustic mechanisms for all regions. However, it is currently computationally prohibitive to solve the Navier-Stokes equations using computational fluid dynamics (CFD) methods for a computational domain that is large enough to encompass all regions. Alternative methods can be used that are more efficient for the computation of propagation and radiation of noise. CFD methods are still regularly used to compute noise sources, as described in Section 2.2.3. More recently, the lattice Boltzmann method (LBM) has also been used to compute noise sources. The LBM solves the discrete Boltzmann equation instead of the Navier-Stokes equations. This method is further described in Section 2.2.3.

Computational aeroacoustics (CAA) methods are generally employed to compute acoustic propagation in Region 2 instead of using conventional CFD methods for the following reasons [11]:

- A vast difference in length scales between the aerodynamic and acoustic fields.
- A need to study a large frequency range, from 20 Hz to 20 kHz.

- The numerical dissipation that occurs in conventional CFD that leads to the damping of acoustic perturbations.
- The numerical dispersion that leads to errors for non-dispersive acoustic perturbations.

The CAA methods solve simplified equations that are valid under certain assumptions, and use acoustic sources from Region 1. These methods are described in Section 2.2.4. Having computed the acoustic propagation in the near-field, an acoustic analogy may be used to compute the radiation of noise to the far-field. This is described in Section 2.2.2.

The solution technique that uses CFD methods to generate acoustic sources followed by CAA methods to compute the propagation is often referred to as the hybrid CFD/CAA method. It should also be noted that the far-field noise may be computed using an acoustic analogy directly from CFD results without the use of a CAA method.

2.2.2 Far-Field Noise Estimation

Acoustic analogies are used to compute far-field noise from near-field flow. The generation and propagation of sound from fluid in motion is replaced by equivalent sources in a stationary media. Each analogy is derived from the compressible Navier-Stokes equations, and results in an inhomogeneous wave equation with the equivalent source terms on the right hand side. The three most important acoustic analogies are:

Lighthill [14] Valid for flows with no solid boundaries present. Used to calculate noise from turbulent jets.

Curle [15] Valid for stationary bodies in a flow.

Ffowcs Williams and Hawkings [16] Valid for bodies in arbitrary motion in a flow.

Due to its generality, the Ffowcs Williams and Hawkings (FWH) analogy is commonly used with CFD and CAA methods in order to predict far-field noise. Pressure data is acquired on a control surface, and the strength of the equivalent sources on this surface are then calculated from this data. Use of the Kirchhoff Integral Theorem results in a surface integral that allows the computation of far-field noise from the equivalent sources through the use of Green's functions. This

is similar to part of the BEM solution process, and an FWH solver can also be accelerated using fast BEM techniques [17]. The control surface may be solid and located on the surface of a noise generating body, or permeable and located so as to enclose the noise source and a region of flow surrounding it. The permeable surface has the advantage of being able to account for near-field propagation through non-uniform flow, and the scattering of noise from any nearby body. To ensure that these effects are correctly accounted for, the control surface should be located in a region of flow that is sufficiently uniform.

2.2.3 Noise Generation

Noise sources in Region 1 may be obtained through the use of a semi-empirical model, or through the use of CFD methods. Semi-empirical models use scaling laws for aerodynamic noise from solid bodies in a flow [15, 16], and correlate these results with experimental data through the use of calibrated empirical constants. Examples of such semi-empirical models for landing gear include those by Smith and Chow [18, 19], and Guo [20].

For the CFD approach, the computational domain is constructed to contain the geometry of interest and the surrounding turbulent flow field. Due to computational constraints, this might only include, for example, a landing gear, or an airfoil. Various CFD methods may be used to compute the turbulent flow field through the solution of the Navier-Stokes equations. These include [21]:

- direct numerical simulation (DNS),
- large eddy simulation (LES),
- detached eddy simulation (DES),
- unsteady Reynolds-averaged Navier-Stokes (URANS).

DNS does not use any turbulence modelling. The result is exact, but is expensive to obtain. LES assumes that geometry-dependent large eddies are resolved by the grid, and uses a sub grid scale (SGS) model to model the small eddies. The computational cost for LES is reduced compared to DNS, although it is still high. All turbulence is modelled in URANS, which means that it is less expensive than LES, however it does not capture all of the turbulent wake structures. Finally, DES combines the strengths of both LES and URANS by using URANS near the walls for its computational efficiency, and LES in the free-stream to capture

the geometry-dependent large eddies. In all cases, the fluctuating pressure can be used as source terms for further acoustic propagation or radiation. It is also possible to use steady Reynolds-Averaged Navier-Stokes (RANS) methods coupled with the stochastic noise generation and radiation (SNGR) method to obtain the fluctuating acoustic pressure [22]. The SNGR method can also be used to generate source terms in the frequency domain [23].

There are many examples of noise generation using CFD methods in the literature. Spalart *et al.* [24] used DES to compute the turbulent flow around a rudimentary four-wheel landing gear. Their method was coupled with an FWH solver, and they evaluated various configurations of solid on-body and permeable off-body control surfaces. Liu *et al.* [25] used DES in order to compute the flow around a generic two-wheel nose landing gear. They computed far-field noise using a solid on-body FWH surface. A different approach was taken by Wolf and Lele [26], who used LES to compute the turbulent flow around a NACA 0012 airfoil in order to investigate trailing-edge noise. Far-field noise was computed using an accelerated FWH solver with a solid on-body control surface.

More recently, the LBM has been used to compute noise sources. The LBM uses a microscopic fluid model with mesoscopic kinetic equations, as opposed to the macroscopic model described by the Navier-Stokes equations. A mesoscopic probability density function is used to describe the probability of finding a given microscopic particle at a given point in space and time with a given velocity. This function obeys the Boltzmann transport equation, which describes the effect of particle streaming and collision on the probability distribution function. The particle velocity space is discretised using a lattice in order to derive the lattice Boltzmann equation, which is used for computational solution. Turbulence modelling may also be incorporated into the lattice Boltzmann equation.

Casalino *et al.* [27] used a LBM solver to compute the turbulent flow around a simplified two-wheel landing gear. Their method was coupled with an FWH solver using a solid on-body control surface, and this allowed comparison with available experimental data. Casalino *et al.* [28] investigated turbofan broadband noise using a LBM solver, with the aim of reproducing experiments performed by the NASA Glenn Research Center. The geometry employed to obtain the numerical solutions was identical to the test rig used to obtain the experimental data. Far-field noise was computed using a permeable off-body FWH control surface. This surface was located so as to enclose the nacelle geometry, and was extended downstream and opened at its downstream extremity in order to avoid contamination of

the acoustic solution by jet shear layer hydrodynamic fluctuations. Both near-field and far-field results showed consistent trends with the experimental data. Fares *et al.* [29] presented an example of the LBM being used for full aircraft noise prediction. An 18 % scale semi-span Gulfstream aircraft model in landing configuration was used to evaluate various noise reduction concepts for the flap and main landing gear. A solid on-body FWH surface was used to predict the far-field noise for each concept.

2.2.4 Noise Propagation and Computational Aeroacoustic Methods

Due to the reasons summarised in Section 2.2.1, CAA methods are used instead of CFD methods for the computation of acoustic propagation. The acoustic pressure is generally at least one or two orders of magnitude lower than the mean flow pressure. Acoustic waves can be easily damped by CFD methods that generally use low-order schemes for stability and robustness. The need to study a large frequency range necessitates the creation of computational grids that are refined enough to properly resolve acoustic waves at the frequency of interest. This level of refinement is much higher than is required to resolve aerodynamic fields in regions of relatively uniform flow, and needs to remain constant throughout the domain of interest. This is in contrast to CFD methods where the grid is refined near to body surfaces in order to accurately compute boundary layers, but can then be coarsened away from this region.

Linearisation of the governing equations splits the problem into the computation of acoustic propagation over a rotational background flow, which helps to allow an accurate solution of acoustic waves. The background flow is assumed to be steady, and is computed before the acoustic solution. The key assumption made in the process of linearisation is that the flow influences the acoustic waves without feedback. Non-linear feedback occurs when the acoustic pressure is of a similar magnitude to the mean flow pressure, and so linearisation is only valid for cases where non-linear effects are not expected. This is true for landing gear noise propagation, but would not be so in the vicinity of a turbofan intake duct for example. Neglecting viscosity from the Navier-Stokes equations gives the full Euler equations (FEE). Linearising the FEE about a mean flow field yields the LEE. The LEE support acoustic, vorticity, and entropy wave solutions.

One solution strategy for the LEE is to use the finite difference method (FDM). High-order FDM spatial schemes on block-structured grids allow the accurate resolution of acoustic waves using a lower grid density than the low-order schemes that are typically employed in CFD methods. Examples of high-order FDM schemes include those by Hixon [30], Kim [31], and Kim and Sandberg [32]. The high-order schemes generally have lower dissipation and dispersion properties than the lower order CFD schemes, which leads to less error in computing the propagation of acoustic waves. However, this also leads to spurious high-frequency waves in the high-order schemes that can lead to instability. Therefore, a filtering scheme, such as one proposed by Kim [33] or Visbal and Gaitonde [34], must be used with these spatial schemes in order to remove the unwanted noise. In order to advance the solution in time, temporal schemes that have low dissipative and dispersive qualities are employed. One example of such a temporal scheme is the low-dissipation and low-dispersion Runge-Kutta (LDDRK) scheme proposed by Hu *et al.* [35].

In order to solve the LEE computationally, the acoustic domain needs to be a finite size. This would cause acoustic reflections from the artificial domain boundaries that would ruin the acoustic solution. Several different non-reflecting boundary condition methods have been proposed to overcome this difficulty. Explicit methods damp the solution vector explicitly after each time step in certain regions added to the edge of the computational domain. These regions are known as buffer zones. Implicit methods add an additional damping term to the governing equations in the buffer zones. The perfectly matched layer (PML) technique solves a different set of equations in the buffer zones, and matches the solution at the boundary with the computational domain where the LEE are solved. Characteristic methods use the LEE expressed in characteristic form on the domain boundaries. The characteristics represent the entropy wave, the vorticity wave, and the acoustic wave propagating in each direction. The characteristics of the waves propagating back into the domain are set to zero to prevent reflections. Studies by Gill *et al.* [36] and Richards *et al.* [37] describe and test various methods.

One drawback of the LEE is that Kelvin-Helmholtz instabilities may arise due to the absence of viscous forces. These instabilities generally arise where shear layers exist in the background flow. Solving the LEE in the frequency domain is one method of overcoming this difficulty [4]. Several time-domain gradient term modification (GTM) methods have been developed in an effort to overcome this drawback. The gradient term suppression (GTS) method neglects mean flow gradient terms from the governing equations [38]. The acoustic perturbation equations (APE) [39] and the gradient term filtering (GTF) method [40] both use filtering

to isolate the acoustic waves from the vortical waves and suppress the instabilities. These methods are reviewed in detail and evaluated by Sun *et al.* [41].

An alternative high-order method of solution for the LEE on unstructured grids is the discontinuous Galerkin method (DGM), which is reviewed in detail by Manoha *et al.* [13]. An alternative to solving the LEE is to solve convected wave equations, for which the finite element method (FEM) is often used [11]. Convected wave equations are generally restricted to irrotational mean flows [11], although methods to overcome this for sheared flows have been developed [42]. The computation of noise propagation through the use of any of the methods described in this section may be as part of a hybrid CFD/CAA method with noise sources provided by a CFD simulation. Alternatively, CAA methods may be used independently with noise sources provided by other means.

2.2.5 Hybrid Method Examples

There are many examples of the use of the hybrid CFD/CAA method for aircraft noise computations. Two examples are presented here. Drage *et al.* [43] used the hybrid method to compute the noise generated from turbulent flow over a half-cylinder geometry and a simplified two-wheel nose landing gear. To obtain the noise sources, they used a steady RANS approach coupled with the SNGR method in order to compute a turbulent velocity distribution in the vicinity of the landing gear. This turbulent velocity distribution was then used as a source term in the LEE, which were solved using an unstructured DGM solver using the RANS solution as the base flow. Pressure data were acquired on a permeable off-body FWH control surface in order to account for reflection and diffraction, and far-field noise was computed using an FWH solver. Experimental data was available for the half-cylinder geometry, and the hybrid method compared favourably with the experiment. An increase in flow velocity resulted in an increase in far-field noise as expected, although the absolute levels were lower for the hybrid method than the experiment.

Ma and Zhang [44] used LES to calculate the unsteady flow over an airfoil with slat deployed. The unsteady pressure was used to calculate source terms for the APE in order to investigate the effect of acoustic liner treatment on broadband slat noise attenuation. The APE were chosen due to the claim that the method was stable for arbitrary mean flow, including shear layers. However, instabilities arose due to the strong shear layer near the slat trailing edge. For this reason, a

uniform background flow was used instead of a non-uniform flow. The APE were coupled with a FWH solver to evaluate far-field noise using a permeable off-body control surface.

2.2.6 Near-Field Propagation Examples

Acoustic source terms are added to the LEE in order to compute solutions to near-field propagation problems. These source terms can be specified so as to generate simple sources and plane waves, as well as complex source regions using results from a CFD computation such as in the hybrid method. Studies using plane waves, simple sources, and pulses are often undertaken in order to better understand the effect of non-uniform flow on the refraction and scattering of acoustic waves in the near-field. Bailly and Juvé [45] presented the implementation of acoustic monopoles, dipoles, and quadrupoles for LEE methods. A monopole point source is singular at its origin, and thus a distributed source must be used in numerical methods where the source is located within the computational domain. Studies have been undertaken by various authors to investigate the effect of various non-uniform flows on the acoustic scattering of simple sources through solution of the LEE. These studies are summarised in Table 2.1, and highlight the suitability of the LEE for these kind of investigations.

The investigations listed in Table 2.1 generally implement harmonic sources. When the LEE are solved in the time-domain, it is also possible to use broadband sources. A broadband monopole source may be implemented by replacing the time-harmonic term in the source with a time-dependent signal. The simplest way to generate a time-dependent signal containing multiple frequencies for this purpose is to sum a number of sine/cosine waves of discrete frequencies with differing phases. This was demonstrated by Bin *et al.* [50] in their development of broadband impedance boundary conditions for CAA methods. However, a signal generated in this way could be temporally or spectrally coherent depending on the frequencies that it contains, which would not be representative of a stochastic turbulent source. In order to obtain an approximation for an incoherent source, multiple simulations of the source with differing phases for each frequency in each simulation would have to be undertaken and then ensemble averaged. Reboul and Polacsek [51] employed ensemble averaging in their investigation into aft radiation of broadband fan noise from a turbofan engine.

Table 2.1: Effect of non-uniform flow on simple sources using LEE.

Author	Year	Contribution
Bailly and Juvé [45]	2000	Harmonic monopole with a 2-D jet modelled with a Bickley's profile.
Redonnet *et al.* [46]	2001	Harmonic monopole with a steady shear layer, and steady vortex, amongst others.
Padois *et al.* [47]	2013	Numerical validation of shear flow corrections for open wind tunnels using a harmonic monopole source.
Si *et al.* [48]	2013	Acoustic pulse with a hyperbolic tangent profile for a shear flow, hyperbolic tangent profile for the flow between two streams, Bickley's profile for a subsonic jet flow, and hyperbolic tangent profile for a transonic flow.
Clair and Gabard [49]	2015	Scattering of a plane wave by a steady and a convected vortex, scattering of a harmonic monopole by a convected vortex. The monopole was located outside of the computational domain and injected through a sponge layer adjacent to the domain boundary.

Dragna *et al.* [52] implemented a moving broadband monopole source in an LEE solver for time-domain simulations of outdoor sound propagation. They gave a detailed mathematical analysis of the effect of the source distribution on the acoustic field. In particular, it was demonstrated that when the characteristic length scale of the distributed source is small with respect to the wavelength, the source can be considered compact and the observed convective amplification is the same as that of a point source. They also showed that the source distribution acts as a filter. This is due to the Fourier transform of the spatial distribution modulating the pressure. A broadband signal was synthesised by first multiplying the Fourier transform of a white noise signal by the desired power spectrum in the frequency domain, and then doing an inverse Fourier transform of the result. This signal was implemented with a distributed monopole that was moved in space parallel to a ground surface on each subsequent time step. Rigid and impedance ground surfaces were investigated. Ten realisations of the random source signal were performed for each case. The instantaneous PSD of pressure was computed at three observers for each realisation using a Fourier transform, and these were then averaged over the ten realisations to obtain a mean value for the instantaneous PSD. The results compared well with an analytical solution. It should be noted that the frequency-dependent analytical solution contained a term to account for the

effect of the source distribution.

Angland and Zhang [53] used single frequency and broadband monopole sources to represent aircraft landing gears in their study on installation effects through solution of the LEE. The broadband signal was obtained from a high-order CFD simulation of a simplified two-wheel landing gear. This is reviewed in detail in Section 2.4.

Casalino *et al.* [54] presented an example of a wave-splitting technique employed to simulate helicopter noise in a complex urban geometry. In this technique, the problem is decomposed into a near-field and a far-field region, and a solution is obtained using two overlapping chimera grids. In the near-field region, which contains a scattering geometry, the propagation of scattered acoustic waves due to prescribed sources is computed. A jump in pressure and its normal derivative is then computed on the interface between the two grids by considering the sources in the absence of the scattering body. The propagation of both the incident and scattered waves in the far-field region is then computed using the jump conditions. Scattering obstacles can also be included in the far-field region. In the investigation, a rotor noise model was used to determine the acoustic source terms. The FEM was used to solve a convective wave equation in the frequency domain in both regions. A helicopter geometry was used in the near-field region, and a set of buildings in the far-field region. The noise on the surface of the buildings was computed for the first and second blade passing frequencies.

2.2.7 Boundary Element Methods for Aeroacoustics

The BEM is a powerful computational method for solving a partial differential equation (PDE) that has been reformulated as a boundary integral equation (BIE). The method has many applications, including acoustics, aerodynamics, electrostatics, and fracture mechanics. Its ability to deal with complex geometries makes it ideal for the investigation of acoustic installation effects. The formulation of the BIE from the governing PDE utilises Green's functions. This means that the method is best suited to acoustic propagation in a stationary media, although flow approximation methods have been developed, and are reviewed in this section. Acoustic sources may be specified at a distance from the geometry, and the method allows the computation of acoustic scattering from the body surface. This makes it an alternative way of computing the acoustic propagation in Region 2,

which was introduced in Section 2.2.1. However, it is important to note that refraction effects are not accounted for by the flow approximation methods. One of the strengths of the method is that only the surface of the scattering body needs to be discretised, and so meshing for the BEM is comparatively simple compared to CFD or CAA methods. Once a solution has been obtained on the surface, the solution at any point in the domain may be obtained through integration of the surface solution. There is no limit to the domain size, due to the use of Green's functions. This is an another advantage compared to CFD or CAA methods, in which the domain has to be meshed and computational constraints limit the maximum size of the domain.

For acoustics, the method is generally formulated in the frequency domain. The governing equation is the Helmholtz equation. There are two ways to formulate the Helmholtz equation as a BIE: the direct method, or the indirect method. The direct method utilises Green's second identity, while the indirect method formulates the BIE in terms of single and double layer potentials. Both methods result in BIEs that contain a Green's function and its derivative. These BIEs are valid both on the exterior and the interior of the boundary surface. It is more difficult to implement generalised boundary conditions in the direct formulation compared to the indirect formulation [55], but the unknowns on the surface have a clear physical meaning in the direct formulation unlike in the indirect formulation [56]. Details of the direct method can by found in [55], [57], [58], and [59]; and the indirect method in [55], [59], [60], [61], and [62].

In order to compute the scattering of an acoustic source, an incident field needs to be added to the BIE. Monopoles, dipoles, quadrupoles, plane waves, or spherical waves may be used as incident acoustic sources. It is also possible to sum any combination of source strength, type, and location for a single simulation, although interference effects will be present due to the time-harmonic governing equation. Acoustically rigid or impedance boundary conditions can be given with the BIE for scattering problems. It is well documented that a standard BIE for an exterior problem is not unique for all frequencies. The frequencies where the solution is not unique are the eigenfrequencies of the corresponding interior problem. Several methods have been developed to overcome this issue through the use of a modified BIE. The most popular of these are the Burton-Miller formulation [63, 64] and the CHIEF method [65].

Having obtained a suitable BIE by either the direct method or indirect method,

two approaches for discretisation exist to enable its solution. These are the collocation approach, and the variational approach. Generally, the collocation approach is applied to direct BIEs, and the variational approach to indirect BIEs [62]. Both approaches rely on a suitable surface discretisation. For a 2-D problem, the one-dimensional (1-D) boundary surface is divided into line segments. For a 3-D problem, the 2-D surface is divided into triangular elements. The two most commonly used type of boundary element are constant and linear boundary elements. For constant boundary elements, the solution is sought at the centre of the element, and is constant across the element. For linear boundary elements, the solution is sought at the vertices of the boundary element, and varies across the element as a linear function. It is generally recommended that an average element size of around one tenth of a wavelength is used for the surface discretisation, with a maximum size of one fifth of a wavelength [66].

In the collocation approach, the solution is computed directly at collocation points on the boundary. These are located depending on the type of element being used, i.e., constant or linear. In the variational approach, the solution is not computed directly at any points on the surface. Instead, the BIE is converted to a so-called weak formulation, and the solution is sought in the form of weighted basis functions in a similar manner to the FEM. The collocation approach is simpler to implement, but the variational approach offers a simpler treatment of singular integrals that arise [56]. Details of the collocation approach can be found in [55], [57], and [58]; and the variational approach in [56], [59], and [62].

An alternative method to the BEM is the source simulation technique (SST), which is also sometimes called the equivalent source method (ESM). Like the BEM, the SST solves the Helmholtz equation. In this method, the scattering surface is first discretised in a similar manner to the BEM. Simple sources are then positioned within the body. The problem is then to compute the strength of each source so as to satisfy the boundary conditions on the discretised surface. Generally, less sources are used than there are surface elements, resulting in a smaller system that needs to be solved than the BEM. However, the solution can be sensitive to the location of the equivalent sources, and care must be taken when deciding where to locate them. A review of the method and a comparison with the BEM was presented by Ochmann [67]. The method was used with uniform and non-uniform flow approximations by Dunn and Tinetti [68] and Tinetti and Dunn [69] respectively.

Although the BEM is more ideally suited to problems in the absence of flow, several

formulations exist that approximate the effect of flow. These include a uniform flow formulation, and several non-uniform flow formulations that are valid under certain assumptions about the mean flow. A summary of the various BEM flow formulations in the literature is given in Table 2.2. The uniform flow formulation is based upon a Lorentz-type transformation, which makes use of the Prandtl-Glauert factor. The transformation changes the problem from a domain with uniform flow to a new domain without flow where the boundary of the scattering body has been stretched and the acoustic wavenumber modified. The transformation yields a regular Helmholtz equation in the transformed domain, which is solved using standard BEM techniques. Once the solution is known in the transformed domain, the acoustic pressure is found in the original domain through use of the inverse transform. Papamoschou and Mayoral [70] presented a thorough explanation of the method, including a discussion on the modification of acoustic source strength in the transformed domain.

Taylor [71] introduced a transformation that reduces a convective wave equation to a regular wave equation under the assumption of low Mach number potential flow. By assuming that the problem is time-harmonic, the transformed convective wave equation can be reduced to a regular Helmholtz equation, which can be solved using standard BEM techniques. Once the solution is known, the flow potential and its derivative are used to modify the acoustic phase and amplitude respectively at any given point. Astley and Bain [72] implemented the method with a BEM solver to investigate the acoustic radiation of a pulsating or juddering sphere in a low Mach number potential flow. A discussion on the low Mach number assumption was also presented, in which an examination of the discarded higher order terms was conducted. It was concluded that in addition to the low Mach number assumption, the characteristic length scale of the mean flow should be the same order or larger than the characteristic length scale of the acoustic disturbance. This suggests that the transformation might not be valid for low frequencies, although the authors note that the choice of characteristic length scale for the acoustic disturbance might not be obvious. Clancy and Rice [75] further extended the Taylor transformation method to take into account a thin wake extending from the trailing edge of a finite zero-thickness wing, across which a discontinuity in flow potential and acoustic potential is allowed.

An alternative non-uniform flow formulation was given by Tinetti and Dunn [69]. This formulation uses generalised local Lorentz transformations, and is valid under the assumption that the spatial derivatives of the flow variables are small and can be neglected. A comparison of the Taylor and the Tinetti and Dunn non-uniform

Table 2.2: BEM flow formulations.

Author	Year	Contribution
Taylor [71]	1978	Transformation of acoustic equations for non-uniform potential flow.
Astley and Bain [72]	1986	Implementation of the Taylor transform in a BEM solver, and analysis of the low Mach number assumption.
Wu and Lee [73]	1994	Convective Green's function formulation for uniform flow BEM.
Lee *et al.* [74]	1994	Extension of Wu and Lee [73] for non-uniform flow by including non-uniform flow effects as source terms.
Dunn and Tinetti [68]	2004	Implementation of Lorentz uniform flow transform in an ESM solver.
Tinetti and Dunn [69]	2005	Extension of Dunn and Tinetti [68] for non-uniform flow.
Clancy and Rice [75]	2009	Modified Taylor transform to include wake effects.
Papamoschou and Mayoral [70]	2013	Detailed description of the Lorentz transform, including a discussion on source strength in the transformed domain.
Wolf and Lele [76]	2013	Assessment of the Taylor [71] and the Tinetti and Dunn [69] non-uniform flow BEM formulations for slat and engine noise.
Mancini *et al.* [77]	2016	Combined Taylor-Lorentz transform using a modified Green's function.
Mancini *et al.* [78]	2016	Extension of Mancini *et al.* [77] with a Burton-Miller BIE formulation.

flow formulations was presented by Wolf and Lele [76]. The formulations were compared against FEE solutions for a plane wave scattered by a cylinder in 2-D. The Taylor formulation performed better than the Tinetti and Dunn formulation for this test case. A comparison between the flow formulations was also made in 3-D for a monopole placed in the slat-gap region of a multi-element high-lift airfoil, although no FEE solution was available for comparison for this case. The results obtained by both formulations were similar in the region below the airfoil, but differences were observed in the suction region above the airfoil.

A different approach was taken by Wu and Lee [73], where a new BIE was derived that utilises a convective Green's function. This is solved in the original domain, not a transformed domain, and this allows a direct coupling of the BEM with

other numerical methods. A discussion of a numerical approach to the solution of the new BIE is also given. Lee *et al.* [74] built on the work by Wu and Lee by including non-uniform flow effects as source terms in the domain. The dual-reciprocity method (DRM) is then used to convert the resulting volume integral to a boundary integral. However, the scheme was reported by the authors to be ill-conditioned at higher frequencies, and dependent on the choice of source interpolating function in the DRM.

Recently, Mancini *et al.* [77] presented a new formulation for acoustic wave propagation over a weakly non-uniform potential flow. A new BIE is derived by combining the physical models associated with the Taylor and Lorentz transforms. The BIE is derived in the physical space using a modified Green's function in a similar manner to Wu and Lee [73]. A collocation approach to the solution of the new BIE is given. The method was shown to be more accurate than both the Taylor and Lorentz transforms independently. The method was further extended by deriving a BIE based on the Burton-Miller formulation to overcome the irregular frequency issue [78]. A description of the solution of this new BIE by the variational approach is given, including a regularisation method for the hyper-singular boundary integral that arises in the formulation.

2.2.8 Accelerated BEM Solution Methods

The high-order spatial schemes for the LEE discussed in Section 2.2.4 result in a tridiagonal or pentadiagonal matrix, for which computationally efficient solution methods exist. One such example is the algorithm proposed by Zhao and Huang [79] to find the inverse of a pentadiagonal matrix. However, the numerical discretisation used in the BEM results in a dense and non-symmetric matrix, which is more computationally demanding to solve. Therefore, a limit on the maximum number of boundary elements that may be employed exists. This leads to a limit on the maximum acoustic frequency that can be investigated, the size of the scattering geometry, or both.

The simplest numerical method available for computing the solution to the system of equations formed in the BEM is Gaussian elimination. However, this is not computationally efficient. Even using an iterative solver does not accelerate the solution enough to allow the use of a large number of boundary elements [80]. To overcome this limitation, three accelerated methods for the BEM have been developed to speed up the solution time [56]. These are the fast multipole method

(FMM), the adaptive cross approximation (ACA) method and the precorrected fast Fourier transform (pFFT) method. Each method estimates far-field interactions between boundary elements to simplify and speed up the construction and solution of the matrix system. A comparison of the computational complexity of each method is given in Table 2.3.

The key idea behind the FMM is that the Green's function can be expanded around an intermediate point. This subsequently leads to the expansion of the BIEs in a similar manner. An iterative solver such as GMRES [82] is utilised such that the entire matrix for the BEM is never formed completely. At each iteration, so-called multipole expansions are formed using intermediate points. These allow the estimation of far-field element interactions without having to recalculate expensive integrals. A hierarchical tree structure with associated expansions and translations further reduces the computational cost. Note that as the method is based on the expansion of the Green's function, the multipole expansions and translations are dependent on the choice of Green's function and are thus problem dependent. For further details on the FMM for acoustics, see [57], [81], and [83].

The ACA method utilises the idea of a hierarchical $\mathcal{H}$-matrix, which is a compressed representation of the original BEM system matrix that is composed of full-rank and low-rank blocks. An iterative solver is utilised so that the $\mathcal{H}$-matrix is never formed in full. An admissibility condition, based upon the distance between boundary elements, determines the rank of each block. If the admissibility condition is satisfied, then the low-rank block is replaced with a compressed representation. If the condition is not satisfied, then the high-rank block is computed as for the standard BEM. A parameter in the admissibility condition controls the level of matrix compression and the associated accuracy for a given problem. The ACA method is an algebraic method that does not depend on the choice of Green's function, and is therefore problem independent. The method is used to accelerate the open-source solver *BEM++* [84]. For further details on the ACA method, see [56], [80], and [85].

Table 2.3: Computational complexity of the BEM and its accelerated methods. N is the number of equations in the system and I is the number of iterations taken by the iterative solver.

BEM [80]	FMM [81]	ACA [80]	pFFT [56]
direct $O(N^3)$	low freq. $O(N)$	low freq. $O(N)$	$O(N)$
iterative $O(IN^2)$	high freq. $O(N \log N)$	high freq. $O(N \log N)$	$+O(N \log N)$

For the pFFT method, a regular Cartesian grid formed of squares in 2-D or cubes in 3-D is superimposed over the mesh of the scattering surface. Once this grid has been established, it is used to determine the near and far-field boundary elements of the surface mesh. The charge on each boundary element, determined by the boundary conditions, is then projected onto the grid points that enclose it. A fast Fourier transform technique is used to compute the grid-to-grid interactions, resulting in the potential at each grid point representing the distributed charges for the entire problem domain. To compute the potential on a given boundary element, the grid potential is interpolated back onto the element from the surrounding grid points. This will include near-field interactions for the element, and so these are subtracted using an approximation method. This is the precorrection stage of the pFFT method. The near-field interactions are then evaluated as for the standard BEM for accuracy and summed with the result of the precorrected grid-to-element interpolation. Similarly to the ACA method, the pFFT method is problem independent. However, unlike both the FMM and ACA method, a hierarchical structure is not constructed, making the pFFT method the simplest of the three accelerated methods to implement [56]. For further details on the pFTT method, see [56] and [86].

These accelerated methods all allow the use of a large number of boundary elements for the solution of acoustic scattering problems. By utilising one of them, it is possible to investigate acoustic scattering from aircraft-sized geometries at realistic frequencies of interest using the BEM. The Lorentz uniform flow approximation [70], and Taylor [71] and Tinetti and Dunn [69] non-uniform flow approximations that were discussed in the previous section all result in a regular Helmholtz equation. Thus, any of the three accelerated methods may be used in the investigation of acoustic scattering from aircraft using one of these flow approximations.

2.2.9 Examples of the Boundary Element Method for Aeroacoustics

There are several examples of the BEM being used for acoustic scattering by aircraft geometries in the literature. A summary of those presented here is given in Table 2.4. Most of these studies focus on engine noise, and consider the installation of an engine with a wing, or an entire aircraft. These studies demonstrate the capability of the BEM to compute aircraft installation effects, especially if an accelerated solver is used that allows computations using large and complex aircraft geometries.

Table 2.4: Computation of aircraft noise using BEM.

Author	Year	Contribution
Delnevo *et al.* [87]	2005	Study of installation effects of engines underneath wings, including the effect of flap angle.
Manoha *et al.* [88]	2005	Investigation of the installation effect of engines in three different configurations.
Cheng *et al.* [81]	2006	Validation of a wideband FMM scheme on an aircraft-shaped object 50 wavelengths in size.
Agarwal and Dowling [89]	2007	Use of the Taylor transform for the scattering of a monopole by a sphere in a flow. Engine shielding investigation using 2-D airfoils and a 3-D flying wing aircraft design.
Brancati *et al.* [80]	2009	Engine noise from a Dassault Falcon aircraft.
Redonnet *et al.* [90]	2010	Validation of CAA solver against BEM solution for engine installed above a wing without flow.
Wolf and Lele [91]	2011	Computation of noise from an engine installed under a wing with uniform flow across a broad range of frequencies.

Redonnet *et al.* [90] presented the validation of a CAA solver against a BEM solver for the study of the installation effects of engines. The installation of an engine above an empennage has the potential to reduce aft fan noise for observers on the ground as the empennage can act as an acoustic shield. The geometry used was an engine exhaust installed above an airfoil, and a single spinning mode was used for excitation for simplicity. A solution was obtained using the CAA solver through the solution of the FEE. For validation purposes a no-flight condition was used, which allowed comparison with a BEM solution. The CAA solution and the BEM solution were in good agreement.

Delnevo *et al.* [87] used a solver accelerated with the FMM in order to investigate the installation effects of an engine beneath a wing. A flow approximation method was not used in this study. The solution was obtained in a two-step process. First, the solution was computed on a simplified axisymmetric engine nacelle with a modal excitation. It was then assumed that installation underneath a wing does not affect the modal excitation. The solution on the nacelle surface was then used as an input for the scattering step, which used a wing with pylon geometry, with and without flap. The SPL was computed for each case, and the installation effect was quantified through comparison between isolated engine, installed without flap, and installed with flap configurations.

Manoha *et al.* [88] used a direct BEM solver to investigate the installation effect of an engine in three different aircraft configurations. These were the under wing nacelle, rear fuselage nacelle, and over wing nacelle configurations. Each configuration featured a different empennage design. An Airbus A318 aircraft was used for the geometry and modified as necessary, at 1/11th scale to enable comparison with experiment. Simulations were conducted at frequencies of 2400 Hz and 4500 Hz. However, the reduction of noise due to the differing configurations was not as high as that seen in the experiment. This was attributed to the use of a single monopole in the simulations, compared to the realistic source used in the experiments. Further BEM simulations were undertaken in 2-D using two in-phase monopoles located inside of a realistic engine geometry installed above a high-lift wing. This showed higher levels of shielding, which was estimated to be representative of the experimental data. The conclusion was that modelling the nacelle is necessary for the correct estimation of engine shielding effects.

Brancati *et al.* [80] implemented a solver based on the ACA method. One of the presented test cases used a Dassault Falcon aircraft geometry. Two monopoles were inserted just in front of the compressors of the two engines. The SPL on the surface of the aircraft was then computed. Far-field pressure was not obtained, and no flow approximation was used, but it demonstrated the applicability of the ACA method to aircraft noise.

Although not for acoustic scattering purposes, Cheng *et al.* [81] used an aircraft shaped object amongst others to validate their wideband FMM scheme. A wideband FMM scheme uses different multipole expansion and translation methods depending on whether the frequency is considered to be low or high with respect to the local hierarchical tree box. This is done in order to optimise stability and efficiency. The potentials on the aircraft surface were computed using a direct method, and using the wideband FMM scheme at three levels of accuracy. The requested levels of accuracy were achieved using the wideband FMM scheme, and in a much faster time than the direct method.

Wolf and Lele [91] also implemented a wideband FMM scheme, and validated it against an analytical solution for the scattering of a monopole by a sphere. The uniform flow approximation was implemented in the solver. The solver was then used to compute the acoustic field from a monopole placed inside an engine nacelle. This was conducted at three discrete frequencies, with and without installation beneath a complete aircraft wing, and with and without a uniform Mach 0.3 flow. The scattering of sound downwards by the wing is seen for the installed cases with

an increase in SPL in that region. Convective amplification is seen in the results with uniform flow, which is also seen to amplify diffraction effects above the wing. Strong shielding effects are seen for the highest of the three frequencies due to the nacelle, although this is reduced with convective amplification for the case with flow.

Agarwal and Dowling [89] described the Taylor transformation, and gave an example calculation of the scattering of a monopole by a sphere in a non-uniform flow using a BEM solver. They highlighted that the transform decouples flow and acoustic solutions, and that for a given scattering geometry, source position, and acoustic frequency, different flow conditions may be investigated without having to recompute the acoustic solution. Various 2-D wing models were investigated without flow with a monopole positioned above each representing an installed engine. The wing models included a flat plate, a biconvex ellipse, an ellipse, and a Zhukovsky airfoil. These were chosen to give an insight into the effect of edge curvature and wing thickness on the acoustic shielding. The flat plate and ellipse BEM solutions compared well with analytical solutions. Finally, a monopole was installed above a 3-D flying wing aircraft geometry, and the SPL was computed on a ground plane using a direct BEM solver without flow. There were several locations on the ground plane where destructive interference in the single frequency simulation could be observed. It was also demonstrated that there was less shielding directly below the wing compared to at positions around the wing. This was attributed to constructive interference from edge diffraction due to the source being located in the centre of a symmetric geometry.

2.3 Landing Gear Noise

Landing gear noise is essentially broadband, although tonal noise is occasionally observed [6]. Broadband noise is generated by turbulent flow separation from the various bluff bodies that constitute the landing gear, and the interaction of these turbulent wake structures with downstream landing gear components [8]. The highest levels of noise typically occur at frequencies up to 3 kHz for current landing speeds and landing gear designs [8]. Low-frequency noise is associated with the larger landing gear components, such as the main struts and the wheels [6]. The comparatively high-frequency noise is associated with small-scale components, such as small struts, linkages, and hydraulic lines [92].

Tonal noise was observed in experiments by Dobrzynski *et al.* [93], which was attributed to resonances in hollow pins that are found in various joints linking gear

components. Aeroacoustic investigations using a simplified two-wheel landing gear showed that a resonance mode can take place in the volume between the wheels, resulting in side radiation of tonal noise [94]. Tonal noise can also be caused by coherent periodic vortex shedding from small struts and hydraulic lines, but experimental evidence suggests that noise generated by this mechanism is not a major problem for current landing gear designs [6].

Curle [15] developed an acoustic analogy in which the unsteady forces on a rigid body in a flow create acoustic fluctuations that can be represented by a distribution of dipole sources. Through dimensional analysis he showed that for a distribution of compact dipoles the sound intensity scales with the sixth power of the flow velocity. Landing gear noise sources can be represented by such a distribution of dipoles. This is the basis of the semi-empirical landing gear models by Smith and Chow [18] and Guo [20], in which scaling laws are correlated with experimental data through the use of empirical constants.

The local mean flow and turbulence characteristics are different over each landing gear component. Thus, the distribution of dipole sources is complex, with varying strengths and orientations [6]. Due to the complex source distribution, landing gear directivity is not strongly directional despite the individual dipole sources being directional. At low Strouhal numbers a small maximum in the noise level is seen in the rear arc in the streamwise direction, while at higher Strouhal numbers a noise level minimum is seen directly below the landing gear in the streamwise direction [8]. In the absence of small-scale components, an almost omni-directional directivity is seen independent of Strouhal number [6].

At low frequencies, the dipole sources are compact with respect to wavelength. Experiments by Guo *et al.* [92] on a full-scale Boeing 737 two-wheel main landing gear including small-scale features confirmed that the sound intensity scales with the sixth power law at these lower frequencies. However, at higher frequencies, they showed that the sound intensity scales with an eighth power law due to the dipoles no longer being compact with respect to wavelength. Liu *et al.* [25] conducted a high-order computational study using DES on a generic two-wheel landing gear without small-scale features. Far-field noise was computed using an FWH solver. The numerical method compared well with experimental results. It was shown that the highest levels of noise generally occurred up to 1 kHz, and that the directivity was almost omni-directional in the streamwise direction. This is in agreement with observations from other authors about the frequency content and directivity of landing gear noise in the absence of small-scale features [6]. They

also showed that the far-field acoustics approximately scaled with the sixth power law, which is expected in the absence of small-scale features.

Examples of landing gear noise spectra in one-third octave bands are shown in Figure 2.1. These spectra were obtained from the experiments by Guo *et al.* [92] on a full-scale Boeing 737 two-wheel main landing gear at various Mach numbers, both in a clean and fully dressed configuration. The experiments were undertaken in Boeing's Low Speed Aeroacoustic Facility, using a 2.7 m by 3.7 m freejet in a large anechoic test chamber. The microphone that was used to obtain these spectra was located approximately 3 m below the gear centre. The spectra were scaled by the seventh power of the Mach number, as high-frequency noise was expected to show most of the differences. The authors note that the seventh power scaling for the SPL in the figure corresponds to the eighth power law for the OASPL, due to integrating the narrowband results over a fixed frequency range. It can be seen that above approximately 800 Hz there is an almost uniform increase in noise from the clean to the fully dressed configuration, confirming that the high-frequency noise is associated with small-scale components. The spectra collapse better for the fully dressed configuration using the seventh power scaling than for the clean configuration. It can be seen that the highest levels of noise occur up to around 3 kHz.

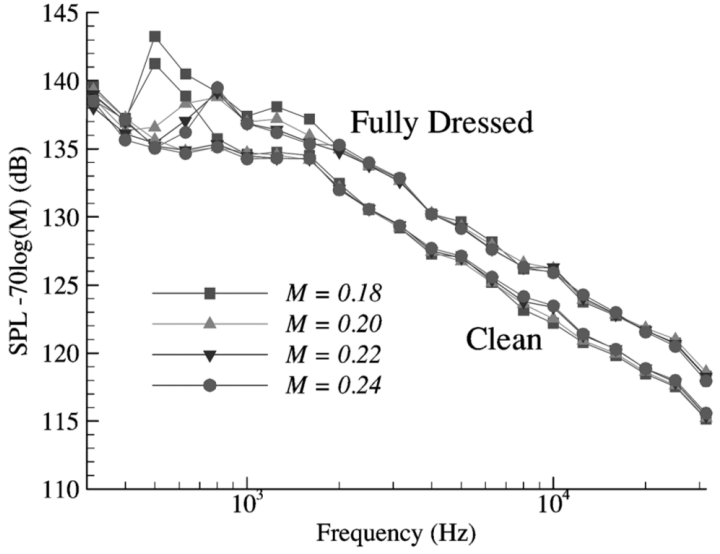

Figure 2.1: Landing gear noise spectra obtained from experiments on a full-scale Boeing 737 two-wheel main landing gear at various Mach numbers, in both clean and fully dressed configurations. Scaled by the seventh power of the Mach number. Copyright The Boeing Company, reproduced with permission from [92].

2.4 Landing Gear Installation Effects

Installation effects can be categorised as one of two types: source installation effects or acoustic installation effects. Source installation effects modify the generation of sound by a component, due to local flow variations around an airframe. This is typically accompanied by a change in acoustic power. For example, a landing gear installed beneath a lifting wing experiences a reduction in oncoming flow velocity compared to the free-stream due to circulation around the wing. As the noise observed in the far-field follows the sixth power law, this reduction in flow velocity over the installed landing gear leads to a significant reduction in noise compared to a landing gear in a free-stream. This must be considered when conducting experiments in a wind tunnel, or in CFD simulations, where a lifting wing may not be present. Acoustic installation effects modify the propagation of an acoustic source. This includes refraction through a non-uniform flow and scattering from aircraft surfaces. The sound power is not modified by acoustic installation effects.

The source installation effect for landing gear under a lifting wing was seen in experimental data obtained by Pott-Pollenske *et al.* [95]. Flyover noise measurements were conducted on an Airbus A319 aircraft for various configurations and operating conditions. This allowed the differentiation of engine and airframe noise sources. It was noted that the landing gear noise levels were indeed lower with the wing in a high-lift landing configuration than compared to the wing in a cruise configuration, with the aircraft flying at the same velocity for each case.

Angland and Zhang [53] investigated the acoustic installation effects of landing gears using a computational approach. The acoustic propagation and scattering was computed through the solution of the LEE in 2-D. Single frequency and broadband monopole sources were used in the acoustic simulations. The choice of monopole sources was made as it was reported that landing gear directivity is almost omni-directional at low Strouhal numbers. For the single frequency simulations, four equivalent monopoles representing wheel, upper leg, lower leg, and axle sources were used in locations representative of their respective positions on a landing gear. The strength of each source was obtained from a high-order CFD simulation on a simplified two-wheel landing gear geometry, which was detailed in Liu *et al.* [25]. The FWH solution from the CFD simulation was obtained using a solid on-body control surface, and the far-field contribution from each landing gear component could be analysed independently. This data was summed over octave bands to give a strength and central frequency for each source. The

broadband simulations used a single monopole source and a time-domain pressure signal acquired from the CFD simulation. Both the single frequency and broadband landing gear models were installed in a wind tunnel geometry, with and without a cavity to represent a landing gear cavity. The installation effect was quantified by the difference in SPL between a free-field case and the installed case. The single frequency sources were also installed beneath a lifting wing geometry, and the installation effect quantified as before. It was noted that destructive interference could be seen in the single frequency simulations, which could potentially overestimate the installation effect.

Guo [96] presented a study on local flows in the vicinity of aircraft landing gear. The local flows were extracted from CFD data for complete aircraft geometries, and these were used to develop a reduced-order model to compute the local flow velocity in the vicinity of landing gears. The CFD data was obtained by Boeing through simulations of their 737, 747, 777, and 787 aircraft in typical landing configuration with flap and slat deployed. The results discussed in the paper focus on the 737 and 777 aircraft, although data for the 747 and 787 aircraft was also used in the development of the model. The CFD data confirmed that the oncoming flow velocity in the vicinity of the installed main landing gear is lower than the free-stream. However, it also showed that the oncoming flow velocity in the vicinity of the nose landing gear can exceed the free-stream velocity depending on gear location and angle of attack. For both main and nose landing gears, it was shown that the local flow velocity decreases as the angle of attack increases. The developed flow prediction model gives the local flow velocity based on the free-stream velocity, the aircraft angle of attack, the maximum aircraft takeoff weight, and the distance from the aircraft. The type of landing gear, either nose gear or main gear, is given through coefficients of a fifth-order polynomial. An example of an application of the prediction model was also presented. The local flow computed using the model was used with the semi-empirical noise prediction model previously developed by Guo [20] in order to account for source installation effects.

Carrilho and Smith [97] presented an analytical method for estimating the scattering of landing gear noise by a wing through the use of the Weiner-Hopf technique. The scattering wing surface was idealised by a 2-D rigid strip, and uncorrelated point monopoles were located in nominal positions representative of landing gear component noise sources. A discussion to extend the method to take into account a uniform flow through use of a Lorentz transform was included. In this extension, complications in the form of singularities in the edge conditions arise due to the

transformation, and these were to be overcome in subsequent work. Results obtained using this method would give an estimation of geometrical scattering and convective amplification, but would not include refraction effects.

Smith *et al.* [98] further extended the semi-empirical model for landing gear noise by Smith and Chow [18, 19] to take into account installation effects. The reduction in flow velocity was computed for a single-element airfoil using conformal mapping of the potential flow around a cylinder. Carrilho and Smith [99] developed a simple model for estimating the flow profile beneath a lifting wing in high-lift configuration at the mid-chord position. The model is based on potential flow theory, and was able to predict the flow profile to within 1 % of CFD data for a wing with flap and slat deployed. This model was used with the semi-empirical landing gear noise model by Smith and Chow [18] in order to specify noise sources taking into account installation effects, which were in turn used in the analytical method by Carrilho and Smith [97] to compute the scattered field. Comparison of the results against those obtained without the source installation effect modification highlights the importance of taking the installation effect into consideration for flight cases.

2.5 Discussion and Summary

A review of the literature for aircraft noise has been presented in this chapter. An overview of computational methods employed for the estimation of aircraft noise was given first. This included CFD methods to compute the generation of noise, CAA methods to compute the propagation of the generated noise in the near-field, and the estimation of noise in the far-field using an acoustic analogy. An alternative approach using the BEM was then presented, including flow approximation methods and accelerated solution methods. The aims of this thesis are related to landing gear noise, and so literature relevant to the generation and characteristics of landing gear noise was then reviewed. Finally, literature relating to the installation effects of landing gear was then presented.

The literature on landing gear noise focuses on two areas: noise generation, and source installation effects. Computational and experimental methods have both been employed to investigate the mechanisms behind landing gear noise generation. This has led to a better understanding of the characteristics of landing gear noise, and how variations in landing gear geometries influence the generated noise. This understanding has aided in the development of several semi-empirical landing gear

noise models. The study of installation effects of landing gears has generally focused on source installation effects. These effects govern the strength of the generated noise, due to local flow variations in the vicinity of the installed landing gear. For a landing gear installed beneath a lifting wing, acoustic installation effects must also be taken into account. These govern the refraction of the noise by the non-uniform flow around the wing, and the scattering of the noise by the wing surface. Although there are studies in the literature that include the effect of the scattering wing surface, no studies into the effect of the non-uniform flow on the propagation of landing gear noise have been found. This thesis focuses on the acoustic installation effects of landing gears in order to further understanding in that area.

In the current work, a CAA method is used to quantify the effect of non-uniform flow due to circulation around a lifting wing on the scattering of landing gear noise sources. In particular, a high-order time-domain LEE solver is employed, with mean flows provided by inviscid CFD simulations. This ensures that refraction effects due to non-uniform flow are accounted for. The effect of non-uniform flow is quantified by the difference in SPL for the scattering of an acoustic source over a non-uniform and a uniform mean flow. Given that the LEE are solved in the time domain in the present work, both single frequency and broadband sources are used. Circulation around a lifting wing is increased by increasing the angle of attack, increasing the free-stream Mach number, or deploying flaps and slats. Flaps and slats also alter the reflective underside of the wing. The effect of each of these are investigated through the solution of the LEE. In a high-lift airfoil configuration, shear layers develop behind the trailing edge of the various airfoil elements. Instabilities that develop in the LEE solutions are controlled through the choice of angle of attack in this work, instead of using a GTM method. It is the effect of mean flow gradients that are under investigation, and so it is preferable to avoid the modification of these terms wherever possible.

It was noted by several authors that landing gear noise is almost omni-directional in the absence of small-scale landing gear features [6, 25, 53]. The investigations in the current work that solve the LEE focus on frequencies up to 500 Hz, which are frequencies associated with the large-scale main struts and wheels. As such, a monopole is used to represent an idealised landing gear source. This is a similar approach to that taken by Angland and Zhang [53]. The use of a simple source also follows the approach used by several authors in their investigations into the effect of non-uniform mean flow on acoustic propagation [45, 46, 47]. It is another aim of the present work to evaluate existing BEM flow formulations for their

suitability for the modelling of landing gear installation. The use of monopoles allows the comparison of results obtained through the solution of the LEE with results obtained using the BEM.

The BEM flow formulations that are evaluated in the current work are the Lorentz uniform flow formulation, and the Taylor non-uniform flow formulation [71]. The Tinetti and Dunn non-uniform flow formulation [69] has more restrictive conditions on the flow than the Taylor formulation, and the Taylor formulation also performed better than the Tinetti and Dunn formulation for slat noise as shown by Wolf and Lele [76]. The non-uniform flow formulation by Lee *et al.* [74] that was derived in the physical space using a modified Green's function is dependent on the choice of an interpolating function, and so is not as general as the other methods. The combined Taylor-Lorentz formulation by Mancini *et al.* [77, 78] has been shown to improve the accuracy of both the Taylor and Lorentz transforms on their own, but was published towards the end of the writing of this thesis.

The BEM flow formulations do not account for refraction through a mean flow, and it was noted by Taylor [71] that the only effect of the potential flow in the far-field using his transform is that of the uniform free-stream. Therefore, in the current work, the near-field is the region of interest in which to investigate the effect of non-uniform flow. As such, far-field approximations using an FWH solver were not required for the LEE solutions.

The final aim of this thesis is to couple a realistic landing gear noise source prediction model with a 3-D BEM solver. This allows the scattering of landing gear noise sources by a realistic aircraft geometry to be investigated, including the effect of flap deployment. The 3-D BEM solver used in the current work is accelerated by the FMM, and allows the computation of acoustic scattering by a large and complex geometry. The source model is provided by an in-house prediction code. The code uses a database of results from CFD computations on individual landing gear components coupled with an acoustic analogy in order to derive the far-field noise directivity and power spectral density for a complete landing gear. The code also includes the ability to estimate the reduction in noise for a landing gear installed beneath a lifting wing due to source installation effects. This is coupled with the BEM solver in order to compute the SPL on a ground plane located 120 m below the nose of the aircraft, which corresponds to the approach reference point in Figure 1.1.

Chapter 3

Mathematical Preliminaries

3.1 Introduction

The relevant equations for acoustics under the influence of flow that are used throughout this thesis are described in this chapter, along with the methods used for their solution. The description begins with an overview of the solvers and codes used throughout this thesis in Section 3.2. The BEM is described in Section 3.3. This begins with a description of the governing Helmholtz equation, its boundary conditions, a fundamental solution in the form of a Green's function, and the specification of an acoustic source. The BEM solvers employed for this thesis are then described and validated. The uniform and non-uniform flow approximations for the BEM that are under investigation in this work are detailed. A 2-D panel method for the computation of potential flow is described in Section 3.4, and a solver based on the implementation of the method is validated. This potential flow solver is required to obtain a flow solution for the non-uniform flow BEM approximation. The LEE are then detailed in Section 3.5, starting with their derivation and acoustic source implementation. The solution of the LEE by the finite difference method is described, including the relevant boundary conditions used for the work in this thesis. A study to determine the effect of the various monopole parameters is also presented, followed by a validation of the solver for scattering simulations. The computational costs of the solvers employed are discussed in Section 3.6. Finally, a summary of the mathematical methods employed in this thesis is given in Section 3.7.

In all that follows, pressure is denoted by p, density by ρ, position vector by $\mathbf{x} = (x, y, z)$ or $\mathbf{y}$, velocity vector by $\mathbf{u} = (u, v, w)$, and time by t. Free-stream values are denoted using subscript ∞. For acoustic properties, frequency is denoted by f, angular frequency by $\omega = 2\pi f$, speed of sound by c, and wavelength by $\lambda = c/f$. The non-dimensional Mach number is given by $M = |\mathbf{u}|/c$. The complex unit is denoted by $i = \sqrt{-1}$.

The standard sea level conditions are used for the atmosphere throughout this work, with a temperature of 288 K and density of $\rho_\infty = 1.22\,\mathrm{kg\,m^{-3}}$. This gives a speed of sound of $c_\infty = 340.2\,\mathrm{m\,s^{-1}}$. The SPL is computed using $\mathrm{SPL} = 20\log_{10}(p_{\mathrm{rms}}/p_{\mathrm{ref}})$, with root mean square (RMS) pressure denoted by p_{rms}. For every calculation of SPL, the reference pressure $p_{\mathrm{ref}} = 2.0 \times 10^{-5}\,\mathrm{Pa}$ is used.

To quantify error throughout this work, the percentage error in p_{rms} of A against B is used

$$\text{percentage error} = \frac{p^A_{\mathrm{rms}} - p^B_{\mathrm{rms}}}{p^B_{\mathrm{rms}}} \times 100. \tag{3.1.1}$$

Here B is assumed to be the correct solution. This may be an analytical solution, or an accurate numerical solution. For example, a LEE solution is taken to be the correct solution in the evaluation of the BEM flow approximation methods. The absolute value is generally not taken in order to show whether the solution is over or underestimated. A measure of the error across a range of observers is obtained by taking the absolute percentage error at each observer in the range and then taking the mean of these values.

3.2 Overview of Employed Solvers and Codes

An overview of the solvers and codes employed for the work in this thesis is given in this section. The acoustic solvers used were the LEE solver *SotonLEE*, and two BEM solvers *ABEMFULL* and *ACTIPOLE*. A panel solver to compute non-uniform potential flow around multi-element airfoils, the commercial CFD solver *ANSYS Fluent*, and the landing gear noise prediction code *SotonLGAP* were also used. A summary of these solvers and codes is given in Table 3.1, including how each was employed.

As discussed in Section 2.5, LEE methods can account for the refraction of acoustic waves by a non-uniform mean flow. *SotonLEE* was used to investigate the effect of non-uniform flow due to circulation on the scattering of idealised landing gear noise sources installed beneath a lifting wing. This solver is a time-domain solver, which

enabled single frequency and broadband sources to be used in the investigations. The solver can solve the LEE in 2-D or 3-D. The investigations were primarily conducted in 2-D, with a quantification of the 2-D assumption further conducted in 3-D. The non-uniform base flows that were required for each LEE simulation were obtained from inviscid simulations using *ANSYS Fluent*.

The BEM solver *ABEMFULL* is an open-source 2-D solver written in FORTRAN [100]. The uniform and non-uniform flow BEM formulations discussed in Section 2.5 were both implemented in this solver for evaluation. Both formulations were implemented in the same version of the code, with the required formulation for any given case selected using an input parameter. This BEM solver is a frequency-domain solver. Results obtained using both flow formulations were evaluated against equivalent results from the 2-D LEE investigations with a single frequency source computed using *SotonLEE*. The non-uniform flow BEM formulation requires a potential flow solution. Thus, a 2-D panel solver capable of computing the non-uniform potential flow around multi-element airfoils was implemented for this purpose.

ACTIPOLE is a 3-D frequency-domain BEM solver. It is accelerated using the FMM, and is capable of handling large and realistic geometries. The uniform flow BEM formulation was already available in the version of the solver used for the current work. The solver was used to compute the acoustic scattering of idealised landing gear noise sources by a realistic aircraft geometry. The strength of the idealised sources was computed using the landing gear noise prediction code *SotonLGAP*. This code uses directional databases and scaling laws to estimate the far-field noise for a given landing gear configuration. *SotonLGAP* is discussed in detail in Section 6.4.

Table 3.1: Overview of employed solvers and codes.

Solver	Type	Dimensions	Use
SotonLEE	LEE	2-D/3-D	Investigations into the scattering of single frequency and broadband sources by a lifting wing. The refraction of acoustic waves by a non-uniform flow is accounted for.
ABEMFULL	BEM	2-D	Evaluation of uniform and non-uniform flow BEM formulations against equivalent solutions from *SotonLEE*.
ACTIPOLE	BEM	3-D	Investigations into the scattering of idealised landing gear noise sources by a realistic aircraft geometry.
Panel Solver	Panel	2-D	Computation of non-uniform potential flows required for the non-uniform flow BEM formulation in *ABEMFULL*.
ANSYS Fluent	CFD	2-D/3-D	Computation of inviscid non-uniform base flows required for each *SotonLEE* simulation.
SotonLGAP	Noise model	3-D	Calculation of a realistic strength for each idealised landing gear noise source for use with *ACTIPOLE*.

3.3 Boundary Element Methods

3.3.1 The Helmholtz Equation, Boundary Conditions, Fundamental Solution, and Acoustic Source

Unlike the LEE described in Section 3.5 that are derived in the time domain, the BEM is derived in the frequency domain. The wave equation of linear acoustics can be written in terms of the time-dependent acoustic potential $\Phi_a(\mathbf{x}, t)$ as

$$\frac{\partial^2 \Phi_a(\mathbf{x}, t)}{\partial t^2} - c_\infty^2 \nabla^2 \Phi_a(\mathbf{x}, t) = 0. \tag{3.3.1}$$

Under the assumption that the solution is time-harmonic such that $\Phi_a(\mathbf{x}, t) = \phi_a(\mathbf{x}) e^{-i\omega t}$, the wave equation can be reduced to the Helmholtz equation

$$\nabla^2 \phi_a(\mathbf{x}) + k^2 \phi_a(\mathbf{x}) = 0, \tag{3.3.2}$$

where $k = \omega / c_\infty$ is the acoustic wavenumber. The total acoustic field can be written as the sum of incident and scattered fields as $\phi_a(\mathbf{x}) = \phi_a^I(\mathbf{x}) + \phi_a^S(\mathbf{x})$.

The boundary condition for acoustically rigid surfaces is given by

$$\frac{\partial \phi_a(\mathbf{x})}{\partial n} = \nabla \phi_a(\mathbf{x}) \cdot \mathbf{n} = 0, \tag{3.3.3}$$

where $\mathbf{n}$ is the normal vector to the boundary at $\mathbf{x}$. Together, (3.3.2) and (3.3.3) may be solved to compute the sound field interior or exterior to any given boundary S.

In order to solve the Helmholtz equation numerically by the BEM, (3.3.2) first needs to be recast as a BIE. An overview of the formulation of a BIE and its subsequent solution by various methods is given in Section 2.2.7. The flow approximation methods detailed in Section 3.3.3 all result in a regular Helmholtz equation that can be solved with any of the methods reviewed, and so details of the methods are omitted here for brevity.

A fundamental solution to the Helmholtz equation exists in the form of a Green's function G. This function is a solution to the corresponding inhomogeneous equation with a unit amplitude source

$$\nabla^2 G(\mathbf{x}, \mathbf{y}) + k^2 G(\mathbf{x}, \mathbf{y}) = -\delta(\mathbf{x}, \mathbf{y}), \tag{3.3.4}$$

where $\delta(\mathbf{x}, \mathbf{y})$ is the Dirac δ function. In 2-D, G is given by

$$G(\mathbf{x}, \mathbf{y}) = \frac{i}{4} H_0^{(1)}(kr), \tag{3.3.5}$$

where $H_n^{(1)}$ is the Hankel function of the first kind of order n, and $r = \|\mathbf{x} - \mathbf{y}\|$. In 3-D, G is given by

$$G(\mathbf{x}, \mathbf{y}) = \frac{1}{4\pi r} e^{ikr}. \tag{3.3.6}$$

Note that $\mathbf{x}$ and $\mathbf{y}$ may be interchanged due to reciprocity.

The complex-valued harmonic acoustic pressure is related to the acoustic potential by

$$p(\mathbf{x}) = i\rho_\infty \omega \phi_a(\mathbf{x}). \tag{3.3.7}$$

The real-valued time-varying pressure is then given by

$$p(\mathbf{x}, t) = \mathrm{Re}\left(p(\mathbf{x}) e^{-i\omega t}\right). \tag{3.3.8}$$

The amplitude of the time-harmonic pressure at a point $\mathbf{x}$ is given by $|p(\mathbf{x})|$, and the root mean square of a sinusoidal function is given by amplitude$/\sqrt{2}$. Thus,

p_{rms} is computed using

$$p_{\text{rms}}(\mathbf{x}) = \frac{|p(\mathbf{x})|}{\sqrt{2}}. \tag{3.3.9}$$

In order to compute the scattering of an acoustic source, an incident field needs to be added to the BIE. For a monopole source located at $\mathbf{x}_s$, this is given by

$$\phi_a^I(\mathbf{x}) = Q(\mathbf{x}_s)G(\mathbf{x}, \mathbf{x}_s), \tag{3.3.10}$$

where Q is the strength of the monopole. Note that it is possible to sum any combination of source strengths and locations for a single simulation, although interference effects will be present due to the single frequency nature of the governing equations. Dipoles and quadrupoles may be implemented through the superposition of multiple monopoles, each with the appropriate phase. The phase of a given source may be changed by multiplying the complex-valued incident acoustic potential $\phi_a^I(\mathbf{x})$ by $e^{i\varphi}$, where φ is the required phase angle.

3.3.2 Overview and Validation of Employed Solvers

BEM solutions were computed throughout this thesis using two solvers; the open-source 2-D solver *ABEMFULL* [100], and the 3-D solver *ACTIPOLE* developed by IMACS at École Polytechnique, France. The solvers and the methods that each uses are summarised in Table 3.2. The uniform and non-uniform flow formulations detailed in Section 3.3.3 were both implemented in *ABEMFULL* for evaluation in the current work. *ACTIPOLE* Version 1.21.0 was used for the current work, and this version has the option to use the uniform flow formulation. Following the generally accepted recommendation, a maximum boundary element size of $\lambda/7.5$ was used throughout the work in this thesis to ensure accuracy, with the average above $\lambda/10$ [66].

Morris derived an analytical solution for the scattering of an axisymmetric cylindrical source by a circular cylinder [101], and for the scattering of a spherically symmetric source by a sphere [102]. These can be used to validate the 2-D *ABEMFULL* and 3-D *ACTIPOLE* solvers respectively for scattering problems. The analytical solutions do not include the effect of flow. The radius of both the solid cylinder and sphere was taken as 1 m, with the source placed on the x-axis 5 m from the centre of the scattering object. The solution was computed at 360 observers on a circle of radius 10 m centred on the centre of the scattering object. The observers are labelled by angle θ, and the $\theta = 0^\circ$ position was located in the

Table 3.2: Overview of employed BEM solvers.

	ABEMFULL	*ACTIPOLE*
Dimensions	2-D	3-D
BIE formulation	direct	indirect
Discretisation approach	collocation	variational
Boundary element type	constant	linear
Acceleration	none	FMM
Matrix solver type	direct: LU factorisation	iterative: gradient descent GMRES

negative x-direction from the source, with θ increasing in an anticlockwise direction. The scattering geometry, source, and observer positions are shown in Figure 3.1.

The 2-D cylinder boundary was described by a circle discretised with 260 line segments. The 3-D sphere boundary was discretised with 1.13×10^4 triangular boundary elements. The source strength for the analytical solution in both 2-D and 3-D was taken to be unity. The validation was conducted at a frequency of 325 Hz. This frequency was chosen as it is in the upper half of the frequency range used for the investigations in Chapter 4 and Chapter 5, and would yield a larger number of directional lobes in the directivity plots than lower frequencies. Figure 3.2 shows a comparison of the computed SPL against the analytical solution for

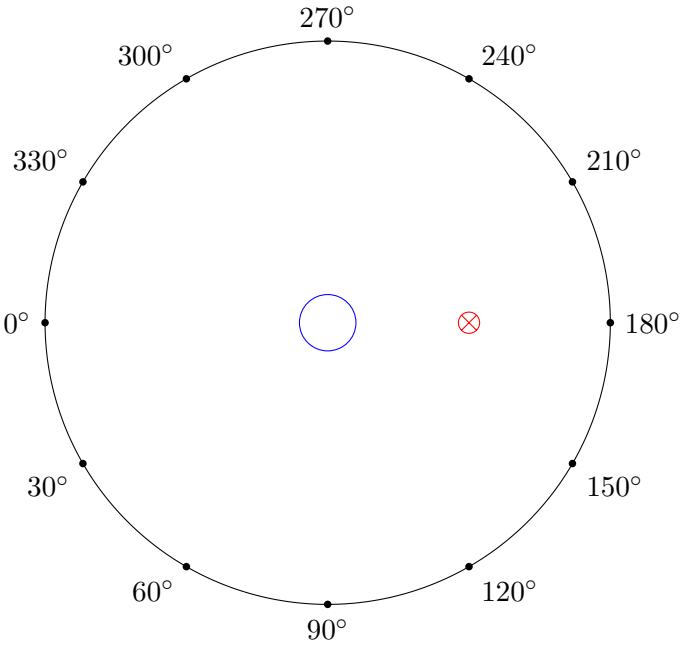

Figure 3.1: Cylinder/sphere geometry with source and observer positions.

the 2-D case, and it can be seen that solutions are in good agreement. The average absolute percentage error in p_{rms} computed over all 360 observers for the 2-D case solved with *ABEMFULL* is 0.208 %. Figure 3.3 shows a similar comparison for the 3-D case, and again the solutions are in good agreement. The average absolute percentage error in p_{rms} for the 3-D case solved with *ACTIPOLE* is 0.018 %. The scattered acoustic field for the 3-D case is shown in Figure 3.4. Further details of the 3-D simulation can be found in Table B.1 in Appendix B. These results confirm the accuracy of these solvers for acoustic scattering problems in the absence of flow. The accuracy of the flow approximation methods are discussed in Section 4.10.

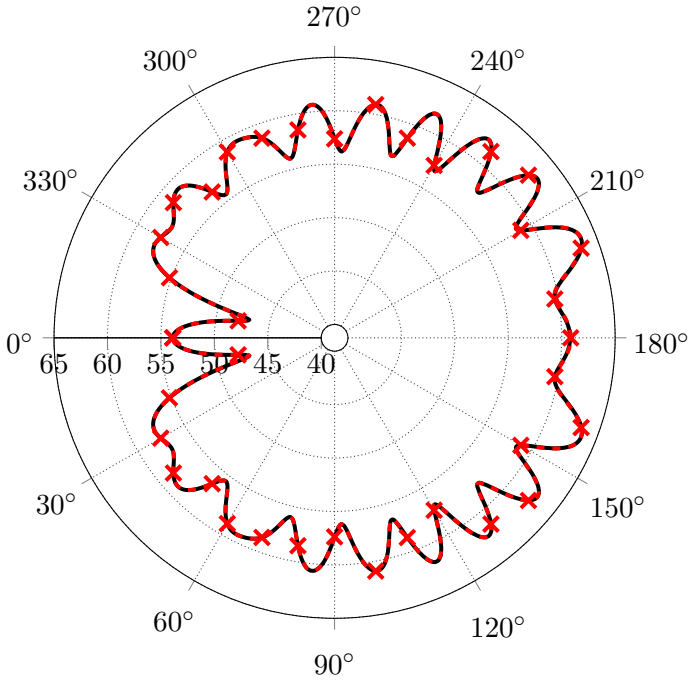

Figure 3.2: Comparison of SPL (dB) between an analytical solution and the numerical solution, evaluated at a radius of 10 m centred on the cylinder. Analytical ——, *ABEMFULL* - -×- -.

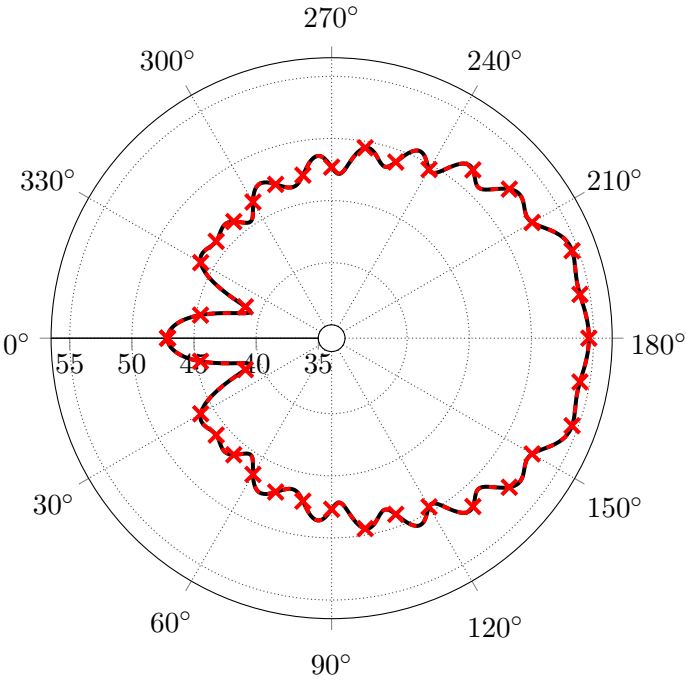

Figure 3.3: Comparison of SPL (dB) between an analytical solution and the numerical solution, evaluated at a radius of 10 m centred on the sphere. Analytical ——, *ACTIPOLE* - -×- -.

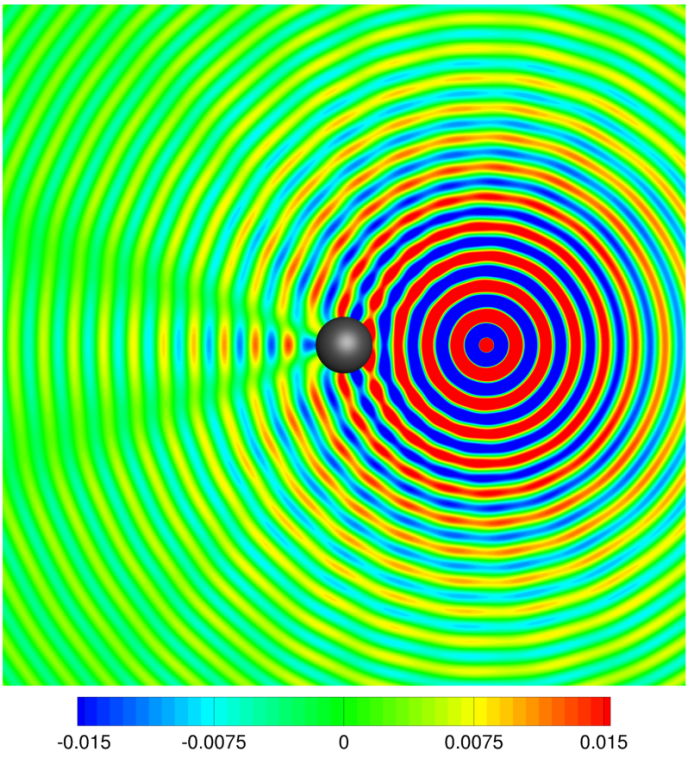

Figure 3.4: Acoustic pressure (Pa) for the scattering of a monopole at 325 Hz at a distance of 5 m from the centre of a sphere of radius 1 m in 3-D.

3.3.3 Flow Approximation Methods

The Lorentz uniform and Taylor non-uniform flow BEM approximation methods that were reviewed in Section 2.2.7 are detailed here. Both methods result in a regular Helmholtz equation that can be solved used regular BEM techniques, including accelerated methods. The Taylor approximation also requires the solution of the Laplace equation for the non-uniform potential flow. A panel solver was implemented for this purpose, and this is also detailed here.

3.3.3.1 Uniform Flow

Both flow BEM approximations begin with the convected wave equation written in terms of the time-dependent acoustic potential $\Phi_a(\mathbf{x}, t)$

$$\left(\frac{\partial}{\partial t} + \nabla\phi_f(\mathbf{x}) \cdot \nabla\right)^2 \Phi_a(\mathbf{x}, t) - c_\infty^2 \nabla^2 \Phi_a(\mathbf{x}, t) = 0. \tag{3.3.11}$$

Here $\phi_f(\mathbf{x})$ is the flow potential at $\mathbf{x}$. This is solved with the boundary condition for acoustically rigid surfaces

$$\frac{\partial \Phi_a(\mathbf{x}, t)}{\partial n} = 0. \tag{3.3.12}$$

Under the assumption that the acoustic potential is time-harmonic with $\Phi_a(\mathbf{x}, t) = \phi_a(\mathbf{x})e^{-i\omega t}$, the convected wave equation given in (3.3.11) is reduced to the convected Helmholtz equation

$$k^2\phi_a(\mathbf{x}) + 2i\frac{k}{c_\infty}\nabla\phi_f(\mathbf{x}) \cdot \nabla\phi_a(\mathbf{x}) - \frac{1}{c_\infty^2}\left(\nabla\phi_f(\mathbf{x}) \cdot \nabla\right)^2 \phi_a(\mathbf{x}) + \nabla^2\phi_a(\mathbf{x}) = 0. \tag{3.3.13}$$

Here the second and third terms are the convective terms.

With the assumption of uniform flow everywhere with velocity V_∞ aligned with the x-axis, this can be simplified further using $\nabla\phi_f(\mathbf{x}) = V_\infty$, and $\nabla\phi_a(\mathbf{x}) = \partial\phi_a(\mathbf{x})/\partial x$ for the convective terms. This gives

$$k^2\phi_a(\mathbf{x}) + 2ikM_\infty\frac{\partial\phi_a(\mathbf{x})}{\partial x} + \left[(1 - M_\infty^2)\frac{\partial^2\phi_a(\mathbf{x})}{\partial x^2} + \frac{\partial^2\phi_a(\mathbf{x})}{\partial y^2} + \frac{\partial^2\phi_a(\mathbf{x})}{\partial z^2}\right] = 0. \tag{3.3.14}$$

This convected Helmholtz equation can then be reduced to a regular Helmholtz equation

$$\nabla_{\tilde{x}}^2\tilde{\phi}_a(\tilde{\mathbf{x}}) + \tilde{k}^2\tilde{\phi}_a(\tilde{\mathbf{x}}) = 0, \tag{3.3.15}$$

using the Lorentz-type transform

$$\begin{gathered}
\mathbf{x} = (x, y, z) \rightarrow \tilde{\mathbf{x}} = (\tilde{x}, y, z), \\
t \rightarrow \tilde{t}, \\
\omega \rightarrow \tilde{\omega}, \\
k \rightarrow \tilde{k}, \\
\phi_a(\mathbf{x}) \rightarrow \tilde{\phi}_a(\tilde{\mathbf{x}}) e^{-i\kappa\tilde{x}}, \\
\nabla = \left(\frac{\partial}{\partial x}, \frac{\partial}{\partial y}, \frac{\partial}{\partial z} \right) \rightarrow \nabla_{\tilde{x}} = \left(\frac{\partial}{\partial \tilde{x}}, \frac{\partial}{\partial y}, \frac{\partial}{\partial z} \right),
\end{gathered} \tag{3.3.16}$$

where

$$\begin{aligned}
\tilde{x} &= \frac{x}{\sqrt{1 - M_\infty^2}}, \\
\tilde{t} &= \sqrt{1 - M_\infty^2}\, t + \frac{1}{\sqrt{1 - M_\infty^2}} \frac{M_\infty}{c_\infty}\, x, \\
\tilde{\omega} &= \frac{\omega}{\sqrt{1 - M_\infty^2}}, \\
\tilde{k} &= \frac{k}{\sqrt{1 - M_\infty^2}}, \\
\kappa &= \frac{k M_\infty}{\sqrt{1 - M_\infty^2}}.
\end{aligned} \tag{3.3.17}$$

The boundary condition becomes

$$\frac{\partial \tilde{\phi}_a(\tilde{\mathbf{x}})}{\partial \tilde{n}} = 0. \tag{3.3.18}$$

The solution $\tilde{\phi}_a(\tilde{\mathbf{x}})$ is found in the transformed domain using the BEM technique outlined previously, where the x-coordinates of the boundary and source are modified using the transform given by (3.3.16). In the transformed domain, a solution is sought using the modified wavenumber $\tilde{k}$. This results in a modification of the source strength in the transformed domain, due to the dependence of the acoustic potential on the source strength and the wavenumber, as seen in (3.3.10). This source strength modification is obtained by adding a monopole source $\phi_a^I(\mathbf{x}) = Q(\mathbf{x}_s) G(\mathbf{x}, \mathbf{x}_s)$ to the right hand side of (3.3.14) before applying the transform. Application of the transform yields

$$\nabla_{\tilde{x}}^2 \tilde{\phi}_a(\tilde{\mathbf{x}}) + \tilde{k}^2 \tilde{\phi}_a(\tilde{\mathbf{x}}) = \frac{Q(\tilde{\mathbf{x}}_s) G(\tilde{\mathbf{x}}, \tilde{\mathbf{x}}_s)}{1 - M_\infty^2}. \tag{3.3.19}$$

The modification to the source strength can then be written as

$$\tilde{Q} = \frac{Q}{1 - M_\infty^2}. \tag{3.3.20}$$

Once $\tilde{\phi}_a(\tilde{\mathbf{x}})$ is known, $\phi_a(\mathbf{x})$ may be found using $\phi_a(\mathbf{x}) = \tilde{\phi}_a(\tilde{\mathbf{x}})e^{-i\kappa\tilde{x}}$. The time-harmonic acoustic pressure is then given by

$$p(\mathbf{x}) = \rho_\infty c_\infty \left(ik - M_\infty \frac{\partial}{\partial x} \right) \phi_a(\mathbf{x}). \tag{3.3.21}$$

For further details of the derivation, see Papamoschou and Mayoral [70].

3.3.3.2 Non-Uniform Potential Flow

The non-uniform flow BEM approximation is valid under the assumptions of steady, low Mach number, irrotational, and inviscid flow. The derivation of the approximation begins, as for the uniform flow approximation, with the convected wave equation written in terms of the time-dependent acoustic potential as in (3.3.11), together with the boundary condition given by (3.3.12) for acoustically rigid surfaces.

The flow potential satisfies the Laplace equation

$$\nabla^2 \phi_f(\mathbf{x}) = 0, \tag{3.3.22}$$

and can be solved with the impermeability condition

$$\frac{\partial \phi_f(\mathbf{x})}{\partial n} = 0. \tag{3.3.23}$$

To derive the non-uniform flow BEM approximation, a source term $\delta(\mathbf{x} - \mathbf{x}_s)$ is added to the right hand side of (3.3.11). The following transform was given by Taylor [71]:

$$\begin{gathered} \mathbf{x} = (x, y, z) \to \mathbf{X} = (X, Y, Z), \\ t \to T, \\ \Phi_a(\mathbf{x}, t) \to \hat{\Phi}_a(\mathbf{X}, T), \\ \nabla = \left(\frac{\partial}{\partial x}, \frac{\partial}{\partial y}, \frac{\partial}{\partial z} \right) \to \nabla_X = \left(\frac{\partial}{\partial X}, \frac{\partial}{\partial Y}, \frac{\partial}{\partial Z} \right), \end{gathered} \tag{3.3.24}$$

where

$$\begin{aligned}(X, Y, Z) &= (x, y, z),\\ T &= t + \phi_f(\mathbf{x})/c_\infty^2.\end{aligned} \tag{3.3.25}$$

Using this transform and neglecting $O(M_\infty^2)$ terms, the convected wave equation given in (3.3.11), with the additional source term described above, can be reduced to an ordinary wave equation

$$\frac{\partial^2 \hat{\Phi}_a(\mathbf{X}, T)}{\partial T^2} - c_\infty^2 \nabla_X^2 \hat{\Phi}_a(\mathbf{X}, T) = \delta(\mathbf{X} - \mathbf{x}_s) e^{i\omega\phi_f(\mathbf{x}_s)/c_\infty^2} e^{-i\omega T}. \tag{3.3.26}$$

Under the transform, the boundary condition for acoustically rigid surfaces given in (3.3.12) becomes

$$\frac{\partial \hat{\Phi}_a(\mathbf{X}, T)}{\partial n} = 0. \tag{3.3.27}$$

With the assumption that the acoustic potential is time-harmonic with $\hat{\Phi}_a(\mathbf{X}, T) = \hat{\phi}_a(\mathbf{X}) e^{-i\omega T}$, (3.3.26) can further be reduced to a Helmholtz equation

$$\nabla_X^2 \hat{\phi}_a(\mathbf{X}) + k^2 \hat{\phi}_a(\mathbf{X}) = -\delta(\mathbf{X} - \mathbf{x}_s) e^{i\omega\phi_f(\mathbf{x}_s)/c_\infty^2}. \tag{3.3.28}$$

Setting $\bar{\phi}_a(\mathbf{X}) = \hat{\phi}_a(\mathbf{X}) e^{-i\omega\phi_f(\mathbf{x}_s)/c_\infty^2}$ yields a Helmholtz equation that can be solved by the BEM technique described previously

$$\nabla_X^2 \bar{\phi}_a(\mathbf{X}) + k^2 \bar{\phi}_a(\mathbf{X}) = -\delta(\mathbf{X} - \mathbf{x}_s), \tag{3.3.29}$$

with the boundary condition

$$\frac{\partial \bar{\phi}_a(\mathbf{X})}{\partial n} = 0. \tag{3.3.30}$$

The acoustic pressure is given in terms of the time-harmonic acoustic potential by

$$p(\mathbf{x}) = -\rho_\infty \big(- i\omega \bar{\phi}_a(\mathbf{x}) + \nabla\phi_f(\mathbf{x}) \cdot \nabla \bar{\phi}_a(\mathbf{x}) \big) e^{\left[i\omega\left(\phi_f(\mathbf{x}_s) - \phi_f(\mathbf{x})\right)/c_\infty^2\right]}. \tag{3.3.31}$$

It can be seen that the acoustic pressure at a point $\mathbf{x}$ is only modified by $\nabla\phi_f(\mathbf{x}) = \mathbf{u}(\mathbf{x})$ at that point, while the flow potential at the point $\mathbf{x}$ and the source point $\mathbf{x}_s$ modify the phase. For further details of the derivation, see Taylor [71] and Agarwal and Dowling [89].

3.4 Potential Flow Solver

3.4.1 Panel Method

As described in the previous section, the Taylor non-uniform flow approximation for the BEM requires a potential flow solution at any locations where the acoustic pressure is to be evaluated. Houghton and Carpenter [103] presented a detailed description of a panel method to compute a 2-D potential flow around a body. They also provided a subroutine written in FORTRAN 77 for part of the solution process. Other available solvers such as *XFOIL* [104] use panel methods to compute the potential flow. However, the flow at a point is generally given as a velocity rather than a potential, and *XFOIL* can only compute the flow around an isolated airfoil. It was decided to implement the subroutine provided by Houghton and Carpenter in a solver, extend the method for multi-element airfoils, and use this to obtain the required data for the Taylor transform. The method is summarised here.

It is assumed that the free-stream flow has velocity $|\mathbf{v}_\infty| = V_\infty$ aligned with the x-axis, and that the flow can be represented as the sum of free-stream and disturbance potentials as

$$\phi_f(\mathbf{x}) = \phi_f^\infty(\mathbf{x}) + \phi_f^d(\mathbf{x}). \tag{3.4.1}$$

Here superscript ∞ indicates the free-stream potential, and superscript d indicates the disturbance potential. The free-stream potential is given by

$$\phi_f^\infty(\mathbf{x}) = V_\infty x. \tag{3.4.2}$$

The disturbance potential can then be modelled as a collection of sources with strength σ distributed over the body surface. Once the source distribution is known, the disturbance potential is calculated by integrating the solution over the surface. To solve for the unknown source strengths, the boundary is discretised using P panels in the same way as for the BEM. Each source is located at the midpoint of each panel, and these points are the collocation points. The normal and tangential velocities induced on the collocation points of each panel i are proportional to the strength of the sources across each panel j and can be written as

$$\mathbf{v}_{i,j} \cdot \check{n}_i = \sigma_j N_{i,j} \tag{3.4.3}$$

and

$$\mathbf{v}_{i,j} \cdot \check{t}_i = \sigma_j T_{i,j} \tag{3.4.4}$$

respectively. Here $\mathbf{v}_{i,j}$ is the velocity induced on the collocation point of panel i by the sources on panel j, $\check{n}_i$ is the unit normal vector to panel i, $\check{t}_i$ is the unit tangential vector to panel i, and σ_j is the strength of the sources on panel j. The entries of the matrices $N_{i,j}$ and $T_{i,j}$ are known as the normal and tangential influence coefficients respectively.

For the panels to represent a solid surface, it is required that the velocity normal to each panel be zero. Taking equation (3.4.3), the velocity normal to panel i can be expressed by also incorporating the influence of the free-stream as

$$\sum_{j=1}^{P} \sigma_j N_{i,j} + \mathbf{v}_\infty \cdot \check{n}_i = 0, \qquad i = 1, \ldots, P. \tag{3.4.5}$$

This system of P equations can then be written as

$$\mathbf{N}\boldsymbol{\sigma} = \mathbf{b}. \tag{3.4.6}$$

The matrix $\mathbf{N}$ and vector $\mathbf{b}$ can be computed, and thus the system can be solved to give the vector of source strengths $\boldsymbol{\sigma}$. Once this is known, the flow potential $\phi_f(\mathbf{x})$ can be computed, as can the velocity vector $\mathbf{u}(\mathbf{x}) = \nabla\phi_f(\mathbf{x})$, both of which are required for the Taylor transform. The computation of the influence coefficients used to construct matrix $\mathbf{N}$ is described in detail by Houghton and Carpenter [103], and a FORTRAN 77 subroutine to do this is provided.

The Kutta condition is used to extend the method to lifting flows. Houghton and Carpenter [103] described the method for an isolated airfoil, and this was then extended in the current work for multi-element airfoils consisting of E elements. To satisfy the Kutta condition on each airfoil element, a vortex is added to each panel. The vortex strength γ_l is the same for all panels on a given airfoil element $l = 1, \ldots, E$. The vortex strength is calculated on each airfoil element l so that the magnitudes of tangential velocity on the two panels that define the trailing edge of element l are equal.

Vortices are added to (3.4.5) to give

$$\sum_{j=1}^{P} \sigma_j N_{i,j} + \sum_{l=1}^{E} \gamma_l N_{i,P+l} + \mathbf{v}_\infty \cdot \check{n}_i = 0, \qquad i = 1, \ldots, P. \tag{3.4.7}$$

The trailing edge condition is then given for each airfoil element l by equating the tangential velocities on the two panels t_l and $t_l + 1$ that define the trailing edge of

the given element. This is expressed as

$$\sum_{j=1}^{P} \sigma_j T_{t_l,j} + \gamma_l T_{t_l,P+l} + \mathbf{v}_\infty \cdot \check{t}_{t_l} = -\left(\sum_{j=1}^{P} \sigma_j T_{t_l+1,j} + \gamma_l T_{t_l+1,P+l} + \mathbf{v}_\infty \cdot \check{t}_{t_l+1} \right), \qquad l = 1, \ldots, E. \tag{3.4.8}$$

Using (3.4.7) and (3.4.8) a system of $P + E$ equations can be written

$$\mathbf{Ma} = \mathbf{b}. \tag{3.4.9}$$

The entries of the matrix and vectors are given by

$$\begin{aligned}
M_{i,j} &= N_{i,j}, && i = 1, \ldots, P, && j = 1, \ldots, P+E, \\
M_{P+l,j} &= T_{t_l,j} + T_{t_l+1,j}, && l = 1, \ldots, E, && j = 1, \ldots, P+E, \\
a_i &= \sigma_i, && i = 1, \ldots, P, \\
a_{P+l} &= \gamma_l, && l = 1, \ldots, E, \\
b_i &= -\mathbf{v}_\infty \cdot \check{n}_i, && i = 1, \ldots, P, \\
b_{P+l} &= -\mathbf{v}_\infty \cdot (\check{t}_{t_l} + \check{t}_{t_l+1}), && l = 1, \ldots, E.
\end{aligned} \tag{3.4.10}$$

Houghton and Carpenter [103] described the modification of their influence coefficient subroutine to take the additional vortices into account for a single-element airfoil. This modification was repeated for each airfoil element in order to calculate the additional matrix entries $N_{i,j}$ and $T_{i,j}$ for $j = P + 1, \ldots, P + E$ with $i = 1, \ldots, P$. A FORTRAN program was written to import an airfoil, set up the case parameters, call the subroutine to calculate the influence coefficients, construct the system (3.4.9), and solve the system using the LU factorisation subroutine provided with *ABEMFULL* [100]. An additional subroutine was written to compute $\phi_f(\mathbf{x})$ and $\mathbf{u}(\mathbf{x}) = \nabla\phi_f(\mathbf{x})$ at evaluation points $\mathbf{x}$ by integrating the solution over the surface. This solution was then exported so that it could be imported into *ABEMFULL* for use with the non-uniform flow BEM approximation.

3.4.2 Validation of Panel Method Solver

The panel solver implemented in the previous section was validated against an inviscid solution from the commercial CFD solver *ANSYS Fluent*. This was done by comparing surface pressure distributions obtained using the two solvers. To

compute the surface pressure coefficient C_p using the panel solver, the tangential velocity V_t on each panel is required. This is computed for each panel i using

$$V_{t_i} = \sum_{j=1}^{P} \sigma_j T_{i,j} + \sum_{l=1}^{E} \gamma_l T_{i,P+l} + \mathbf{v}_\infty \cdot \check{t}_i, \qquad i = 1, \ldots, P. \tag{3.4.11}$$

The pressure coefficient on each panel is then computed through Bernoulli's equation

$$C_{p_i} = 1 - \left(\frac{V_{t_i}}{V_\infty} \right)^2, \qquad i = 1, \ldots, P. \tag{3.4.12}$$

Two different airfoil configurations were used to validate the panel solver. These were the NACA 0012 airfoil, and the RA16SC1 airfoil with flap at 20°. The RA16SC1 airfoil is a multi-element high-lift airfoil designed by ONERA Lille, France for the EUROPIV 2 project [105]. It is used extensively in the current work. The NACA 0012 airfoil was discretised using 260 panels, and the RA16SC1 airfoil with 500 panels for the main element and 150 for the flap. The retracted airfoil chord length a was chosen to be 5 m to reflect the size of wing found on smaller commercial airliners. The free steam velocity was taken as $M_\infty = 0.2$. The symmetric NACA 0012 airfoil was validated at an angle of attack $\alpha = 5°$ to ensure that it was lifting, and the RA16SC1 airfoil at $\alpha = 0°$. The free-stream flow is aligned with the x-axis, and so the angle of attack is taken into account by rotating the discretised airfoil geometry.

Domain grids were created around each airfoil in order to obtain flow solutions for the LEE. The creation of the grids and the subsequent flow solution using *ANSYS Fluent* is explained in detail in Sections 4.3 and 4.4. These flow solutions were used here for the validation of the panel solver. Figure 3.5 shows the surface pressure distribution computed by both solvers for the NACA 0012 airfoil, where it can be seen that the two solutions are in good agreement. Figure 3.6 shows the surface pressure distribution for the RA16SC1 airfoil with flap 20°. The two solutions are again in good agreement, showing that the modification of the method for multi-element airfoils was implemented successfully. The variations in the distribution near to the leading edge of the main airfoil element are due to the airfoil surface discretisation. This discretisation was used both to determine the surface panels for the panel method, and to create the domain mesh for the CFD solution. Figure 3.7 shows a visualisation of the Mach number magnitude and streamlines of the solution for the RA16SC1 airfoil with flap 20° computed using the panel solver. The streamlines can be seen to leave the trailing edge of each airfoil element smoothly.

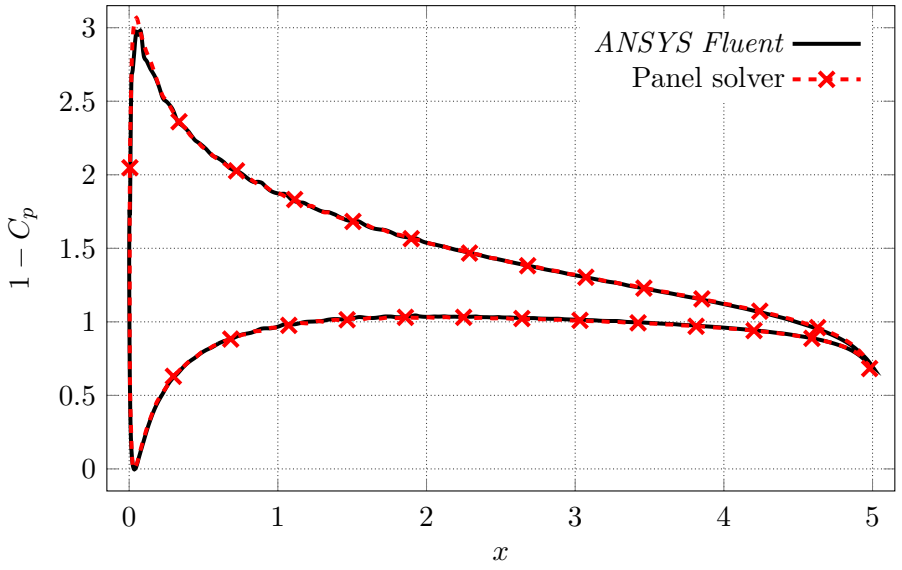

Figure 3.5: Validation of panel solver. NACA 0012 airfoil, $\alpha = 5°$, $M_\infty = 0.2$.

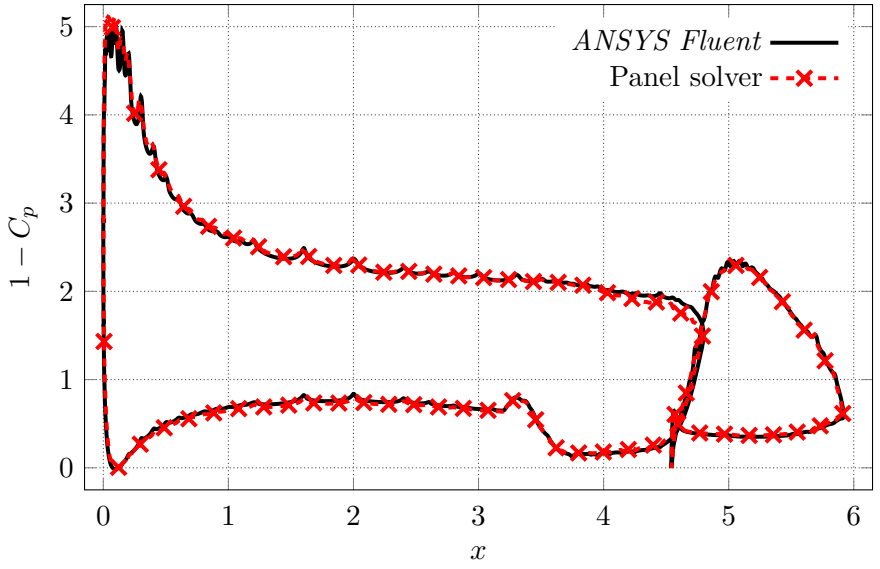

Figure 3.6: Validation of panel solver. RA16SC1 airfoil with flap 20°, $\alpha = 0°$, $M_\infty = 0.2$.

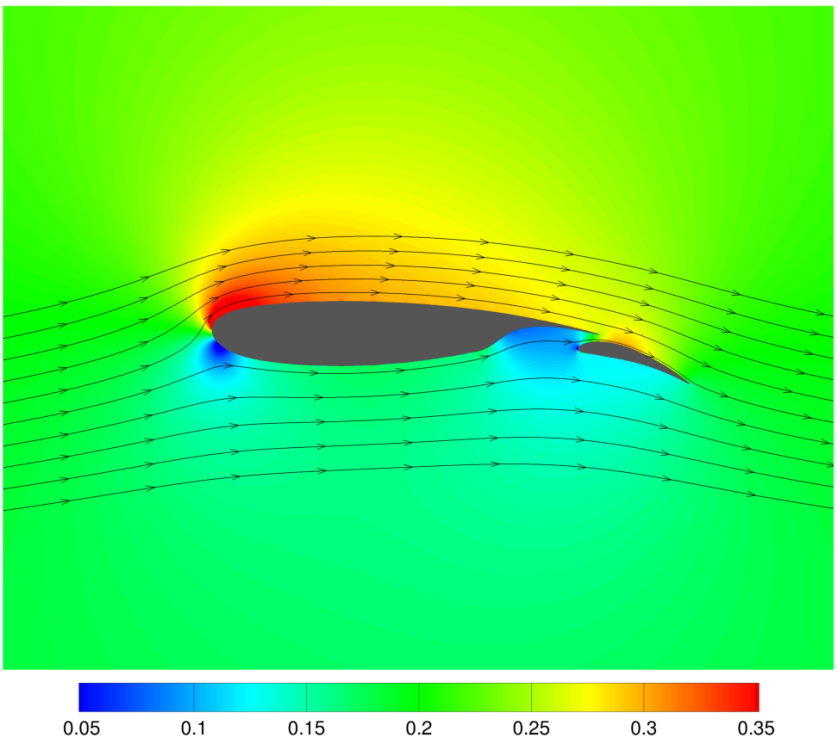

Figure 3.7: Mach number magnitude and streamlines, RA16SC1 airfoil with flap 20°, $\alpha = 0°$, $M_\infty = 0.2$.

3.5 Linearised Euler Equations

3.5.1 Derivation and Acoustic Source

The Euler equations are derived from the Navier-Stokes equations with the assumptions of inviscid and isentropic flow. The linearised Euler equations are in turn derived by linearising the Euler equations around a mean flow field. In order to conduct this linearisation, it is assumed that acoustic perturbations are small compared to mean flow values, and that the acoustic perturbations do not affect the mean flow. Thus, pressure, density, and velocity can be written as

$$p = p_0 + p', \qquad \rho = \rho_0 + \rho', \qquad \mathbf{u} = \mathbf{u}_0 + \mathbf{u}'. \tag{3.5.1}$$

Here mean flow variables are denoted with subscript 0, and acoustic variables with superscript $'$.

The mean flow is described by the Euler equations, written here with subscript 0,

$$\begin{aligned} \frac{\partial \rho_0}{\partial t} + \nabla \cdot (\rho_0 \mathbf{u}_0) &= 0, \\ \frac{\partial \mathbf{u}_0}{\partial t} + \mathbf{u}_0 \cdot \nabla \mathbf{u}_0 + \frac{1}{\rho_0} \nabla p_0 &= \mathbf{0}. \end{aligned} \tag{3.5.2}$$

To obtain the linearised Euler equations, the flow decomposition (3.5.1) is substituted into the Euler equations. As acoustic perturbations are assumed to be small compared to the mean flow, non-linear products of acoustic variables will be negligible compared to the mean flow terms. Thus, neglecting these non-linear terms and using (3.5.2), the linearised Euler equations are given by

$$\begin{aligned} \frac{\partial \rho'}{\partial t} + \nabla \cdot (\rho_0 \mathbf{u}' + \rho' \mathbf{u}_0) &= 0, \\ \frac{\partial \mathbf{u}'}{\partial t} + \mathbf{u}_0 \cdot \nabla \mathbf{u}' + \mathbf{u}' \cdot \nabla \mathbf{u}_0 + \frac{1}{\rho_0} \left(\nabla p' - \frac{\rho'}{\rho_0} \nabla p_0 \right) &= \mathbf{0}. \end{aligned} \tag{3.5.3}$$

An acoustic source must be added to the linearised Euler equations to generate noise. A monopole source was used to represent an idealised landing gear noise source throughout this thesis, for the reasons outlined in Section 2.5. A monopole point source is singular at its origin, and thus a distributed source must be used in numerical methods where the source is located within the computational domain. A monopole source at a single frequency was implemented in a similar manner to Bailly and Juvé [45], by adding a source term to the right hand side of (3.5.3). For a monopole located at (x_s, y_s, z_s) this term is given by

$$\mathbf{S}(x, y, z, t) = \sin(\omega t) F(x, y, z), \tag{3.5.4}$$

with

$$F(x, y, z) = \epsilon \exp\left(-\beta \Big[(x - x_s)^2 + (y - y_s)^2 + (z - z_s)^2 \Big] \right). \tag{3.5.5}$$

Here ϵ controls the amplitude of the monopole, and β controls the width of the monopole forcing region. Equation (3.5.5) describes a Gaussian distribution. It can be shown that for a required source radius R, the monopole forcing region parameter β is given by

$$\beta = \frac{1}{2} \left(\frac{s}{R} \right)^2, \tag{3.5.6}$$

where s is the number of required standard deviations of the Gaussian distribution

contained within this radius. A value of $s = 3$ was used for all LEE simulations throughout this thesis as 99.73 % of a Gaussian distribution falls within three standard deviations of the centre.

3.5.2 Solution by the Finite Difference Method and Boundary Conditions

For numerical solution, the linearised Euler equations given by Equation (3.5.3) are non-dimensionalised using

$$\rho^* = \frac{\rho}{\rho_\infty}, \qquad p^* = \frac{p}{\rho_\infty c_\infty^2}, \qquad \mathbf{u}^* = \frac{\mathbf{u}}{c_\infty}, \qquad t^* = t c_\infty, \qquad \omega^* = \frac{\omega}{c_\infty}. \tag{3.5.7}$$

The non-dimensionalised linearised Euler equations were solved using the high-order time-domain solver *SotonLEE* [106]. *SotonLEE* is a multi-block finite difference solver for structured grids that has been used by various authors for aeroacoustic investigations [53, 106, 107, 108, 109]. It uses a fourth-order compact spatial discretisation scheme [31, 32] with a sixth-order compact filtering scheme [33], and a fourth-order LDDRK explicit temporal scheme [35]. The spatial scheme allows resolution of acoustic waves with 8 points per wavelength (PPW), but at least 10 PPW were used throughout the current work to ensure accuracy.

The acoustic domain must be artificially truncated for numerical solution. To prevent acoustic reflections from the boundaries of this truncated domain that would contaminate the acoustic solution, non-reflecting boundary conditions must be used. For all LEE simulations in this thesis, a non-reflecting optimised zonal transverse characteristic boundary condition [36] was used on the edges of the computational domain. The width of the non-reflecting zone was 10 grid nodes for all simulations, unless otherwise specified. The acoustically rigid scattering surfaces were treated with a slip-wall boundary condition. Impedance conditions were not considered in this work.

3.5.3 Monopole Parameter Study

Initial simulations of a harmonic monopole in the free-field with a uniform flow aligned with the x-axis were conducted in 2-D in order to evaluate the effect of varying the monopole parameters. For this evaluation, 360 observers labelled by angle θ were defined on a circle of radius 5 m centred on the source. The

$\theta = 0°$ observer was located directly upstream of the source with θ increasing in an anticlockwise direction. For an omni-directional monopole at a given frequency and strength, p_{rms} will be equal at all observer positions without flow. For a monopole of the same frequency and strength in a uniform flow, p_{rms} will increase at the 0° observer and decrease at the 180° observer due to convective amplification. The value of p_{rms} should remain unchanged at the 90° observer with varying Mach number.

The initial simulations showed that the value of p_{rms} obtained at the 90° observer depends on several different factors. These factors are:

- The value of amplitude parameter ϵ.
- The radius R of the monopole forcing region.
- The grid covered by the forcing region.
- The time step of the simulation Δt.
- The acoustic frequency.
- The Mach number.

This makes obtaining a specified p_{rms} at a given observer *a priori* challenging. However, the governing equations are linear, and so linear scaling may be applied once a solution has been computed in order to obtain the required p_{rms} at the chosen observer. As the value of p_{rms} should remain unchanged at the 90° observer with varying Mach number for a monopole in the free-field, this observer was chosen as the most appropriate for computing the required scaling factor.

A study in 2-D was conducted in order to determine the best values to use for the various parameters to ensure that the distributed source behaved as a point source. In particular, the optimum value of the source radius with respect to the acoustic wavelength was of interest. It was seen in the initial simulations that if the source region was too large with respect to the wavelength then incorrect convective amplification effects were observed. When the source radius was close in size to the wavelength, the convective amplification occured in the backward direction. This was also noted by Dragna *et al.* [52]. The results of the study are presented in this section.

In order to determine the accuracy of the results obtained by the numerical method, a 2-D analytical solution for a monopole in the free-field in a uniform flow was required. This may be obtained through use of Green's functions and the

Lorentz transform described in (3.3.16) and (3.3.17), as used for the uniform flow BEM approximation. The acoustic potential in the absence of flow for a monopole located at $\mathbf{x}_s$ is given by $\phi_a(\mathbf{x}) = QG(\mathbf{x}, \mathbf{x}_s)$. In 2-D, this is

$$\phi_a(\mathbf{x}) = Q\frac{i}{4}H_0^{(1)}(kr), \tag{3.5.8}$$

with

$$r = \sqrt{(x - x_s)^2 + (y - y_s)^2}. \tag{3.5.9}$$

Equations (3.5.8) and (3.5.9) are transformed under the Lorentz transform given by (3.3.16) and (3.3.17) to become

$$\tilde{\phi}_a(\tilde{\mathbf{x}}) = Q\frac{i}{4}H_0^{(1)}(\tilde{k}\tilde{r}), \tag{3.5.10}$$

and

$$\tilde{r} = \frac{1}{\sqrt{1 - M_\infty^2}}B, \tag{3.5.11}$$

where $B = \sqrt{(x - x_s)^2 + (1 - M_\infty^2)(y - y_s)^2}$ for convenience. The acoustic pressure is computed using (3.3.21), into which $\phi_a(\mathbf{x}) = \tilde{\phi}_a(\tilde{\mathbf{x}})e^{-i\kappa\tilde{x}}$ is substituted to give

$$p(\mathbf{x}) = \rho_\infty c_\infty \left(ik - M_\infty \frac{\partial}{\partial x}\right)\tilde{\phi}_a(\tilde{\mathbf{x}})e^{-i\kappa\tilde{x}}. \tag{3.5.12}$$

Substituting (3.5.10) into (3.5.12), and then using (3.5.11), $\tilde{x} = x/\sqrt{1 - M_\infty^2}$, $\tilde{k} = k/\sqrt{1 - M_\infty^2}$, and $\kappa = kM_\infty/\sqrt{1 - M_\infty^2}$ to simplify gives

$$p(\mathbf{x}) = Q\frac{i}{4}\rho_\infty c_\infty \left(ik - M_\infty \frac{\partial}{\partial x}\right)\exp\left(\frac{-ikM_\infty x}{1 - M_\infty^2}\right)H_0^{(1)}\left(\frac{kB}{1 - M_\infty^2}\right). \tag{3.5.13}$$

After differentiation, this becomes

$$\begin{aligned} p(\mathbf{x}) = Q\frac{i}{4}\rho_\infty c_\infty \exp\left(\frac{-ikM_\infty x}{1 - M_\infty^2}\right)\Bigg[&ikH_0^{(1)}\left(\frac{kB}{1 - M_\infty^2}\right) \\ &+ \frac{ikM_\infty^2}{1 - M_\infty^2}H_0^{(1)}\left(\frac{kB}{1 - M_\infty^2}\right) + \frac{kM_\infty(x - x_s)}{(1 - M_\infty^2)B}H_1^{(1)}\left(\frac{kB}{1 - M_\infty^2}\right)\Bigg]. \end{aligned} \tag{3.5.14}$$

Using this equation along with (3.3.9), p_{rms} could be computed at each observer. These values of p_{rms} could then be used to evaluate the numerical method.

The study to determine the effect of source radius with respect to wavelength on the accuracy of the numerical method was conducted at a fixed frequency of 250 Hz, and a Mach number of $M_\infty = 0.2$. The analytical solution for this frequency and

Mach number was obtained at each observer using (3.5.14) and (3.3.9). The value of Q was chosen so as to give a p_{rms} of 2 Pa, or equivalently an SPL of 100 dB, at the 90° observer. This gives values for p_{rms} of 2.376 Pa upstream at $\theta = 0°$, and 1.584 Pa downstream at $\theta = 180°$. For the numerical method, the source radius R was varied to give different values of the ratio $\chi = \lambda_{\text{upstream}}/R$. The upstream wavelength $\lambda_{\text{upstream}}$ at $\theta = 0°$ was used, as the wavelength is smallest at this observer angle. It is computed using

$$\lambda_{\text{upstream}} = \frac{(1 - M_\infty)c_\infty}{f}. \tag{3.5.15}$$

A structured quadrilateral grid was constructed for an empty square domain with sides 12 m in length. The maximum Δx was 4.5×10^{-2} m, which was enough to resolve the acoustic waves with at least 10 PPW in the upstream direction. The source was placed on a grid node at the centre of the domain, and for each value of R the grid was locally refined around this node so that the source radius covered approximately 3 nodes in the radial direction. The value of the monopole amplitude parameter was set as $\epsilon = 0.2$ for all cases. As scaling was conducted as a post-processing step, the value chosen for ϵ would not affect the result as long as it was large enough for rounding errors to be avoided in the numerical method. Each simulation was run for 3.2×10^{-2} s in order for the initial acoustic pulse to reach the domain boundaries, before pressure was sampled at all observers for 5 periods at 25 samples per period. This sampled pressure data was then used to compute a value for p_{rms} at each observer. For each simulation, a scaling factor was computed at the 90° observer that scaled the computed p_{rms} to a value of 2 Pa to match the analytical solution. This scaling factor was then applied to the computed value of p_{rms} at each observer for that simulation.

The values of χ chosen for the study are shown in Table 3.3, along with the associated source radii. The average absolute percentage error in p_{rms} evaluated against the analytical solution over all observers is shown to be around 1 % for all values of χ. The maximum percentage error at any given observer is also shown for each value of χ, and this is less than 3.2 % once $\chi \geq 25$. The percentage error of p_{rms} upstream at $\theta = 0°$ and downstream at $\theta = 180°$ for the various values of χ is shown graphically in Figure 3.8. It can be seen that as χ is increased, the error both upstream and downstream tends to a value of around 0.4 %. A value of $\chi \approx 50$ was chosen for the rest of the work in this thesis, as this value is a good compromise between accuracy and minimising the amount of required source region refinement. A more refined source region requires the use of a smaller time step in the simulation. It was also intended to examine the effect of refining the

source region with more than 3 nodes radially. However, as the errors observed here were satisfactorily small, and further refinement would mean the use of a smaller time step, it was decided that using 3 nodes in the radial direction would be sufficient. The chosen values of $\chi \approx 50$ with R discretised using around 3 nodes radially are in agreement with values used by Dragna *et al.* [52].

It has been discussed that the value of p_{rms} computed at a given observer in the free-field depends on several factors. This also has implications for cases that involve a scattering geometry. It has been shown in this section that a scaling factor can be computed for a free-field case that gives a specified value of p_{rms} at a given observer. For a scattering case, the required value of p_{rms} at any given observer is not known in advance. However, for each scattering case, the required

Table 3.3: Source radii, and average and maximum percentage error in p_{rms} against the analytical solution across all observers.

χ	R	Average % error	Maximum % error
10	1.089×10^{-1}	0.990	3.471
25	4.355×10^{-2}	0.963	3.125
50	2.177×10^{-2}	1.054	3.167
100	1.089×10^{-2}	1.063	3.170
150	7.258×10^{-3}	1.079	3.184

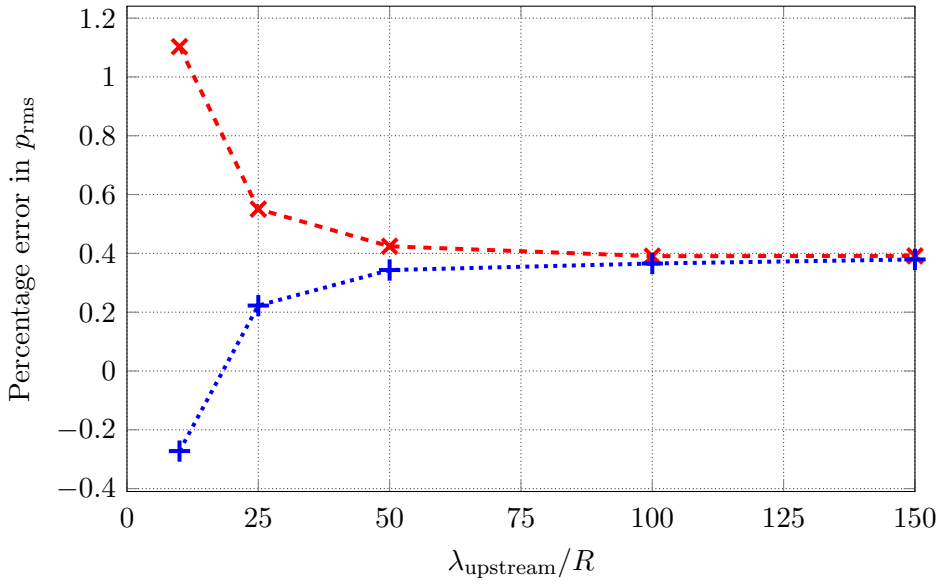

Figure 3.8: Percentage error of p_{rms} against the analytical solution for various values of R. Upstream -×-, downstream ···+···.

scaling factor can be obtained from an equivalent free-field case, provided that the factors that affect the obtained p_{rms} discussed earlier are the same in both simulations. This is discussed further in Section 4.3.

3.5.4 Validation of Solver for Scattering Problems

The analytical solution by Morris [101] for the scattering of a cylindrical source by a circular cylinder was used again in order to validate *SotonLEE* for scattering problems in 2-D. The validation was conducted at a frequency of 325 Hz, which is the same frequency as used in Section 3.3.2 for the validation of the BEM solvers. This frequency was chosen as it is in the upper half of the frequency range used for the investigations in Chapter 4 and Chapter 5, and directivity plots obtained using this frequency show a larger number of directional lobes than they would for lower frequencies. The same geometry, source, and observer locations as seen in Figure 3.1 were used. A structured quadrilateral grid was constructed around the circular geometry for numerical computation using *SotonLEE*. The computational domain was a square with sides 24 m in length, with the scattering geometry located in the centre. The maximum Δx was 4.5×10^{-2} m, which allowed the resolution of acoustic waves with at least 10 PPW. The topology of the grid can be seen in Figure A.1 in Appendix A.

A source radius of 3.6×10^{-2} m was used. This is approximately 1/25th of a wavelength, which is sufficient to represent a point source in the absence of flow. The simulation was run for 5.8×10^{-2} s to allow the initial acoustic pulse to reach the domain boundaries at the furthest points from the source. The pressure was then sampled for 10 periods at 25 samples per period. Further details of the simulation can be found in Table A.1 in Appendix A. The computed acoustic pressure as at the end of the simulation is shown in Figure 3.9. The non-reflecting boundary conditions can be seen to have minimised acoustic reflections from the domain boundaries.

The sampled pressure was used to compute p_{rms} at each observer, and this was then scaled so as to match the computed solution with the analytical solution at its maximum value. The SPL was computed for each solution and plotted against each other. The numerical solution is in good agreement with the analytical solution, as seen in Figure 3.10. The percentage error in p_{rms} against the analytical solution was computed at each observer using (3.1.1). This is shown for observers in the range $0° \leq \theta \leq 180°$ in Figure 3.11. The percentage error is generally less than

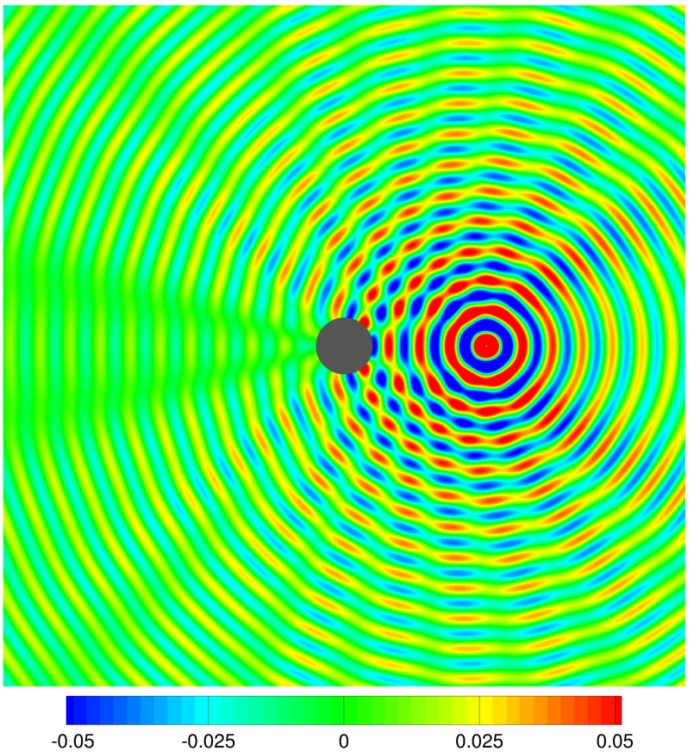

Figure 3.9: Acoustic pressure (Pa) for the scattering of a monopole at 325 Hz at a distance of 5 m from the centre of a circular cylinder of radius 1 m in 2-D.

3 % at any given observer, and the average absolute percentage error across all 360 observers is 1.354 %. This confirms the accuracy of the solver for acoustic scattering problems in the absence of flow.

3.6 Computational Costs of the Solvers

Having validated the employed acoustic solvers for scattering problems, the computational costs of the solvers can be discussed and compared. All LEE simulations undertaken for this thesis using *SotonLEE*, in both 2-D and 3-D, were conducted on the high-performance computing cluster *Iridis 4* at the University of Southampton. All computations of non-uniform base flows for the LEE simulations were also computed on *Iridis 4* using *ANSYS Fluent*. Each compute node of the *Iridis 4* cluster has dual 2.6 GHz Intel Sandybridge processors giving 16 cores per node with 64 GB of memory. In contrast, all 2-D BEM and panel solver simulations were conducted on a desktop computer with an Intel Core i7-2600 3.4 GHz processor and 16 GB of memory. All 3-D BEM simulations were conducted using *ACTIPOLE* on *Iridis 4*.

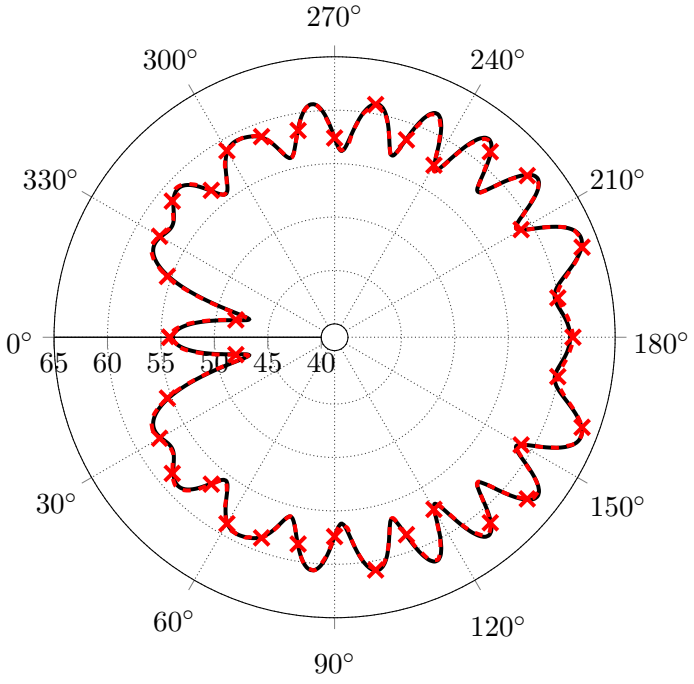

Figure 3.10: Comparison of SPL (dB) between an analytical solution and the numerical solution, evaluated at a radius of 10 m centred on the cylinder centre. Analytical ——, *SotonLEE* - -×- -.

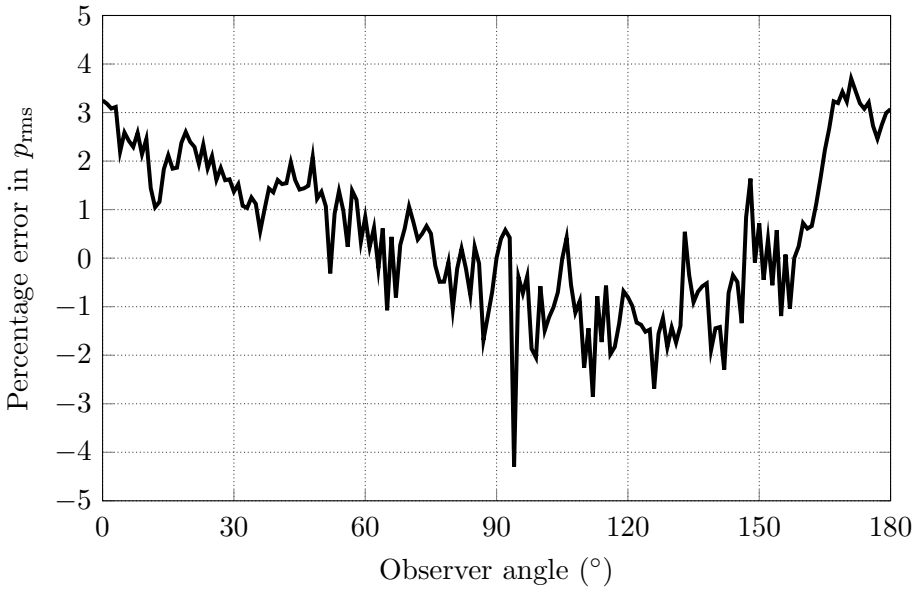

Figure 3.11: Percentage error of p_{rms} against the analytical solution.

Full details of all LEE simulations undertaken for this thesis are given in Appendix A, and all BEM simulations in Appendix B. Details of some of these are summarised here for discussion. In general, each 2-D BEM simulation computed the acoustic solution at only 360 observers in order to generate directivity plots. Each simulation took at most 1 s to complete using a single core, regardless of the flow approximation method that was employed. This was also true for the 2-D scattering validation case without flow shown in Section 3.3.2. The associated 2-D panel solver solutions required for the non-uniform flow approximation similarly only computed the flow potential and its derivative at the 360 observers, and also took at most 1 s using a single core to complete.

The LEE methods compute the solution at all grid nodes in the computational domain. The time taken to complete each simulation depends on the total number of grid nodes, the chosen time step Δt for the simulation, the total required simulation time, and the number of cores employed by the solver. The time step for each simulation was chosen so as to enable the accurate recording of pressure data at the required sample rate, while also minimising the computation time and ensuring that the Courant-Friedrichs-Lewy (CFL) number was at most approximately 0.5. Each simulation needed to be run for a period of time that was long enough for the initial acoustic pulse to propagate to the domain boundaries before pressure sampling could begin. This time also needed to account for the propagation of reflections of this initial pulse from any scattering bodies to the domain boundaries, so that interference effects could be accurately recorded. The 2-D scattering validation simulation for the LEE solver shown in Section 3.5.4 took approximately 12 minutes to complete using 128 cores on *Iridis 4*. This 2-D LEE validation simulation was computationally more expensive than the equivalent 2-D BEM simulation. It can be seen from Appendix A and Appendix B that the 2-D LEE simulations were more expensive than all of the equivalent 2-D BEM simulations undertaken for this thesis.

Later in Section 4.9, two 3-D LEE simulations are described that were undertaken for the scattering of a single frequency source by a NACA 0012 airfoil. One was conducted over a uniform base flow, and the other over a non-uniform base flow. The airfoil had a constant spanwise cross-section, and was assumed to be infinite in span so that wing tip effects could be neglected. Non-reflecting boundary conditions were applied to the spanwise domain boundaries in order to satisfy this assumption. The base flow was assumed to be constant in the spanwise direction. Each of these 3-D LEE simulations was conducted using 400 cores, and the simulation with a uniform base flow took approximately 55 hours to complete. An

equivalent 3-D BEM simulation using the uniform flow approximation was also conducted for comparison using *ACTIPOLE*. This 3-D BEM simulation was conducted using 64 cores and took approximately 8 minutes to complete. It is shown in Section 4.9 that these solutions are in good agreement. This further highlights the expense of LEE solvers in comparison to BEM solvers for equivalent scattering problems. However, the LEE solvers account for the refraction of acoustic waves by a non-uniform flow. The BEM cannot account for this, even with the use of a flow approximation method.

The scattering of single frequency and broadband sources by an airfoil is presented in Chapter 4 and Chapter 5 respectively. The effect of non-uniform flow due to circulation around a lifting wing on the acoustic scattering was investigated systematically by varying the angle of attack, Mach number, and airfoil flap configuration. The LEE solver was chosen for these investigations to ensure that refraction effects were accounted for. Solutions were required over both uniform and non-uniform base flows for each combination of parameters. Thus, a large number of simulations needed to be completed for these investigations. It was decided to conduct the investigations using 2-D simulations due to the expense of the single frequency 3-D LEE simulations using the NACA 0012 airfoil. The 2-D grids for the high-lift airfoil configurations used in the investigations had a finer grid refinement than that for the NACA 0012 airfoil due to the curvature of the geometries. This led to longer computation times for these configurations. For the broadband simulations, pressure needed to be sampled for a longer time in order for the PSD of the scattered source to be accurately computed. These additional requirements and the large number of parameters under investigation meant that running all of the simulations in 3-D was not feasible.

3.7 Summary

The mathematical preliminaries that were required for the work throughout this thesis have been presented in this chapter. This discussion began with a summary of the solvers and codes that were used throughout this thesis. An overview of the governing equations for the BEM was given, and the solvers employed for the current work were validated. The governing equations for the uniform and non-uniform flow BEM approximation methods were described. The non-uniform BEM flow approximation requires a potential flow solution. Thus, a 2-D panel method to compute a potential flow solution that satisfies the Kutta condition on

each element of a multi-element airfoil was described. This was implemented in a solver, and validated against an inviscid CFD solution. The LEE and the employed solution methods were then presented, including the implementation of an acoustic monopole source. The results of a parameter study for the monopole source were presented. This included the derivation of an expression for the complex acoustic pressure for a monopole in the free-field in a uniform flow, which was used to determine the accuracy of the solution obtained using different values of the various parameters. Optimum values for various monopole parameters were obtained, and the employed LEE solver was validated for scattering problems. Finally, the computational costs of the employed solvers were discussed.

Chapter 4

The Scattering of a Single Frequency Source by an Airfoil

4.1 Introduction

The first step in the investigation of installation effects of landing gear noise sources was to examine the scattering of a single frequency source by an airfoil. The BEM solvers that were employed for the work in this thesis were frequency-domain solvers. It was explained in Section 2.5 that BEM flow formulations do not account for the refraction of acoustic waves by a mean flow. The effect of refraction on the acoustic scattering needed to be investigated using an appropriate alternative solver in order to determine if the effect was significant. Therefore, investigations were undertaken using the LEE solver, which can account for refraction effects. These LEE investigations were conducted using single frequency sources so that the uniform and non-uniform flow BEM formulations could be evaluated against the LEE results.

Acoustic waves emitted from a source installed beneath an airfoil are reflected by the airfoil surface and propagate back into the path of waves that were emitted from the source at a later time. At a single frequency, the superposition of these incident and reflected waves leads to constructive and destructive interference. This results in directional lobes in the obtained directivity plots. It was of interest to determine if refraction effects altered the observed interference. The LEE and BEM investigations into the scattering of a single frequency source by an airfoil are presented in this chapter. Interference is reduced for acoustic waves that are uncorrelated in time, such as those generated by a broadband source. Therefore,

further LEE investigations were conducted using a broadband source, and these are presented in Chapter 5.

It is shown in Figure 1.3 that the non-uniform flow around a lifting airfoil can be decomposed into a uniform free-stream and circulation. The circulation creates velocity gradients in the non-uniform flow that cause the refraction of acoustic waves. The upstream and downstream refraction of acoustic waves from a point source due to a velocity gradient typical of that found beneath a lifting airfoil is illustrated in Figure 1.4. The effect of non-uniform flow due to circulation around the lifting airfoil was quantified as the difference in acoustic scattering over uniform and non-uniform base flows. This difference allowed the effect of acoustic refraction due to flow velocity gradients to be quantified. The circulation was varied systematically by altering the angle of attack, Mach number, and airfoil flap configuration.

The investigations primarily concentrated on an acoustic source in the approximate location of a landing gear, using Mach numbers representative of a commercial airliner on approach. However, the effect of higher Mach numbers and an alternative source location were also investigated. Given the range of parameters that was to be investigated, these investigations were conducted using 2-D simulations due to the computational expense of 3-D simulations. However, a 3-D example was also undertaken in order to determine if the conclusions drawn from the 2-D simulations were also applicable to 3-D.

The model used for the investigations in this chapter is described in Section 4.2. Section 4.3 discusses the computational grids that were created to solve the LEE for the investigation. An overview of the computation of the non-uniform and uniform base flows that are required for the LEE simulations is presented in Section 4.4. The investigation of the effect of circulation is presented in Section 4.5. A discussion on the accuracy of the observed results is given in Section 4.6. The effect of a higher Mach number is shown in Section 4.7, and an alternative source location in Section 4.8. The extension of the investigation to 3-D is discussed and example simulations presented in Section 4.9. The uniform and non-uniform flow BEM approximation methods are evaluated in Section 4.10. Finally, a summary for the investigation of the scattering of a single frequency source is given in Section 4.11.

4.2 Model Description

Two different airfoils were chosen for use as the scattering geometry. These were the NACA 0012 airfoil, and the RA16SC1 airfoil. The symmetric NACA 0012 airfoil was chosen as it is non-lifting at zero angle of attack. As discussed in Section 3.4.2, the RA16SC1 airfoil is a multi-element high-lift airfoil designed by ONERA Lille, France for the EUROPIV 2 project [105]. Four different flap and slat configurations of the RA16SC1 airfoil were used throughout this thesis. The deployment of flaps and slats increases the circulation around a lifting wing for a fixed angle of attack, and also alters the shape of the reflective underside of the scattering airfoil surface. The investigation of the effect of the increase in circulation and the change in scattering geometry are both key aims of this thesis. The two airfoil geometries, including all employed flap and slat configurations, are shown in Figure 4.1. The retracted airfoil chord length a for both airfoils was chosen to be 5 m to reflect the size of wing found on smaller commercial airliners.

Following the discussion in Section 2.5, a single monopole source was used to represent an idealised landing gear noise source. An omni-directional monopole is a good approximation for the almost omni-directional far-field directivity of a landing gear in the free-field at low frequencies. However, landing gear noise source regions are non-compact, and so a monopole is not representative of the directivity in the near-field. The propagation of acoustic waves from a monopole source in a uniform flow is well understood. For this reason, a monopole source was used here as an approximation of a landing gear source in order to better understand the effect of non-uniform flow due to circulation on the propagation

(a) NACA 0012 airfoil.

(b) RA16SC1 airfoil.

(c) RA16SC1 airfoil with flap 20°.

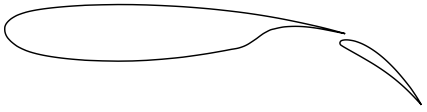

(d) RA16SC1 airfoil with flap 40°.

(e) RA16SC1 airfoil with flap 40° plus slat.

Figure 4.1: Airfoil geometries.

and scattering of the source installed beneath an airfoil. Three discrete acoustic frequencies at octave intervals representative of low-frequency landing gear noise were chosen for the investigation. These frequencies, which correspond to noise from large-scale landing gear components such as struts and wheels, were chosen as 125 Hz, 250 Hz, and 500 Hz. Using the retracted airfoil chord length $a = 5\,\mathrm{m}$ as a characteristic length scale, these frequencies correspond to the non-dimensional Helmholtz numbers $ka = 11.54$, 23.09, and 41.17 respectively.

The source was positioned at $(+a/2, -a/2)$ from the leading edge of the main airfoil element in each configuration. Observer locations, where pressure was to be sampled, were defined at 360 locations on a circle of radius a centred on the source. The observers were labelled by angle θ, with $\theta = 0°$ located in the negative x-direction from the source. An example geometry, along with source and observer locations, is shown in Figure 4.2. The angle of attack was altered by changing the free-stream Mach vector as shown in Figure 4.2, which kept the observers in the same position relative to the airfoil. This also allowed the re-use of computational grids for different angles of attack, with only a different base flow being required. This in turn helped to minimise any error in the results between different angles of attack, which might otherwise have been caused due to any variations in the spatial discretisation.

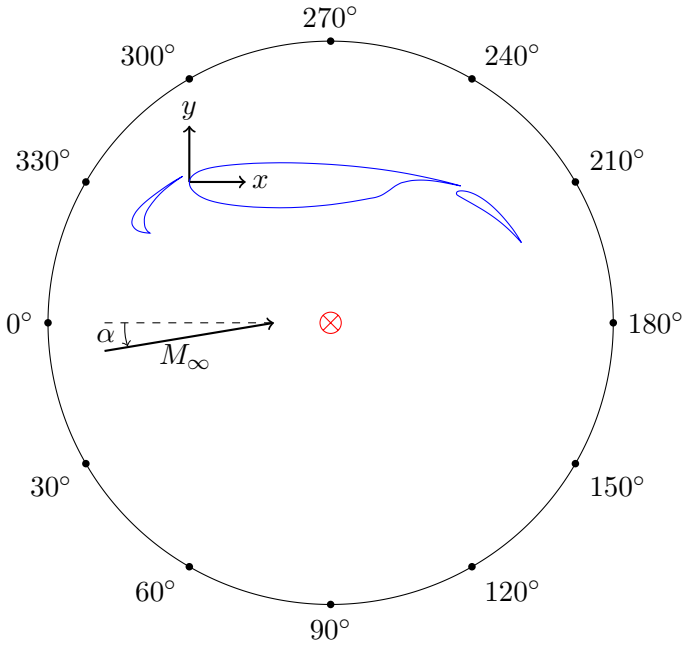

Figure 4.2: RA16SC1 airfoil with flap 40° plus slat, with source and observer locations.

Circulation around a lifting wing increases as angle of attack α and Mach number M_∞ is increased, and as high-lift devices such as flaps and slats are deployed. The following cases were chosen in order to investigate the effect of an increase in circulation on the scattering of the acoustic source:

- NACA 0012, $M_\infty = 0.2$: $\alpha = 0°$, $1°$, $\ldots$, $8°$.
- NACA 0012, $\alpha = 5°$: $M_\infty = 0.1$, 0.15, 0.2, 0.25, 0.3.
- RA16SC1, $M_\infty = 0.2$, $\alpha = 0°$: flap and slat retracted, flap 20°, flap 40°, flap 40° plus slat.

All of these cases would be conducted over both uniform and non-uniform mean flows, for all three acoustic frequencies. Experimental evidence exists to show that the flow remains attached for a NACA 0012 airfoil up to $\alpha = 8°$ [110], and thus the use of an inviscid flow to model the base flow is valid for these cases.

4.3 Computational Grids

As discussed in Section 3.5.3, the required p_{rms} of the monopole in the free-field is dependent on multiple factors. Linear scaling was used in the free-field case to give the required p_{rms} at the observer radius. In the present work, it was also important to ensure that the recorded value of p_{rms} was accurate when the monopole was installed under a lifting wing. Three of the factors that this depends upon are related to the forcing region. These are the amplitude parameter ϵ, the radius of the forcing region R, and the grid covered by the forcing region. The other three factors are the time step of the simulation, the Mach number, and the acoustic frequency. As long as the factors relating to the forcing region were kept the same, for each airfoil case an equivalent free-field case with the same time step, Mach number, and frequency could be run to determine the correct scaling factor.

Given the requirement that a maximum value of $R \approx \lambda_{\text{upstream}}/50$ be used for each frequency, the required source radii were computed using the maximum planned Mach number of $M_\infty = 0.3$. These are summarised in Table 4.1. A 2-D structured quadrilateral grid defining a square region with 15 m long sides was created for the free-field cases. A single block that would contain the forcing region was created at the centre of the domain. The source was positioned on a grid node at the centre of this block, and the forcing region was refined for each frequency using approximately 3 nodes in the radial direction, ensuring that the growth rate

between neighbouring grid nodes was no greater than 1.1. These forcing regions, normalised to enable comparison, are shown in Figure 4.3. Outside of this forcing region block, the grid was grown up to a maximum distance between grid nodes of $\Delta x = 4.0 \times 10^{-2}$ m. This allowed the resolution of acoustic waves at 500 Hz with at least 10 PPW up to $M_\infty = 0.3$.

A 2-D structured quadrilateral grid was then created for each airfoil configuration. For each configuration, the block created for the forcing region for each frequency in the free-field case was copied into the correct location underneath each airfoil geometry to ensure that it was identical in each grid. Details of the grid created for each configuration can be found in Table A.2 in Appendix A. The maximum values of Δx were such that acoustic waves at 500 Hz were resolved with at least 10 PPW up to $M_\infty = 0.3$. In fact, for the RA16SC1 configurations, the curvature of the geometry necessitated a smaller Δx than the NACA 0012 configuration. Thus the acoustic waves were resolved with a higher number of PPW for the RA16SC1 configurations than was necessary for accuracy. The topology of the most complicated airfoil configuration, the RA16SC1 airfoil with flap 40° plus slat, is shown in Figure 4.4. The blocks created for the refined source region can be seen in the topology. Two detailed views of the grid in the area of the flap and slat are also included in the figure. Grid topologies for all airfoil configurations can be seen in Figures A.2-A.6 in Appendix A.

Table 4.1: Required source radius R for each frequency given a maximum Mach number of $M_\infty = 0.3$.

Acoustic frequency (Hz)	$\lambda_{\text{upstream}}$ (m)	Source radius R (m)
125	1.91	3.81×10^{-2}
250	9.53×10^{-1}	1.91×10^{-2}
500	4.76×10^{-1}	9.53×10^{-3}

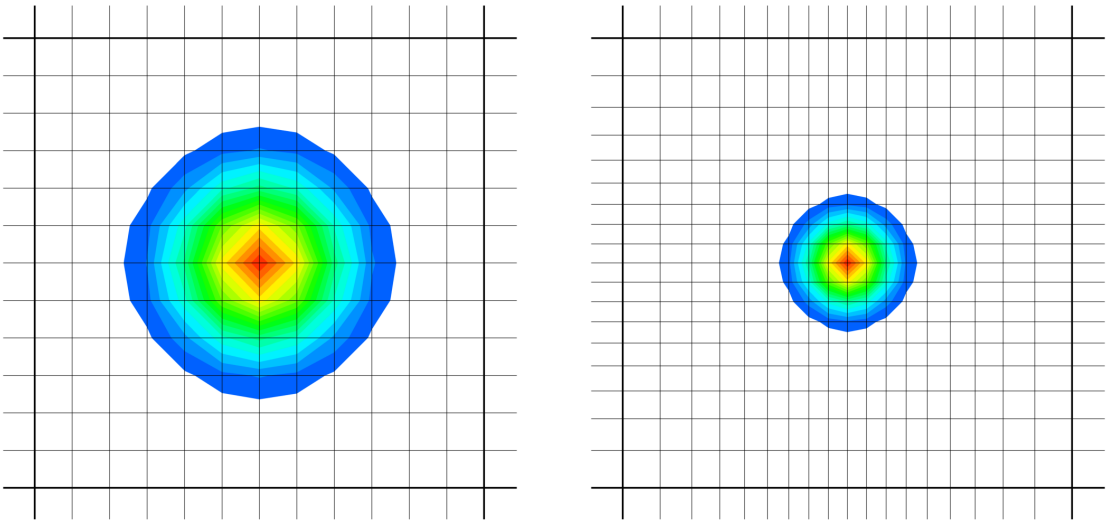

(a) 125 Hz. (b) 250 Hz.

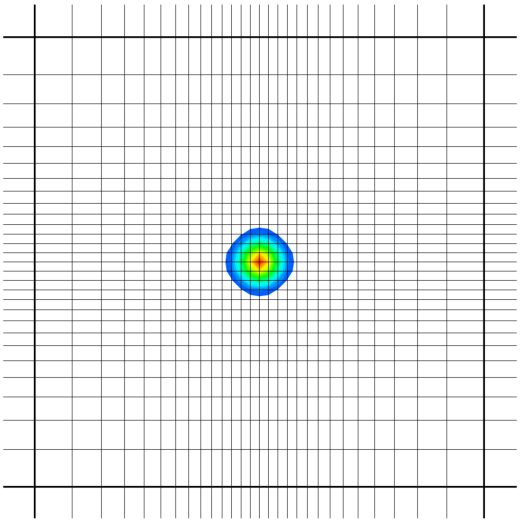

(c) 500 Hz.

Figure 4.3: Monopole forcing region and local grid refinement for each frequency. Containing block is 1.08×10^{-1} m long on each edge. Normalised Gaussian distribution plotted with contours in the range 0.05 to 1.

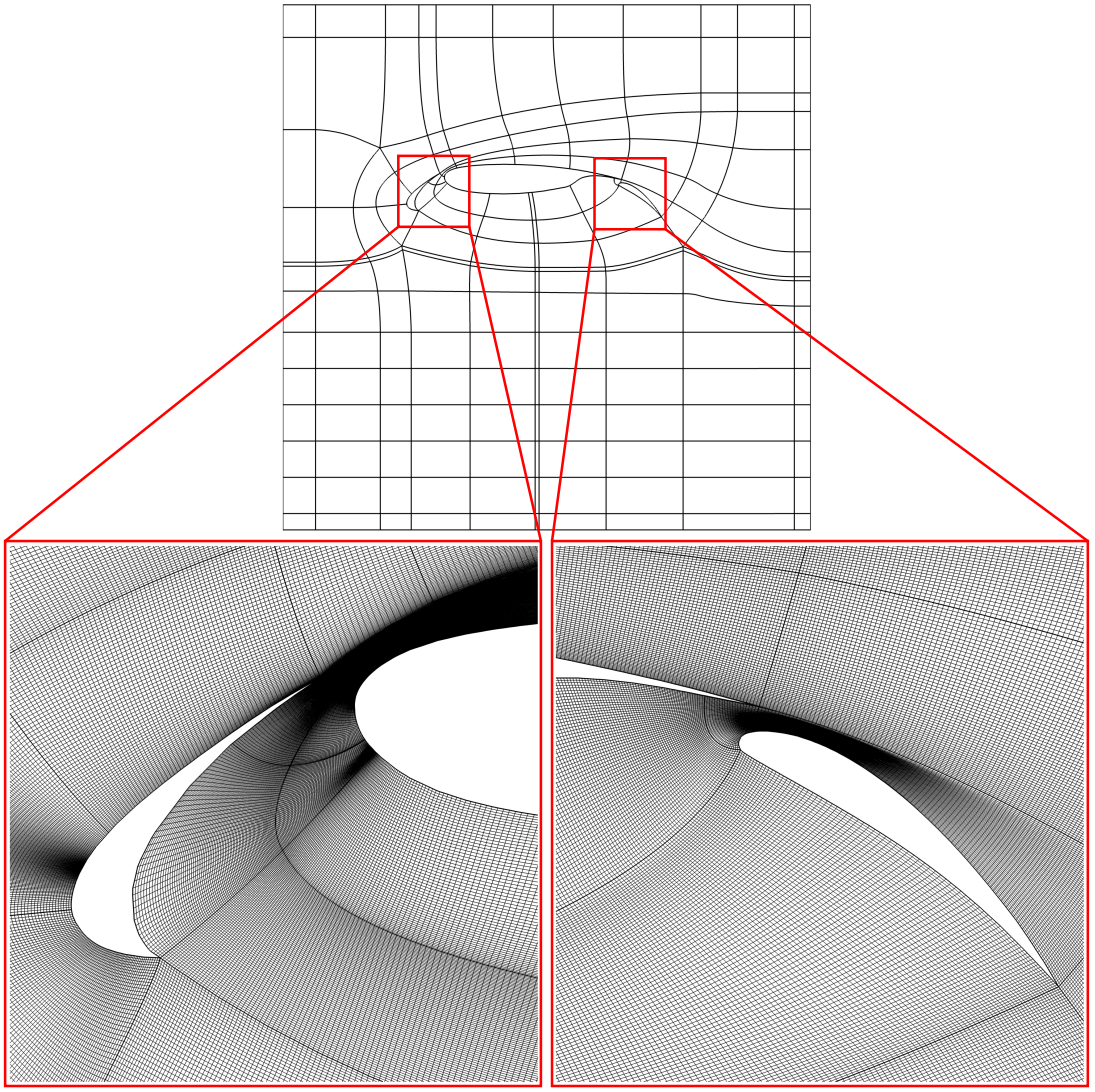

Figure 4.4: RA16SC1 with flap 40° plus slat, mesh topology and details.

4.4 Base Flows

To compute the non-uniform base flows required for each of the planned simulations, each airfoil grid was extended to a distance of $10a$ in all directions around the airfoil. This ensured that the pressure far-field boundaries were far enough away from the airfoil in order to obtain an accurate flow solution. The distance between grid nodes was gradually grown towards the domain boundaries in order to minimise computation time. By extending the existing acoustic grid to create the flow grid, the flow solution was computed directly at the nodes of the acoustic grid and interpolation was not required.

Each inviscid non-uniform flow solution was obtained using *ANSYS Fluent*, varying the free-stream Mach vector components as required. The inviscid assumption led to boundary layer effects being neglected. If boundary layer effects were included there would be additional shear layers present in the flow near to the airfoil surface, which could give rise to instabilities in the solution of the LEE. The use of an inviscid base flow also allowed the comparison of LEE solutions with equivalent BEM solutions obtained using the non-uniform flow formulation, as the non-uniform flow BEM formulation assumes a potential flow. An example of one of the computed base flows for the RA16SC1 airfoil with flap 40° plus slat at $\alpha = 0°$ and $M_\infty = 0.2$ is shown in Figure 4.5. A recirculation region behind the slat is visible. For the high-lift configurations of the RA16SC1 airfoil, a shear layer is formed behind the trailing edge of each airfoil element. These are also visible in Figure 4.5. Further examples of some of the obtained non-uniform base flows can be seen in Appendix D.

For the uniform base flows that were also required for each planned simulation, a uniform flow was specified everywhere on the grid except at nodes defining the solid airfoil surface in certain regions. In these regions, which were on the upper and lower surfaces near to and including the trailing edges of each airfoil element,

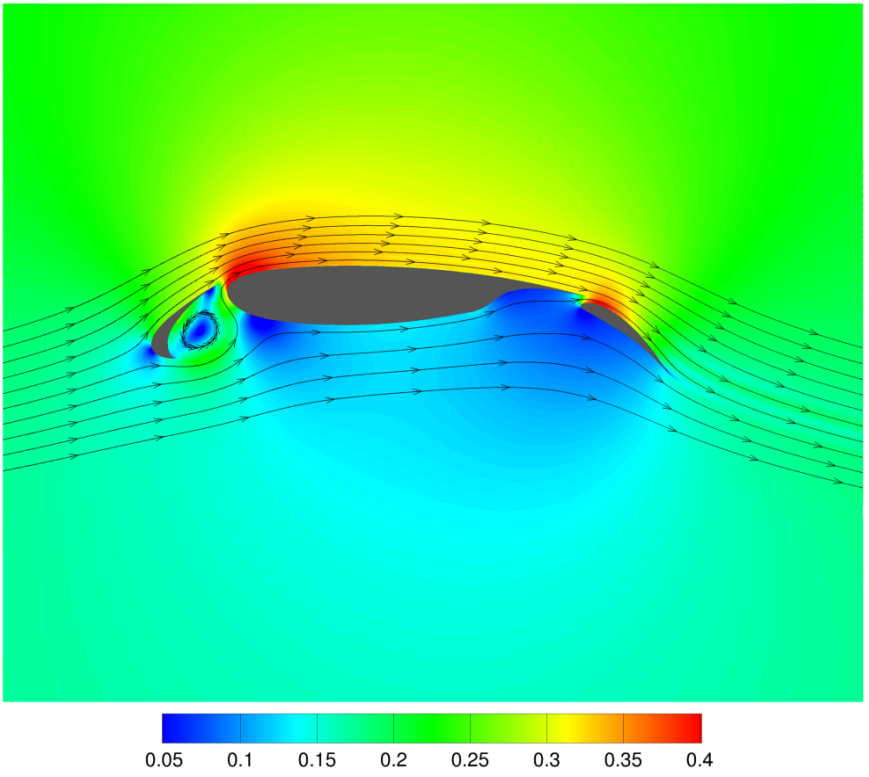

Figure 4.5: Mach number magnitude and streamlines, RA16SC1 airfoil with flap 40° plus slat, $\alpha = 0°$, $M_\infty = 0.2$.

the flow was specified to be tangential to the surface. This was required in order for the acoustic simulation to remain stable at the trailing edge of each airfoil element, and prevent the production of spurious noise. If the flow was specified to be tangential over the entire airfoil surface then spurious noise was produced at the leading edges of each airfoil element. Thus, the flow was specified as uniform in the regions near to the leading edges. These regions are shown for the various airfoil configurations in Figure 4.6.

4.5 The Effect of Circulation on the Scattering of a Single Frequency Source

Initial acoustic simulations over non-uniform base flows using the RA16SC1 airfoil with various flap and slat configurations showed that certain configurations suffered from Kelvin-Helmholtz instabilities. The shear layer in the base flow behind each airfoil element becomes larger with increasing angle of attack, and this causes larger instabilities in the acoustic solution. It was found that using an angle of attack of $\alpha = 0°$ minimised these instabilities for the configurations with flap. Thus, this angle of attack was chosen for the RA16SC1 simulations, as listed in Section 4.2. However, even at this angle of attack, the shear layer behind the slat caused instabilities in acoustic simulations at 125 Hz and 250 Hz that grew until the acoustic solution was destroyed. Therefore, the slat configuration was not used for the single frequency simulations.

The equivalent free-field simulations for each airfoil configuration were conducted. For each case, the simulation was run for a minimum of 6.0×10^{-2} s in order for the initial acoustic pulse to reach the domain boundaries. Acoustic pressure was then

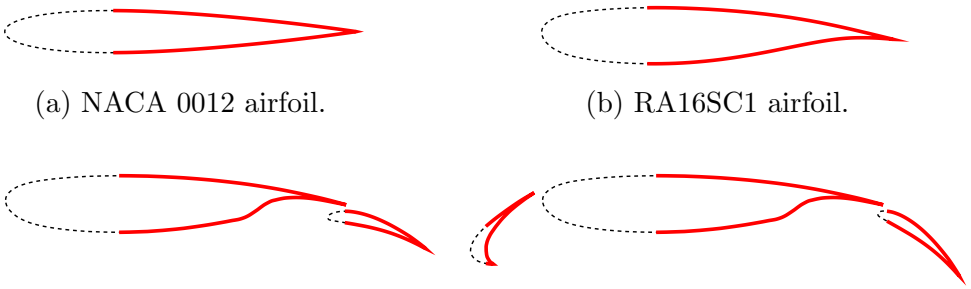

(a) NACA 0012 airfoil.

(b) RA16SC1 airfoil.

(c) RA16SC1 airfoil with flap 20°.

(d) RA16SC1 airfoil with flap 40° plus slat.

Figure 4.6: Region of flow tangential to the airfoil surface in an otherwise uniform flow. Tangential ——, uniform - - - - -.

sampled at each observer for 5 periods at a rate of 25 samples per period. The sampled pressure at each observer was used to compute p_{rms}, and this was used to determine a scaling factor for each case that gave $p_{\text{rms}} = 2.0\,\text{Pa}$, or equivalently 100 dB, at the 90° observer. This observer was chosen as the SPL at this position should not change with varying Mach number.

Having obtained the required scaling factors, the various airfoil simulations listed in Section 4.2, apart from those using the RA16SC1 with flap 40° plus slat configuration, were then conducted. For each case, the simulation was again run for a minimum of $6.0 \times 10^{-2}\,\text{s}$ in order for the initial acoustic pulse to reflect off of the airfoil surfaces and reach the domain boundaries. Acoustic pressure was then sampled at each observer for 5 periods at a rate of 25 samples per period. A full list and further details of the simulations can be found in Table A.3 in Appendix A. Figure 4.7 shows the resulting acoustic pressure field at the end of one of the simulations after scaling using the NACA 0012 airfoil, and Figure 4.8 shows the same using the RA16SC1 airfoil with flap 40°. Further examples across all three frequencies, and over both non-uniform and uniform base flows, are shown in Appendix D. These include various Mach numbers for the NACA 0012 airfoil, and various configurations for the RA16SC1 airfoil.

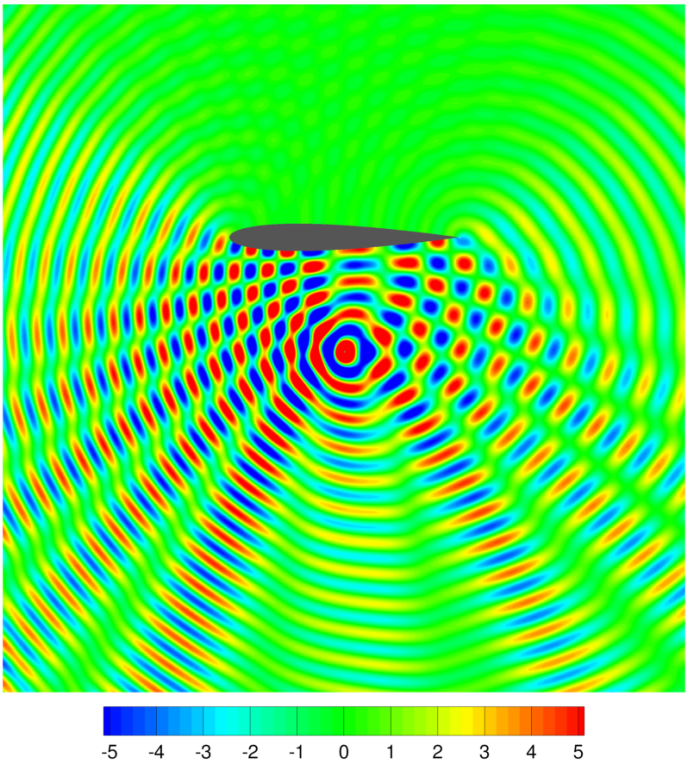

Figure 4.7: Acoustic pressure (Pa) for the scattering of a monopole at 500 Hz by a NACA 0012 airfoil in a non-uniform $M_\infty = 0.2$ flow at $\alpha = 5°$.

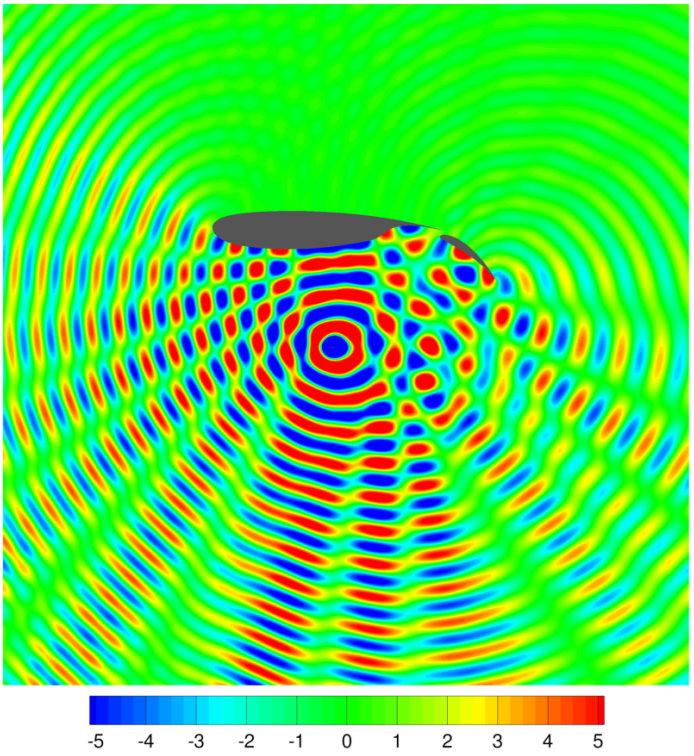

Figure 4.8: Acoustic pressure (Pa) for the scattering of a monopole at 500 Hz by an RA16SC1 airfoil with flap 40° in a non-uniform $M_\infty = 0.2$ flow at $\alpha = 0°$.

The sampled pressure was used to compute p_{rms} at each observer, which was then scaled using the factors obtained from the free-field cases. These values of p_{rms} were then used in turn to compute the SPL. It is shown in Figure 1.3 that the difference between the uniform and non-uniform base flows is due to circulation. For each combination of angle of attack, Mach number, and airfoil configuration, the strength of the circulation in the non-uniform flow takes the unique value that ensures that the Kutta condition is satisfied. The circulation creates velocity gradients in the non-uniform flow, and these velocity gradients cause the refraction of propagating acoustic waves. Figure 1.4 shows an example of a typical velocity gradient below a lifting wing due to circulation, and illustrates the refraction of acoustic waves from a point source due to this flow velocity gradient. In order to determine the effect of non-uniform flow due to circulation on the acoustic scattering of an installed source, the quantity $\text{SPL}_{\text{non-uniform}} - \text{SPL}_{\text{uniform}}$ was computed at each observer. This quantity shows the difference in SPL at each observer due to the circulation in the non-uniform flow. The significance of refraction on the computed scattering is quantified through the values of $\text{SPL}_{\text{non-uniform}} - \text{SPL}_{\text{uniform}}$.

4.5.1 Varying Angle of Attack and Mach Number

Circulation around a lifting wing increases as the angle of attack and Mach number is increased. The NACA 0012 airfoil is ideal for investigating the effect of varying each of these parameters, as it is symmetric and therefore non-lifting at zero angle of attack. This allows the effect of airfoil camber to be neglected from the investigation. The cases listed in Section 4.2 were chosen so as to investigate the effect of changing one parameter while the other remains fixed. The angle of attack was investigated with a fixed Mach number of $M_\infty = 0.2$, which is typical of a commercial airliner on approach.

The value of SPL computed at each observer with varying angle of attack over a non-uniform mean flow is shown in Figure 4.9 in the form of a contour plot for each frequency. It can be seen that varying the angle of attack does not have a large effect on the computed SPL at each observer. The largest variation in SPL between the investigated angles of attack is seen in the $75° \leq \theta \leq 105°$ observer region for each frequency.

A contour plot of $\mathrm{SPL}_{\text{non-uniform}} - \mathrm{SPL}_{\text{uniform}}$ for each frequency is shown in Figure 4.10. Small shifts in the position of directional lobes lead to large differences in the regions where the lobes for each base flow intersect. In order to determine if any clear trends exist with varying angle of attack, the observer range was restricted to $60° \leq \theta \leq 120°$. This observer range corresponds to the region where sound is radiated directly towards the ground. The quantity $\mathrm{SPL}_{\text{non-uniform}} - \mathrm{SPL}_{\text{uniform}}$ is shown across this observer range for various angles of attack across all three frequencies in Figure 4.11. Clear trends can be seen in this observer range. At 125 Hz and 500 Hz, increasing the angle of attack leads to a reduction in $\mathrm{SPL}_{\text{non-uniform}} - \mathrm{SPL}_{\text{uniform}}$ in this range. There is a directional lobe in the corresponding directivity plot in this observer range at these frequencies.

This decreasing trend in $\mathrm{SPL}_{\text{non-uniform}} - \mathrm{SPL}_{\text{uniform}}$ at 125 Hz and 500 Hz can be explained using Figure 4.12. The difference between the non-uniform and uniform base flows around the NACA 0012 airfoil with $M_\infty = 0.2$ and varying α are shown using the Mach number magnitude difference and streamlines. This is obtained through subtracting the uniform flow vector from the local non-uniform flow vector. It can be seen at $\alpha = 0°$ that the flow velocity below the airfoil is slightly higher than the free-stream. This leads to greater convective amplification, meaning that $\mathrm{SPL}_{\text{non-uniform}} > \mathrm{SPL}_{\text{uniform}}$ for this angle of attack. As the angle of attack is increased, the flow velocity beneath the airfoil becomes approximately

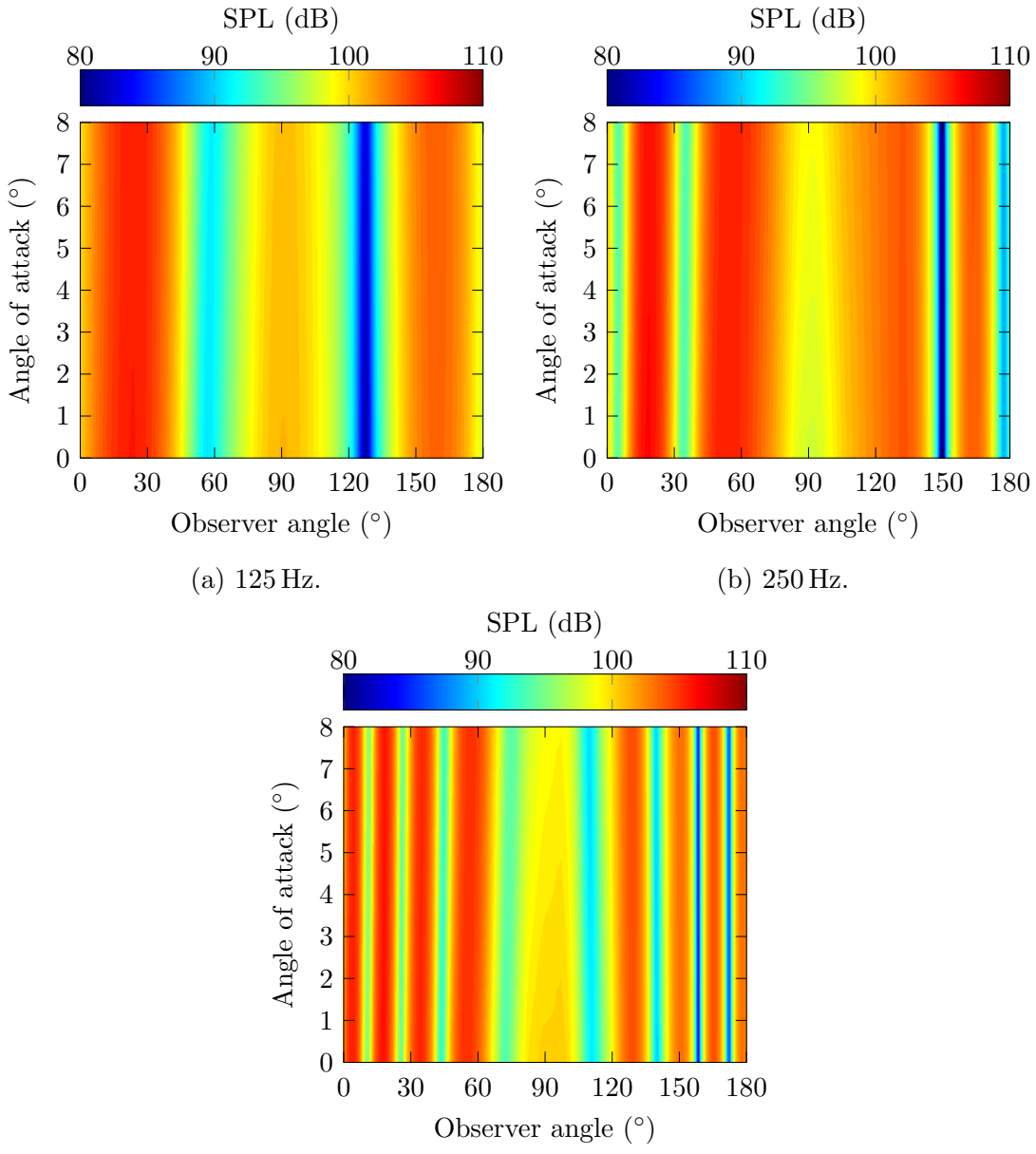

(a) 125 Hz.

(b) 250 Hz.

(c) 500 Hz.

Figure 4.9: SPL contour (dB) for the scattered source over a non-uniform flow at observer angles $0° \leq \theta \leq 180°$, NACA 0012 airfoil, varying α, $M_\infty = 0.2$.

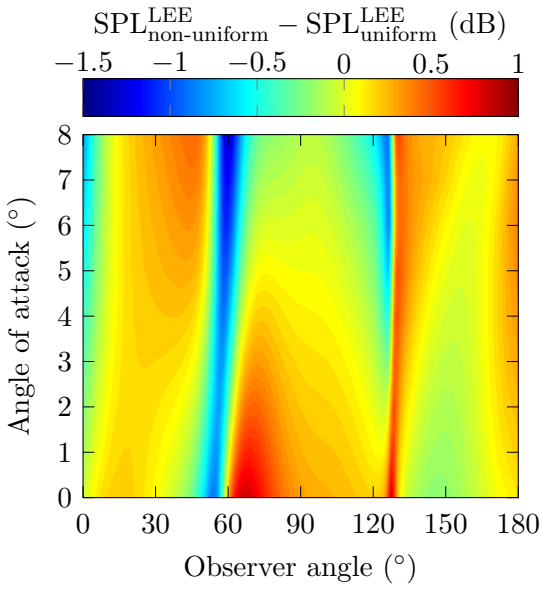

(a) 125 Hz.

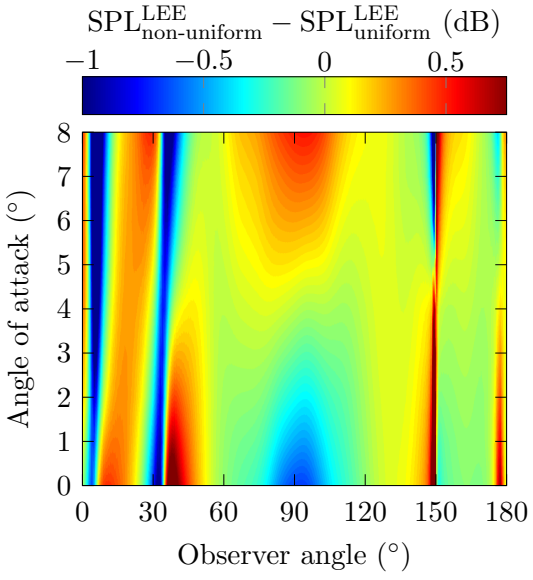

(b) 250 Hz.

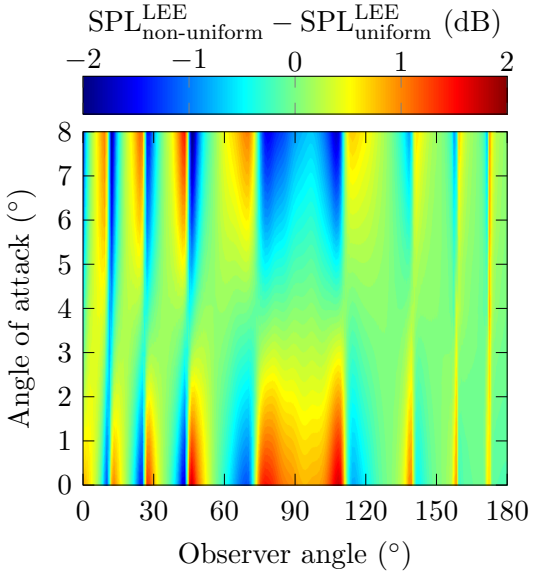

(c) 500 Hz.

Figure 4.10: Contour of $\mathrm{SPL}_{\text{non-uniform}} - \mathrm{SPL}_{\text{uniform}}$ (dB) for the scattered source at observer angles $0° \leq \theta \leq 180°$, NACA 0012 airfoil, varying α, $M_\infty = 0.2$.

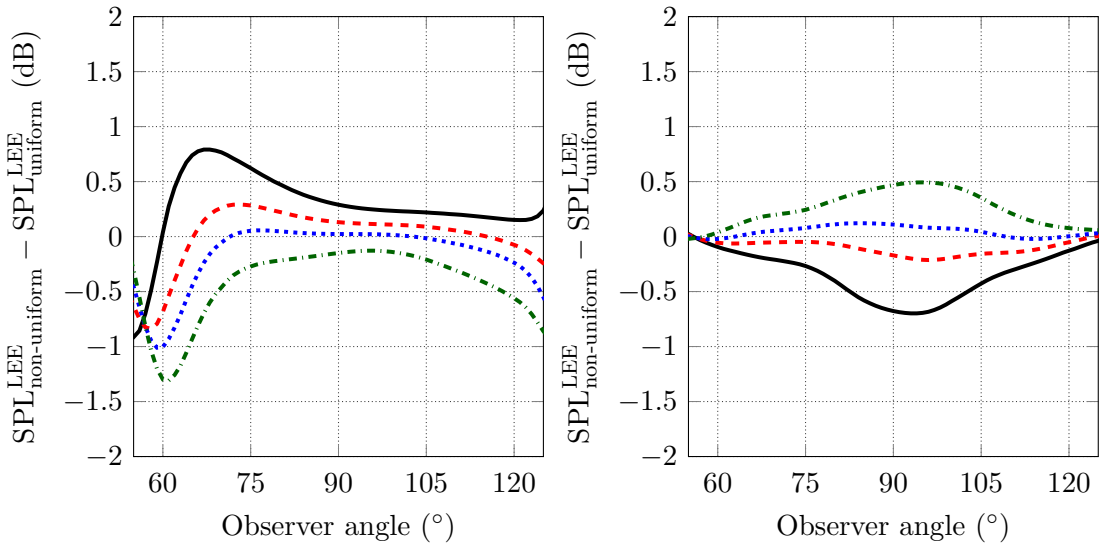

(a) 125 Hz.

(b) 250 Hz.

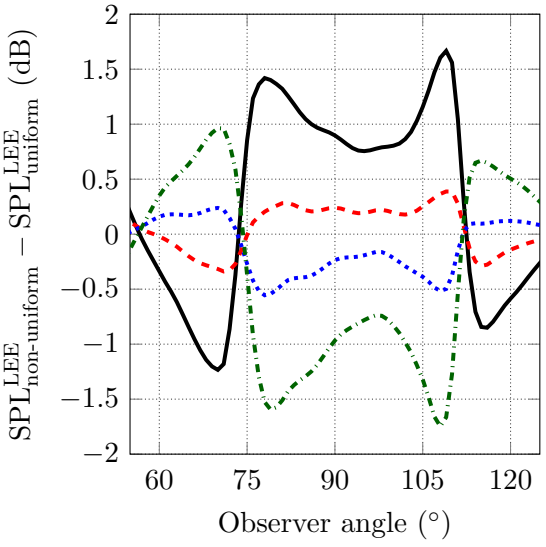

(c) 500 Hz

Figure 4.11: Difference in SPL between non-uniform and uniform base flows across various frequencies, NACA 0012, varying α, $M_\infty = 0.2$. $\alpha = 0°$ ——, $\alpha = 3°$ - - -, $\alpha = 5°$ ·····, $\alpha = 8°$ -·-·-.

equal to and then lower than the free-stream. As this happens, the convective amplification lessens, leading to $\text{SPL}_{\text{non-uniform}} < \text{SPL}_{\text{uniform}}$. It can be seen from Figure 4.11 that the angle of attack where the flow velocity beneath the airfoil is approximately equal to the free-stream is $\alpha \approx 4°$.

At 250 Hz, a local minimum is located in the directivity plot for this observer range. It can be seen in Figure 4.11b that the decreasing trend observed where a directional lobe existed is reversed where there is a local minimum. At $\alpha = 0°$, the flow velocity beneath the airfoil is higher than the free-stream. In the case of a local minimum in this observer range, an increase in flow velocity leads to an increase in destructive interference. Thus, $\text{SPL}_{\text{non-uniform}} < \text{SPL}_{\text{uniform}}$ at lower

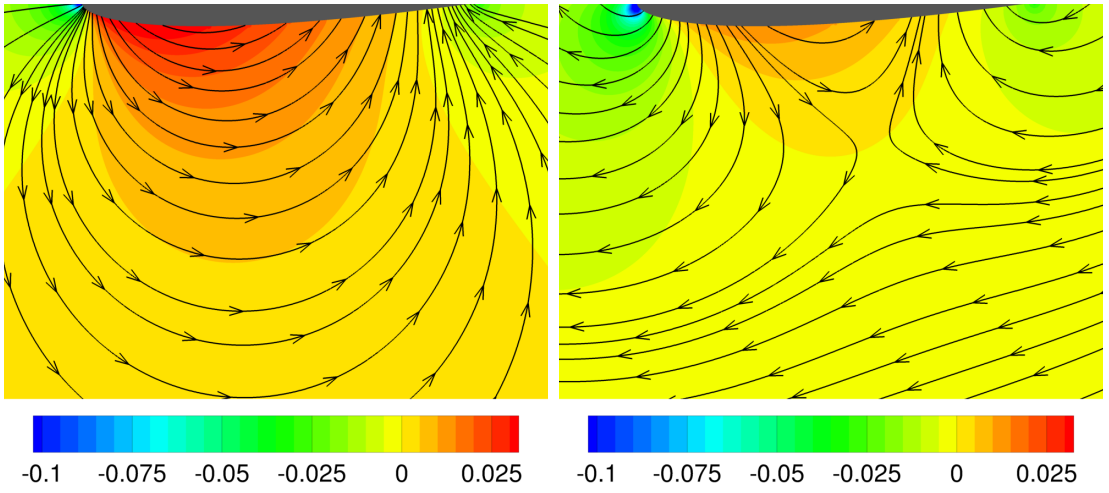

(a) $\alpha = 0°$.

(b) $\alpha = 3°$.

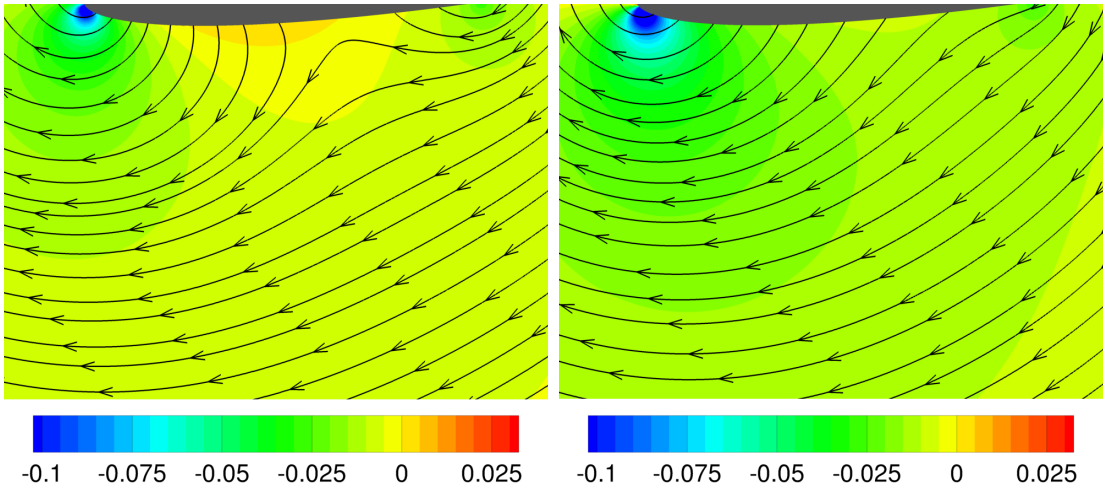

(c) $\alpha = 5°$.

(d) $\alpha = 8°$.

Figure 4.12: Mach number magnitude and streamlines showing the difference between non-uniform and uniform flows. NACA 0012 airfoil, varying α, $M_\infty = 0.2$.

angles of attack. As the angle of attack is increased, the flow velocity beneath the airfoil decreases relative to the free-stream, and thus the destructive interference decreases. This leads to $\mathrm{SPL}_{\text{non-uniform}} > \mathrm{SPL}_{\text{uniform}}$ at higher angles of attack. This is also seen at 500 Hz in Figure 4.11c at angles $\theta < 75°$ and $\theta > 110°$, where the directional lobe in the directivity plot turns into local minima.

Having investigated the effect of angle of attack with a fixed Mach number, an angle of attack of 5° was fixed and the Mach number varied. The SPL computed at each observer with varying Mach number over a non-uniform mean flow is shown in Figure 4.13 as a contour plot for each frequency. The directional lobes at each Mach number can be seen to change position and shape. This is particularly evident in the $60° \leq \theta \leq 120°$ observer region. This is due to the convective effect of the flow effectively changing the propagation distance between the source and the reflective airfoil surface. This is explained further in Section 5.6.1 in the discussion on the frequency analysis of a scattered broadband source. A contour plot of $\mathrm{SPL}_{\text{non-uniform}} - \mathrm{SPL}_{\text{uniform}}$ was shown previously for varying angle of attack with a fixed Mach number. However, for a fixed angle of attack and varying Mach number, the discretisation of the Mach number range was not fine enough to produce an accurate contour plot.

The quantity $\mathrm{SPL}_{\text{non-uniform}} - \mathrm{SPL}_{\text{uniform}}$ at observers in the range $60° \leq \theta \leq 120°$ is shown for the various chosen values of Mach number across all three frequencies in Figure 4.14. Unlike varying the angle of attack, there are no clear trends for varying the Mach number. Increasing the angle of attack increases the circulation, which reduces the flow velocity beneath the airfoil relative to the free-stream. This causes the changes in SPL discussed previously. Fixing an angle of attack and increasing the Mach number also increases the circulation around the airfoil. However, in this case the reduction in flow velocity beneath the airfoil due to the increase in circulation is offset by the increase in free-stream velocity. Thus, the relative difference between the non-uniform and uniform base flows remains similar as the Mach number is increased. Several larger peaks can be seen in this range, but these are due to small shifts in the directional lobes in the associated directivity plots.

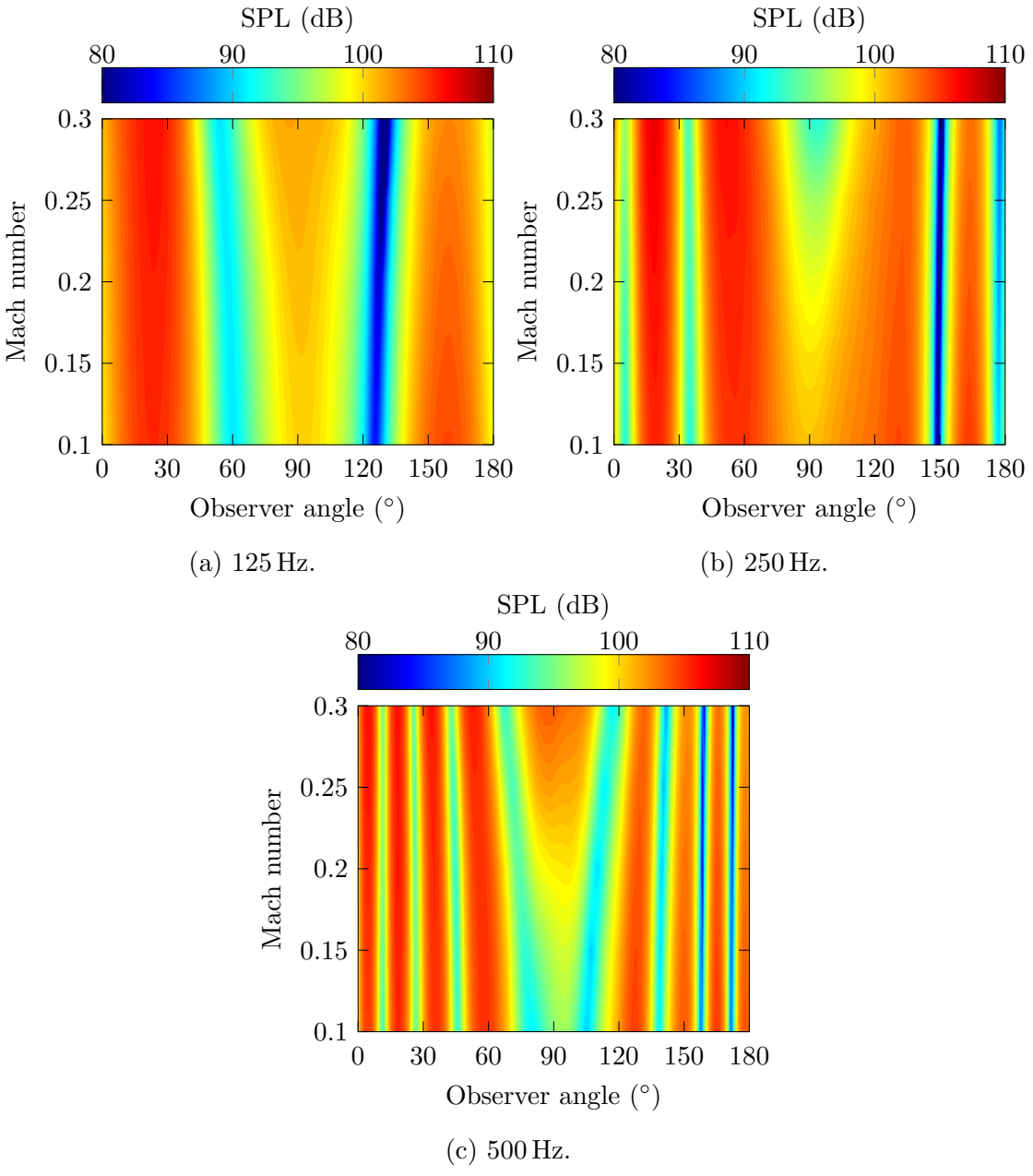

(a) 125 Hz.

(b) 250 Hz.

(c) 500 Hz.

Figure 4.13: SPL contour (dB) for the scattered source over a non-uniform flow at observer angles $0° \leq \theta \leq 180°$, NACA 0012 airfoil, varying M_∞, $\alpha = 5°$.

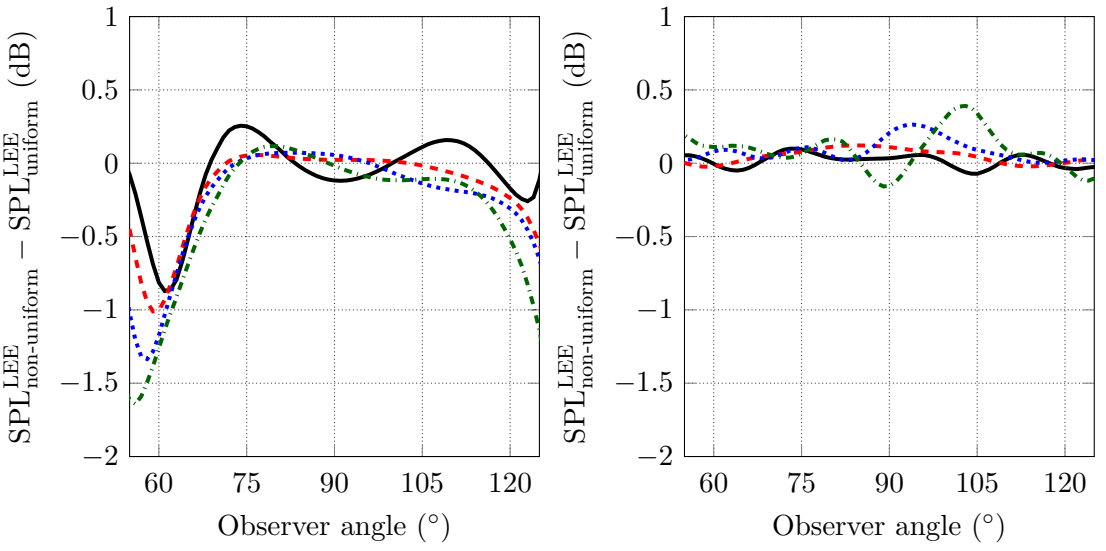

(a) 125 Hz. (b) 250 Hz.

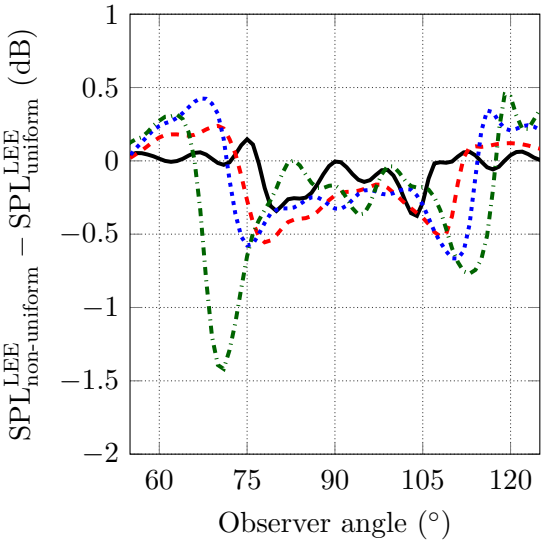

(c) 500 Hz.

Figure 4.14: Difference in SPL between non-uniform and uniform base flows across various frequencies, NACA 0012, varying M_∞, $\alpha = 5°$. $M_\infty = 0.1$ ——, $M_\infty = 0.2$ - - - -, $M_\infty = 0.25$ ·····, $M_\infty = 0.3$ -·-·-.

4.5.2 Varying Flap Configuration

Having investigated the effect of varying the angle of attack and Mach number on the scattering of a single frequency source, the next step was to investigate the effect of varying flap angle. This was conducted with a fixed Mach number of $M_\infty = 0.2$ and angle of attack of $\alpha = 0°$. Figure 4.15 shows $\mathrm{SPL}_{\text{non-uniform}} - \mathrm{SPL}_{\text{uniform}}$ at observers in the range $60° \leq \theta \leq 120°$. The flap retracted configuration generally shows similar differences in $\mathrm{SPL}_{\text{non-uniform}} - \mathrm{SPL}_{\text{uniform}}$ to the NACA 0012 airfoil in the previous section. The peaks that are observed for the higher flap angles are due to directional lobes in the associated directivity plots shifting position. This is caused by the larger difference between the non-uniform and uniform base flows for these configurations. It is peaks such as these that led to the restriction of the observer range to $60° \leq \theta \leq 120°$ in Section 4.5.1.

Although there are no clear trends in Figure 4.15, unlike for varying the angle of attack in Figure 4.11, it can be observed that the peaks generally increase in height with increasing flap angle. This can be attributed to two factors. Firstly, deploying the flap adds another surface for the incident acoustic wave to reflect from. This creates a complex sound field beneath the airfoil. Secondly, increasing the flap angle increases the circulation and reduces the flow velocity beneath the airfoil. Figure 4.16 shows the difference between non-uniform and uniform base flows, quantified by the difference in velocity magnitude. It can be seen that with the flap at 40° the reduction in flow velocity beneath the airfoil is substantial. At the source position the flow Mach number magnitude is approximately 0.07 lower than the free-stream Mach number of 0.2. This increasing difference between the base flows with increasing flap angle leads to a larger modification of the complex sound field. This in turn leads to the increase in peak height observed in Figure 4.15 for increasing flap angle.

In particular, the flap 40° configuration at 500 Hz shows the largest differences in $\mathrm{SPL}_{\text{non-uniform}} - \mathrm{SPL}_{\text{uniform}}$ out of the frequencies investigated here. This is due to the higher frequency source being more directional, combined with the high flap angle that reflects the incident wave back towards these observers. The difference in SPL over the non-uniform and uniform base flows is shown more clearly for this frequency and flap angle in Figure 4.17. Along with the shifts in the directional lobes, it can be seen that the convective amplification upstream of the source is reduced over the non-uniform flow compared to the uniform flow. This is due to the large reduction in flow velocity beneath the airfoil for this flap angle.

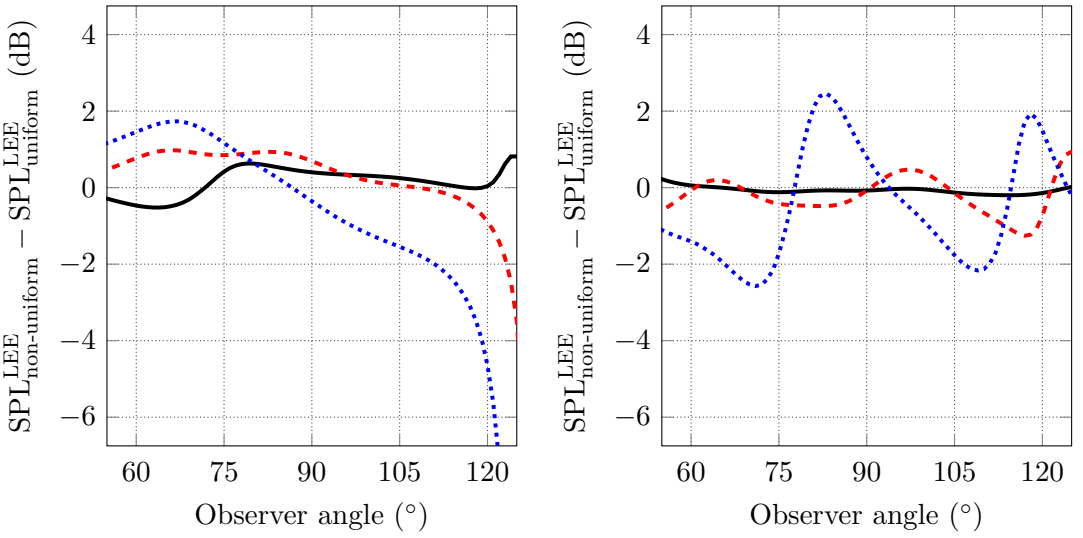

(a) 125 Hz.

(b) 250 Hz.

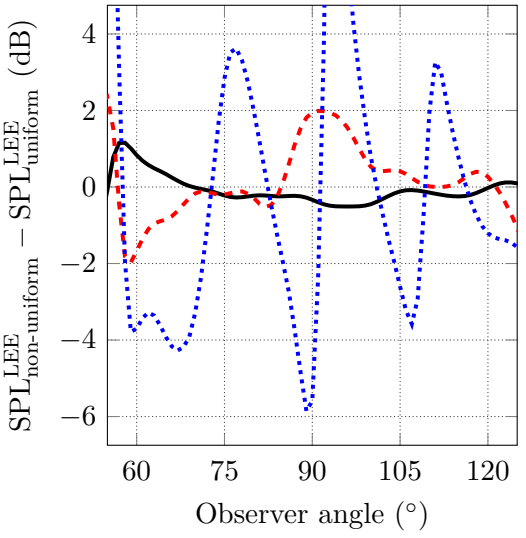

(c) 500 Hz.

Figure 4.15: Difference in SPL between non-uniform and uniform base flows across various frequencies, RA16SC1, varying flap configuration, $M_\infty = 0.2$, $\alpha = 0°$. Flap retracted ——, flap 20° - - - -, flap 40° ·····.

The directional lobes seen in the directivity plots in this chapter are due to the constructive and destructive interference that occurs at a single frequency. This makes trends harder to see in the results, in particular for the airfoil configurations with flap seen in this section. This was a motivating factor for furthering the investigation using a broadband source. The use of a broadband source greatly reduces constructive and destructive interference in the overall SPL, and allows trends to be seen. The investigation using a broadband source is presented in Chapter 5.

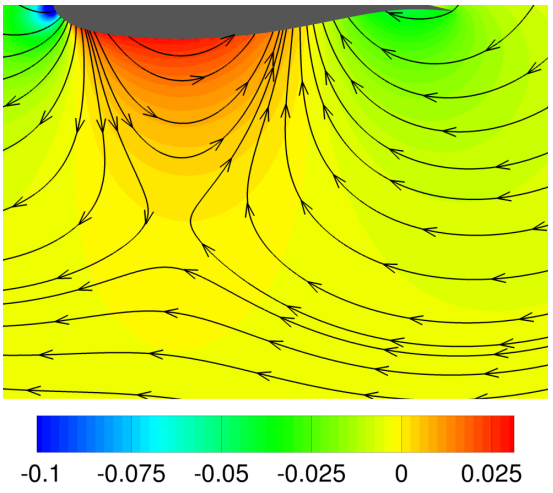

(a) Flap retracted.

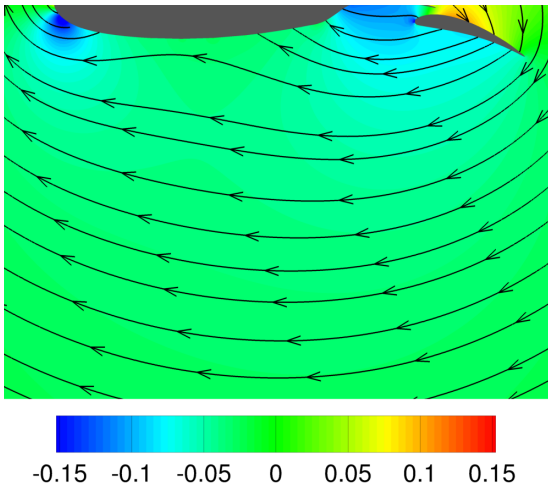

(b) Flap 20°.

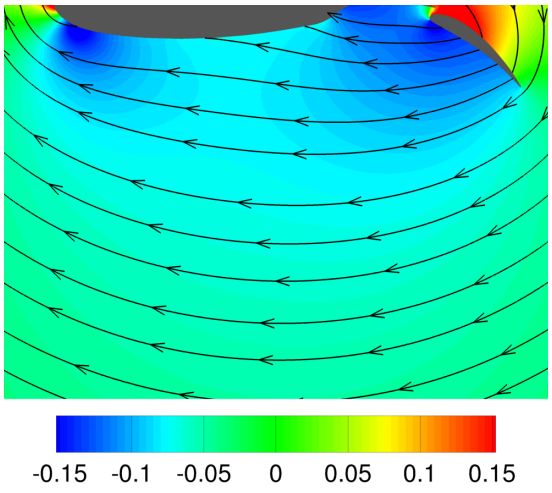

(c) Flap 40°.

Figure 4.16: Mach number magnitude and streamlines showing the difference between non-uniform and uniform flows. RA16SC1 airfoil, varying configuration, $\alpha = 0°$, $M_\infty = 0.2$.

4.6 A Discussion on Accuracy

In some cases, the computed values of $\text{SPL}_{\text{non-uniform}} - \text{SPL}_{\text{uniform}}$ seen in Section 4.5 are relatively small. These results needed to be assessed in order to determine if these values were greater than the numerical error introduced by the LEE solver, and thus could be considered accurate. No analytical solution exists for the scattering of a monopole source by a geometry with arbitrary shape in a flow. However, the solver was validated both for the convective amplification of a monopole in the free-field with a uniform flow in Section 3.5.3, and for the scattering of a monopole by a cylinder geometry without flow in Section 3.5.4. It was shown that

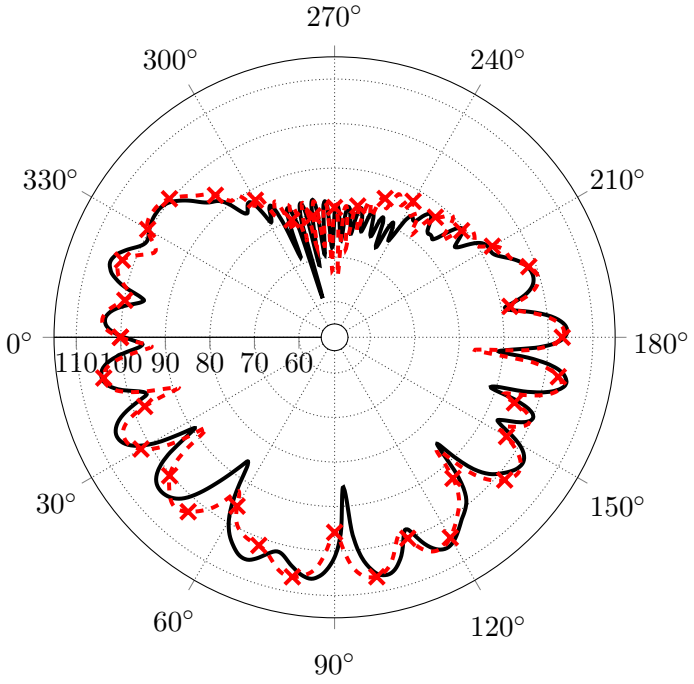

Figure 4.17: SPL (dB). RA16SC1 with flap 40°, 500 Hz, $\alpha = 0°$, $M_\infty = 0.2$. Uniform ——, non-uniform - -×- -.

for a distributed source as used for LEE methods, the ratio of upstream wavelength to source radius $\chi = \lambda_{\text{uptsream}}/R$ influences the error in the solution. For the monopole in a uniform flow, the average percentage error in p_{rms} computed over all observers was approximately 1.1 % provided that a value of $\chi \approx 50$ was used, and the error upstream and downstream using this value of χ was approximately 0.4 %. It was then shown that the average percentage error in p_{rms} over all observers for the monopole scattered by a cylinder was approximately 1.4 %. The maximum percentage error at any given observer was generally around 3 % for both validation cases. In order to determine the accuracy of the results seen in Section 4.5, the percentage change in p_{rms} in the results could be computed and compared to the percentage error values from the validation cases.

The computed values of $\text{SPL}_{\text{non-uniform}} - \text{SPL}_{\text{uniform}}$ at each observer show the difference in acoustic scattering due to the difference in base flows. This difference in base flows is due to the circulation in the non-uniform flow, as seen in Figure 1.3. The percentage change in p_{rms} due to the circulation can be calculated at any observer using the two corresponding values of SPL. The values of p_{rms} corresponding

to these values of SPL are given by

$$\begin{aligned} p_{\text{rms}}^{\text{non-uniform}} &= p_{\text{ref}} \times 10^{\frac{\text{SPL}_{\text{non-uniform}}}{20}}, \\ p_{\text{rms}}^{\text{uniform}} &= p_{\text{ref}} \times 10^{\frac{\text{SPL}_{\text{uniform}}}{20}}. \end{aligned} \tag{4.6.1}$$

The percentage change in p_{rms} due to circulation is given by

$$\text{percentage change in } p_{\text{rms}} = \frac{p_{\text{rms}}^{\text{non-uniform}} - p_{\text{rms}}^{\text{uniform}}}{p_{\text{rms}}^{\text{uniform}}} \times 100. \tag{4.6.2}$$

Substituting (4.6.1) into (4.6.2) and simplifying gives

$$\text{percentage change in } p_{\text{rms}} = \left(10^{\frac{\text{SPL}_{\text{non-uniform}} - \text{SPL}_{\text{uniform}}}{20}} - 1\right) \times 100. \tag{4.6.3}$$

The maximum percentage error in p_{rms} that was seen in the validation cases was generally around 3 %. This value was therefore chosen as an error bound in the evaluation of the results. Using (4.6.3), it can be found that a 3 % increase in p_{rms} corresponds to a 0.257 dB increase in SPL, whereas a 3 % decrease in p_{rms} corresponds to a 0.265 dB decrease in SPL.

For the investigation of the effect of angle of attack and Mach number conducted using the NACA 0012 airfoil, it is important to note that the same grid and simulation parameters were used for all cases at a given frequency. It was only the base flow that was changed for each case. Thus, any error introduced by the spatial or temporal discretisation, or boundary conditions, would be minimised from case to case. For the effect of angle of attack seen in Figure 4.11, it can be seen that at the minimum and maximum angles of attack, the values of $\text{SPL}_{\text{non-uniform}} - \text{SPL}_{\text{uniform}}$ are generally above the values of SPL computed above to give a percentage change of 3 %. At angles of attack between the minimum and maximum, $\text{SPL}_{\text{non-uniform}} - \text{SPL}_{\text{uniform}}$ does not always give a percentage change in p_{rms} of 3 %.

However, the values of $\text{SPL}_{\text{non-uniform}} - \text{SPL}_{\text{uniform}}$ at the minimum and maximum angles of attack show a change that can be considered significant. Consider the convective amplification of a source in the free-field with a uniform flow. The acoustic pressure can be computed using (3.5.14), and it can be seen that the result is both frequency and Mach number dependent. The convective amplification upstream and downstream at $M_\infty = 0.2$ of a source with a strength that gives 100 dB at the 90° observer is summarised in Table 4.2. These values are equal for the three frequencies that have been used throughout the investigations in this

chapter up to the number of decimal places displayed. Now consider Figure 4.18, which shows the values of $\mathrm{SPL}_{\text{non-uniform}} - \mathrm{SPL}_{\text{uniform}}$ computed for each frequency at the 90° observer for the NACA 0012 airfoil at $M_\infty = 0.2$ with varying angle of attack. It can be seen that the difference in $\mathrm{SPL}_{\text{non-uniform}} - \mathrm{SPL}_{\text{uniform}}$ between the minimum and maximum angle of attack for the higher frequencies is comparative to the convective amplification. It can also be seen that there is an almost linear trend in $\mathrm{SPL}_{\text{non-uniform}} - \mathrm{SPL}_{\text{uniform}}$ at each frequency with increasing angle of attack at this observer, which further supports that the results for varying angle of attack can be considered significant.

The results for the effect of Mach number given in Figure 4.14 show that the values of $\mathrm{SPL}_{\text{non-uniform}} - \mathrm{SPL}_{\text{uniform}}$ are generally less than the values of SPL computed

Table 4.2: Convective amplification for a monopole in a uniform free-stream at $M_\infty = 0.2$. These values are equal for 125 Hz, 250 Hz and 500 Hz to these number of decimal places.

θ (°)	SPL (dB)	p_{rms} (Pa)	percentage change in p_{rms}
0	101.50	2.376	+18.85
90	100.00	2.000	-
180	97.97	1.584	−20.84

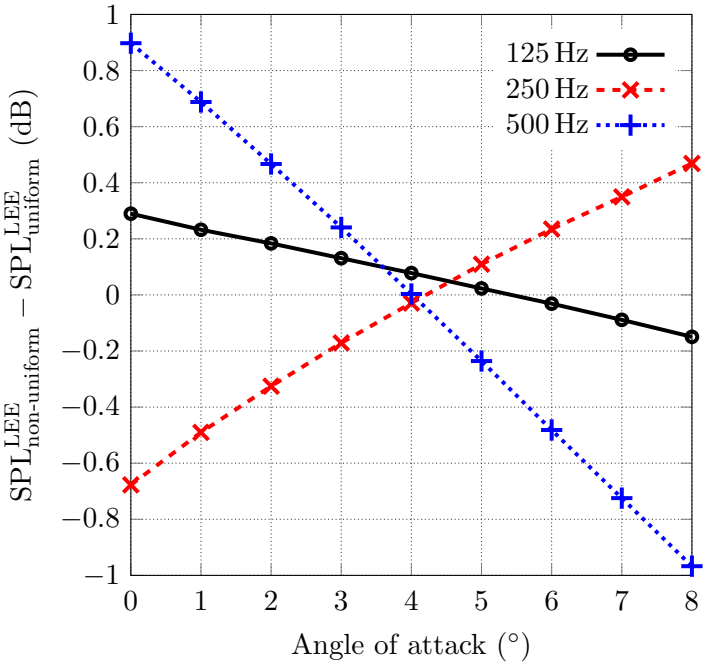

Figure 4.18: The difference in SPL (dB) between uniform and non-uniform flows at the $\theta = 90°$ observer. NACA 0012 airfoil, $M_\infty = 0.2$, varying α.

above to give a percentage change in p_{rms} of 3 %. It is also seen that there is not a clear trend in $\text{SPL}_{\text{non-uniform}} - \text{SPL}_{\text{uniform}}$ with increasing Mach number at these observer angles. The observed large peaks were attributed in Section 4.5.1 to shifts in position of directional lobes in the associated directivity plots. Therefore, it can be concluded that increasing the Mach number does not introduce a change in $\text{SPL}_{\text{non-uniform}} - \text{SPL}_{\text{uniform}}$ that can be considered significant for the Mach numbers and frequencies investigated here.

The grids for the RA16SC1 airfoil employed in the investigation of the effect of flap deployment were different for each configuration. However, due to the curvature and complexity of the geometry, a much smaller Δx was used in the creation of the grids than was required for the accuracy of the acoustic solution, even at 500 Hz. There are no obvious trends seen in the results in Figure 4.15. This is due to the directional source creating a complex sound field beneath the airfoil with flap deployed. The difference in acoustic scattering over uniform and non-uniform flows leads to a shift in the directional lobes in the corresponding directivity plots, yielding the large peaks seen in the figure, and masking any trends that might be present. This was a motivating factor behind the extension of the investigation with the use of a broadband source, as presented in Chapter 5. However, the values of $\text{SPL}_{\text{non-uniform}} - \text{SPL}_{\text{uniform}}$ computed for the cases with flap at 40° are generally higher than the values of SPL computed above to give a percentage change in p_{rms} of 3 %. This, combined with the increasing magnitude of the peaks with increasing flap deflection angle seen in Figure 4.15, suggests that the difference in acoustic scattering between each configuration is significant.

4.7 The Effect of a Higher Mach Number

It has been shown that for Mach numbers similar to that of a commercial airliner on approach, with the monopole located in the approximate position of a landing gear, the difference in SPL over non-uniform and uniform flows can be relatively small. It was of interest to determine if there was a source location and set of flow parameters such that this difference was significantly larger. The NACA 0012 airfoil was chosen for this additional investigation, as higher free-stream Mach numbers can be used while keeping the local Mach number subsonic in the non-uniform base flow. If the flow were to be locally supersonic, then shock waves would exist in the base flow that could adversely affect the solution of the LEE. A Mach number of $M_\infty = 0.6$ and angle of attack of $\alpha = 3°$ were chosen, which

led to a local Mach number magnitude over the top surface of the leading edge of the airfoil of approximately 0.95.

A frequency of 250 Hz was chosen, which enabled the resolution of the upstream wavelength with 10 PPW at $M_\infty = 0.6$ using the existing NACA 0012 airfoil grid, whereas this would not be the case at 500 Hz. The same grid as used for the previous 250 Hz simulations was used again, as well as the same source radius for this frequency as listed in Table 4.1. At this higher Mach number $\chi = \lambda_{\text{upstream}}/R \approx 30$. This is less than the value of $\chi \approx 50$ used elsewhere, but still gives accurate convective amplification as shown in Section 3.5.3. Initial simulations of this airfoil case showed that the employed non-reflecting boundary conditions were unstable at this higher Mach number, and that the simulations would not remain stable. To overcome this, the extended domain grid that was used to obtain an accurate flow solution was used here for the acoustic solution as well. The simulations were run for 6.7×10^{-1} s, which was long enough for the initial acoustic pulse to reflect off of the airfoil and propagate out of the domain of interest. Pressure was then sampled for 5 periods at 25 samples per period. Due to the use of the larger domain, the initial acoustic pulse had not reached the domain boundary by this time. Thus, any instabilities due to the non-reflecting boundary conditions at this higher Mach number were avoided. Further details of the simulations can be found in Table A.4 in Appendix A.

The corresponding free-field monopole simulation was conducted in order to obtain the correct scaling factor to give 100 dB at 5 m for this higher Mach number. The acoustic simulations over both a uniform flow and a non-uniform flow were then conducted, and the results scaled accordingly. The directivity for both solutions is shown in Figure 4.19. It can be seen that the difference in SPL for the scattering over the two base flows is still relatively small at this higher Mach number, with only a small change of position for the lobe in the $30° \leq \theta \leq 60°$ region. The difference at 35° is approximately 3 dB, and at 60° it is approximately 6 dB. A small difference in the $320° \leq \theta \leq 340°$ region can also be seen, due to the high flow gradients near to the leading edge of the airfoil. However, other than these localised changes, the difference is relatively small at this higher Mach number for the source in this location.

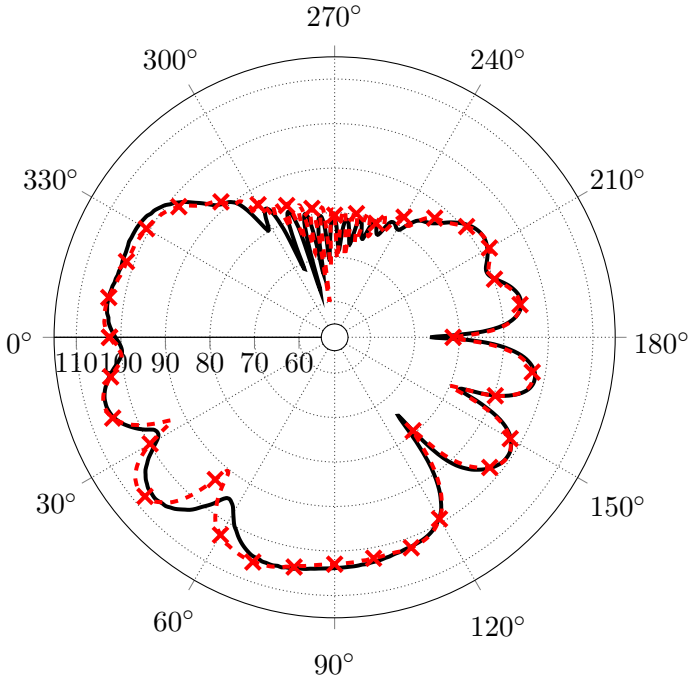

Figure 4.19: SPL (dB). NACA 0012, 250 Hz, $\alpha = 3°$, $M_\infty = 0.6$. Uniform ——, non-uniform - -×- -.

4.8 The Effect of an Alternative Source Location

It has been shown that the effect of non-uniform flow due to circulation on the acoustic scattering of a single frequency source in the approximate location of a landing gear is relatively small. It was of interest to determine if there was an alternative source location where the difference in acoustic scattering over non-uniform and uniform base flows was larger than previously observed. With the NACA 0012 airfoil at a positive angle of attack, there is an increase in flow velocity over the top surface of the leading edge of the airfoil relative to the free-stream. At a free-stream Mach number of $M_\infty = 0.6$, this increase leads to a local flow velocity that is almost supersonic. The investigations up until this point have focused on placing the monopole source in the approximate position of a landing gear beneath the airfoil, on the opposite side of the airfoil to where the flow velocity increase is largest. By placing the source above the airfoil, the effect of this local flow velocity increase on the acoustic propagation could be investigated.

Although this source position is not representative of a landing gear noise source,

the investigation would determine the effect of non-uniform flow due to circulation on the acoustic shielding of a source from observers on the ground. Agarwal and Dowling [89] used a source in a similar position in their investigation into the acoustic shielding of engines installed above the body of a blended-wing design aircraft. For the investigations undertaken for this section, the source was positioned at $(+a/2, +a/2)$ from the leading edge of the airfoil. The 360 observers were located on a circle of radius a centred on the source, as before. The new source location, and the location of the observers relative to the airfoil, are shown in Figure 4.20. This choice of source location keeps the source in the same position relative to the airfoil as in the previously conducted simulations, which allows the re-use of the previously created grids with localised source region refinement. Mach numbers in the range $0.2 \leq M_\infty \leq 0.6$ at a single angle of attack of $\alpha = 3°$ were investigated using this new configuration. As in Section 4.7, a frequency of 250 Hz was chosen, to allow the re-use of the existing grids.

In order to re-use the existing grids, the required flow solutions were obtained by taking the angle of attack to be negative. The resulting acoustic field and the observer labels were then flipped top to bottom to give the correct result. The $M_\infty = 0.2$ and 0.3 simulations were conducted in exactly the same manner as in Section 4.5, and the $M_\infty = 0.4, 0.5$, and 0.6 simulations as in Section 4.7. Further details of the simulations can be found in Table A.5 in Appendix A. The results for each were scaled using a scaling factor computed from equivalent free-field

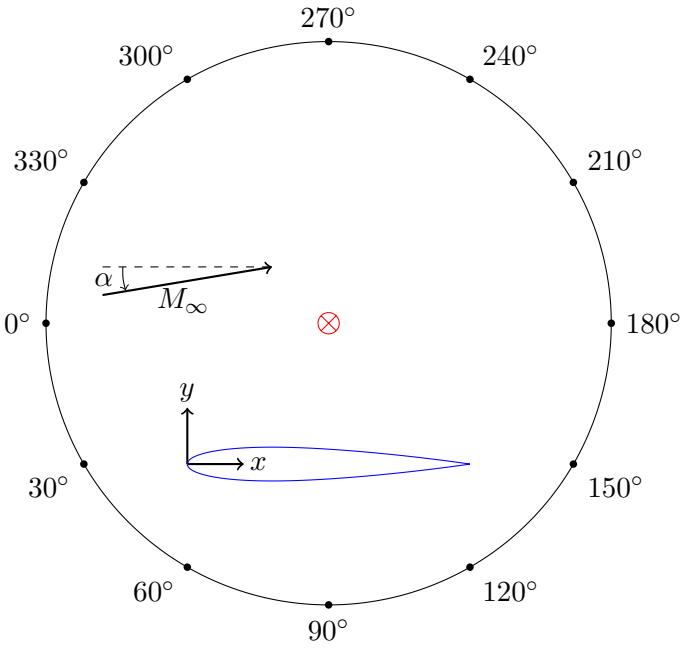

Figure 4.20: NACA 0012 airfoil, with source location above the airfoil, and observer locations.

simulations. The obtained directivities at $M_\infty = 0.2$ and $M_\infty = 0.3$ again showed that there is only a small difference in the scattering over non-uniform and uniform base flows at these Mach numbers. This is similar to what was observed in Section 4.5 for the source below the wing using these flow parameters. The directivity for the $M_\infty = 0.3$ case is shown in Figure 4.21a.

However, as the Mach number is increased, larger differences in the obtained directivities due to the difference in base flows begin to emerge. The directivities

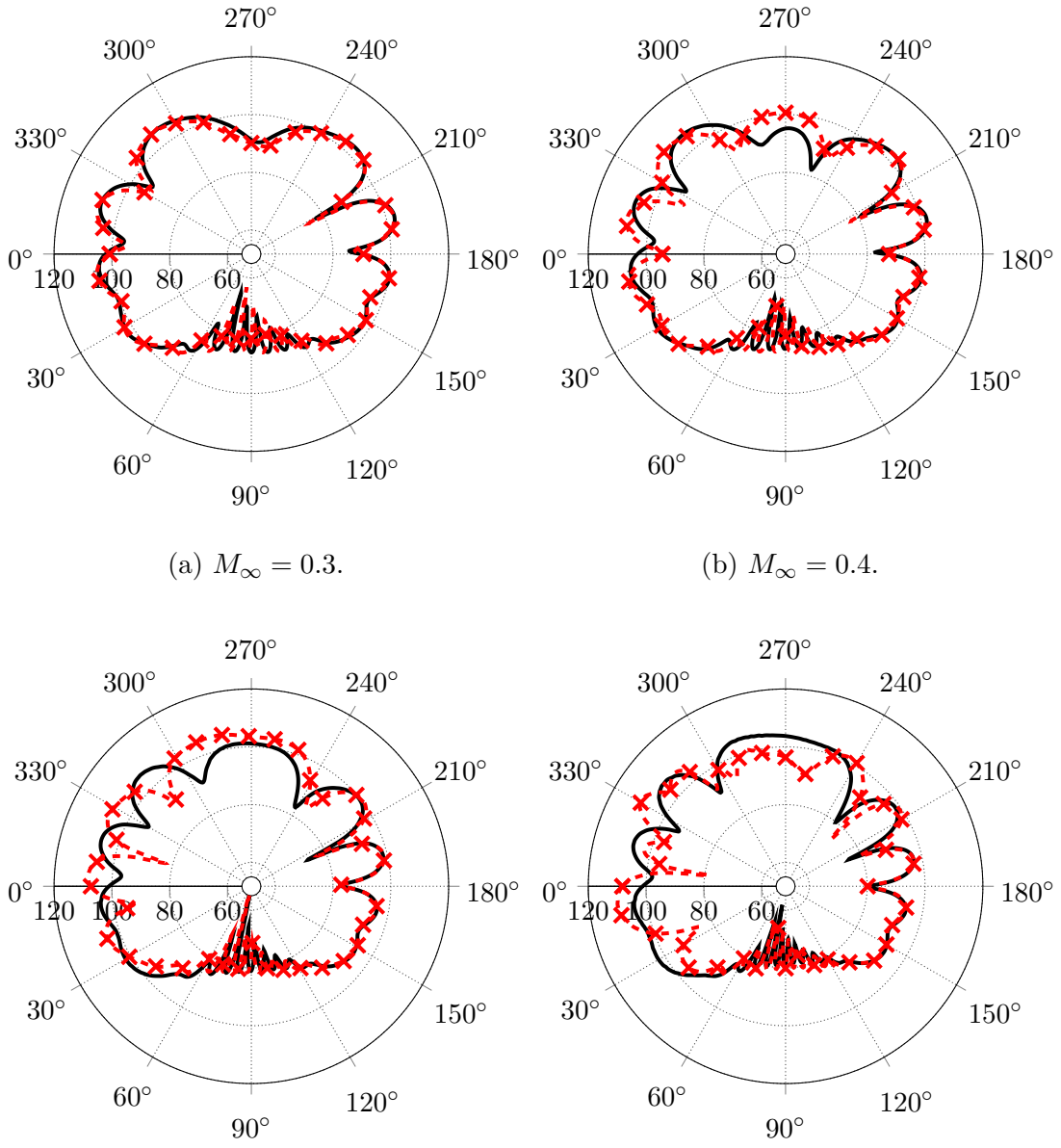

(a) $M_\infty = 0.3$.

(b) $M_\infty = 0.4$.

(c) $M_\infty = 0.5$.

(d) $M_\infty = 0.6$.

Figure 4.21: SPL (dB). NACA 0012, 250 Hz, $\alpha = 3°$, varying M_∞. Uniform ——, non-uniform - -×- -.

obtained at $M_\infty = 0.4$, 0.5 and 0.6 can be seen in Figure 4.21. As the Mach number is increased, it can be seen that the upstream lobes for the solutions computed over a non-uniform base flow change position and strength relative to those computed over a uniform base flow. The lobes in the $60° \leq \theta \leq 220°$ region remain in approximately the same position with increasing Mach number, suggesting that it is the flow over the top surface of the leading edge of the airfoil that is the cause of the observed differences.

In particular, for the non-uniform flow at $M_\infty = 0.6$, the local flow velocity over the top surface of the leading edge of the airfoil is approximately $M_0 = 0.95$. This causes the acoustic propagation in this region to be attenuated, leading to a large difference in the SPL at the $20° \leq \theta \leq 45°$ observers. The SPL for the uniform flow is approximately 10 dB higher than for the non-uniform flow at the 30° observer. A similar large difference is seen in the $355° \leq \theta \leq 20°$ region, with the SPL being approximately 7 dB higher for the non-uniform flow at the 0° observer. There are also large differences directly above the source, with the SPL for the uniform flow being approximately 7.5 dB higher at the 270° observer.

The acoustic fields obtained at the end of the $M_\infty = 0.6$ simulations over both non-uniform and uniform base flows are shown in Figure 4.22. The transonic region of flow over the upper surface of the leading edge of the airfoil for the non-uniform flow case can immediately be seen to have a large effect on the acoustic propagation in that region. This causes further large differences in constructive and destructive interference throughout the acoustic field, which leads to many lobes changing position and strength, as seen in the directivity plot for this Mach number in Figure 4.21d. Further examples of the computed acoustic fields for the other Mach numbers can be seen in Appendix D.

It can be concluded that for a source installed above an airfoil with a Mach number that is almost that of an airliner at cruise, the difference between non-uniform and uniform flows gives a significant difference in the obtained SPL. It should be noted that at $M_\infty = 0.6$ this is true for observer angles that could dramatically alter a prediction of SPL at observers on the ground. Thus, this must be considered if accurate predictions of shielding effects for similar physical models are to be obtained.

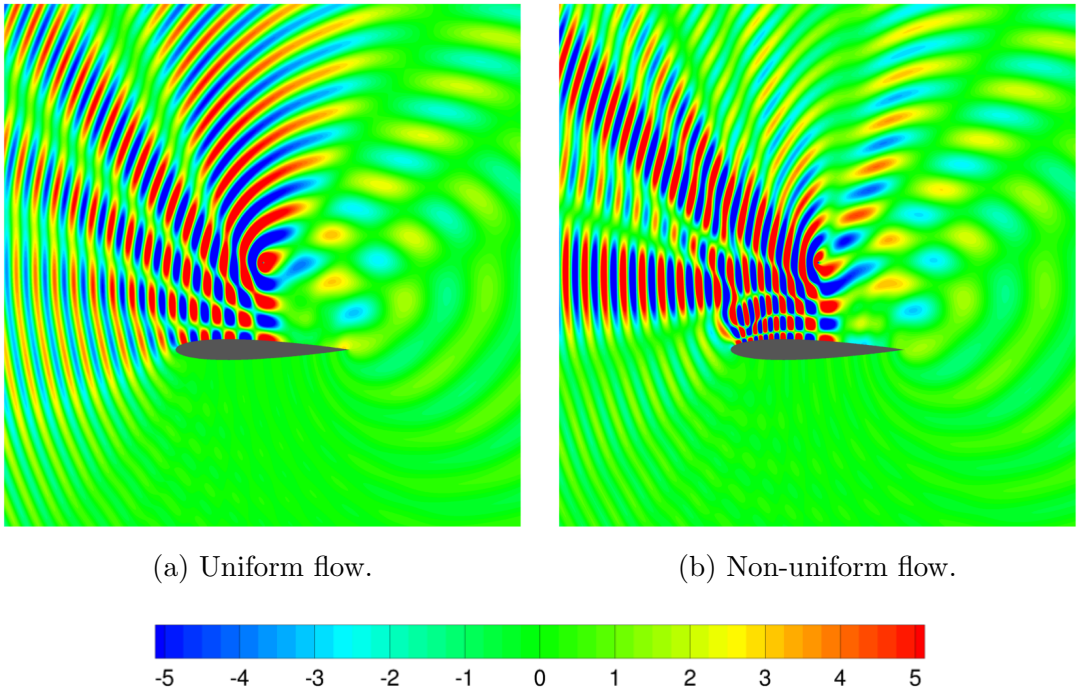

(a) Uniform flow.

(b) Non-uniform flow.

Figure 4.22: Acoustic pressure (Pa), NACA 0012, 250 Hz, $\alpha = 3°$, $M_\infty = 0.6$.

4.9 Quantification of the 2-D Assumption

The simulations undertaken up to this point have all been conducted in 2-D. This is due to 3-D simulations currently being computationally expensive, as discussed in Section 3.6. However, the geometrical spreading of acoustic energy is cylindrical in 2-D, whereas it is spherical in 3-D. This difference is quantified in this section, in order to determine if the 2-D results and the conclusions drawn from them are representative of what would be observed if the investigations were conducted in 3-D. The computational resources currently available at the University of Southampton limit the complexity of a 3-D case. These limitations include the use of a single frequency source, a constant cross-section airfoil with a limited span, and a base flow that is constant in the spanwise direction. Throughout this thesis, the effect of circulation on the acoustic scattering was quantified as the difference in SPL at the observers over uniform and non-uniform base flows. To determine the effect of running the simulations in 2-D compared to 3-D on this difference, equivalent scattering cases at a single frequency were run in 2-D and 3-D.

For the 3-D simulations, the source was located in the centre of the span, along with the observers as shown in Figure 4.2. It was assumed that the airfoil was infinite in span so that wing tip effects would not be present in either the base flow or acoustic solution. Non-reflecting boundary conditions were used at the

edges of the 3-D domain in the spanwise direction to satisfy this assumption for the acoustic solution. With this 3-D model, there are two main differences in the acoustic physics between 2-D and 3-D. These are the geometrical spreading of the acoustic energy, and edge diffraction effects. In 2-D, the spreading is cylindrical with amplitude $\propto 1/\sqrt{\text{distance}}$, whereas in 3-D the spreading is spherical with amplitude $\propto 1/\text{distance}$. In 3-D, the spherical incident wave interacting with the airfoil leading and trailing edges is diffracted depending on the incident angle, and some acoustic energy might be diffracted back into the plane of the observers.

The NACA 0012 airfoil was chosen as the scattering geometry. The grid for this geometry contained the least number of grid nodes of all the 2-D airfoil grids. A single frequency of 250 Hz was chosen, along with the parameters $\alpha = 4°$, and $M_\infty = 0.2$. The 2-D grid for the NACA 0012 airfoil described in Section 4.3 was used to construct the 3-D grid. The blocks were rearranged for computational efficiency in the 3-D case. This modified grid was then extruded in the spanwise direction to a width of 6.61 m using a maximum Δx of 4.0×10^{-2} m. The same local grid refinement for the monopole forcing region in the 2-D grid was also used in this direction. The resulting 3-D grid consisted of 4.36×10^7 nodes in 1802 blocks.

The non-reflecting boundary condition was applied at the six faces that bounded the domain. For stability, this condition was also applied to the airfoil surface at grid nodes located within the non-reflecting boundary condition zone in the spanwise direction. The width of the non-reflecting boundary condition zone was 11 nodes in the 3-D case. This width was used so that the airfoil surface where the non-reflecting boundary condition was also applied was completely covered by the boundary condition zone on the domain boundary in the spanwise direction. The spanwise width of the domain allowed approximately 2 acoustic wavelengths at a frequency of 250 Hz between the source located in the centre of the span and the edge of the non-reflecting boundary zones at the spanwise domain boundaries.

To obtain the required 3-D base flows, each flow solution was first obtained on the 2-D grid. This was then copied to the corresponding nodes of the 3-D grid in the spanwise direction. For the 2-D non-uniform base flow, the modified 2-D grid was extended to a distance of $10a$ from the airfoil in all directions in the same manner as in Section 4.4. The uniform flow was also created as in Section 4.4 on the modified 2-D grid. The 2-D acoustic simulations were run for 7.9×10^{-2} s and the 3-D acoustic simulations for 5.1×10^{-2} s to allow the initial acoustic pulse to reflect off of the airfoil surface and reach the domain boundaries before sampling.

This difference was due to a different time step being used in 2-D and 3-D, and the rounding up of the total number of time steps. Pressure was sampled for 5 periods at 25 samples per period for both 2-D and 3-D simulations in order to compute the SPL. Further details of the 3-D simulations can be found in Table A.6 in Appendix A.

The result of the 3-D simulation over a non-uniform mean flow is shown in Figure 4.23. Destructive interference can be seen at this single frequency. An equivalent simulation was undertaken using *ACTIPOLE* with a uniform mean flow for comparison. A BEM surface mesh for the NACA 0012 airfoil with 5 m chord and 20 m span was created. This mesh consisted of 7.54×10^4 boundary elements, with a maximum element size of $\lambda/7.5$. The source and observers were located in a plane in the centre of the span. Further details of the *ACTIPOLE* simulation can be found in Table B.2 in Appendix B. Directivity plots for the two LEE solutions and the BEM solution are shown in Figure 4.24, where it can be seen that all three solutions are in good agreement. The quantity $\mathrm{SPL}_{\text{non-uniform}} - \mathrm{SPL}_{\text{uniform}}$ was computed at each observer from the LEE solutions, and this is shown in Figure 4.25. It can be seen that the difference computed in 2-D and in 3-D is in agreement, despite the difference in geometrical spreading. The additional edge diffraction effects that might have been expected to influence the results in 3-D also appear to be negligible at these observers, especially for $0° \leq \theta \leq 180°$ as shown in Figure 4.25a. Following this result, it can be concluded that the results observed in 2-D can be considered representative of what would be observed in 3-D.

4.10 Evaluation of Boundary Element Method Flow Approximations

One of the aims of this thesis is to evaluate two existing BEM flow approximation methods for uniform or non-uniform flow. These methods both use transformations to reduce a convected wave equation to a regular Helmholtz equation, which can then be solved using standard BEM techniques. The uniform flow approximation uses a Lorentz-type transform [70], and the non-uniform flow approximation uses a transform proposed by Taylor [71]. These methods were both detailed in Section 3.3.3. The preceding investigations in this chapter that solved the LEE with a single frequency source have given an insight into the effect of both uniform

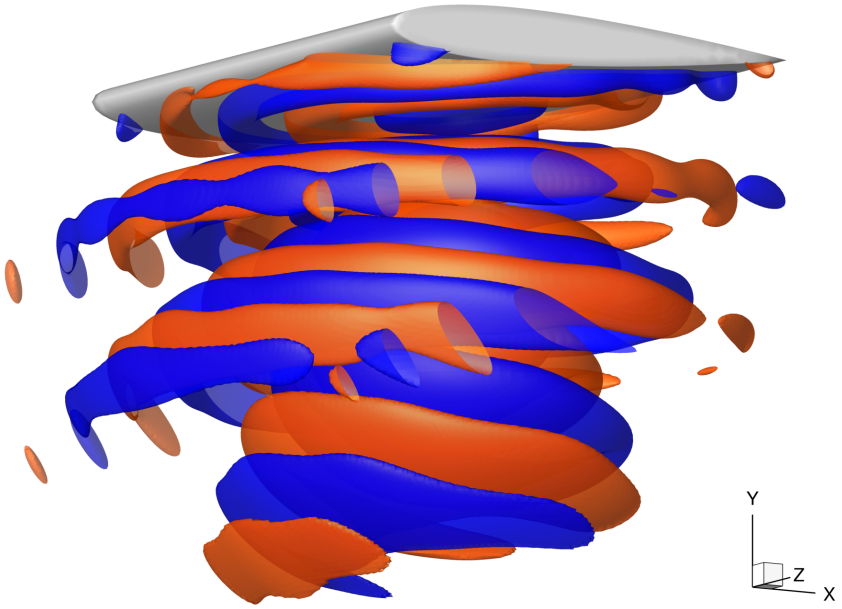

Figure 4.23: Isocontours of acoustic pressure, ±8.4 Pa. NACA 0012, $\alpha = 4°$, $M_\infty = 0.2$, non-uniform flow, source at 250 Hz.

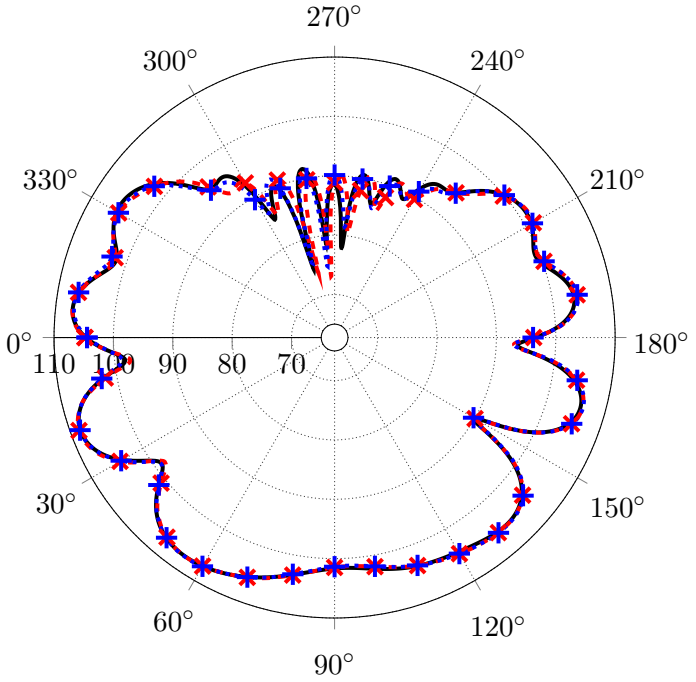

Figure 4.24: Comparison of 3-D BEM and LEE results. SPL (dB) for the scattering of a monopole at 250 Hz by a NACA 0012 airfoil at $\alpha = 4°$ and $M_\infty = 0.2$. *ACTIPOLE* ——, *SotonLEE* non-uniform - -×- -, *SotonLEE* uniform ···+···.

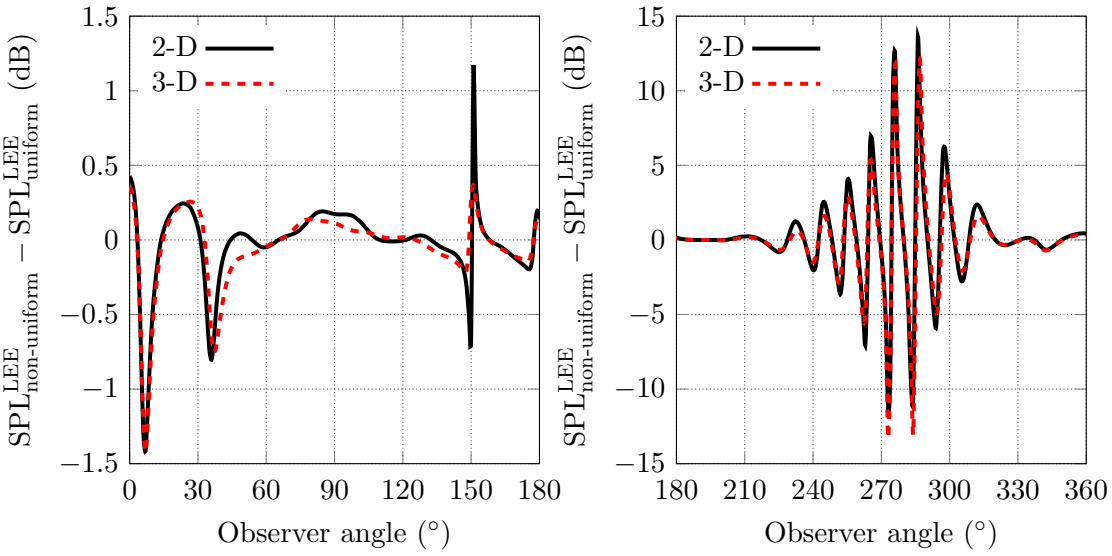

(a) 0° - 180°. (b) 180° - 360°.

Figure 4.25: Comparison between the difference in SPL over non-uniform and uniform base flows in 2-D and 3-D. NACA 0012, $\alpha = 4°$, $M_\infty = 0.2$, source at 250 Hz.

and non-uniform flows on the acoustic scattering. The results from these investigations were then used to evaluate the BEM flow approximations to determine which is more suitable for modelling the scattering of landing gear noise.

The uniform and non-uniform flow approximations were both implemented in the open-source 2-D BEM solver *ABEMFULL* [100], which was validated for scattering problems in Section 3.3.2. The required flow approximation method is specified as an input parameter, and the corresponding code is executed when the solver is run. The implementation for the non-uniform flow approximation imports a flow solution computed using the potential flow solver described and validated in Section 3.4. Boundary discretisations for each airfoil configuration were created using line segments of approximately equal length. The average element length was at most 4.0×10^{-2} m, which allowed the resolution of acoustic waves up to $M_\infty = 0.3$ with 10 elements per wavelength. For the non-uniform flow approximation, the same boundary discretisation was used for both flow and acoustic solutions. Details of the created boundary discretisations are given in Table B.3 in Appendix B.

The implementation of the potential flow solver satisfies the Kutta condition at the trailing edge of each airfoil element, as described in Section 3.4. However, the RA16SC1 with flap 40° plus slat configuration also has a sharp corner at the bottom of the slat. The flow velocity around this corner in the potential flow

solution becomes unrealistically large, and thus this configuration could not be investigated using this implementation. It was explained previously that the LEE solution using this configuration with a non-uniform base flow was unstable for certain frequencies due to the strong shear layer behind the trailing edge of the slat. Thus, regardless of whether an accurate non-uniform flow BEM solution could be acquired for this configuration, there was no equivalent LEE solution available for its evaluation.

The model for the BEM investigation was identical to that used for the LEE investigations, which was described in Section 4.2. BEM solutions were obtained using both flow approximation methods for all cases listed in Section 4.2 at frequencies of 125 Hz, 250 Hz, and 500 Hz. This is with the exception of the RA16SC1 with flap 40° plus slat configuration, as explained previously. For all cases, the value of the monopole source strength Q was chosen to give 100 dB at 5 m in the free-field without flow for the given frequency. Thus, there were corresponding LEE solutions over both uniform and non-uniform base flows for all BEM solutions. There is no analytical solution available for a general geometry with flow with which to check the implementation of the flow methods in *ABEMFULL*. However, the evaluation of the methods that is detailed later in this section shows that the methods were implemented correctly.

Example acoustic fields are shown in Figure 4.26 for one of the NACA 0012 airfoil cases at 250 Hz, $M_\infty = 0.2$, and $\alpha = 5°$, computed using both BEM flow methods. Each case was computed using the same solver, with the required flow approximation method specified as an input parameter. In both flow approximation methods, a regular Helmholtz equation is solved using a standard BEM technique with variables modified using the respective transforms, as detailed in Section 3.3.3. It can been seen for both cases in Figure 4.26 that there is a compression of the wavelength upstream and dilation downstream as expected. Figure 4.27 shows the corresponding directivity plots for these two cases, as well as for the equivalent case without flow. It can be seen that in the upstream and downstream regions the two BEM flow solutions have approximately the same convective amplification. However, in the $30° \leq \theta \leq 150°$ region the non-uniform flow approximation is closer to the no-flow case. These differences can also be seen in Figure 4.26, and will be explained later. Although not shown here, the uniform flow BEM formulation is close to the LEE solution over a non-uniform flow in this region, similar to what was seen in 3-D in Figure 4.24.

In order to evaluate the BEM flow approximations, the average absolute percentage

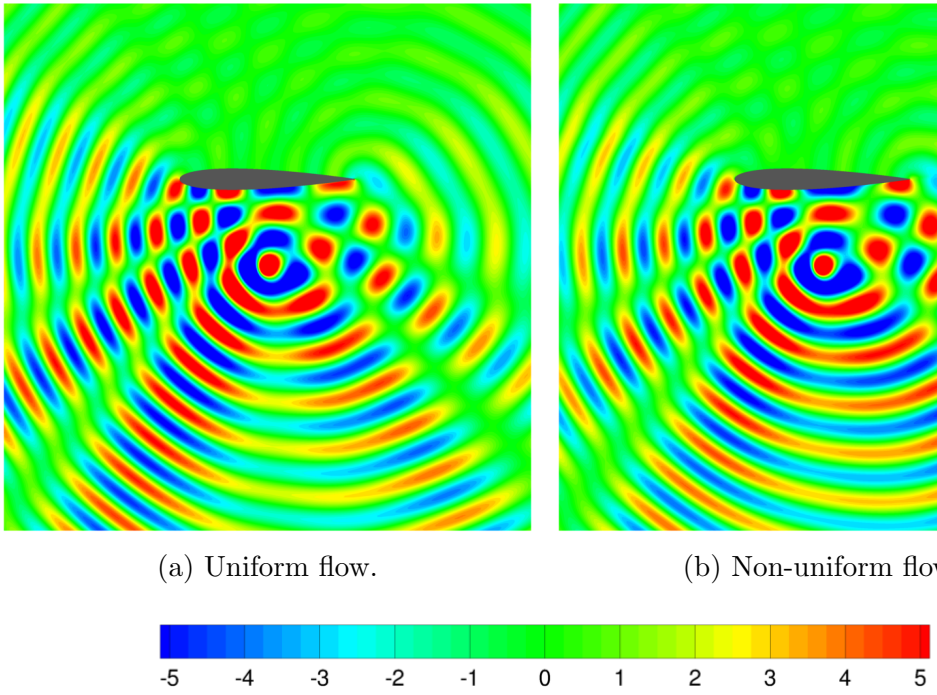

(a) Uniform flow. (b) Non-uniform flow.

Figure 4.26: Acoustic pressure (Pa) for the two BEM flow approximations, NACA 0012, 250 Hz, $\alpha = 5°$, $M_\infty = 0.2$.

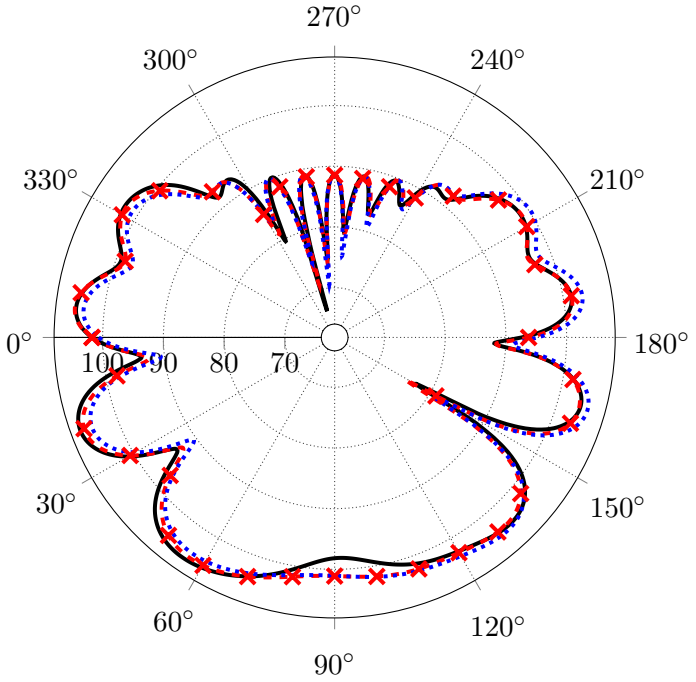

Figure 4.27: SPL (dB) showing a comparison of BEM solutions for the NACA 0012 airfoil at 250 Hz. $M_\infty = 0.0$ ·····; uniform $M_\infty = 0.2$, $\alpha = 5°$ ——; non-uniform $M_\infty = 0.2$, $\alpha = 5°$ - -×- -.

error in p_{rms} was computed over observers in the range $0° \leq \theta \leq 180°$. This value was denoted here by ψ, and was computed using

$$\psi = \frac{1}{181} \sum_{\theta=0}^{180} \left| \frac{p_{\text{rms}}^{\text{BEM}}(\theta) - p_{\text{rms}}^{\text{LEE}}(\theta)}{p_{\text{rms}}^{\text{LEE}}(\theta)} \times 100 \right|. \tag{4.10.1}$$

This restricted observer range was chosen as this is the primary region of interest for landing gear noise, in which noise is scattered towards the ground. Minor differences in the location of directional lobes in the shadow zone above the wing as computed by the BEM and LEE solutions could otherwise dramatically alter the average error.

In order to better understand the values obtained in the evaluation of the BEM flow approximations, solutions for each configuration at each frequency were obtained without flow using both BEM and LEE solvers. The LEE solution for each frequency was obtained using the grid with the appropriate source refinement that was created in Section 4.3. The LEE solutions were computed as in Section 4.5, including an equivalent free-field case to compute the scaling factor, only without the need for a base flow. Values for the average absolute percentage error were computed for these cases using (4.10.1), and these are shown in Table 4.3. The value of ψ is generally less than 5 %, except for a few combinations of configuration and frequency. Figure 4.28 shows the SPL directivity for the two configurations that show the largest value of ψ. It can be seen that the larger average error observed for these cases is caused by differences at a selection of observer angles where there is destructive interference. However, despite the slightly higher values of ψ for these cases, the solutions are generally in good agreement.

Table 4.3: Average absolute percentage error in p_{rms}, denoted by ψ, for observers in the range $0° \leq \theta \leq 180°$. BEM vs LEE, without flow.

	Frequency		
Airfoil	125 Hz	250 Hz	500 Hz
NACA 0012	1.382	1.439	5.609
RA16SC1	1.604	2.406	2.807
RA16SC1 with flap 20°	4.292	7.522	1.904
RA16SC1 with flap 40°	3.386	3.580	9.754

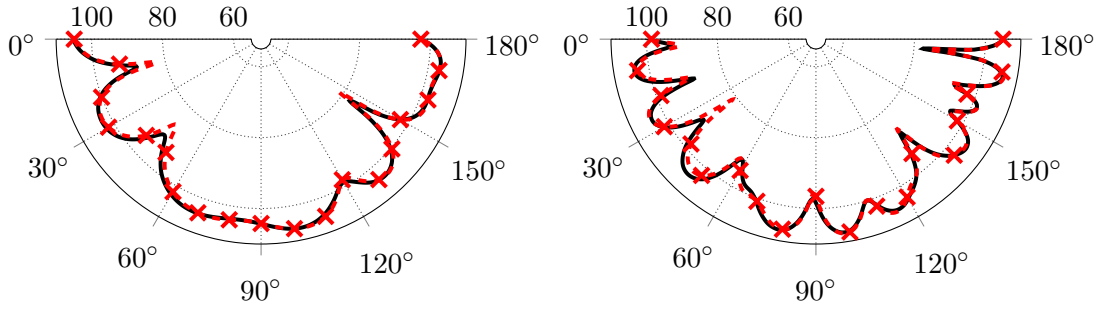

(a) RA16SC1 with flap 20°, 250 Hz.

(b) RA16SC1 with flap 40°, 500 Hz.

Figure 4.28: SPL (dB) showing a comparison of BEM solutions against LEE solutions without flow for observers in the range $0° \leq \theta \leq 180°$. LEE ——, BEM - -×- -.

4.10.1 Single Element Airfoil

The derivations of the two BEM flow approximations under evaluation were detailed in Section 3.3.3. It was shown that in order to reduce the convective wave equation to an ordinary wave equation using the Taylor transform, $O(M_\infty^2)$ terms are neglected. This would suggest that as the Mach number is increased, the error in the non-uniform flow approximation would become larger. The NACA 0012 airfoil was used to investigate the effect of varying the angle of attack and Mach number on the accuracy of the BEM flow approximation methods. Figure 4.29 shows the computed values of ψ with increasing Mach number and fixed angle of attack of $\alpha = 5°$ for both flow formulations compared to the LEE solution over a non-uniform flow. It can be seen that both approximations become less accurate with increasing Mach number. However, the non-uniform flow approximation is much worse than the uniform flow approximation. For low frequencies at $M_\infty = 0.1$, the two approximations show a similar error. However, by $M_\infty = 0.2$, the error at the low frequency is already around three times larger for the non-uniform flow approximation. As the Mach number is increased, this error continues to grow much faster for the non-uniform flow approximation than for the uniform flow approximation. This is the source of the observed difference between the approximation methods seen in Figure 4.26 and Figure 4.27.

The effect on the error of fixing the Mach number at $M_\infty = 0.2$ and varying the angle of attack is shown in Figure 4.30. This was again computed with comparison against the LEE solution over a non-uniform flow. From the results shown in Figure 4.29, it was expected that the non-uniform flow approximation would be worse for all angles of attack than the uniform flow approximation at this Mach

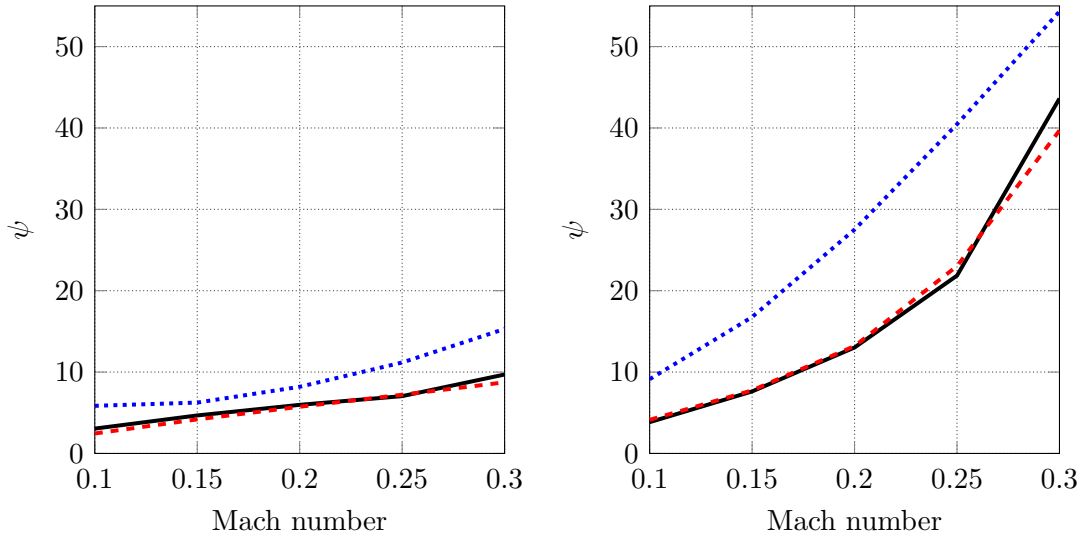

(a) $\text{BEM}_{\text{uniform}}$ vs $\text{LEE}_{\text{non-uniform}}$. (b) $\text{BEM}_{\text{non-uniform}}$ vs $\text{LEE}_{\text{non-uniform}}$.

Figure 4.29: NACA 0012 airfoil, varying M_∞, $\alpha = 5°$. 125 Hz ——, 250 Hz - - - -, 500 Hz ·····.

number. This is indeed the case. However, as the angle of attack is increased, the error for the non-uniform flow approximation decreases. This is due to the increase in angle of attack increasing the circulation around the airfoil, and therefore reducing the local flow velocity beneath the airfoil. In the non-uniform flow approximation, the derivative of the flow potential at a given point modifies the magnitude of the complex pressure at that point, as seen in Equation (3.3.31) in Section 3.3.3.2. Thus, as the flow velocity becomes lower beneath the airfoil, the error due to neglecting terms of $O(M_\infty^2)$ decreases.

Conversely, the uniform flow approximation gets slightly worse with increasing angle of attack. This is due to the increasing difference between the local flow velocity below the airfoil and the free-stream. It was seen in Figure 4.12 that at $\alpha = 0°$ there is an increase in flow velocity below the symmetric airfoil. By $\alpha = 3°$ the increase in circulation offsets this velocity increase so that the local flow velocity is of a similar magnitude to the free-stream. As α is increased, the local flow velocity is further reduced. This can be seen in the results for the uniform flow approximation, in particular at 500 Hz. It should be noted however that although the error for the uniform flow approximation grows with increasing angle of attack, it is still better than the non-uniform flow approximation at this Mach number, even at the highest angle.

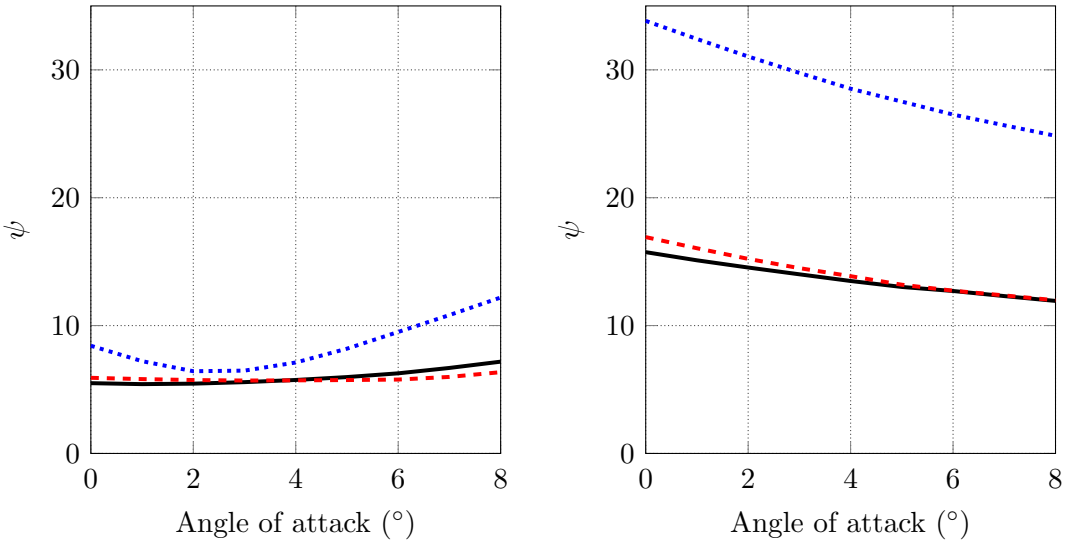

(a) $\text{BEM}_{\text{uniform}}$ vs $\text{LEE}_{\text{non-uniform}}$. (b) $\text{BEM}_{\text{non-uniform}}$ vs $\text{LEE}_{\text{non-uniform}}$.

Figure 4.30: NACA 0012 airfoil, varying α, $M_\infty = 0.2$. 125 Hz ——, 250 Hz - - - -, 500 Hz ·····.

4.10.2 Airfoil With Flap

Having investigated the accuracy of the two BEM flow approximation methods using a single element airfoil, the effect of flap deployment on the accuracy of the methods was then investigated. This was conducted using the RA16SC1 airfoil at a fixed Mach number of $M_\infty = 0.2$ and angle of attack of $\alpha = 0°$. The various configurations of the flap for this airfoil geometry can be seen in Figure 4.1. Figure 4.31a and Figure 4.31b show the evaluation of the two BEM flow approximations against the corresponding LEE solutions over a non-uniform flow. With the flap retracted, the uniform flow approximation is better than the non-uniform flow approximation, similar to what was seen for the NACA 0012 airfoil in the previous section. However, it can be seen that the non-uniform flow approximation outperforms the uniform flow approximation when the flap is deployed.

The reason for this is similar to that for the improvement in the non-uniform flow approximation with increasing angle of attack seen in Figure 4.30b. In the non-uniform flow approximation, the magnitude of the complex pressure at a given point is modified by the derivative of the flow potential at that point, as seen in Equation (3.3.31). As the flap is deployed, and its deployment angle subsequently increased, there is a large increase in circulation that reduces the flow velocity below the airfoil. It was shown in Figure 4.16 that this reduction in flow velocity beneath the airfoil is substantial with increasing flap angle. For the flap 40° configuration, the flow Mach number magnitude is approximately 0.07 lower than

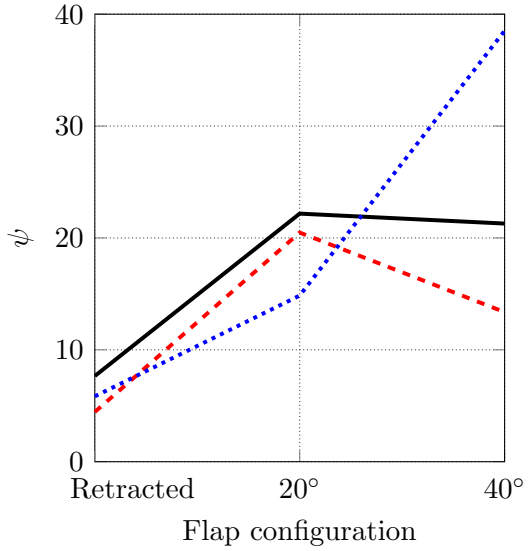

(a) $\text{BEM}_{\text{uniform}}$ vs $\text{LEE}_{\text{non-uniform}}$.

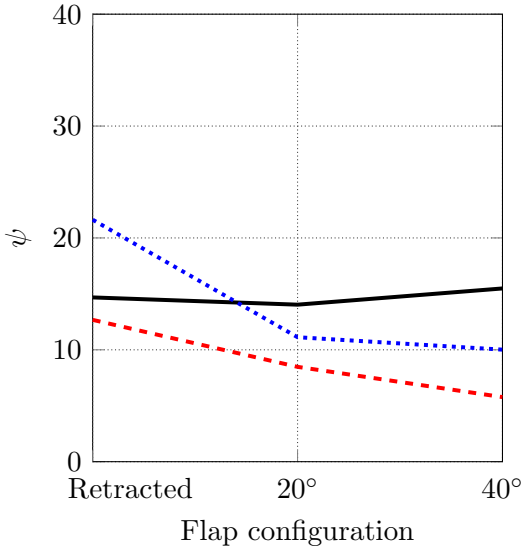

(b) $\text{BEM}_{\text{non-uniform}}$ vs $\text{LEE}_{\text{non-uniform}}$.

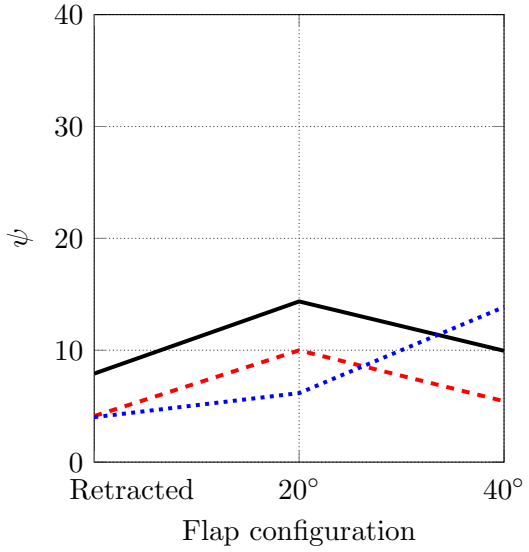

(c) $\text{BEM}_{\text{uniform}}$ vs $\text{LEE}_{\text{uniform}}$.

Figure 4.31: RA16SC1 airfoil, varying configuration, $M_\infty = 0.2$, $\alpha = 0°$. 125 Hz ——, 250 Hz - - - -, 500 Hz ·····.

the free-stream Mach number of 0.2 at the source position. It was shown in Figure 4.29b that the non-uniform flow approximation becomes more accurate as the local Mach number is decreased. This was attributed to neglecting $O(M_\infty^2)$ terms in the derivation of the approximation. Thus, for the flap 40° configuration with a free-stream Mach number of $M_\infty = 0.2$, the reduced local flow velocity at the observers due to circulation leads to the observed improvement in accuracy.

Conversely, the uniform flow approximation becomes less accurate with increasing flap deployment angle when compared to the LEE results over a non-uniform

base flow, as seen in Figure 4.31a. This is due to the large difference between the uniform and non-uniform flows in the region below the airfoil, caused by the increase in circulation in the non-uniform flow due to flap deployment. To confirm that it is the difference between uniform and non-uniform flows that is creating this larger observed error, ψ was computed for the uniform flow approximation with comparison against the LEE solution over a uniform flow. This is shown in Figure 4.31c. It can be seen that the error for the uniform flow BEM approximation when compared to the uniform flow LEE solution is indeed generally lower than when it is compared to the non-uniform flow LEE solution.

For this particular free-stream Mach number and airfoil configuration with deployed flap, it has been shown that the non-uniform flow approximation is more accurate than the uniform flow approximation. However, it cannot be said that this is true in general for an airfoil with deployed flap. It has been shown that the accuracy of the non-uniform flow formulation depends on the local Mach number at the observer locations, due to the neglecting of $O(M_\infty^2)$ terms in the derivation of the approximation. The local Mach number is influenced by the free-stream Mach number, the angle of attack, and the geometry of the airfoil and flap. As an example, consider a similar case to that shown in this section, but with $M_\infty = 0.3$. With the deployment of the flap and the associated increase in circulation, there will be a reduction in flow velocity at the observers. However, it could be that the local Mach number at the observers is still high enough despite the deployment of the flap to cause a significant error in the non-uniform flow approximation. Depending on the local Mach number, this error might be larger than for the uniform flow approximation, despite the large difference between uniform and non-uniform flows. Thus, the suitability of the non-uniform flow approximation for cases with a deployed flap needs to be assessed on a case-by-case basis.

4.11 Summary

An investigation into the scattering of a single frequency source by an airfoil has been presented in this chapter. A monopole source was used to represent an idealised landing gear source, located beneath a lifting wing. The effect of circulation on the scattering was investigated using a LEE solver, which can account for the refraction of an acoustic wave as it propagates through a flow. For each case, the acoustic scattering was computed over both a non-uniform and uniform base flow.

The effect of the non-uniform flow due to circulation around the airfoil was quantified at various observers by calculating $\mathrm{SPL}_{\text{non-uniform}} - \mathrm{SPL}_{\text{uniform}}$. This gave a measure of the difference in SPL due to the difference between the non-uniform and uniform base flows. It was shown that at a free-stream Mach number of $M_\infty = 0.2$, representative of a commercial airliner on approach, a large increase in the angle of attack had a small but significant impact on the computed values of $\mathrm{SPL}_{\text{non-uniform}} - \mathrm{SPL}_{\text{uniform}}$ at the observers. However, varying the Mach number within the range $0.1 \leq M_\infty \leq 0.3$ did not show any significant differences. The deployment of a flap and its subsequent increase in deflection angle also showed a significant difference in the results, although there were not any clear trends in the results.

The investigation was extended in order to determine if there was a higher Mach number or alternative source location such that the values of $\mathrm{SPL}_{\text{non-uniform}} - \mathrm{SPL}_{\text{uniform}}$ were significantly larger. It was shown that for a Mach number of $M_\infty = 0.6$ with the source in the location of a landing gear, there was not a large change in the observed results compared to the lower Mach numbers investigated previously. The source was then installed above the airfoil, and the effect of varying the Mach number in the range $0.2 \leq M_\infty \leq 0.6$ was investigated. It was shown that at $M_\infty = 0.2$ and 0.3, the differences in the acoustic scattering due to the non-uniform and uniform base flows at each Mach number were similar to those seen with the source located below the wing. However, for Mach numbers in the range $0.4 \leq M_\infty \leq 0.6$, larger differences in the acoustic scattering were observed. These were attributed to the flow being transonic over the top surface of the leading edge of the airfoil in the non-uniform flow. This results in the acoustic propagation being attenuated in this region, which further leads to large differences in interference throughout the acoustic field. Further simulations were conducted in 3-D that showed that the simulations that had been conducted in 2-D were representative of what would be observed in 3-D for the simplified geometry under investigation.

Finally, the results from the LEE simulations were used to evaluate two existing BEM flow formulations. It was shown that neglecting terms of $O(M_\infty^2)$ in the derivation of the non-uniform flow approximation leads to large errors in the computed SPL if the local flow velocity is larger than $M_0 \approx 0.15$. Comparisons were made with LEE solutions over non-uniform flows under the assumption that these were correct and that refraction effects had been accounted for. It was shown that the uniform flow BEM approximation outperformed the non-uniform flow BEM approximation using a single-element airfoil for the set of parameters used in the

investigation. However, it was also shown that due to the large reduction in flow velocity below an airfoil with flap deployed, the non-uniform flow BEM approximation outperformed the uniform flow BEM approximation for the single Mach number investigated here using this geometry. This is due to the non-uniform flow BEM approximation using the local flow velocity to modify the acoustic pressure at the observer locations. It cannot be said however that the non-uniform BEM flow approximation is generally better than the uniform flow BEM approximation for cases using an airfoil with flap. This is because the accuracy of the solution depends on the magnitude of the reduction in flow velocity at the observer locations for such a geometry.

Chapter 5

The Scattering of a Broadband Source by an Airfoil

5.1 Introduction

Noise from aircraft landing gear is essentially broadband, as discussed in Section 2.3. The solution of the LEE in the current work is conducted in the time domain, and so the method is ideal for studying acoustic propagation from a broadband source as well as single frequency sources. As seen in Chapter 4, large directional lobes are seen in the results at a single frequency due to constructive and destructive interference. This makes trends in the results hard to see, especially for the airfoil configurations with a deployed flap. As will be seen in this chapter, furthering the investigation using a broadband source gives further insight into the effect of non-uniform flow due to circulation around a lifting wing on the acoustic scattering of an idealised landing gear noise source.

As will be discussed, a broadband monopole can be introduced into LEE methods by modifying the single frequency source as originally described by Bailly and Juvé [45]. A broadband input signal with a specified PSD can be used with this source term in order to force acoustic pressure waves in the LEE simulation. A suitable input signal was created using an existing method from the literature. However, initial simulations of this broadband monopole in the free-field showed that the PSD obtained at a distance from the source is different from that of the input signal. The reason for this was deduced, and a method to construct a modified input signal that reconstructs the intended PSD at the observer distance was developed. An investigation into the installation of a broadband monopole

beneath various airfoil configurations was then undertaken using this modified input signal. The effect of circulation on the acoustic scattering was quantified through examination of the OASPL and the PSD of the scattered source at the observers.

This chapter presents the investigations undertaken using a broadband source with an isolated airfoil as the scattering geometry. Section 5.2 presents the generation of a broadband signal with a specified PSD, and explains the difference in observed PSD at a distance from the source. The creation of a modified input signal that reconstructs the desired PSD at the observer location is detail in Section 5.3. The model, cases, and computational grids used for the investigations of an installed broadband source are summarised in Section 5.4. The investigation into the effect of circulation on the OASPL of the installed broadband source is presented in Section 5.5. An analysis of the frequency content of the scattered source for varying airfoil configurations is described in Section 5.6. Results for a single frequency are extracted from the broadband results in Section 5.7, and these are compared to the results from the equivalent single frequency simulations from Chapter 4. Finally, a summary of the investigations using a broadband source is given in Section 5.8.

5.2 The Generation and Testing of a Broadband Signal

A broadband monopole can be implemented in LEE methods by replacing the time-harmonic $\sin(\omega t)$ term in (3.5.4) with a time-dependent pressure signal $\eta(t)$ to give

$$\mathbf{S}(x, y, z, t) = \eta(t)F(x, y, z). \tag{5.2.1}$$

The forcing region function F describes a Gaussian distribution as in (3.5.5).

A method for generating a random signal corresponding to a stationary process using a specified PSD function and probability density function (PDF) was described by Nichols *et al.* [111]. An algorithm written for *MATLAB* was presented along with the method. The algorithm generates a sequence of samples taken from the specified PDF, and then makes use of an iterative shuffling procedure to reorder the samples such that the signal conforms to the specified PSD function while preserving the original PDF. It is a requirement of the algorithm that the specified PSD be two-sided and symmetric, and integrate to unity. This algorithm was used to generate an input signal to be used as $\eta(t)$ in (5.2.1). This method of

generating a signal to be imported by *SotonLEE* was chosen, instead of summing sine waves of differing discrete frequencies within the code, in order to ensure that the signal was not correlated in time.

For the present work, a one-sided PSD function that was equal in power for all frequencies $20\,\text{Hz} \leq f \leq 500\,\text{Hz}$ was created. This frequency range was chosen as 20 Hz is the lower limit of human hearing, and 500 Hz is the highest frequency supported by the computational meshes created in Chapter 4. Using an input signal that was equal in power for all frequencies would easily allow the effect of installing the broadband source beneath a lifting wing to be seen in the PSD computed at the observers. The created one-sided PSD was made symmetric around 0 Hz to create a two-sided PSD function and normalised so that it integrated to unity, as required for the algorithm presented by Nichols *et al.* [111]. A sample rate of 312.5 kHz was chosen to give a Δt of 3.2×10^{-6} s for the generated signal. This value of Δt was determined by the maximum CFL number requirement of 0.5 for the planned simulations.

With a full normal distribution used for the PDF, the peaks in the signal generated by the algorithm were not always smooth. A signal generated by the algorithm is composed of samples that are generated using the specified PDF. In the case of using a full normal distribution for the PDF, the higher peaks in the generated signal correspond to the samples generated from the full normal distribution that are far from the mean. With the chosen sample rate for the present work, not enough samples were generated from the full normal distribution to smoothly resolve the higher peaks in the signal following the iterative shuffling procedure of the algorithm. To overcome this, a truncated normal distribution with $f(x) = 0$ for $|x| > 3$ was used for the PDF. This limited the generated samples to within three standard deviations of the mean, and prevented the generation of unphysical peaks that could not be smoothly resolved. A 3 s signal was generated, which was composed of 9.375×10^5 samples given the chosen sampling rate.

It is assumed from here on that the samples of the generated signal are of pressure in pascals varying in time. Figure 5.1 shows a segment of the generated pressure signal. The one-sided PSD of this generated signal was computed using a discrete Fourier transform (DFT) in *MATLAB* in order to check that the desired PSD was obtained, and this is shown in Figure 5.2. The RMS of the generated signal is 1 Pa, which is equal to one standard deviation of the truncated normal distribution used to generate the signal. Integrating the PSD shown in Figure 5.2 and taking the square root gives the correct value for the RMS of 1 Pa. Figure 5.3 demonstrates

that the PDF of the generated signal is in good agreement with the target PDF. The autocorrelation of the generated signal is shown in Figure 5.4, where it can be seen that the signal is uncorrelated in time as intended.

In order to test the methodology, the generated signal was used as input signal η in order to force acoustic pressure waves in a 2-D LEE simulation through the use of (5.2.1). This was conducted without flow using the free-field computational mesh constructed in Chapter 4, with source refinement for 500 Hz. The simulation was run for 6.4×10^{-2} s in order for the initial acoustic pulse to reach the domain boundaries, before pressure was sampled at the 90° observer for 2.4 s at a sample rate of 312.5 kHz. The received signal ζ was scaled to give an overall p_{rms} of 2 Pa, or equivalently an OASPL of 100 dB. In order to obtain an estimate of the PSD for the received signal, the method proposed by Welch [112] for power spectrum estimation was used throughout the current work. Welch's method divides the acquired signal into overlapping segments, windows each segment using a suitable window function, computes a periodogram on each windowed segment using a

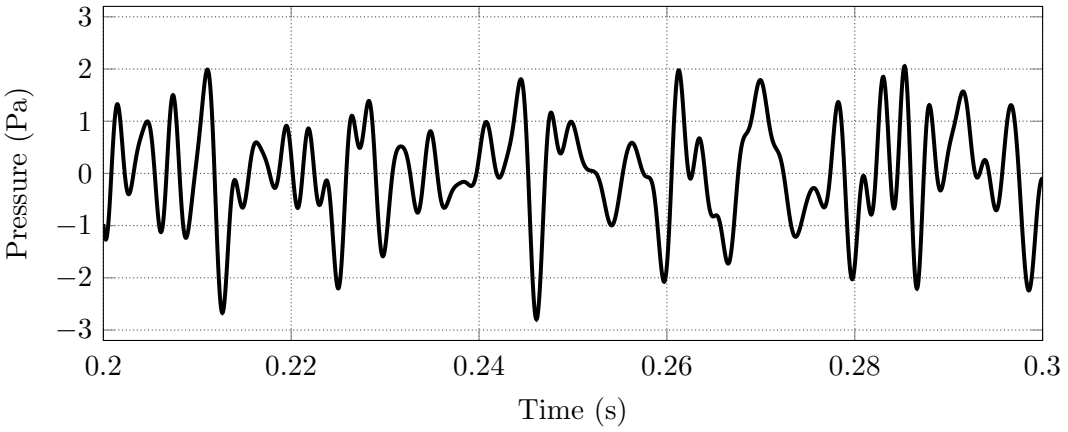

Figure 5.1: Segment of generated time series.

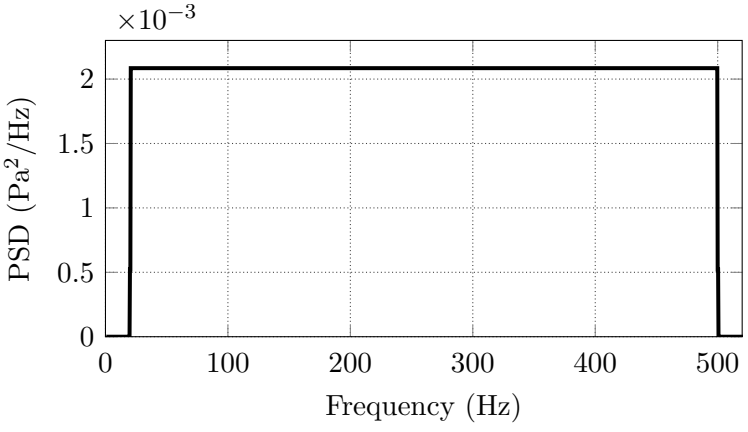

Figure 5.2: One-sided PSD of the generated time series.

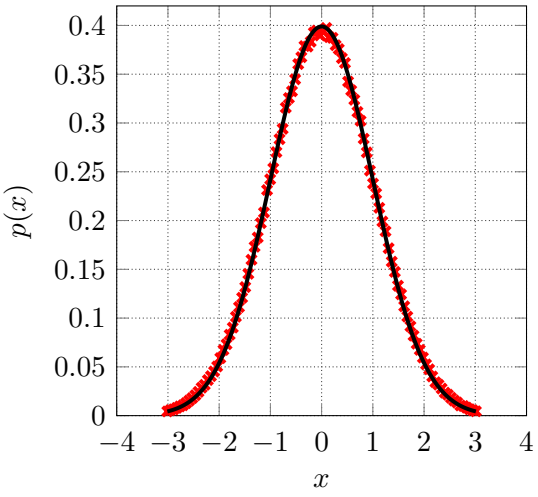

Figure 5.3: PDF of the generated time series. Target ——, generated ×.

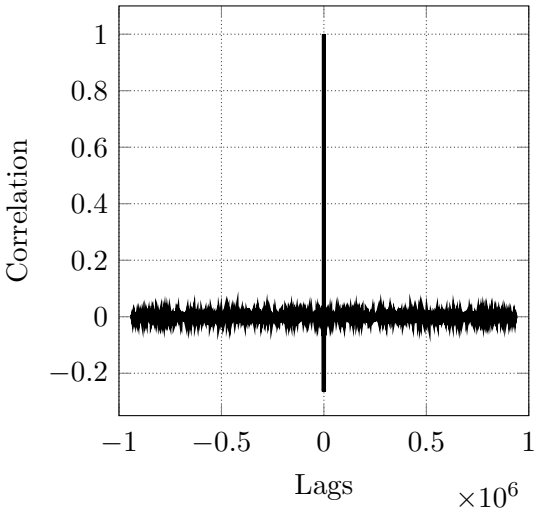

Figure 5.4: Autocorrelation of the generated time series.

DFT, then averages across these periodograms. This method reduces noise in the estimated PSD. Given a signal consisting of D samples, the segment length was chosen as $L = D/10$ with a 50% overlap, giving 19 segments. The `pwelch` function in the *MATLAB* Signal Processing Toolbox was used to obtain a one-sided PSD estimate using these parameters. A Hanning window was applied to each segment, which has good frequency resolution with reduced spectral leakage.

Gabard [113] presented a discussion on post-processing results from broadband LEE simulations using Welch's method to obtain an estimate of the PSD. It was explained that as Welch's method averages over neighbouring frequencies for any given frequency bin, a spectrum estimate can be obtained using a result from a single simulation. This is valid under the condition that the input signal uses a frequency distribution that is denser than the frequency distribution in the spectrum estimate, which is the case in the current work. If this condition is true, then the averaging process reduces the variance in the spectrum estimate. The running of multiple simulations using different signals consisting of frequencies with differing phases, and ensemble averaging the results, is not required.

Applying Welch's method to the signal obtained from the simulation at the 90° observer, which is at a distance of 5 m from the source, gives the PSD shown as the numerical solution in Figure 5.5. It can be seen that the obtained PSD at this observer radius is not the same as that of the input signal, which is shown in Figure 5.2. The mechanism behind the observed difference in PSD for η and ζ can be explained through examination of a solution to the Helmholtz equation. The time-harmonic complex acoustic pressure is written in terms of the acoustic potential

using (3.3.7). The acoustic potential for a monopole is given using (3.3.10), along with the 2-D free-field Green's function (3.3.5). Combining these equations gives

$$p(\mathbf{x}) = -\frac{Q}{4}\rho_\infty \omega H_0^{(1)}(kr), \tag{5.2.2}$$

where $r = \sqrt{(x - x_s)^2 + (y - y_s)^2}$ is the radial distance from the source. This equation shows that for a fixed value of Q, the resultant acoustic pressure at a given distance r is dependent on frequency. For a numerical method using a single broadband monopole implemented through (5.2.1), it is the case that the value of Q for each frequency is determined by the input signal. Due to the use of a single source, these values of Q are fixed. Therefore, the PSD of the received signal at a distance r from the source will be different than that of the input signal. Using (5.2.2), a PSD function was computed at the radial distance of 5 m for frequencies $20\,\text{Hz} \leq f \leq 500\,\text{Hz}$. A value of Q that was equal for all frequencies was used, which replicated the PSD of the input signal used in the simulation. This value of Q was chosen so that the square root of the integral of this function gave the required overall p_{rms} of 2 Pa. This is shown converted to dB/Hz as the analytical solution in Figure 5.5, and is in good agreement with the obtained numerical solution.

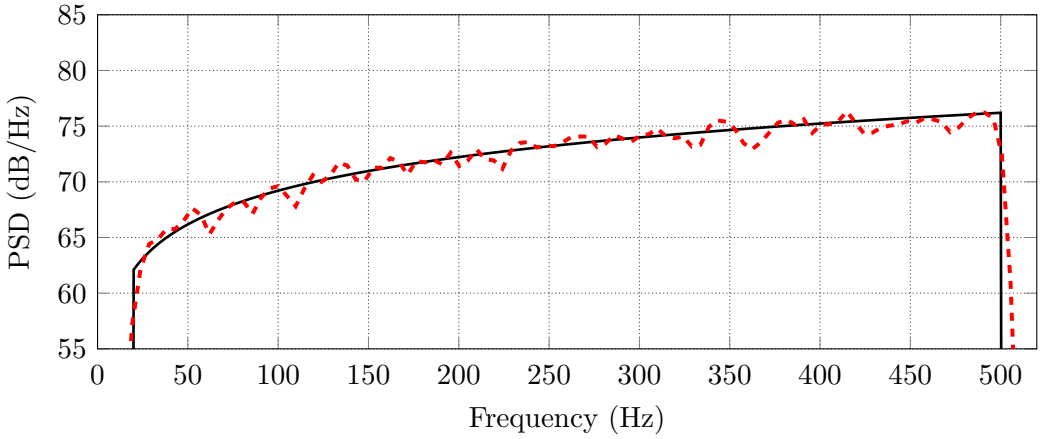

Figure 5.5: PSD (dB/Hz) at a radius of 5 m for a broadband monopole in the free-field without flow using the original input signal. Analytical ——, numerical - - - - -.

5.3 The Creation of a Modified Input Signal for the Correct Power Spectral Density

The following method is now proposed to generate a modified input signal that allows the intended PSD to be obtained at the observer. The received signal ζ at the observer in the original simulation can be written as the convolution of the input signal η with an unknown impulse response ξ as

$$\eta * \xi = \zeta.$$

Using deconvolution, the Fourier transform $\mathcal{F}$ of impulse response ξ, or transfer function $\Xi = \mathcal{F}(\xi)$, is expressed as

$$\Xi = \frac{Z}{H}, \tag{5.3.1}$$

where $Z = \mathcal{F}(\zeta)$, and $H = \mathcal{F}(\eta)$. The required signal at the observer radius, which is taken as the original input signal, can then be written as the convolution of a modified input signal η_m with the impulse response as

$$\eta_m * \xi = \eta.$$

The modified input signal can then be expressed through deconvolution as

$$H_m = \frac{H}{\Xi}, \tag{5.3.2}$$

where $H_m = \mathcal{F}(\eta_m)$. With Ξ known through Eq. (5.3.1), H_m is computed using Eq. (5.3.2). The modified input signal is then given through an inverse Fourier transform $\eta_m = \mathcal{F}^{-1}(H_m)$. This method is applicable in 2-D or 3-D, and with any desired PSD function.

In the current work, the goal was to obtain a PSD that was equal in power for all frequencies $20\,\text{Hz} \leq f \leq 500\,\text{Hz}$ at a radius of 5 m. Given an OASPL of 100 dB, the PSD is given by a constant 73.19 dB/Hz across the frequency range. This is shown as the analytical solution in Figure 5.6. For the numerical solution, the 3 s input signal used in the original simulation was truncated to 2.4 s in order to match the length of the received signal. This truncation was done in such a way as to account for the propagation time between the source and the observer and match the starting time of each signal. The method outlined previously was then applied using a DFT on each discretely sampled signal, resulting in a modified

input signal 2.4 s in length. This signal was further truncated to 2.1 s to remove unwanted artefacts from each end of the newly created signal. These artefacts, which only occur at the ends of the newly created signal, are due to the use of a DFT on discretely sampled non-periodic signals in the deconvolution process. The `smooth` function in the *MATLAB* Curve Fitting Toolbox was applied to the result in order to yield a smooth signal for use with the numerical LEE solver.

This modified input signal was then tested, using the same grid and parameters as before. The simulation was again run for 6.4×10^{-2} s in order for the initial acoustic pulse to reach the domain boundaries. Pressure was then sampled at the same observer for 2 s at a sample rate of 312.5 kHz, and the received signal scaled so that the overall p_{rms} was 2 Pa. A sample of the received pressure signal is shown in Figure 5.7. The PSD was computed using Welch's method, and is shown as the numerical solution in Figure 5.6. It can be seen that the solution is in good agreement with the analytical solution, and that the required PSD at this observer radius has been recovered. The autocorrelation of the received pressure signal is shown in Figure 5.8. It can be seen that this signal is still uncorrelated in time following the process of generating the modified input signal.

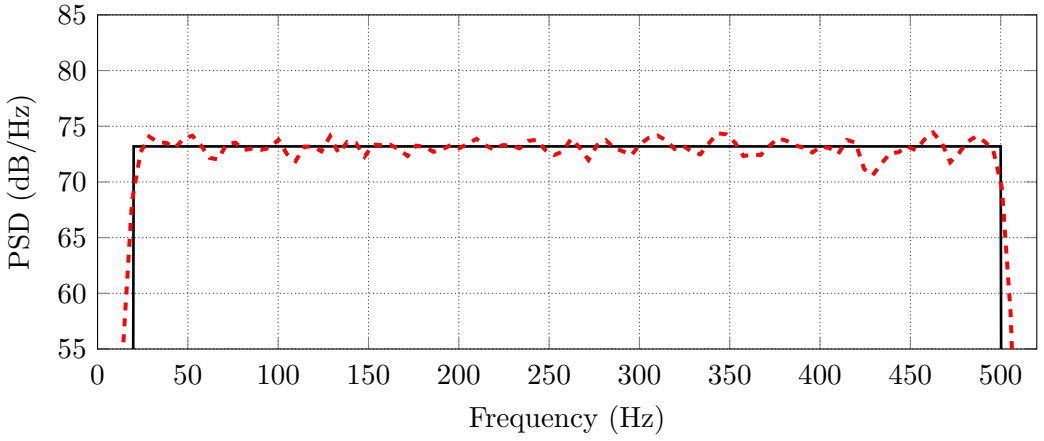

Figure 5.6: PSD (dB/Hz) at a radius of 5 m for a broadband monopole in the free-field without flow using the modified input signal. Analytical ——, numerical - - - - -.

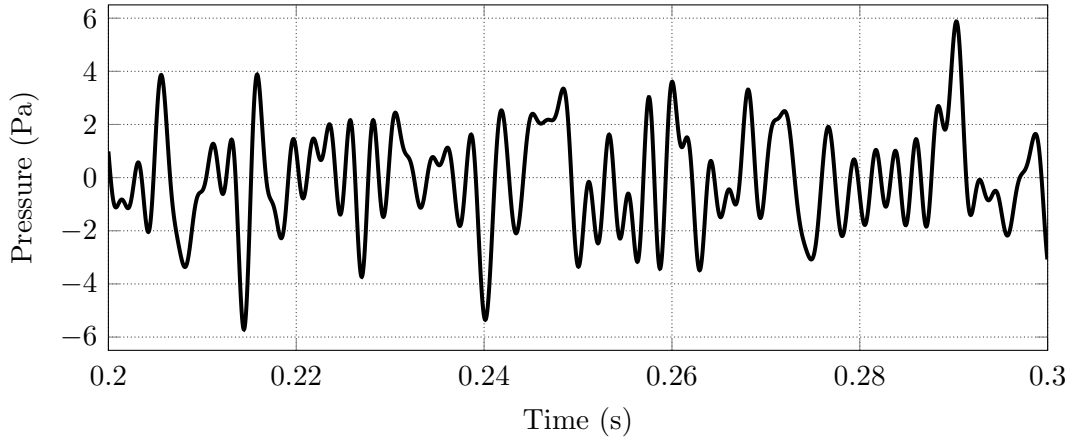

Figure 5.7: Segment of received pressure signal.

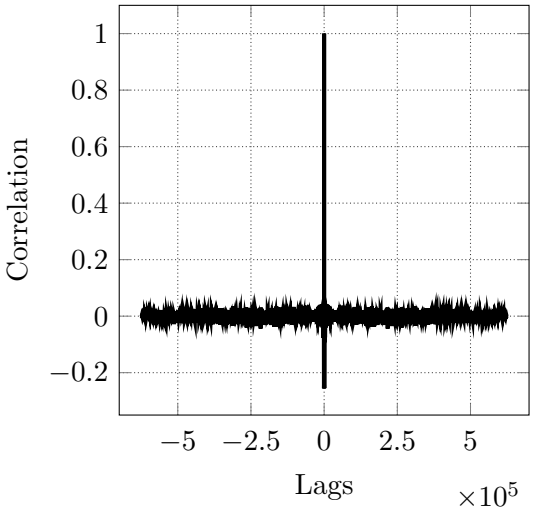

Figure 5.8: Autocorrelation of received pressure signal.

5.4 Model Description and Computational Grids

An input signal has been constructed that gives a PSD that is equal in power across a range of frequencies at a given observer radius from a broadband source. It was expected that installing the broadband source beneath a lifting wing would result in a change in the observed PSD at any given observer compared to the PSD of the broadband source in the free-field. By using an input signal that gives a PSD that is equal in power for a range of frequencies in the free-field, the change in the PSD due to the installation of the source beneath a lifting wing can easily be seen. In order to investigate the installation of this broadband source beneath

a lifting wing, the same model as described in Section 4.2 was used. The following cases, similar to those undertaken at discrete frequencies in Chapter 4, were chosen to investigate the effect of circulation on the propagation and scattering of the installed broadband source:

- NACA 0012, $M_\infty = 0.2$: $\alpha = 0°$, $1°$, $\ldots$, $8°$.
- NACA 0012, $\alpha = 5°$: $M_\infty = 0.1$, 0.2, 0.3.
- RA16SC1, $M_\infty = 0.2$, $\alpha = 0°$: flap and slat retracted, flap 20°, flap 40°, flap 40° plus slat.

All of these cases would be conducted over both uniform and non-uniform mean flows using the same modified input signal that was constructed in Section 5.3. The computational grids that were constructed for each airfoil configuration in Section 4.3 could be used again here for the broadband investigation. In each case, the version of the grid with source refinement for 500 Hz was used due to the maximum frequency in the constructed broadband signal. The same flow parameters were to be used in the broadband investigation as in the single frequency investigation, and thus the same uniform and non-uniform base flows as computed in Section 4.4 could be used again here.

5.5 The Effect of Circulation on Sound Pressure Level

Unlike some of the single frequency simulations in Chapter 4, initial broadband simulations using the RA16SC1 configuration with a slat over a non-uniform flow remained stable despite the shear layers in the base flow. Thus, all cases listed in Section 5.4 could be completed for the broadband simulations. For each airfoil configuration, the equivalent free-field simulation was undertaken in order to determine the scaling factor for each installation case. These were run for 6.4×10^{-2} s in order for the initial acoustic pulse to reach the domain boundaries. Pressure was then sampled for 2 s at a sample rate of 312.5 kHz. The received signal was used to compute p_{rms}, and this was in turn used to calculate a scaling factor that gave an overall p_{rms} of 2 Pa at the 90° observer.

Having obtained the required scaling factors, all of the planned installation cases were conducted. For each case, the simulation was run for 6.4×10^{-2} s, which allowed the initial acoustic pulse to reflect off of the airfoil surfaces and reach the

domain boundaries. Pressure was then sampled at each observer for a further 2 s at a rate of 312.5 kHz. A full list and further details of the simulations can be found in Table A.7 in Appendix A. The acquired pressure signal at each observer was then scaled for each configuration by the factor computed from the equivalent free-field case. Figure 5.9 shows the computed acoustic field after scaling at the end of one of the NACA 0012 airfoil simulations. Figure 5.10 shows the same for the RA16SC1 airfoil with flap 40° plus slat. It can be seen that the simulation has remained stable for both of these examples. Further examples are shown in Appendix D, including various Mach numbers for the NACA 0012 airfoil, and configurations for the RA16SC1 airfoil.

In the same manner as for the single frequency simulations in Chapter 4, the quantity $\mathrm{SPL}_{\text{non-uniform}} - \mathrm{SPL}_{\text{uniform}}$ was computed at each observer for each case using the obtained OASPL. It was seen in Chapter 4 that there are large lobes in the directivity plots for each case, due to constructive and destructive interference at a single frequency. Small changes in the position of these lobes led to large jumps in $\mathrm{SPL}_{\text{non-uniform}} - \mathrm{SPL}_{\text{uniform}}$, which led to examining results in a restricted observer range. These lobes are greatly reduced for a broadband source. Hence, results for

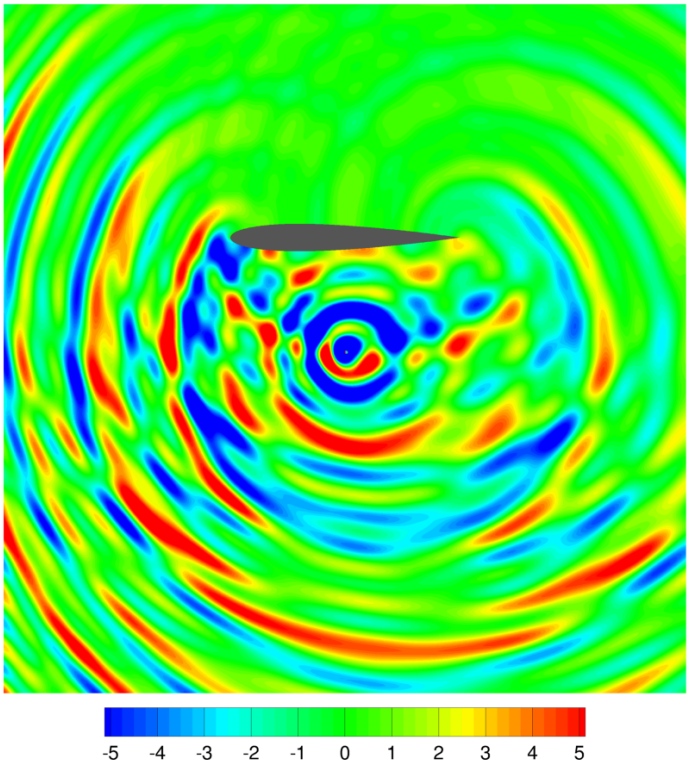

Figure 5.9: Acoustic pressure (Pa) for the scattering of a broadband monopole by a NACA 0012 airfoil in a non-uniform $M_\infty = 0.2$ flow at $\alpha = 5°$.

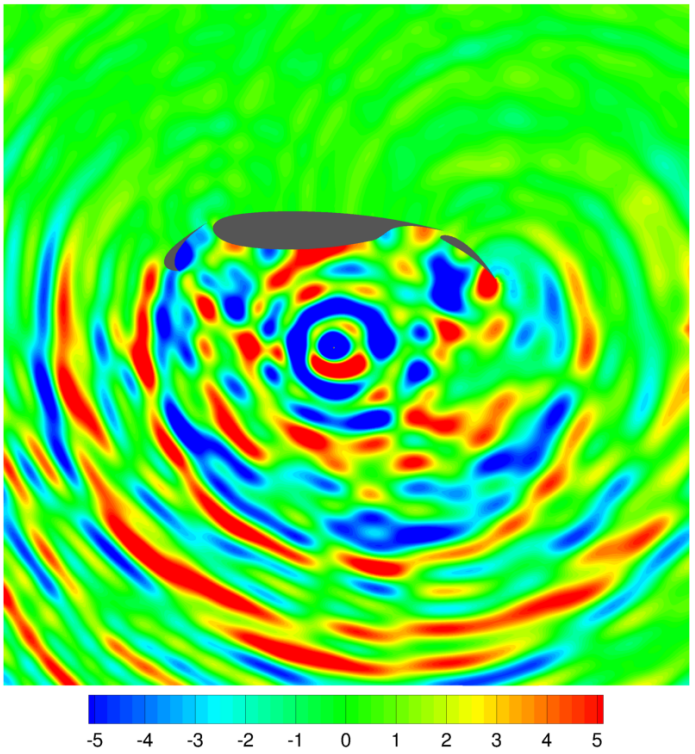

Figure 5.10: Acoustic pressure (Pa) for the scattering of a broadband monopole by an RA16SC1 airfoil with flap 40° plus slat in a non-uniform $M_\infty = 0.2$ flow at $\alpha = 0°$.

the broadband cases are presented here for observers in the range $0° \leq \theta \leq 180°$, which is the primary region of interest for landing gear noise.

5.5.1 Varying Angle of Attack and Mach Number

The effect of varying the angle of attack with a fixed Mach number of $M_\infty = 0.2$ is shown in Figure 5.11. Although the NACA 0012 airfoil is non-lifting at zero angle of attack, there is still an increase in flow velocity in the region near to the airfoil surface compared to the uniform flow, as shown in Figure 4.12. This leads to an increase in convective amplification compared to the uniform flow, leading to a positive value of $\text{SPL}_{\text{non-uniform}} - \text{SPL}_{\text{uniform}}$ in the $0° \leq \theta \leq 60°$ region, and a negative value of $\text{SPL}_{\text{non-uniform}} - \text{SPL}_{\text{uniform}}$ in the $120° \leq \theta \leq 180°$ region. As seen in Figure 4.12, as the angle of attack is increased and the circulation increases, the reduction in oncoming flow velocity increases. This leads to the general reduction of convective amplification, which can be seen by the reduction in magnitude of $\text{SPL}_{\text{non-uniform}} - \text{SPL}_{\text{uniform}}$ in the upstream and downstream regions. There is comparatively little difference between each angle of attack in the $60° < \theta < 120°$ region, which is where convective amplification effects are at their weakest.

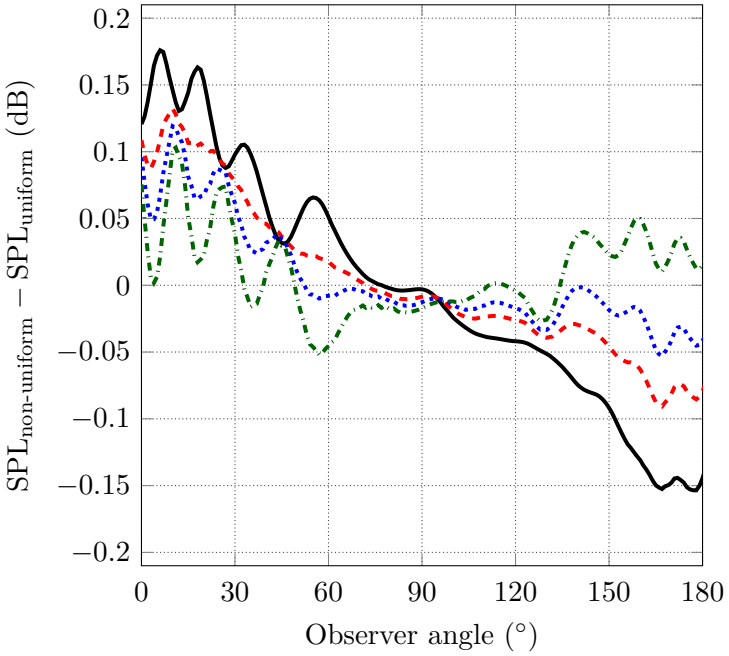

Figure 5.11: Difference in acoustic scattering (dB) between non-uniform and uniform base flows. Scattering of a broadband monopole by a NACA 0012 airfoil at $M_\infty = 0.2$ and varying α. $\alpha = 0°$ ——, $\alpha = 3°$ - - -, $\alpha = 5°$ ·····, $\alpha = 8°$ -·-·-.

The effect of varying the Mach number for a fixed angle of attack of $\alpha = 5°$ is shown in Figure 5.12. It can be seen that there is not a significant change in $\text{SPL}_{\text{non-uniform}} - \text{SPL}_{\text{uniform}}$ with increasing Mach number at the $50° < \theta \leq 180°$ observers. As the Mach number is increased the circulation increases, which reduces the flow velocity below the airfoil. However, this local velocity magnitude decrease is offset by the increase in the free-stream Mach number. Thus, the relative difference between the non-uniform and uniform base flows with increasing Mach number remains similar as the Mach number is increased. As the Mach number increases, the leading edge stagnation point influences the flow velocity to a larger extent in a progressively larger area. The influence of the stagnation point can be seen in the acoustic solution at the $0° \leq \theta \leq 50°$ observers. These are the observers at which waves reflected from the airfoil surface would be most influenced by the velocity reduction in the flow due to the stagnation point.

In can be seen from both Figure 5.11 and Figure 5.12 that the maximum computed value of $\text{SPL}_{\text{non-uniform}} - \text{SPL}_{\text{uniform}}$ for the range of values of α and M_∞ investigated here is approximately 0.2 dB. Similarly, the minimum computed value of $\text{SPL}_{\text{non-uniform}} - \text{SPL}_{\text{uniform}}$ is approximately -0.15 dB. Using (4.6.3), these differences in SPL correspond to a percentage increase in p_{rms} of 2.33 % and decrease of 1.71 % respectively. Following the discussion in Section 4.6 on the accuracy of

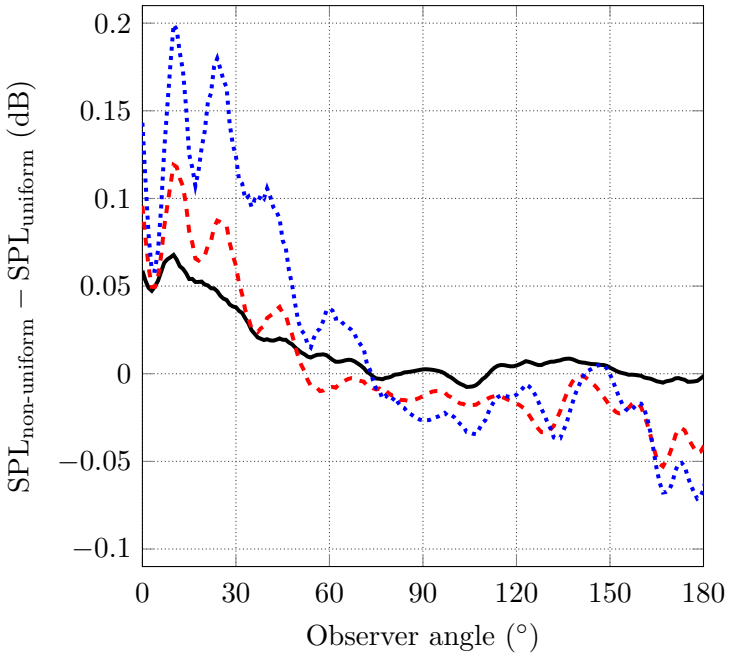

Figure 5.12: Difference in acoustic scattering (dB) between non-uniform and uniform base flows. Scattering of a broadband monopole by a NACA 0012 airfoil at $\alpha = 5°$ and varying M_∞. $M_\infty = 0.1$ ——, $M_\infty = 0.2$ - - -, $M_\infty = 0.3$ ·····.

the results observed for a single frequency, it can be seen that these values fall below the error bound of 3 %. Thus, for the range of α and M_∞ investigated here, the effect of circulation on the OASPL of a scattered broadband source can be considered insignificant. The significance of the results seen in this section are similar to those seen for varying the Mach number at a single frequency in Section 4.5.1. However, at a single frequency, varying the angle of attack showed results that were considered significant although small. This is due to the interference that occurs at single frequencies. This is discussed further in Section 5.7.

5.5.2 Varying Flap and Slat Configuration

Having investigated the effect of varying the angle of attack and the free-stream Mach number on the scattering of a broadband source, the effect of flap and slat deployment was investigated. The OASPL for the scattering of the source by each RA16SC1 configuration over a non-uniform flow at $M_\infty = 0.2$ and $\alpha = 0°$ is shown in Figure 5.13. The increase in OASPL between the monopole in the free-field and the flap and slat retracted configuration at the 90° observer is 1.82 dB. Using (4.6.3), this corresponds to a percentage increase in p_{rms} of 23.31 %. Compare this to the upstream convective amplification of the monopole in the free-field, which

gives an increase in OASPL of 1.51 dB at the 0° observer. This corresponds to a percentage increase in p_{rms} of 18.99 %. This highlights the significance of the installation effect.

It can be seen in Figure 5.13 from the increase in OASPL in the $75° \leq \theta \leq 120°$ region that increasing the flap angle from 20° to 40° reflects a greater proportion of the incident wave downwards towards these observers. There is a corresponding shielding effect in the $140° \leq \theta \leq 170°$ region caused by the flap deployment. Aside from the additional shielding effect above the leading edge of the airfoil, the addition of the slat to the flap 40° configuration slightly increases the OASPL in the $120° \leq \theta \leq 180°$ region. This can be attributed to reflections from the inner surface of the slat. Unlike the flap, the slat does not appear to significantly increase the OASPL in the $75° \leq \theta \leq 120°$ region.

For each flap and slat configuration, $\text{SPL}_{\text{non-uniform}} - \text{SPL}_{\text{uniform}}$ was computed, and the results are shown in Figure 5.14. The RA16SC1 airfoil with flap and slat retracted is asymmetric, and is lifting at $\alpha = 0°$. As seen in Figure 4.16, the front stagnation point is near to the leading edge for this angle of attack, and the flow velocity increases compared to the uniform flow over the bottom surface of the

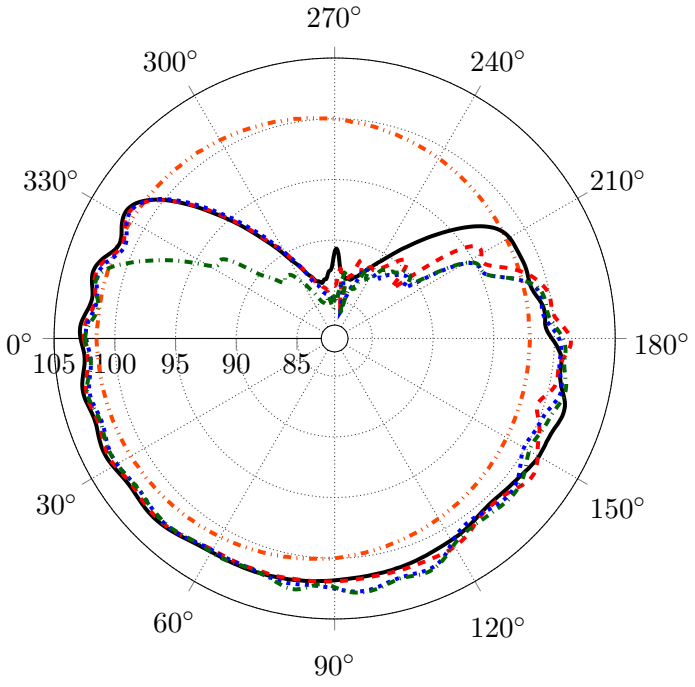

Figure 5.13: SPL (dB) for the scattering of a broadband monopole by an RA16SC1 geometry with varying configuration, $M_\infty = 0.2$, $\alpha = 0°$, non-uniform flow. Monopole, Flap retracted, Flap 20°, Flap 40°, Flap 40° plus slat.

airfoil upstream of the source. This leads to an increase in convective amplification and a positive $\mathrm{SPL}_{\text{non-uniform}} - \mathrm{SPL}_{\text{uniform}}$ in the $0° \leq \theta \leq 90°$ region. The flow velocity decreases compared to the uniform flow over the concave section of the lower surface near the trailing edge, also seen in Figure 4.16. This reduction in flow velocity leads to a reduction in convective amplification, and this reduction is large enough to make $\mathrm{SPL}_{\text{non-uniform}} - \mathrm{SPL}_{\text{uniform}}$ positive in the downstream $90° < \theta \leq 180°$ region. It should also be noted that $\mathrm{SPL}_{\text{non-uniform}} - \mathrm{SPL}_{\text{uniform}}$ for this RA16SC1 configuration is generally higher than that seen for the NACA 0012 airfoil in Figure 5.11. This is explained by the flow velocity variations over the bottom surface of the asymmetric RA16SC1 airfoil being larger in magnitude than for the NACA 0012 airfoil.

Extending the flap to 20° increases the circulation around the airfoil, leading to a reduction in oncoming flow velocity compared to the uniform flow. This reduces $\mathrm{SPL}_{\text{non-uniform}} - \mathrm{SPL}_{\text{uniform}}$ in the $0° \leq \theta \leq 120°$ region compared to the flap retracted case, as seen in Figure 5.14. Extension of the flap to 40° further reduces the oncoming flow velocity, to the extent that $\mathrm{SPL}_{\text{non-uniform}} - \mathrm{SPL}_{\text{uniform}}$ becomes negative in this region. Addition of the slat to the flap 40° configuration increases the flow velocity around the outer edge of the recirculation region. This leads to an increase in convective amplification in the $0° \leq \theta \leq 30°$ region for the flap

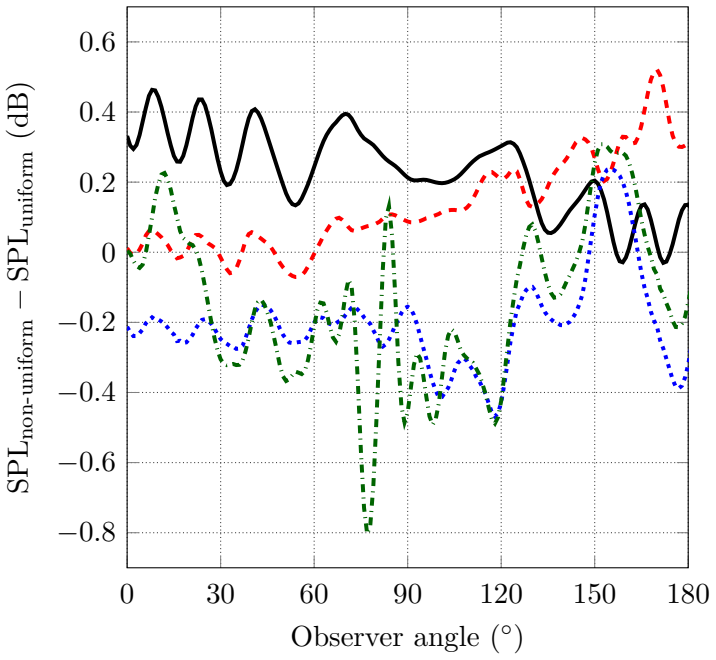

Figure 5.14: Difference in acoustic scattering (dB) between non-uniform and uniform base flows. Scattering of a broadband monopole by an RA16SC1 airfoil at $\alpha = 0°$, $M_\infty = 0.2$, and varying configuration. Flap retracted ——, Flap 20° - - -, Flap 40° ·····, Flap 40° plus slat -·-·-.

40° configuration with slat compared to without slat. The addition of the slat also leads to large differences in $\mathrm{SPL}_{\text{non-uniform}} - \mathrm{SPL}_{\text{uniform}}$ in the $75° \leq \theta \leq 90°$ region. This can be attributed to the incident wave and its reflections propagating through the recirculation region behind the slat.

In the $120° < \theta \leq 180°$ region, extending the flap to 20° reduces the oncoming flow velocity in that region compared to the flap retracted configuration. This reduces the convective amplification and increases $\mathrm{SPL}_{\text{non-uniform}} - \mathrm{SPL}_{\text{uniform}}$ in this downstream region compared to the flap retracted configuration. Extending the flap to 40° further reduces the oncoming flow velocity in this region. However, due to the high flap angle, the vertical velocity component has a larger magnitude than for the flap 20° case. Thus, despite the lower oncoming flow velocity in this region for the flap 40° case compared to the flap 20° case, the reduction in convective amplification is not as large. As a consequence, $\mathrm{SPL}_{\text{non-uniform}} - \mathrm{SPL}_{\text{uniform}}$ in this region for the flap 40° case is not as large as for the flap 20° case. The addition of the slat has only a minor impact on $\mathrm{SPL}_{\text{non-uniform}} - \mathrm{SPL}_{\text{uniform}}$ in this downstream region.

As discussed in Section 4.6, values of $\mathrm{SPL}_{\text{non-uniform}} - \mathrm{SPL}_{\text{uniform}}$ that give a percentage change in p_{rms} of less than 3 % are considered insignificant. This corresponds to a 0.257 dB increase or a 0.265 dB decrease in SPL. It can be seen in Figure 5.14 that the values of $\mathrm{SPL}_{\text{non-uniform}} - \mathrm{SPL}_{\text{uniform}}$ computed for the broadband source are generally less than these bounds, apart from at a selection of observer angles for certain configurations. Thus, despite the large differences between the non-uniform and uniform base flows, there are not large differences in the scattered acoustic fields over these flows using the broadband source. This is in contrast to some of the conclusions drawn for similar configurations using a single frequency source in Chapter 4. This is due to the reduced constructive and destructive interference seen for a broadband source in comparison with a single frequency source of the same strength. This is discussed further in Section 5.7.

5.6 Frequency Analysis of the Scattered Source

The motivation for developing the method described in Section 5.3 was to obtain a prescribed PSD for a broadband monopole in the free-field at a given observer radius. By choosing a PSD that was equal in power for all frequencies in the free-field, the effect of installing the broadband source beneath a lifting wing could easily be seen in the PSD of the signal recorded at the observers. The observers

are defined on a circle centred on the source, as described in Section 4.2. Hence, the PSD in the free-field is the same at each observer, subject to convective amplification by flow. Given the simulations listed in Section 5.4 that were conducted, the effect of varying the angle of attack, Mach number, and airfoil configuration on the PSD could be investigated. From this point on, Welch's method was applied to a signal of length $D = 6.25 \times 10^5$ samples for each case. This corresponds to a signal 2 s in length given the sample rate of 312.5 kHz. With the chosen segment length for Welch's method of $L = D/10$ with a 50 % overlap, this gave a frequency bin width of 4.8 Hz.

5.6.1 Single Element Airfoil

The PSD of the source scattered by the NACA 0012 airfoil in a non-uniform $M_\infty = 0.2$ flow with varying angle of attack was computed at the $\theta = 90°$ observer location, and this is shown in Figure 5.15. Peaks at certain frequencies corresponding to constructive interference can be seen. It can be seen that there is only a minor difference in the PSD at each angle of attack. A similar result for the PSD was observed at the 60° and 120° observer locations. Thus, it can be concluded that that the increase in circulation around this airfoil at this free-stream Mach number does not alter the flow enough to alter the frequency content of the scattered signal by a significant amount.

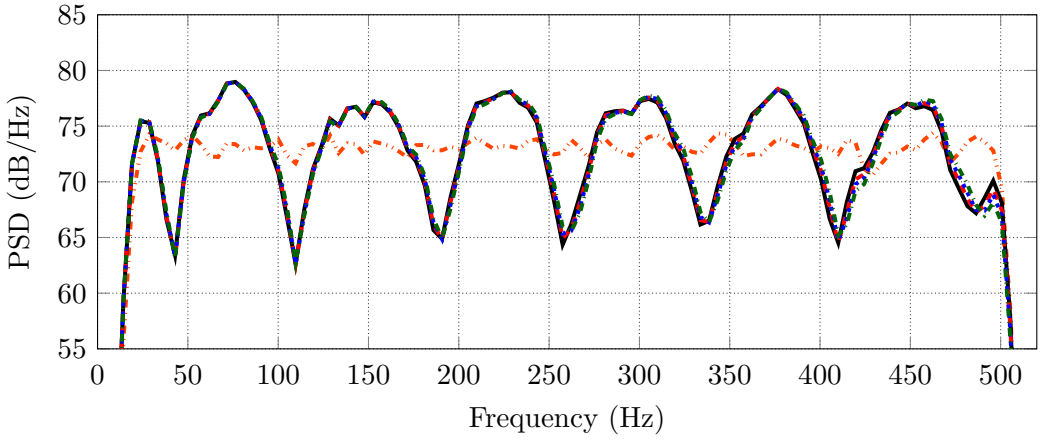

Figure 5.15: PSD (dB/Hz) at the $\theta = 90°$ observer for the scattering of a broadband monopole by a NACA 0012 airfoil with varying α, $M_\infty = 0.2$, non-uniform flow. Monopole, $\alpha = 0°$, $\alpha = 3°$, $\alpha = 5°$, $\alpha = 8°$.

The frequencies at the $\theta = 90°$ observer angle where peaks of constructive interference occur can be explained as follows. The NACA 0012 airfoil surface is approximately flat in the region directly above the source, and the angle that this surface creates with respect to the x-axis is relatively small. Thus, the mechanism behind the observed PSD is similar to that of a source near a flat wall. Incident waves from the source propagate towards the airfoil surface and are reflected by it. The incident waves that are normal to the surface are reflected and propagate back towards and through the source region. The distance of the source from the airfoil surface in the y-direction is denoted here by d. For a wave emitted by the source towards the surface, the distance that it must propagate before it reaches the source location again after reflection is $2d$. When $l\lambda \approx 2d$ for the integer multiple l, the peaks in the reflected wave coincide with peaks in the waves emitted from the source at a later time in the direction away from the airfoil. The in-phase superposition of these two waves that are propagating towards the 90° observer results in constructive interference.

Conversely, if the reflected wave is offset by half a wavelength compared to the emitted wave, the superposition of these two waves as they propagate towards the 90° observer results in destructive interference. This occurs when $(1/2 + l)\lambda \approx 2d$. The distance of the source from the NACA 0012 airfoil surface in the y-direction for the current investigation is $d = 2.235\,\text{m}$. Frequencies where constructive and destructive interference are expected to occur for this value of d are listed in Table 5.1. It can be seen that the maxima and minima of the PSD seen in Figure 5.15 approximately coincide with these frequencies. It is also seen in Figure 5.15 that the convective effect of the flow does not have a large effect on these predicted frequencies at this Mach number. This suggests that the shape of the airfoil surface, and the distance of the source from this surface, are the major contributors to the frequency content of the scattered sound field at this Mach number.

The effect of varying the Mach number on the PSD at the $\theta = 90°$ observer position for the source scattered by the NACA 0012 airfoil in a non-uniform flow with $\alpha = 5°$ was then computed. This is shown in Figure 5.16. The peaks of constructive interference are shifted slightly down in frequency with increasing Mach number, particularly at the more directional higher frequencies. This can be attributed to the convective effect of the mean flow on the acoustic field. This effects the propagation of waves between the source position and the airfoil surface, and effectively increases the propagation distance $2d$. Similar results for the PSD with varying Mach number were obtained at the 60° and 120° observer locations.

Table 5.1: The relationship at the $\theta = 90°$ observer between the acoustic wavelength λ and the distance d between the source and the airfoil surface in the y-direction. NACA 0012 airfoil, $d = 2.235\,\text{m}$.

(a) Constructive interference when $l\lambda \approx 2d$.

l	f (Hz)
1	76.1
2	152.2
3	228.3
4	304.4
5	380.5
6	456.6

(b) Destructive interference when $(1/2 + l)\lambda \approx 2d$.

l	f (Hz)
0	38.1
1	114.2
2	190.3
3	266.4
4	342.5
5	418.6
6	494.7

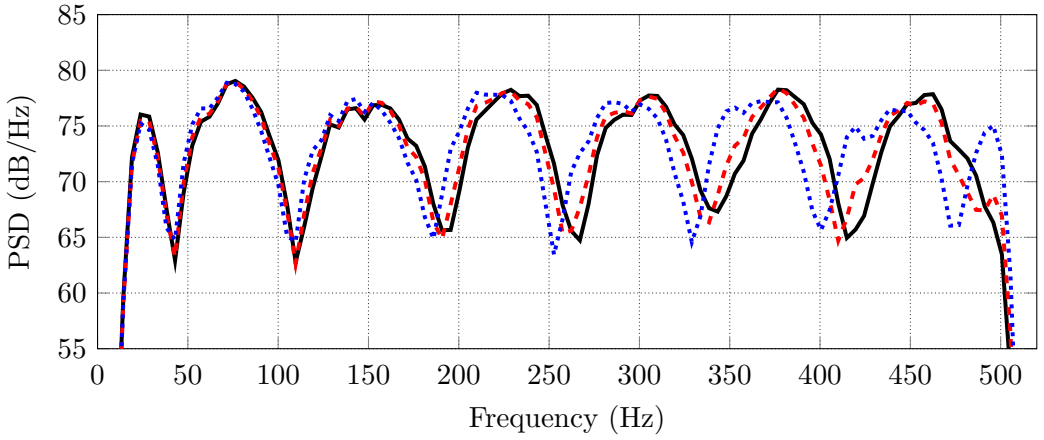

Figure 5.16: PSD (dB/Hz) at the $\theta = 90°$ observer for the scattering of a broadband monopole by a NACA 0012 airfoil with varying M_∞, $\alpha = 5°$, non-uniform flow. $M_\infty = 0.1$ ——, $M_\infty = 0.2$ - - - -, $M_\infty = 0.3$ ·····.

Having recorded pressure data at each observer in each simulation, a PSD contour plot for any given case over a given observer range could be constructed. For the plot, the PSD at each observer was obtained using Welch's method with the parameters described at the start of Section 5.6. This resulted in the PSD at each observer angle having a frequency bin width of 4.8 Hz, and so the resulting PSD was linearly interpolated to 1 Hz intervals for plotting. The PSD contour for the NACA 0012 airfoil in a non-uniform $M_\infty = 0.2$ flow at $\alpha = 5°$ was computed over the $0° \leq \theta \leq 180°$ observer range, and this is shown in Figure 5.17. The symmetry of the constructive interference pattern for this airfoil, with its approximately flat surface, supports the suggestion that it is the shape of the airfoil that is the major

contributor to the frequency content of the scattered sound field at this Mach number. The effect of convective amplification can be seen, with levels being generally higher in the $0° \leq \theta \leq 90°$ region and lower in the $90° < \theta \leq 180°$ region.

5.6.2 Multi-Element High-Lift Airfoil

Having investigated the effect of angle of attack and Mach number on the frequency content of the broadband source scattered by a NACA 0012 airfoil, the next step was to investigate the effect of flap and slat deployment using the RA16SC1 airfoil. The PSD at the 90° observer for the RA16SC1 airfoil in a non-uniform $M_\infty = 0.2$ flow at $\alpha = 0°$ with varying configuration is shown in Figure 5.18. For the RA16SC1 airfoil, the distance between the source and the airfoil surface in the y-direction is $d = 2.098\,\text{m}$. For the flap and slat retracted geometry, the peaks due to constructive interference again occur at frequencies where $l\lambda \approx 2d$.

It can be seen that changing the configuration of the airfoil has a larger influence on the PSD in comparison to increasing the angle of attack of the NACA 0012

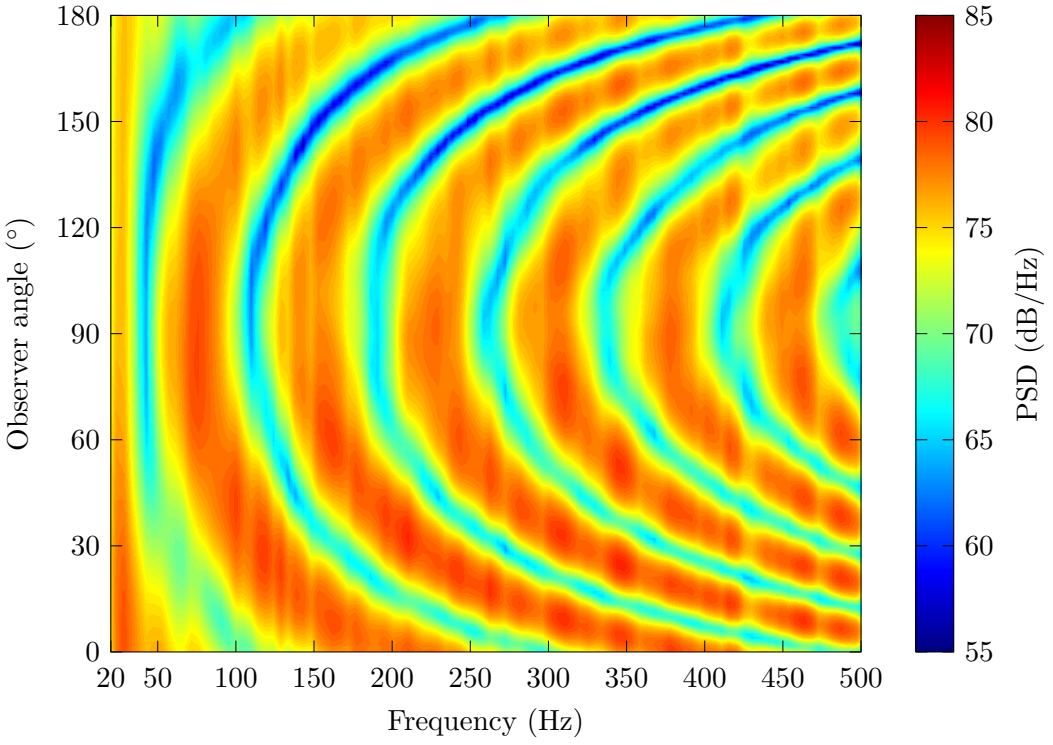

Figure 5.17: PSD contour (dB/Hz) of the scattered signal over a non-uniform flow at observer angles $0° \leq \theta \leq 180°$, NACA 0012 airfoil, $M_\infty = 0.2$, $\alpha = 5°$.

airfoil, which was seen in Figure 5.15. However, it is unclear from Figure 5.18 if the observed changes are primarily due to the change in reflective underside of the airfoil, or due to the reduction in flow velocity beneath the high-lift configurations. It was shown in Figure 4.16 that the reduction in flow velocity beneath the flap 40° configuration compared to the free-stream was substantial, with a reduction in Mach number magnitude of 0.07 at the source location compared to the free-stream magnitude of 0.2. This comparatively large reduction in flow velocity might lead to a similar effect as was seen for varying the Mach number for NACA 0012 airfoil in Figure 5.16.

In order to investigate this further, a PSD contour was computed for each airfoil configuration in a non-uniform $M_\infty = 0.2$ flow at $\alpha = 0°$. These are seen for the flap 20° configuration in Figure 5.19, the flap 40° configuration in Figure 5.20, and the flap 40° plus slat configuration in Figure 5.21. The contour obtained for the flap and slat retracted configuration was similar to the symmetric one shown in Figure 5.17 for the NACA 0012 airfoil, and so has been omitted here. It can immediately be seen for the flap 20° configuration that the otherwise symmetric peaks of constructive interference are disturbed in the $\theta \approx 120°$ and $\theta \approx 165°$ regions. This can be attributed to additional reflections of the incident wave from the inside of the flap cove, and reflections from the lower flap surface respectively. It can be seen that increasing the flap angle to 40° adds additional disturbances to the constructive interference peaks in the upstream direction. This can be attributed to the flap at the higher angle reflecting a larger proportion of the incident wave towards these observers. Finally, the addition of the slat further

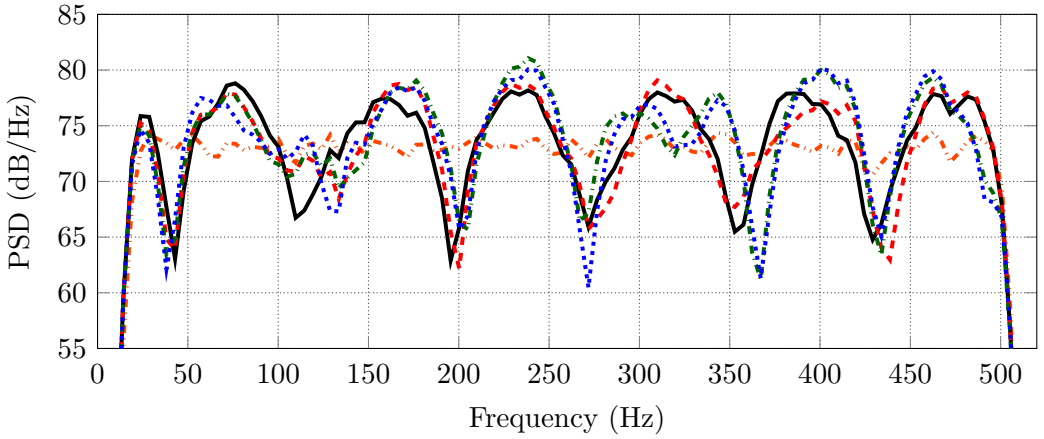

Figure 5.18: PSD (dB/Hz) at the $\theta = 90°$ observer for the scattering of a broadband monopole by an RA16SC1 airfoil with varying configuration, $\alpha = 0°$, $M_\infty = 0.2$, non-uniform flow. Monopole, Flap retracted, Flap 20°, Flap 40°, Flap 40° plus slat.

disturbs the peaks in the contour, especially in the $100° \leq \theta \leq 180°$ region. This can be attributed to a higher proportion of the incident wave being reflected back towards these observers from the inside of the slat. The results seen in these contour plots suggest that it is the shape of the reflective underside of the airfoil surface, combined with the distance of the source from this surface, that primarily determines the frequency content of the scattered field at this Mach number.

5.7 Comparison to the Scattering of a Single Frequency Source

Simulations of a broadband monopole installed beneath a lifting wing have been conducted in this chapter for various airfoil configurations and flow parameters. A broadband input signal was constructed that gave a PSD with equal power across a range of frequencies at a given observer radius from a monopole in the free-field. The investigations in Section 5.5 were undertaken using this input signal to determine the effect of non-uniform flow due to circulation on the scattering

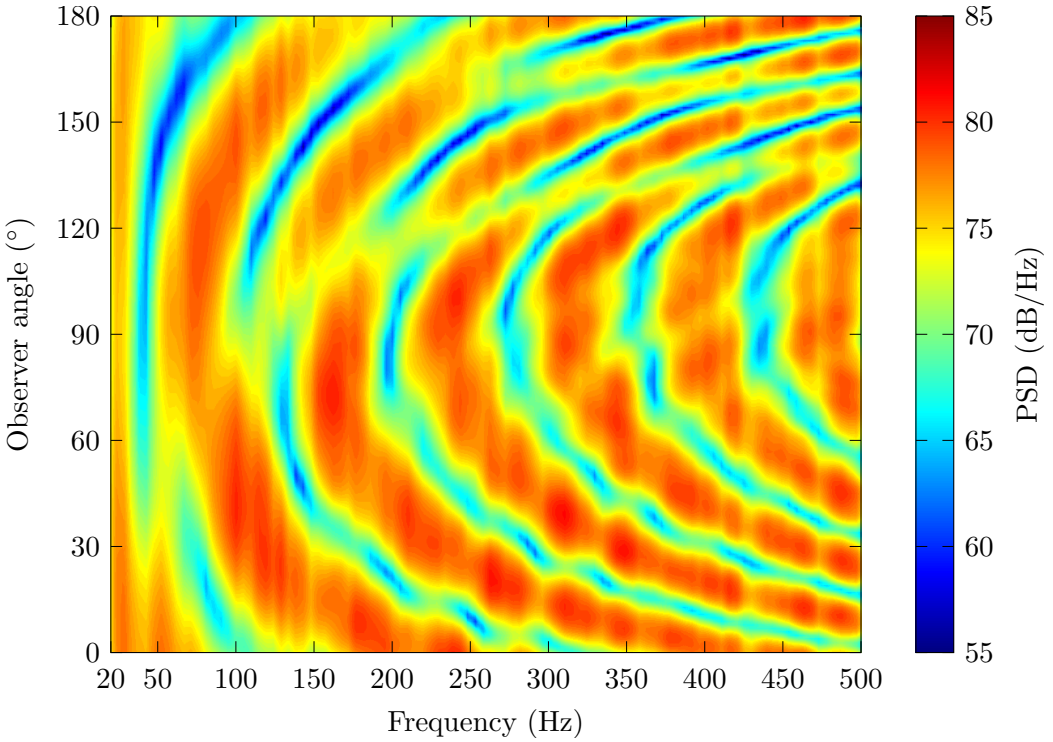

Figure 5.19: PSD contour (dB/Hz) of the scattered signal over a non-uniform flow at observer angles $0° \leq \theta \leq 180°$, RA16SC1 airfoil with flap 20°, $M_\infty = 0.2$, $\alpha = 0°$.

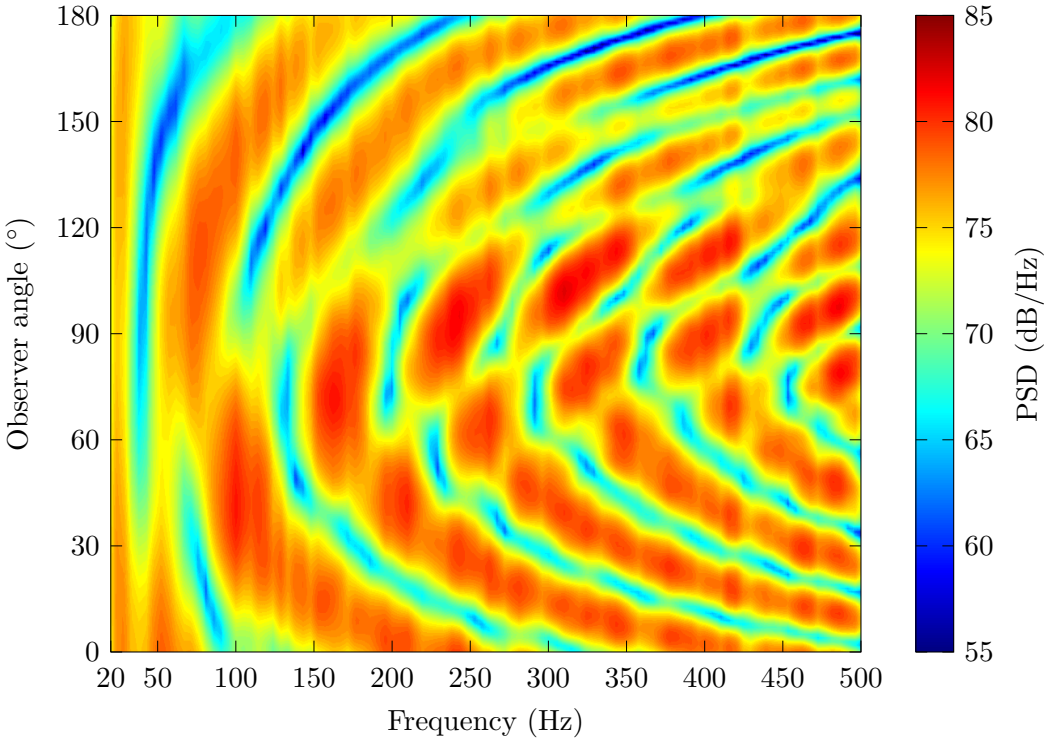

Figure 5.20: PSD contour (dB/Hz) of the scattered signal over a non-uniform flow at observer angles $0° \leq \theta \leq 180°$, RA16SC1 airfoil with flap 40°, $M_\infty = 0.2$, $\alpha = 0°$.

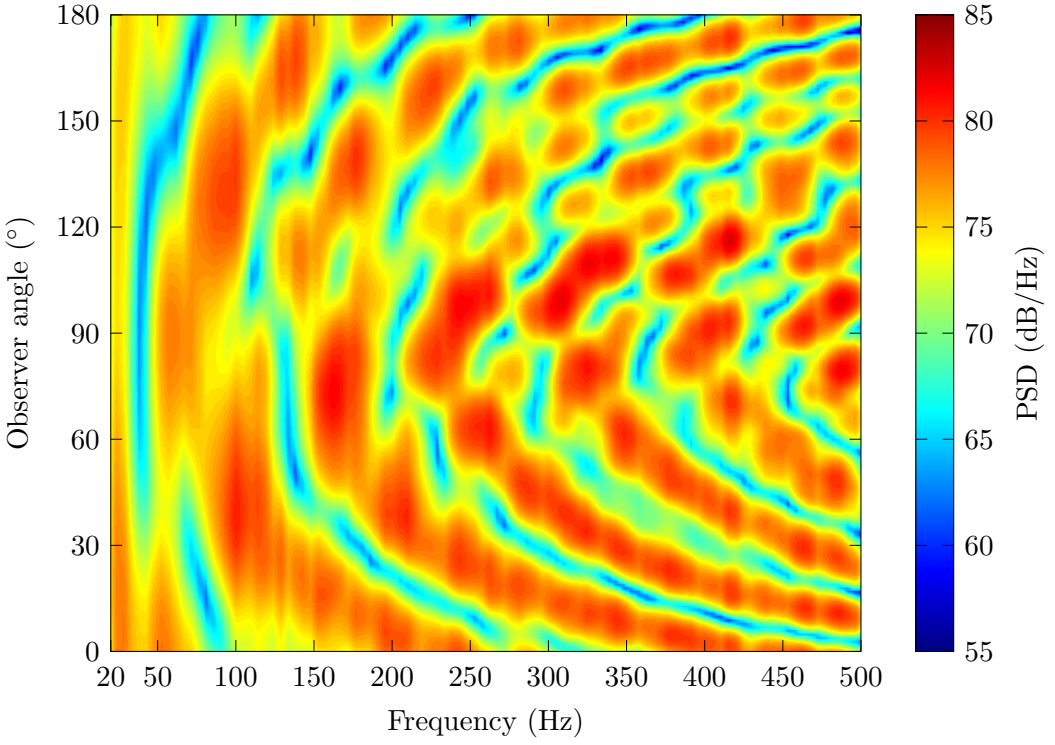

Figure 5.21: PSD contour (dB/Hz) of the scattered signal over a non-uniform flow at observer angles $0° \leq \theta \leq 180°$, RA16SC1 airfoil with flap 40° plus slat, $M_\infty = 0.2$, $\alpha = 0°$.

of a broadband source. The source in each case was set to a strength that gave an OASPL of 100 dB in the free-field. The effect of the non-uniform flow was quantified as the difference in acoustic scattering over non-uniform and uniform base flows, computed using $\mathrm{SPL}_{\text{non-uniform}} - \mathrm{SPL}_{\text{uniform}}$. It was shown in Section 5.5.1 that systematically increasing the angle of attack and Mach number in order to increase the circulation did not result in significant values of $\mathrm{SPL}_{\text{non-uniform}} - \mathrm{SPL}_{\text{uniform}}$ for the broadband source.

This was in contrast to results obtained by varying the angle of attack using a single frequency source in Section 4.5.1. These single frequency simulations used a source strength for each case that gave an OASPL of 100 dB in the free-field, which was the same as for the broadband sources in this chapter. Due to interference that occurs at a single frequency, the results of the single frequency investigations were evaluated across a limited observer range of $60^\circ \leq \theta \leq 120^\circ$. It was shown that varying the angle of attack had a small but significant effect on the computed values of $\mathrm{SPL}_{\text{non-uniform}} - \mathrm{SPL}_{\text{uniform}}$ at these observers. It was shown that there was either a decreasing or an increasing trend in these values, depending on whether a directional lobe or a local minimum existed in that observer range due to constructive or destructive interference respectively. Varying the Mach number resulted in values of $\mathrm{SPL}_{\text{non-uniform}} - \mathrm{SPL}_{\text{uniform}}$ that were considered insignificant.

Similarly, the results of the broadband investigations conducted using an airfoil with varying flap configuration in Section 5.5.2 showed values of $\mathrm{SPL}_{\text{non-uniform}} - \mathrm{SPL}_{\text{uniform}}$ that were not considered significant. However, the single frequency investigations with varying flap configuration in Section 4.5.2 showed values of $\mathrm{SPL}_{\text{non-uniform}} - \mathrm{SPL}_{\text{uniform}}$ that were considered significant. Unlike varying the angle of attack at a single frequency, varying the flap configuration at a single frequency did not show any clear trends. This was due to small differences in the locations of directional lobes due to the difference in base flows. This lack of clear trends was a motivating factor behind extending the investigation using a broadband source. It can be summarised from these comparisons that the use of a single frequency source with the same acoustic power as a broadband source can lead to the exaggeration of the effect of non-uniform flow due to circulation. This is due to interference effects that exist at a single frequency.

The range of frequencies chosen for the broadband input signal used in this chapter included the frequencies that were used for the single frequency simulations in Chapter 4. Thus, the results for a given frequency could be extracted from the broadband results and compared against the equivalent single frequency results.

This would show how closely the single frequency simulations capture the results obtained for a given frequency from a broadband source. This has particular relevance in the current work to the BEM methods used, which are formulated in the frequency domain and generally showed good agreement with equivalent LEE solutions in Section 4.10.

For this comparison, a directivity plot over all 360 observers was created for a selection of cases at a frequency of 250 Hz. This frequency was chosen as there are a greater number of directional lobes at 250 Hz than at 125 Hz, and because the computed PSD for the scattered broadband source at 500 Hz was slightly lower than it should be. The latter is due to Welch's method averaging over neighbouring frequencies, and there being no frequency content in the signal above 500 Hz. Four airfoil cases were chosen for the comparison. These were the NACA 0012 airfoil in a non-uniform $M_\infty = 0.2$ flow at $\alpha = 5°$, and the RA16SC1 airfoil in a non-uniform $M_\infty = 0.2$ at $\alpha = 0°$ with flap and slat retracted, flap 20°, and flap 40° configurations.

In order to extract the directivity at a single frequency from the broadband results, a similar method to that used to create the PSD contour plots in Section 5.6 was used. The PSD was computed at each observer using Welch's method, and this result was then linearly interpolated to 1 Hz intervals. The value for 250 Hz at each observer was then used to create the directivity plot. The scaling factor for each broadband simulation was computed such that an OASPL of 100 dB at the 90° observer in the equivalent free-field simulation was obtained. It was shown in Section 5.3 that with an OASPL of 100 dB, the power in any given frequency is 73.19 dB/Hz for this particular input signal. In order to enable comparison with the single frequency results, the scaling factors for the single frequency simulations used in Chapter 4 were recomputed. This was done such that the result of each equivalent free-field simulation gave 73.19 dB at the 90° observer, instead of the value of 100 dB used in Chapter 4.

The directivity plots for these four cases are shown in Figure 5.22. It can be seen for each case that the two solutions are generally in good agreement, with some differences at certain observer angles where the extent of destructive interference is underpredicted in the broadband cases. This shows that the single frequency simulations, whether LEE or BEM, are capable of accurately capturing a given frequency from a broadband case. It also shows that the method developed in Section 5.3 has been implemented successfully and can deliver accurate results.

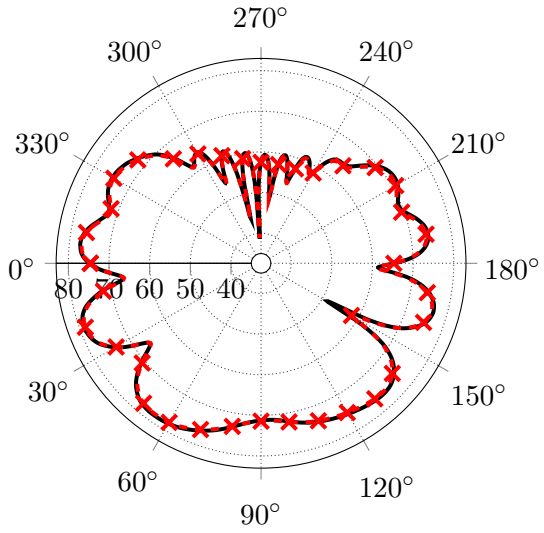

(a) NACA 0012, $M_\infty = 0.2$, $\alpha = 5°$.

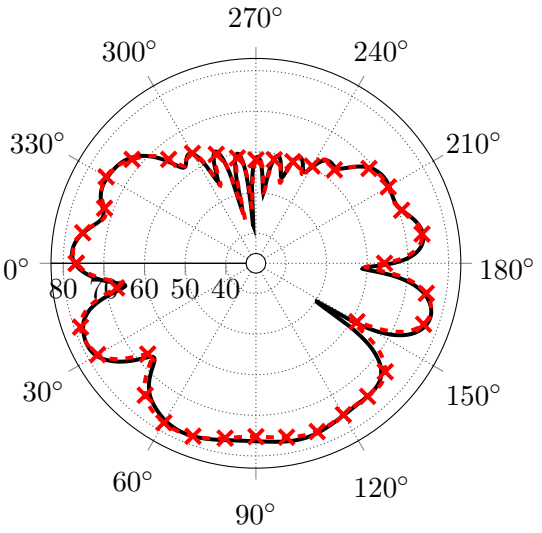

(b) RA16SC1, $M_\infty = 0.2$, $\alpha = 0°$.

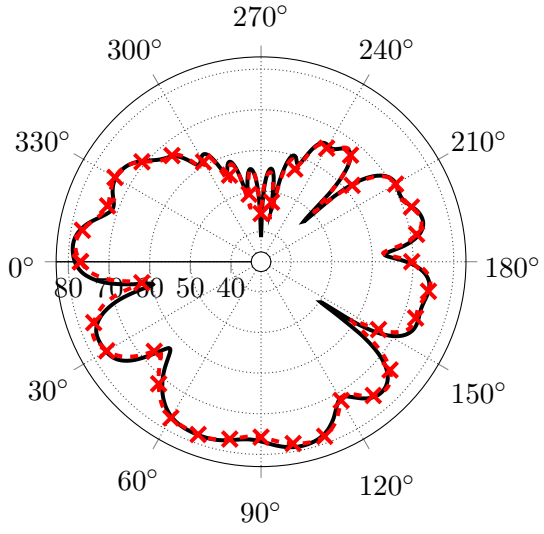

(c) RA16SC1 with flap 20°, $M_\infty = 0.2$, $\alpha = 0°$.

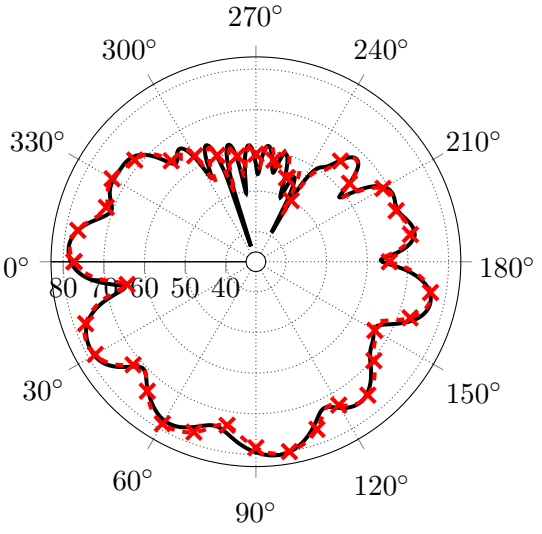

(d) RA16SC1 with flap 40°, $M_\infty = 0.2$, $\alpha = 0°$.

Figure 5.22: Comparison of the SPL (dB) obtained from the broadband and single frequency simulations at 250Hz. Single frequency ——, extracted from broadband - -×- -.

It has been shown in this section that simulations using a single frequency source are capable of representing a given frequency from an equivalent broadband source. The OASPL for a broadband source can thus be estimated by the incoherent summation of a set of single frequency results. It has also been shown in this chapter that the effect of non-uniform flow due to circulation on the acoustic scattering of an idealised broadband landing gear noise source is negligible at Mach numbers representative of an airliner on approach. Together, these conclusions imply that the OASPL for a broadband landing gear source installed beneath a lifting wing may be estimated at these Mach numbers through single frequency BEM simulations using the uniform flow approximation. The greater the number of frequencies used in the incoherent summation, the larger the reduction in interference in the OASPL estimate. However, it may be computationally prohibitive to run simulations for every required frequency. One alternative is to integrate the PSD of the broadband source over one-third or full octave bands to give a source of equivalent power at each band centre frequency. This will reduce the interference in the OASPL estimate, while minimising the number of simulations used. This is the approach that is taken in Chapter 6.

5.8 Summary

The effect of installing a broadband monopole source beneath a lifting wing has been investigated in this chapter. The source was implemented in the numerical LEE solver by replacing the relevant time-harmonic term in the governing monopole source equation that was used in Chapter 4 with a time-dependent pressure signal. A random signal was created from prescribed PSD and PDF functions using an existing method from the literature. This signal was equal in power for all frequencies. However, when a simulation of the source in the free-field was undertaken using this signal, it was seen that the PSD of a signal received at a distance from the source was different from that of the input signal. The reason for this was explained, and a method proposed to construct a modified input signal that reconstructs the desired PSD at a given observer radius. The method was used to construct a modified input signal that gave a PSD that was equal in power for all frequencies at the observer radius that was used throughout Chapter 4.

This modified input signal was then used to investigate the effect of installing the broadband source beneath an airfoil. The effect of non-uniform flow due to circulation around the lifting wing was investigated in a similar manner to

Chapter 4. The circulation around a NACA 0012 airfoil was varied by varying the angle of attack and Mach number, and around an RA16SC1 airfoil by varying the configuration of flap and slat. The OASPL was to compute the value of $\mathrm{SPL}_{\text{non-uniform}} - \mathrm{SPL}_{\text{uniform}}$ at each observer. It was seen for the broadband cases that the difference in SPL between the non-uniform and uniform base flows was relatively small. The values seen were smaller than those seen in Chapter 4, due to the reduction of constructive and destructive interference in the OASPL for the broadband source. Evaluating the obtained values using the error bound of a 3 % change in p_{rms} discussed in Chapter 4, it was seen that the differences observed were so small that they could be considered insignificant.

An investigation into the frequency content of the scattered source was then conducted. It was shown using a single-element airfoil that the major contributor to the obtained PSD at a given observer angle was the shape of the airfoil surface, and the distance of the source from this surface. Varying the angle of attack with a fixed Mach number did not alter the obtained PSD by a significant amount. Varying the Mach number with a fixed angle of attack did slightly alter the PSD at the highest Mach number that was investigated. This was attributed to the increased convective effect of the mean flow on the acoustic field, which effectively increases the distance between the source and the airfoil surface, and thus changes the frequencies where interference occurs. It was shown through the construction of PSD contour plots that the deployment of flap and slat had the largest effect on the observed PSD. This was due to the additional reflective surfaces creating complex patterns of interference at certain frequencies.

Finally, a comparison was given between the broadband results shown in this chapter and the single frequency results from Chapter 4. In all single frequency and broadband cases a source strength that gave 100 dB in the free-field was used. It was shown that although values of $\mathrm{SPL}_{\text{non-uniform}} - \mathrm{SPL}_{\text{uniform}}$ were generally considered insignificant for the broadband cases undertaken in this chapter, there were some equivalent single frequency cases where the computed values of $\mathrm{SPL}_{\text{non-uniform}} - \mathrm{SPL}_{\text{uniform}}$ were considered significant. These differences were attributed to interference effects at a single frequency, which exaggerate the effect of non-uniform flow due to circulation on the computed SPL. Results for a single frequency of 250 Hz were extracted from a selection of the broadband results and used to construct directivity plots, which showed good agreement with equivalent single frequency directivity results. This showed that the simulations at a single frequency, whether LEE or BEM, could accurately capture a given frequency of a broadband case.

In this chapter, it has been shown that single frequency simulations can accurately represent a single frequency from an equivalent broadband simulation. It was also shown that the effect on the acoustic scattering of non-uniform flow due to circulation is negligible for broadband landing gear sources at Mach numbers representative of an airliner on approach. Thus, it was concluded that the OASPL for a broadband landing gear source installed beneath a lifting wing could be estimated through the incoherent summation of results from single frequency BEM simulations using the uniform flow approximation. It was discussed that it might be computationally prohibitive to run a single frequency simulation for every required frequency. An alternative method is to integrate the required PSD over one-third or full octave bands to give an equivalent source at each band centre frequency. This would reduce the observed interference in the OASPL estimate, while also minimising the required number of simulations.

Chapter 6

The Scattering of Single Frequency Sources by an Aircraft

6.1 Introduction

Having investigated the acoustic scattering of sources installed beneath an isolated airfoil, this chapter focuses on the scattering of sources by a full aircraft geometry. The 3-D FMM accelerated BEM solver *ACTIPOLE* is used to compute the acoustic scattering using a flow approximation method. This BEM solver is capable of computing the scattering of sources by a large and complex 3-D geometry in a relatively short time compared to the LEE solver. Computational resources available at the University of Southampton restrict the use of the LEE solver in 3-D to a constant cross-section airfoil of limited span for this type of scattering problem. The conclusions reached in the preceding chapters determined the modelling decisions made in this chapter. A method to couple a realistic landing gear source model with the acoustic solver is presented. Sources generated using this method are used to compute the SPL obtained on a ground plane by installing the sources beneath the aircraft geometry. The effect of flap deployment on the SPL computed on the ground is investigated.

Section 6.2 describes the model used for the investigations in this chapter. The creation of the aircraft geometry and associated computational surface meshes is presented in Section 6.3. The coupling method for the landing gear source model and the acoustic solver is presented in Section 6.4. An investigation into the estimated SPL on a ground plane and the effect of flap deployment is presented in Section 6.5. The effect of alternative source positions on the estimated SPL

on the ground plane is investigated in Section 6.6. Finally, a summary for the investigation of the scattering of single frequency sources by a full aircraft is given in Section 6.7.

6.2 Model Description

Simple sources have been used in all investigations up to this point to represent an idealised landing gear noise source, and so they were also chosen for use here. Thus, any conclusions reached from the previous investigations would also apply to this investigation. It will be explained in Section 6.4 that the coupling procedure between a realistic landing gear source model and the acoustic solver makes use of the omni-directionality of the monopole sources. An Airbus A320-style aircraft was chosen as the scattering geometry for this investigation. A computational mesh for this commercial aircraft was constructed that allowed the resolution of acoustic waves up to 1000 Hz using the available computational resources. This frequency limit would be lower if a larger aircraft were chosen. The A320 has a two-wheel main landing gear (MLG) beneath each wing, along with a smaller two-wheel nose landing gear (NLG). The position of the idealised source could be more readily determined with the two-wheel MLG than if the aircraft had four-wheel or six-wheel MLG.

The SPL from the scattered sources was computed on a 0.25 km^2 ground plane, centred on the fuselage centreline at the approximate streamwise position of the MLG. The aircraft altitude was chosen to be 120 m, which corresponds to the approach reference point seen in Figure 1.1. The ground plane was fixed with respect to the aircraft and idealised landing gear sources, and so Doppler effects were not accounted for. The size and location of the ground plane relative to the runway at the approach reference point can be seen in Figure 6.1. A Mach number of $M_\infty = 0.2$ and angle of attack of $\alpha = 0^\circ$ were chosen for the investigation. These values are representative of the approach conditions for a commercial airliner in a high-lift configuration. The free-stream Mach vector was aligned with the runway and parallel to the ground. Two configurations of the aircraft were chosen for the investigation: flaps retracted and flaps deployed. These configurations were investigated at the same angle of attack and Mach number. Although physically unrealistic for the flap retracted configuration, the use of the same flow parameters allowed the effect of the change in scattering geometry to be investigated.

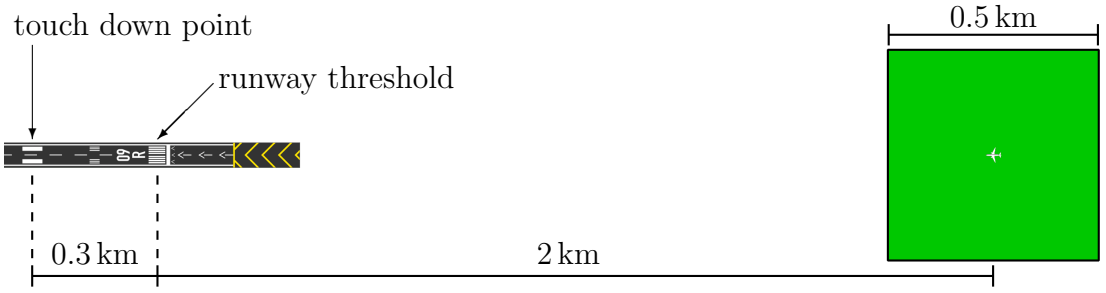

Figure 6.1: The size and location of the ground plane in relation to the runway at the approach reference point. Drawn to scale.

The uniform flow approximation, which was already implemented as an option in *ACTIPOLE*, was chosen as the most appropriate for this investigation. The acoustic pressure in the non-uniform flow approximation is computed at each observer by modifying the scattered acoustic potential using the flow velocity and flow potential at that point, as seen in Equation (3.3.31). There are two consequences of this. Firstly, due to the neglecting of $O(M_\infty^2)$ terms in the derivation of the approximation, the error in the solution at a given observer increases as the local Mach number increases. It was shown in Section 4.10 that when the local Mach number at the observer locations is $M_0 \approx 0.1$, the uniform and non-uniform flow approximations show a similar error. As the local Mach number increases beyond this value, the error in the non-uniform flow approximation becomes larger at a faster rate than for the uniform flow approximation.

It was shown in Section 4.10 that for the case of observers located in the near-field below an airfoil with a deployed flap at $M_\infty = 0.2$, the non-uniform flow approximation was more accurate than the uniform flow approximation. There is a large reduction in flow velocity in this region compared to the free-stream as a consequence of the large increase in circulation due to the deployment of the flap. However, outside of this region the local flow velocity will generally be closer to the free-stream velocity. The results presented in Section 4.10 suggest that the uniform flow approximation would be more accurate than the non-uniform flow approximation for observers located outside of this region.

The second consequence of Equation (3.3.31) is that refraction effects are not accounted for by the non-uniform flow approximation. The scattered acoustic potential is computed with standard BEM techniques that use Green's functions. The acoustic pressure at a point is then computed by modifying the scattered acoustic potential at that point, using the flow potential and its derivative at that point. At a large enough distance from the scattering body, the flow will return to

a uniform free-stream. Thus, the only effect of the approximation on the acoustic propagation in the far-field is that of the free-stream, and there is no refraction due to the streamlines of the potential flow bending around the scattering body in the near-field. This was also noted by Taylor [71]. As discussed in Section 2.5, this is the reason that the BEM flow formulations were evaluated in the near-field in Chapter 4. For the current investigation, given the distance of the ground plane from the scattering geometry, it is the case that the observers are in the far-field. Thus, there would be no benefit to using the non-uniform flow approximation over the uniform flow approximation for this investigation.

6.3 Geometry and Computational Meshes

The aircraft geometry was both created and meshed using *Larosterna Sumo* [114], a free software distributed under a GNU General Public License. *Larosterna Sumo* is a surface modeller and automatic unstructured surface mesh generation software specialised towards aircraft configurations. Fuselage, wing box, nacelle, and pylon surfaces are modelled by specifying the cross-section at a number of locations. Reference images may be loaded and used to specify control nodes that define the shape of each of these cross-sections. Wing surfaces are modelled by specifying a suitable NACA airfoil cross-section at a number of locations. The airfoil tips can be automatically closed by the software. Surface triangulations can be generated by the software using the created surface model. The mesh is automatically refined around the leading and trailing edges of wing surfaces, and at intersections between components. The level of refinement both in these regions and globally can be specified by the user. The software was developed to generate meshes that could be used with potential flow solvers, or further used to generate unstructured volume meshes. However, the surface meshes generated by the software are ideal for use with *ACTIPOLE*. The global refinement parameters can be set so as to discretise the surface with elements of a size suited to resolve acoustic waves of a given frequency.

A suitable set of reference images were found from which to create the A320-style geometry. These can be seen in Figure B.1 in Appendix B. Firstly, the fuselage and wing box were created by defining control nodes over the reference images. The creation of the fuselage surface is shown in Figure B.2 in Appendix B. The wing and horizontal and vertical stabilisers were then created using the reference images as a guide. The wing was approximated using a NACA 2315 airfoil cross-section with size and rotation specified at the root, point of change in taper, and

tip. The horizontal stabiliser was also approximated using a NACA 2315 airfoil, specified at the root and tip. The vertical stabiliser was approximated using a symmetric NACA 0012 airfoil, specified at the root, point of change in taper, and tip. A pylon and nacelle were created on one side of the aircraft, which were then mirrored for the other side. Finally, the complete geometry was scaled preserving the aspect ratio so that it had a length of 37.59 m and a wingspan of 36.03 m. These values are close to the actual dimensions of an A320 [115]. For the flaps deployed geometry, the additional flap surfaces were approximated using NACA 4308 airfoil cross-sections placed in appropriate locations.

Various views of the A320-style geometry in both configurations are shown in Figure 6.2. The origin of the coordinate system was located at the nose of the aircraft. With the geometry created, the locations of the idealised source locations relative to the scattering geometry were chosen. These were chosen to be in the approximate locations of the axles for each landing gear. These positions were $(5, 0, -3.5)$ for the NLG, $(18, 3.7, -3.5)$ for the starboard MLG, and $(18, -3.7, -3.5)$ for the port MLG. These values are close to actual distances given for the landing gear locations [115]. The source locations are also shown in Figure 6.2.

Having created the aircraft geometry, the computational surface meshes were then generated. It was decided to create two meshes for each configuration; one that would resolve acoustic frequencies up to 500 Hz, and one up to 1000 Hz. This would minimise the computation time for the lower frequencies. The global refinement was set to give a maximum boundary element size of $\lambda/10$ for the maximum intended frequency of each mesh [66]. The refinement for the leading edges of wing surfaces, and tightly curved surfaces of the pylons and nacelles, was set so as to accurately capture these geometric details. The wing trailing edge refinement was reduced as it was not required in these generally flat areas, which minimised the total number of generated boundary elements.

Details of the generated meshes for each configuration can be found in Table B.4 in Appendix B. The maximum boundary element size generated was $\lambda/8.5$ for the 500 Hz mesh, and $\lambda/7.5$ for the 1000 Hz mesh. Elements of this size were only located in the wing tips, which had been automatically closed by the software during the geometry creation. Elsewhere, the maximum element size generated was $\lambda/10$ as specified. These values are all below the maximum required for accuracy [66]. Figure 6.3 and Figure 6.4 show detail views of the 500 Hz mesh. The refinement around the intersection of components and the leading edges of the flap surfaces can be seen in the figures.

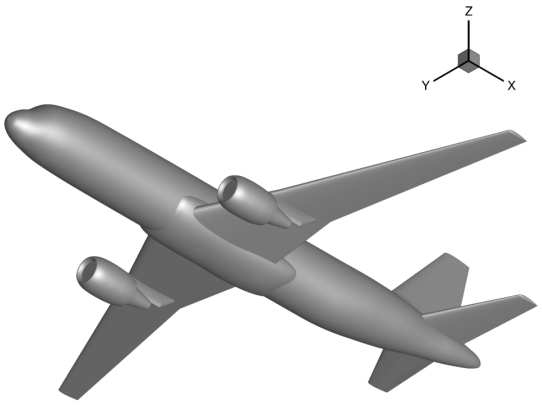

(a) Isometric projection, flaps retracted.

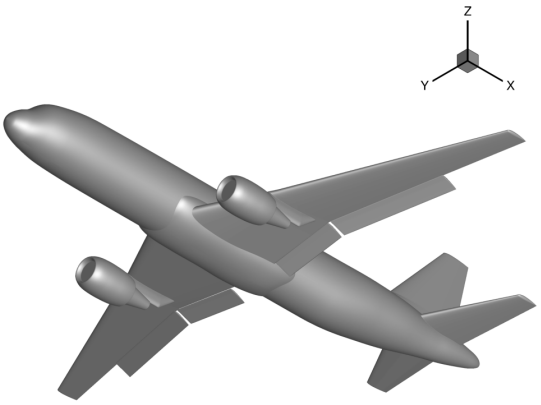

(b) Isometric projection, flaps deployed.

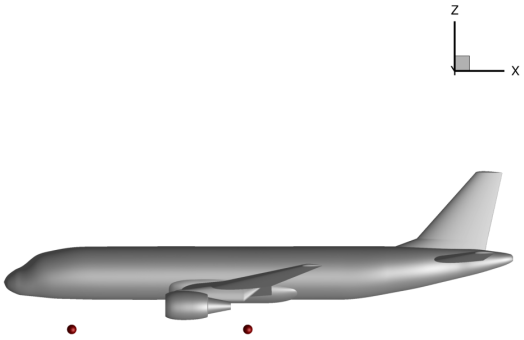

(c) Side view, flaps retracted.

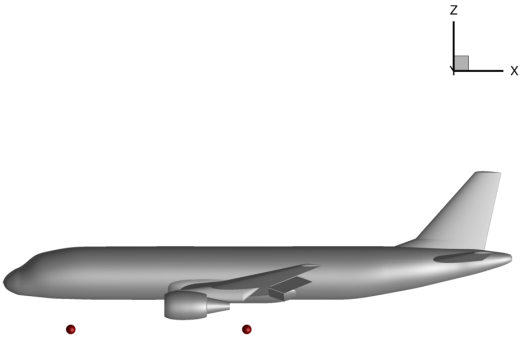

(d) Side view, flaps deployed.

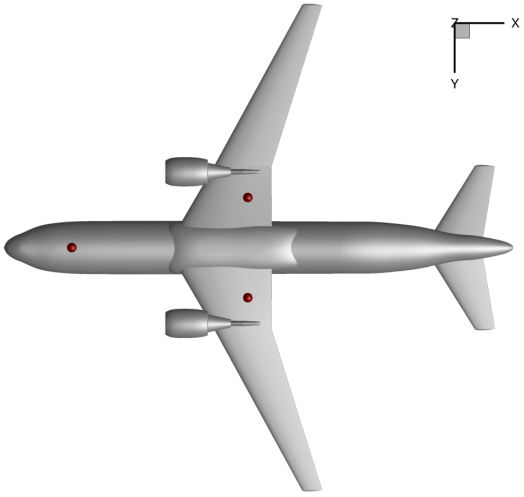

(e) Bottom view, flaps retracted.

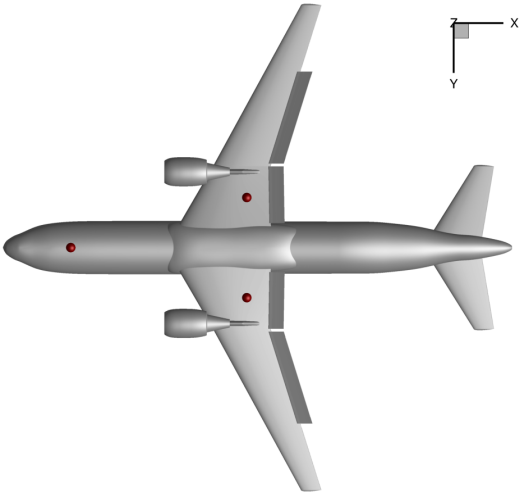

(f) Bottom view, flaps deployed.

Figure 6.2: Airbus A320-style geometry with CFM56 engine nacelles, showing monopole source locations.

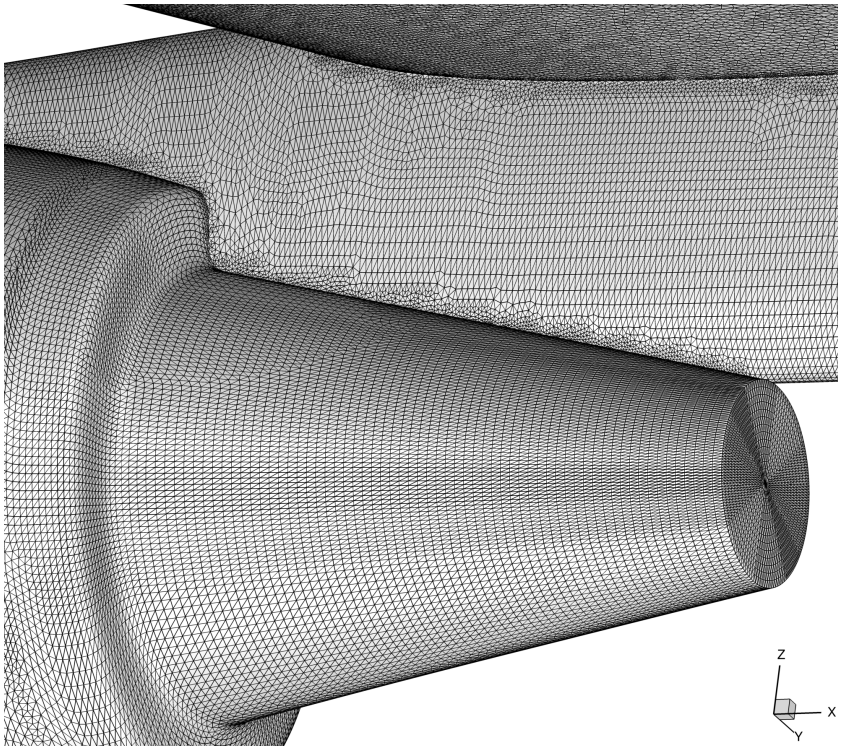

Figure 6.3: Mesh detail of the 500 Hz mesh with flaps deployed, showing the starboard nacelle, pylon, and lower wing surface.

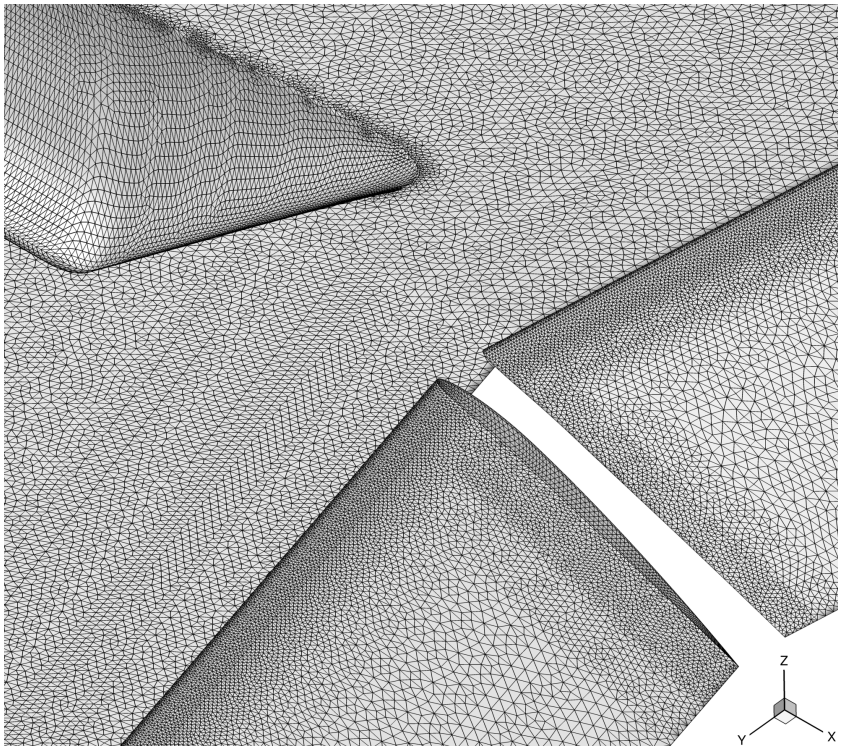

Figure 6.4: Mesh detail of the 500 Hz mesh with flaps deployed, showing the starboard pylon, lower wing surface, and flaps.

6.4 Landing Gear Noise Source Model

One of the aims of this thesis is to couple an existing landing gear noise source model with a BEM solver. This section provides an overview of the landing gear noise source model, and the coupling methodology that was implemented. An estimate of the far-field directivity for the noise generated by a particular landing gear configuration was obtained using the prediction code *SotonLGAP* [116]. This code was developed at the Airbus Noise Technology Centre at the University of Southampton. *SotonLGAP* creates a far-field noise directivity estimate for a given landing gear configuration using directional databases for isolated landing gear components and scaling laws.

The directional database for each isolated component was obtained from a DES simulation in the near-field, with the far-field noise spectra subsequently computed using an FWH solver with an on-body control surface. The far-field noise was obtained on a sphere of observers of radius r at 10° intervals. The obtained spectra for each component were then non-dimensionalised using the relevant scaling laws. For example, for strut components, the square of acoustic pressure was scaled using

$$p^2 \propto (\rho_\infty c_\infty^2)^2 \left(\frac{V_\infty}{c_\infty}\right)^6 \left(\frac{l_c}{r}\right)^2, \tag{6.4.1}$$

and the frequency using

$$f \propto V_\infty / d_c, \tag{6.4.2}$$

where l_c and d_c are the length and diameter of each component respectively.

To create a directivity estimate using *SotonLGAP*, a particular landing gear configuration is specified from a selection of components, each of which having a specified diameter, length, and rotation. The relevant scaling laws, such as (6.4.1) and (6.4.2) for strut noise, are applied to the relevant directional database for each component in order to obtain a far-field narrowband PSD estimate. The observer coordinates are transformed to take into account the rotation of the component with respect to the observer reference frame. A piecewise cubic Hermite interpolating polynomial is used if the component rotation is not a multiple of 10°. The free-stream flow velocity is specified as an input to *SotonLGAP*. This value is used in the scaling laws, and results in the modification of the amplitude of the generated noise. An estimate for the total noise is obtained by summing the contribution from each component. The PSD can be given in one-third or full

octave bands by integrating the narrowband PSD over the required frequencies, or the OASPL obtained by integrating over the entire narrowband PSD.

The far-field directional databases obtained from applying an FWH solver to the near-field CFD results were computed assuming a quiescent medium. This allows convective amplification to be estimated by *SotonLGAP* for any required Mach number. For the uniform flow BEM formulation, the convective amplification of a source is accounted for by the Lorentz-type transform. The strength of the source is specified as it would be without flow. Thus, a noise estimate without convective amplification can be obtained using *SotonLGAP*, and the convective amplification subsequently accounted for by the BEM solver.

It was explained in Section 2.4 that there are two types of installation effects: source installation effects and acoustic installation effects. The investigations in this thesis up to this point have concentrated on acoustic installation effects. These effects modify the propagation of an acoustic source, and include the effect of scattering by a geometry and refraction through a non-uniform flow. There is no modification of the source sound power. Source installation effects modify the strength of the acoustic source, due to local flow variations in the vicinity of the scattering body. These effects were not included in the previous investigations, as it was the effect of the non-uniform flow on the acoustic propagation that was under investigation.

However, the focus of this chapter is the coupling between a realistic source model and the BEM solver, and so it is important to ensure that these effects can also be accounted for if required. *SotonLGAP* has the ability to estimate the reduction in noise due to the reduction in flow velocity beneath a lifting wing due to circulation. The parameters required for this estimate are the wing chord a and an approximate value for the coefficient of lift C_L for the intended configuration. Using these parameters, a new value for the flow velocity beneath a lifting wing at the approximate location of the landing gear wheels is computed. This modified flow velocity is then used when applying the scaling laws instead of the specified free-stream velocity.

In the current work, *SotonLGAP* was used to generate PSD estimates in octave bands for MLG and NLG configurations representative of those found on an A320. BEM simulations were conducted at octave band centre frequencies of 125 Hz, 250 Hz, 500 Hz, and 1000 Hz. The landing gear components and associated directional databases used to obtain these estimates are given for the MLG and NLG in Table B.7 and Table B.8 respectively in Appendix B. For each configuration, the

estimates were obtained at 36 observers at 10° intervals located in the streamwise plane, with the 0° observer located upstream. Scaling laws were applied using a Mach number of $M_\infty = 0.2$ and an observer radius of 1 m. A directivity pattern for each configuration was obtained by extracting the result for each octave band centre frequency at each observer. These are shown in Figure 6.5a and Figure 6.6a for the MLG and NLG respectively. Source strength modification due to installation was not included for these estimates. It can be seen that the directivity for both the MLG and NLG is almost omni-directional at these octave band centre frequencies. As described in Section 2.3, these frequencies correspond to the noise associated with large-scale landing gear components such as struts and wheels.

In order to complete the coupling between the prediction code and the BEM solver, an appropriate way to specify acoustic sources in the BEM solver for a given landing gear configuration was required. Three methods to do this were considered, which were as follows:

- Use a single monopole to represent the almost omni-directional landing gear directivity at each frequency, with the strength of the monopole set to give the average SPL of the directivity obtained from *SotonLGAP* in the streamwise direction.

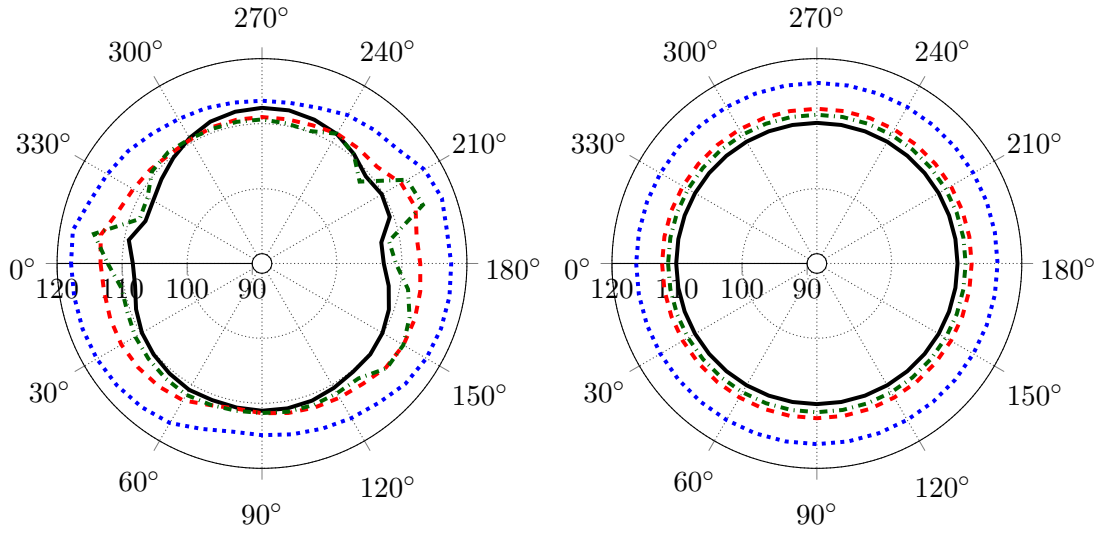

(a) As computed. (b) Averaged.

Figure 6.5: SPL (dB), directivities from *SotonLGAP* in the streamwise direction. A320 MLG without installation effect. 125 Hz ——, 250 Hz - - -, 500 Hz ·····, 1000 Hz -·-·-.

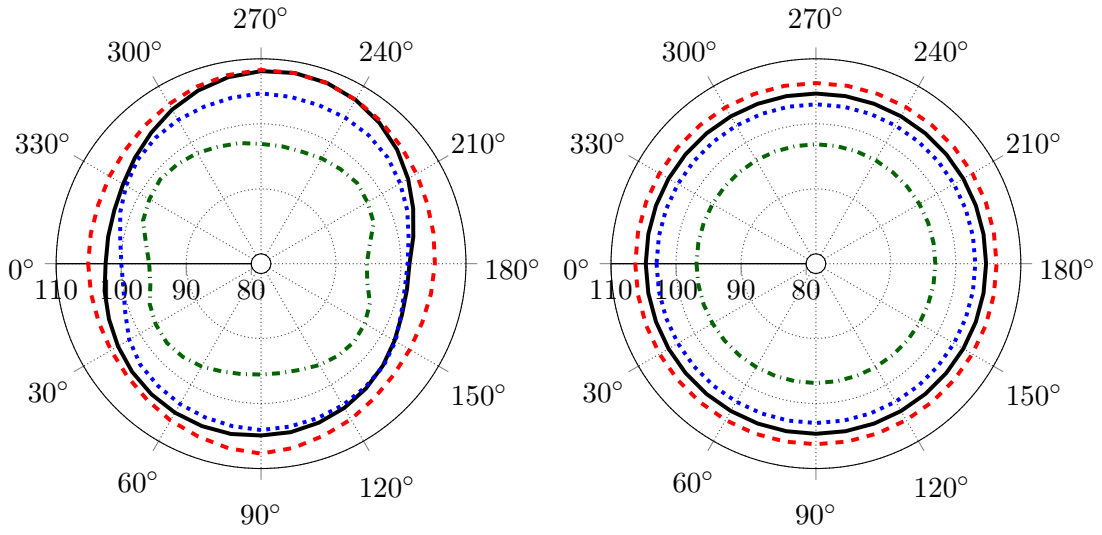

(a) As computed. (b) Averaged.

Figure 6.6: SPL (dB), directivities from *SotonLGAP* in the streamwise direction. A320 NLG without installation effect. 125 Hz ——, 250 Hz - - -, 500 Hz ·····, 1000 Hz -·-·-.

- Use *ACTIPOLE*'s spherical wave acoustic source formulation, in which a far-field directivity pattern is given as an input to the solver. Initial simulations were conducted using this formulation with an omni-directional directivity pattern, the uniform flow approximation, and an isolated NACA 0012 airfoil geometry. Comparing the results against those from an equivalent simulation using a point source showed that the spherical wave formulation was not accurate when the flow approximation method was used. An *ACTIPOLE* developer at IMACS advised that the spherical wave formulation not be used with the flow approximation due to known issues with accuracy and stability.

- Use a method proposed by Vecherin *et al.* [117, 118], in which a point source distribution is constructed that reproduces a given directivity pattern in the far-field. A set of elementary configurations are built using point sources, each of which corresponding to a spherical harmonic. The elementary configurations are then linearly combined to reconstruct the required far-field directivity pattern. However, the authors noted that there will be errors in the source distribution if outliers exist in the directivity data. The directivity estimated by *SotonLGAP* can contain outliers at higher frequencies, as seen in Figure 6.5a for the A320 MLG estimate at 1000 Hz. The authors also noted that there will be errors in the near-field if no phase information exists for the directivity, as is the case for the output from *SotonLGAP*.

Due to the issues with *ACTIPOLE*'s spherical wave formulation and the Vecherin *et al.* method, the option of using a single monopole to represent the almost omni-directional directivity for each frequency was chosen. Using a single monopole in this manner does not allow the directivity to be exactly recreated. However, as seen in Figure 6.5a and Figure 6.6a, the directivities for the frequencies of interest are almost omni-directional for both nose and main landing gears. The sound power of the landing gear noise is recreated through the use of the idealised source. For each landing gear configuration and frequency, the directivity obtained in the streamwise plane was converted from SPL to p_{rms} at each observer, and then averaged over the 36 observers to give a mean value $p^{\text{av}}_{\text{rms}}$. This was then used to determine the equivalent monopole source strength for that configuration and frequency using

$$Q(k) = \frac{p^{\text{av}}_{\text{rms}}(k)\sqrt{2}}{|e^{ikr}/4\pi r|}. \tag{6.4.3}$$

A value of $r = 1\,\text{m}$ was used for the observer radius, as this was the value used in *SotonLGAP* to obtain the directivity estimates.

The mean SPL for each frequency was computed using $p^{\text{av}}_{\text{rms}}$, and is shown in Figure 6.5b and Figure 6.6b for the MLG and NLG respectively. The strengths computed for the equivalent monopole sources are given in Table B.9 in Appendix B. The standard deviation of the directivity at each frequency for both configurations is shown in Figure 6.7. It can be seen that between 125 Hz and 1000 Hz the standard deviation is less than 2 dB. Above 1000 Hz, the databases used for the MLG geometry that corresponded to small components resulted in the directivity estimate becoming more directional than at lower frequencies. This can be seen in the larger values of the standard deviation above 1000 Hz for this configuration. The simplified NLG geometry does not contain these small-scale details, and so is less directional above 1000 Hz.

One of the strengths of the *ACTIPOLE* solver is that it can solve for multiple right-hand sides simultaneously, and give each solution independently. Each right-hand side corresponds to a different monopole source. The advantage of this is that one simulation can be conducted for each frequency and aircraft configuration, and the result for each source scaled independently by the required strength as a post-processing step. In order to facilitate this, the source strengths were set as unity for all simulations. All planned simulations as described in Section 6.2 were completed. Details of the simulations can be found in Table B.5 in Appendix B. An example of the acoustic pressure on the aircraft surface at each frequency due to the equivalent sources representing the starboard MLG is shown in Figure 6.8.

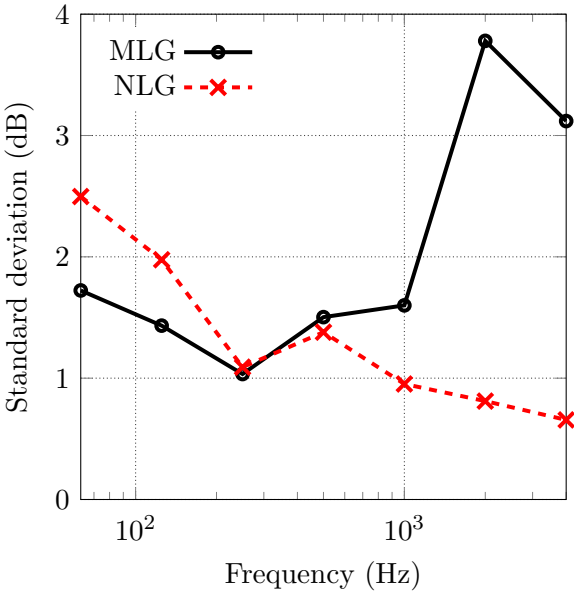

Figure 6.7: Standard deviation (dB) of the directivity at each frequency for the A320 MLG and NLG directivity estimates from *SotonLGAP*.

The variation in the levels of surface pressure with frequency due to the varying source strengths can be seen.

6.5 Sound Pressure Level on the Ground and the Effect of Flap Deployment

The landing gear noise source model was used in conjunction with the BEM solver to obtain an estimate of the SPL on a $0.25\,\mathrm{km}^2$ square ground plane. The aircraft geometry was located at an altitude representative of the approach reference point. The ground plane was centred on $(18, 0, -120)$ with respect to the origin of the coordinate system, which was located at the nose of the aircraft. This streamwise location coincides with the location of the equivalent sources for the MLG. The ground plane was discretised using quadrilateral elements $1\,\mathrm{m}^2$ in size. This gave a total of 2.51×10^5 observer locations where the SPL was computed. In order to compute SPL values on the ground for a particular aircraft configuration, the scaled landing gear sources needed to be summed across all frequencies. Direct summation of the complex pressure field for each source results in interference due to spectral coherence. Therefore, it was assumed that the sources were incoherent in order for them to approximate a stochastic turbulent source. The incoherent summation of the obtained p_{rms} at the observers for each landing gear source across

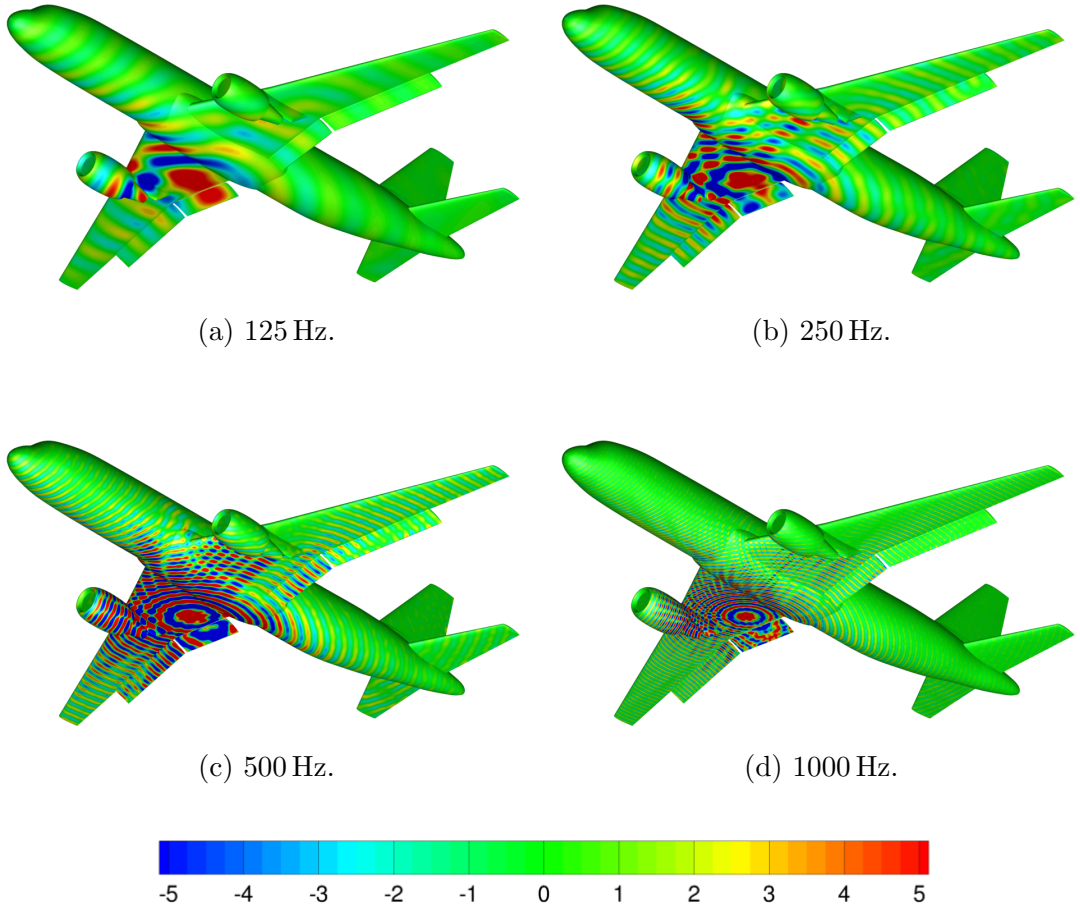

(a) 125 Hz. (b) 250 Hz.

(c) 500 Hz. (d) 1000 Hz.

Figure 6.8: Acoustic pressure (Pa) of the starboard MLG on the aircraft surface. Flaps deployed, source strengths without installation effect.

all frequencies was conducted on a pressure squared basis as described by Bies and Hansen [119].

The effect of flap deployment was investigated in two ways. Firstly, the geometrical effect of the flap deployment was investigated using sources of the same strength for each configuration. The source installation effect was then included in the prediction, by using MLG sources with strengths modified due to the reduction in flow velocity beneath a lifting wing. The NLG source strengths without installation effect as computed in Section 6.4 were used for all cases.

6.5.1 Constant Strength Sources

In order to investigate the effect of the change in scattering geometry with flap deployment, the same MLG and NLG source strengths were used for each configuration to scale the obtained values of p_{rms} at the observers. The MLG source strengths used for this were computed in Section 6.4 and do not include the effect

of source strength reduction due to installation. Figure 6.9 shows the computed SPL on the ground plane from the starboard MLG for both configurations. It can be seen that deploying the flaps primarily increases the SPL in a region directly below and immediately surrounding the aircraft. This is due to a larger proportion of the incident wave being reflected downwards by the additional reflective surfaces. The larger peaks in SPL located upstream on the port side are due to reflections from the starboard nacelle. The role of the starboard nacelle in causing this can be seen due to the proximity of the sources from the nacelle in Figure 6.8, which shows the surface pressure computed for the sources that were summed for Figure 6.9b. Due to the use of omni-directional sources and a symmetric geometry, the obtained SPL for the port MLG is the same as that seen in Figure 6.9, but mirrored in the streamwise direction about the aircraft fuselage centreline.

The SPL on the ground plane due to the NLG is shown in Figure 6.10. It can be seen that there are minimal differences in the computed SPL between the configurations. This can be attributed to the relatively large distance of the NLG sources from the additional reflective surfaces of the deployed flaps. The results for all three landing gear were summed incoherently to provide an estimate of the SPL for the total landing gear noise, and this is shown in Figure 6.11. As expected from the preceding results showing the SPL from each isolated landing gear, the

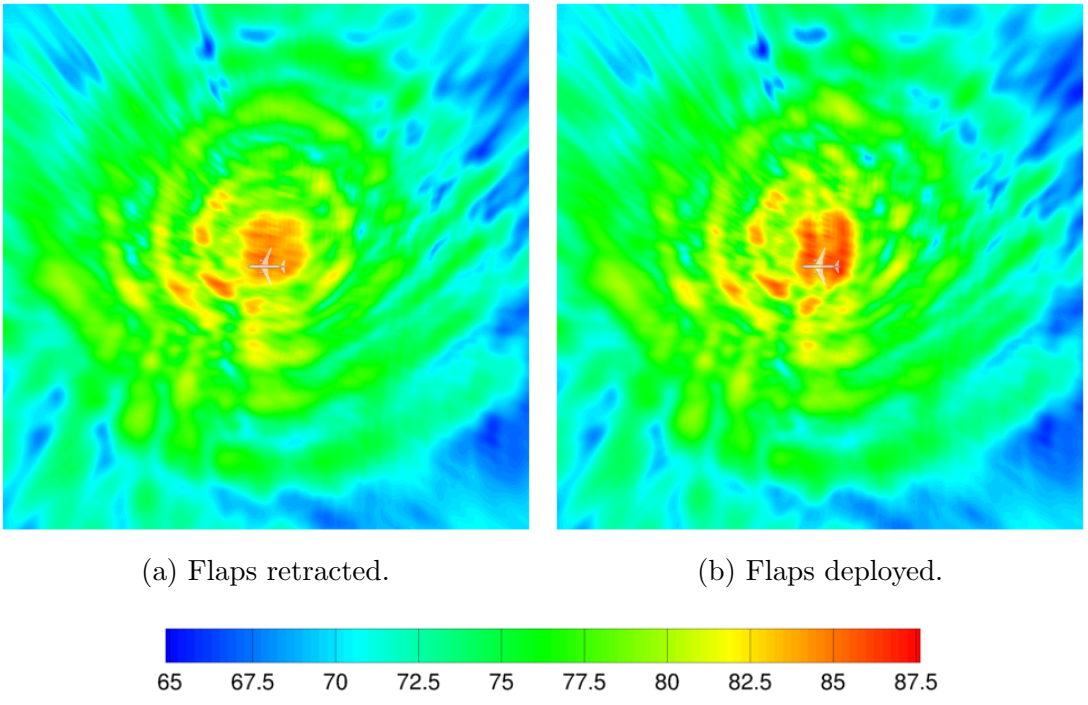

(a) Flaps retracted.

(b) Flaps deployed.

Figure 6.9: Sound pressure level (dB) of the starboard MLG on the ground plane. MLG source strengths without installation effect.

primary effect of flap deployment with the constant strength sources is to increase the SPL in a region directly below and immediately surrounding the aircraft.

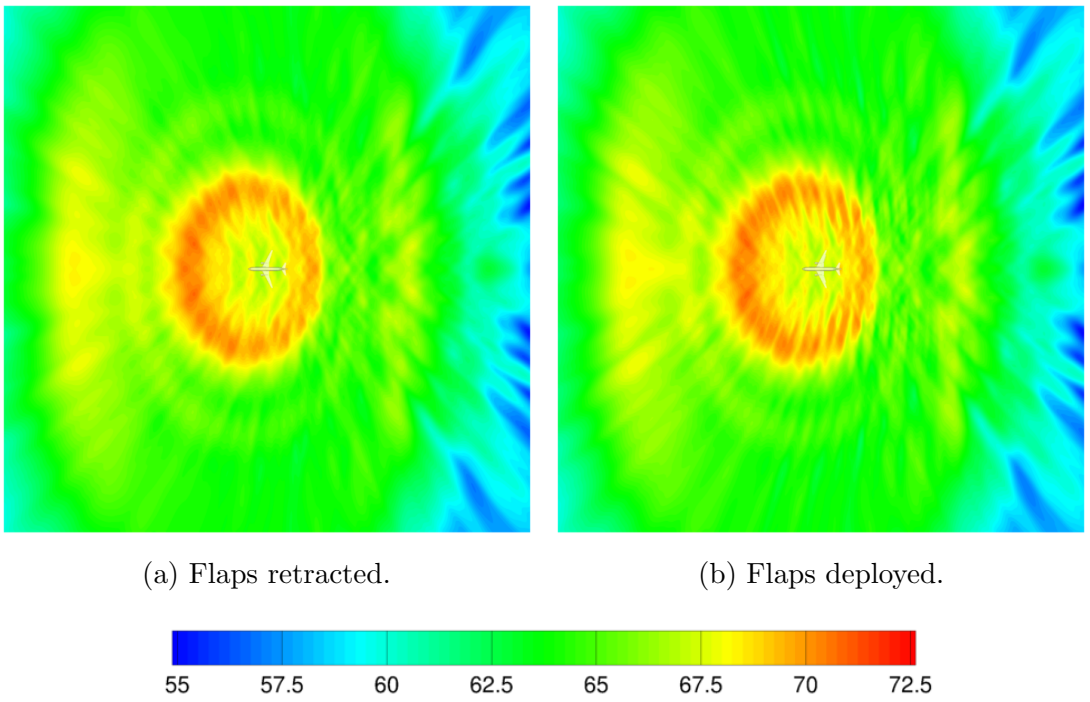

(a) Flaps retracted. (b) Flaps deployed.

Figure 6.10: Sound pressure level (dB) of the NLG on the ground plane.

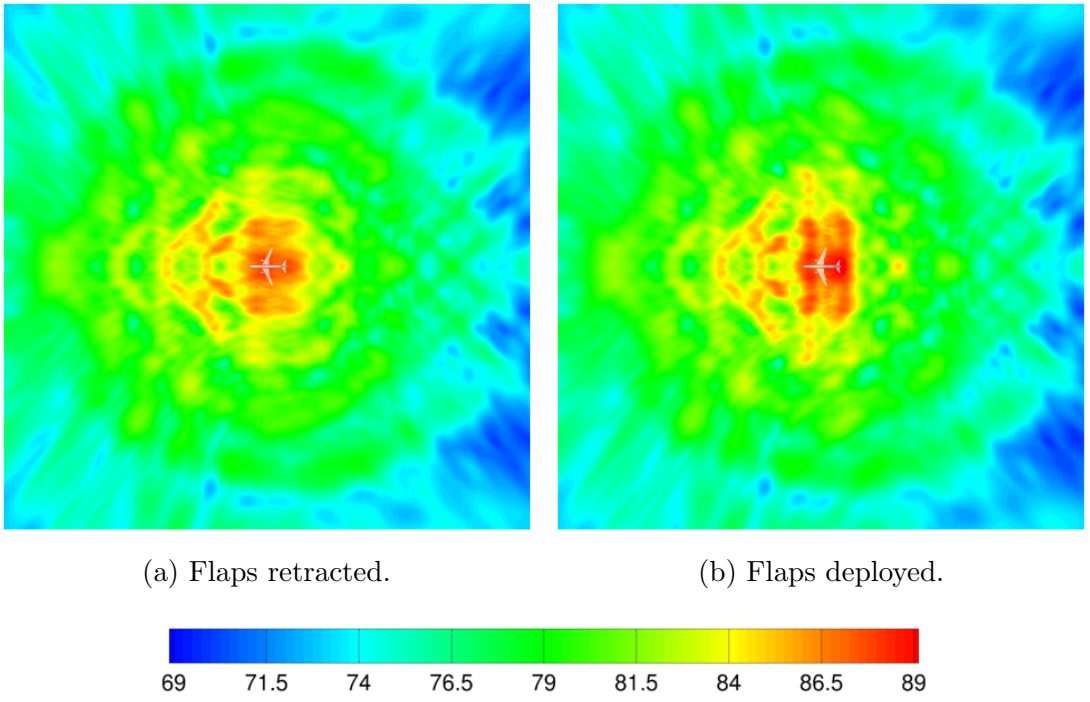

(a) Flaps retracted. (b) Flaps deployed.

Figure 6.11: Sound pressure level (dB) of all landing gears on the ground plane. MLG source strengths without installation effect.

6.5.2 Source Strength Reduction for Installed Main Landing Gear

Having investigated the effect of the change in scattering geometry with constant strength sources, source installation effects were then added to the predictions. New values of the MLG source strengths for all frequencies were obtained in the same manner as before using *SotonLGAP*. The parameters used with *SotonLGAP* to estimate the reduction in noise due to landing gear installation beneath a lifting wing were wing chord $a = 5.775\,\mathrm{m}$, flaps retracted $C_L = 0.6$, and flaps deployed $C_L = 2.5$. The mean values of SPL for each configuration and frequency are shown in Table 6.1. It can be seen that there is a large reduction in the generated noise at each frequency with the deployment of flaps. The strengths computed for the equivalent monopole sources with installation effect are given in Table B.10 in Appendix B.

As the source scaling is conducted as a post-processing step, no additional BEM simulations needed to be run. The existing results, obtained using sources with unity strength, were rescaled using the new MLG source strengths. The results were incoherently summed across all frequencies for all three landing gear to give an estimate of the total SPL, and this is shown in Figure 6.12. It can be seen that there is a large reduction in the predicted SPL on the ground with the deployment of flaps. It should be noted that the same NLG source strengths without any installation effects that were used in Section 6.5.1 were used here for both configurations. Thus, the differences observed here are due only to the differing MLG source strengths. This highlights the importance of taking the source installation effect into account for installed landing gear noise predictions. However, it should be noted that the results presented here do not account for the interaction of the landing gear wake with the deployed flap. This interaction would

Table 6.1: Values of mean SPL at 1 m for the A320 MLG with installation effect.

	Mean SPL (dB)	
Frequency (Hz)	Flaps retracted	Flaps deployed
125.0	109.636	101.044
250.0	111.754	103.215
500.0	115.563	107.198
1000.0	113.877	102.290

produce additional noise. Thus, the large reduction in SPL observed here might be overestimated.

6.6 The Effect of Alternative Locations for the Main Landing Gear Source

Up until this point, the equivalent landing gear sources were located in the approximate location of each landing gear axle. This location was chosen as the reduction in flow velocity beneath a lifting wing compared to the free-stream is computed in *SotonLGAP* at the position of the wheels. However, it was of interest to determine the effect on the predicted SPL of alternative MLG source locations. For this investigation, the MLG source strengths without installation effect computed in Section 6.4 were used. The investigation was conducted at a single frequency of 500 Hz. This frequency was chosen as it had the highest mean SPL of the octave band centre frequencies as seen in Figure 6.5b, and was therefore the largest contributor to the total estimated SPL. The flaps deployed geometry was chosen for the investigation, as the extra reflective surfaces of the deployed flaps have already been shown in Section 6.5.1 to be a large influence on the scattered sound field.

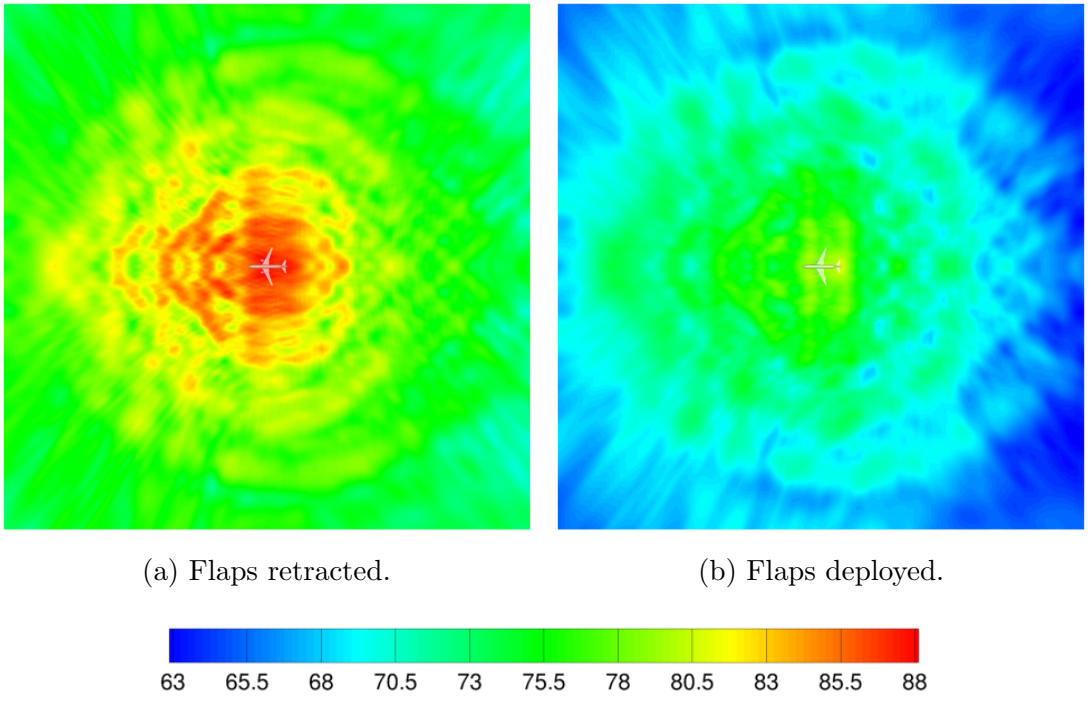

(a) Flaps retracted. (b) Flaps deployed.

Figure 6.12: Sound pressure level (dB) of all landing gears on the ground plane. MLG source strengths with installation effect.

The starboard MLG source was chosen as the source whose position would be varied. The original location of this source was $(18, 3.7, -3.5)$, and this location is labelled LG here for convenience. The additional source locations were obtained by moving LG backwards by 1 m in the x-direction, forwards by 1 m in the x-direction, and upwards by 1 m in the z-direction. These new source locations are labelled LG_{x-1}, LG_{x+1}, and LG_{z+1} respectively, and are shown in Figure 6.13. These new source locations required additional simulations to be completed. Further details of these additional simulations can be found in Table B.6 in Appendix B.

The acoustic pressure computed on the surface of the aircraft from the sources in the new locations are compared to the original location in Figure 6.14. It can be seen that moving the source from LG to LG_{x-1} moves the source closer to the nacelle, whereas moving it to LG_{x+1} moves it closer to the flap. The effect of this on the predicted SPL on the ground plane can be seen in Figure 6.15. At LG_{x-1}, the closer proximity of the source to the starboard nacelle increases the shielding on the starboard side of the aircraft. At LG_{x+1} a larger proportion of the incident wave is reflected forwards than at LG, due to the closer proximity of the source to the deployed flap.

Moving the source to LG_{z+1} does not result in any obvious additional shielding on the ground plane unlike the other two alternative locations, as seen in Figure 6.15. However, the peaks of constructive and destructive interference change position. This is to be expected for single frequency simulations using a single point source. It was shown in Chapter 5 that single frequency simulations can accurately predict a single frequency from an equivalent broadband source. As discussed in Section 5.7, increasing the number of frequency bands used to estimate the total SPL

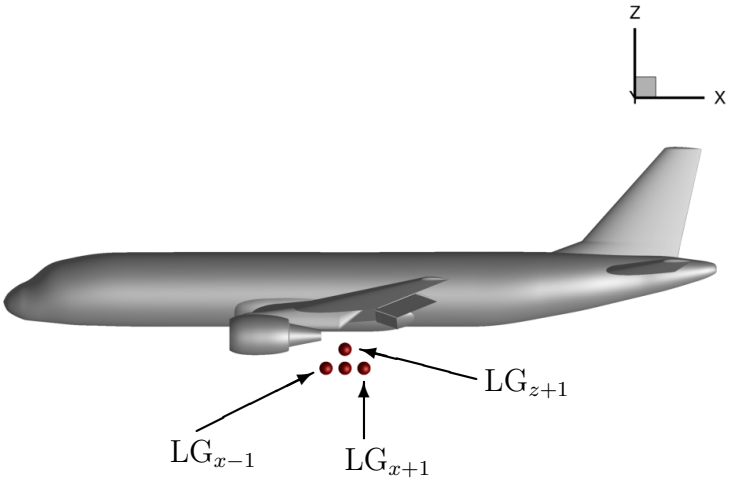

Figure 6.13: Alternative starboard MLG source locations.

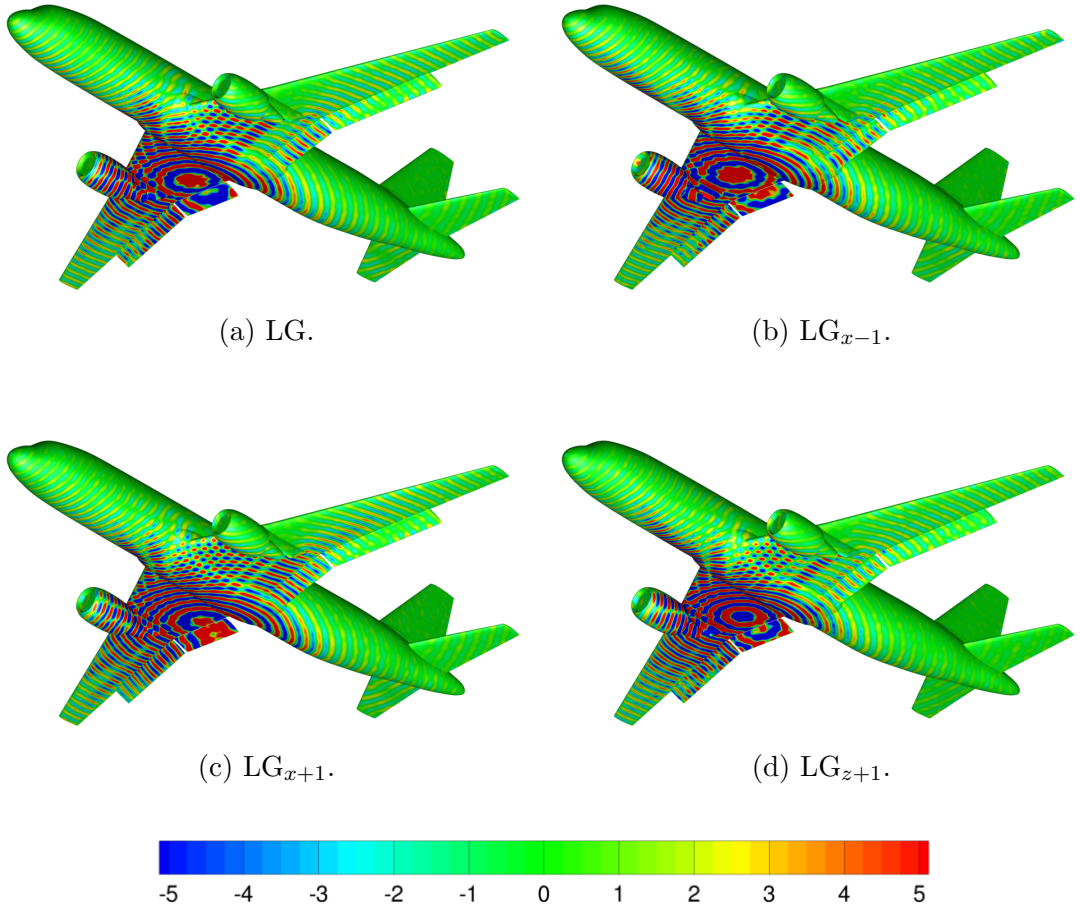

(a) LG. (b) LG$_{x-1}$.

(c) LG$_{x+1}$. (d) LG$_{z+1}$.

Figure 6.14: Acoustic pressure (Pa) of the starboard MLG at 500 Hz on the aircraft surface. Flaps deployed, source strength without installation effect.

will reduce the interference in the estimate, although this would require a greater number of single frequency simulations to be undertaken.

The results presented in this section suggest that the estimated SPL on the ground plane is sensitive to the location of the equivalent monopole sources. In particular, the estimated SPL is influenced by the proximity of each source to flaps, nacelles or pylons. This is one drawback of using omni-directional monopoles to represent the noise from each landing gear. Real landing gear noise source regions are non-compact, unlike a monopole source. Using a monopole source enables the far-field directivity and associated noise levels of a landing gear to be recreated. However, the acoustic near-field is different, which leads to the observed sensitivity to position. Therefore, the method used to generate each equivalent source strength must also give its location. A further study was conducted using *SotonLGAP* with A320 and A340 MLG geometries in order to determine an appropriate location for the equivalent source. This showed that the source should be located at 60 % of

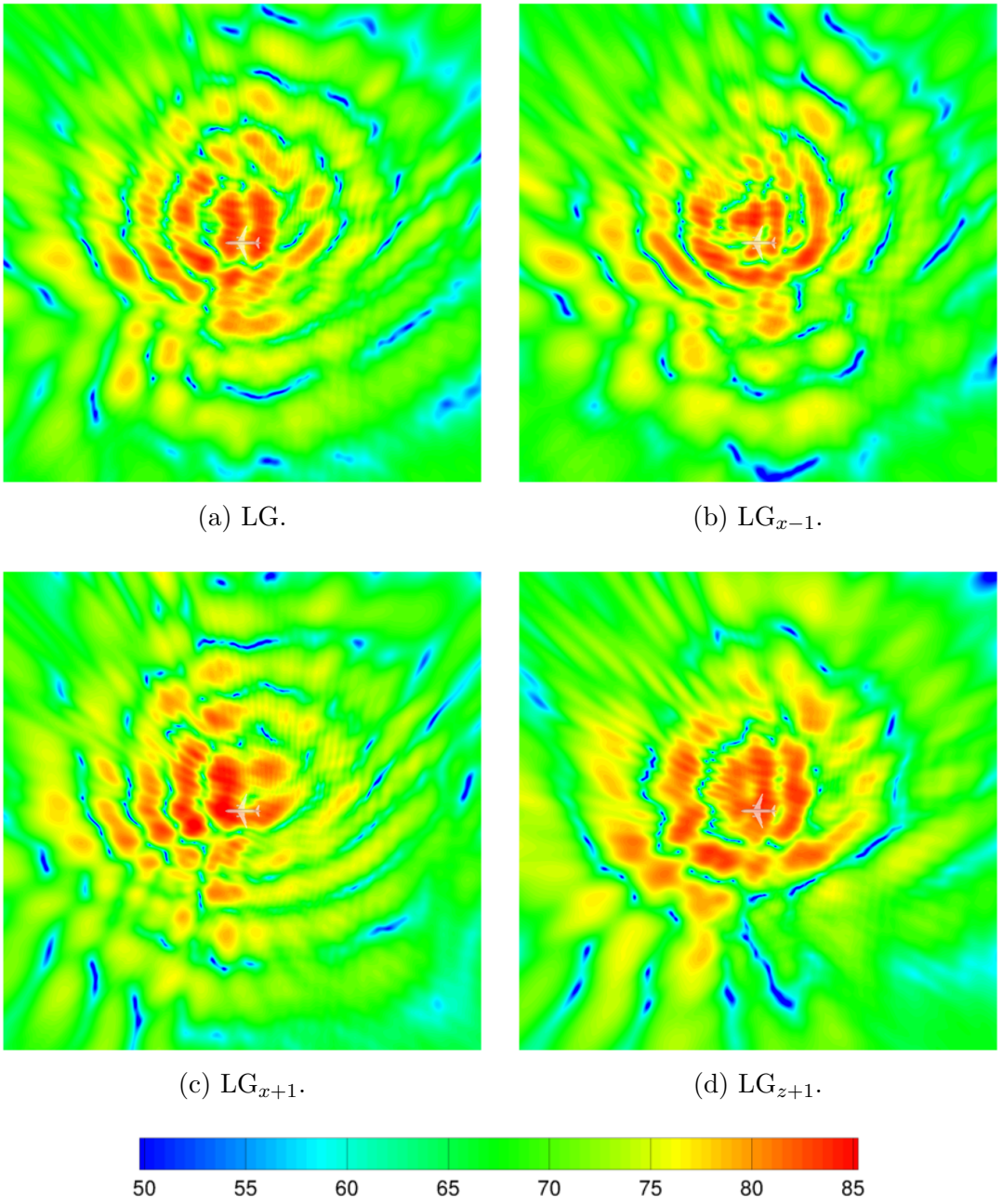

(a) LG. (b) LG_{x-1}.

(c) LG_{x+1}. (d) LG_{z+1}.

Figure 6.15: SPL (dB) on the ground plane for the starboard MLG at 500 Hz with flaps deployed. Source strength without installation effect.

the main leg total length beneath the wing surface. An idea for how the method presented in this chapter could be improved is discussed in Section 7.2.2.

6.7 Summary

A method for coupling a realistic landing gear noise source model with an acoustic BEM solver has been presented in this chapter. The SPL of the noise for a particular landing gear configuration was estimated using *SotonLGAP*. This code uses directional databases for landing gear components and scaling laws to estimate the far-field directivity of a specified landing gear configuration. The directivity for an A320 MLG and NLG was obtained in octave bands from *SotonLGAP*. It was shown that these directivity estimates were almost omni-directional, especially at lower frequencies. An omni-directional monopole was used to represent an idealised landing gear noise source for each frequency. The strength of each monopole was chosen so that the SPL at a given distance matched the mean SPL of the directivity estimate from *SotonLGAP*. It was shown for this methodology that the standard deviation was less than 2 dB for the frequencies under investigation in this chapter.

This source model was employed with the BEM solver *ACTIPOLE* in order to estimate the SPL on a 0.25 km^2 ground plane. An Airbus A320-style aircraft was chosen as the scattering geometry, with the sources located at the approximate locations of the landing gear axles. The ground plane was located 120 m below the nose of the aircraft, which corresponded to the approach reference point discussed in Section 1.1. Two configurations of the aircraft were investigated: flaps retracted and flaps deployed. This was conducted at an angle of attack of $\alpha = 0°$ and a Mach number of $M_\infty = 0.2$ for both configurations. The uniform flow BEM approximation was chosen as the most appropriate for the investigations. The use of the same flow parameters for both configurations allowed the effect of the change in scattering geometry to be investigated.

Using constant strength sources without any source installation effect showed that the effect of flap deployment was to increase the SPL directly below and in the region immediately surrounding the aircraft. This was attributed to the extra reflective surfaces reflecting a higher proportion of the incident wave downwards towards the ground. Taking the source installation effect into account, the mean SPL values corresponding to the directivity estimates from *SotonLGAP* for an airfoil with deployed flap were reduced compared to those with a retracted flap.

These mean SPL values were used to set the strength for each representative monopole source, and so this resulted in a reduction of approximately 8 dB in the estimated SPL on the ground. This was due entirely to the reduction in strength of the MLG equivalent sources, and highlights the importance of taking the source installation effect into account for landing gear noise predictions.

Finally, SPL estimates on the ground plane obtained by varying the starboard MLG source position at a single frequency of 500 Hz showed that the SPL estimate was sensitive to the location of the source. The SPL estimate was most sensitive to streamwise changes in the source position. This was due to the changing proximity of the source to the nacelle, pylon, and the deployed flap in this direction, which led to additional shielding being observed in the SPL estimate on the ground plane. It was discussed that this is a drawback of the implemented methodology. Although an omni-directional monopole recreates the almost omni-directional far-field directivity and associated noise levels of a landing gear, it does not recreate the non-compact acoustic source in the near-field.

Chapter 7

Conclusion

7.1 Summary of Results

The results of investigations into some of the effects of installing landing gear noise sources beneath a lifting wing have been presented in this thesis. Investigations using 2-D LEE and BEM solvers concentrated on the acoustic installation effects of an idealised monopole source located in the approximate position of a landing gear beneath a lifting wing. Acoustic installation effects include the scattering of a source by a geometry and the effect of non-uniform flow on the propagation of a source, and do not modify the source strength. Source installation effects, which modify the strength of the source due to local flow variations around the scattering body, were not included in these investigations. A realistic landing gear noise source model was coupled with a 3-D acoustic BEM solver, and predictions of the SPL on a ground plane were made that further included source installation effects. The results of these investigations are summarised in this section.

7.1.1 The Effect of Non-Uniform Flow on the Scattering of Landing Gear Noise Sources

One of the aims of this thesis was to quantify the effect of non-uniform flow due to circulation around a lifting wing on the scattering of landing gear noise sources. Circulation increases as the angle of attack or Mach number is increased, or as flaps and slats are deployed. Increasing the circulation around the wing decreases the flow velocity in the region below the wing compared to the free-stream. The

effect of this on the acoustic scattering was investigated using a 2-D LEE solver for both single frequency and broadband monopole sources, as seen in Chapter 4 and Chapter 5 respectively. Solution of the LEE accounts for refraction through a non-uniform flow, unlike the available BEM methods.

A symmetric NACA 0012 airfoil was used to investigate the effect of varying angle of attack and Mach number, and a high-lift RA16SC1 airfoil was used to investigate the effect of varying flap and slat configurations. The SPL for each case was computed at 360 observers in the near-field located on a circle centred on the source. This was conducted over both non-uniform and uniform base flows for each combination of airfoil configuration, angle of attack, and Mach number. For a single frequency, the obtained directivity has peaks of constructive and destructive interference. The effect of the non-uniform flow was then quantified by the difference in SPL at each observer over non-uniform and uniform base flows, computed using $\mathrm{SPL}_{\text{non-uniform}} - \mathrm{SPL}_{\text{uniform}}$.

A Mach number of $M_\infty = 0.2$ was fixed to approximate that of a commercial airliner on approach, and the angle of attack of the NACA 0012 airfoil was varied in the range $0° \leq \alpha \leq 8°$. The results at single frequencies showed small values of $\mathrm{SPL}_{\text{non-uniform}} - \mathrm{SPL}_{\text{uniform}}$ with a maximum magnitude of approximately 1 dB. Using results from the solver validation in Chapter 3, an error bound of 3 % difference in p_{rms} was chosen. The computed values of $\mathrm{SPL}_{\text{non-uniform}} - \mathrm{SPL}_{\text{uniform}}$ were above this error bound at the extremes of the angle of attack range. The computed values varied linearly with angle of attack between these extremes, showing that they were proportional to the lift, and therefore the circulation. However, fixing an angle of attack of $\alpha = 5°$ for the NACA 0012 airfoil and varying the Mach number in the range $0.1 \leq M_\infty \leq 0.3$ did not show any values above the error bound.

The RA16SC1 airfoil was then used to determine the effect of flap deployment. The angle of attack was fixed at $\alpha = 0°$ and Mach number at $M_\infty = 0.2$. The deployment of the flap and the subsequent increase in its deflection angle resulted in values of $\mathrm{SPL}_{\text{non-uniform}} - \mathrm{SPL}_{\text{uniform}}$ above the error bound. However, small changes in the position of directional lobes in the computed directivities resulted in large jumps in plots of $\mathrm{SPL}_{\text{non-uniform}} - \mathrm{SPL}_{\text{uniform}}$, and no clear trends could be seen. This was a motivating factor for extending the investigation using a broadband source.

A new method was proposed in Chapter 5 to generate an input signal for use with the LEE solver that gave a prescribed PSD in the free-field at a given radius from

a monopole source. A signal was generated to give a PSD that was equal in power for all frequencies at the observer radius in the free-field. This choice of PSD would enable the effect of installing the broadband source beneath a lifting wing on the frequency content of the scattered source to easily be seen. This is discussed further in Section 7.1.4. Using this broadband source, the effect of non-uniform flow due to circulation was investigated using the same airfoil configuration, angle of attack, and Mach number combinations as the previous investigation at single frequencies. Values of $\mathrm{SPL}_{\text{non-uniform}} - \mathrm{SPL}_{\text{uniform}}$ were computed using the OASPL obtained at each observer. However, although trends could be seen for these cases, the computed values were less than the error bound of a 3 % change in p_{rms} and so were not considered significant.

The results from the broadband investigations were in contrast to the results of the single frequency investigations. Both the single frequency and broadband investigations used a source strength that gave 100 dB in the free-field for each case. The computed values of $\mathrm{SPL}_{\text{non-uniform}} - \mathrm{SPL}_{\text{uniform}}$ were considered insignificant for all broadband cases. However, it was shown for some single frequency cases that there were values of $\mathrm{SPL}_{\text{non-uniform}} - \mathrm{SPL}_{\text{uniform}}$ that were considered significant although small. It was concluded that the effect of non-uniform flow due to circulation on the acoustic scattering is exaggerated by interference effects at a single frequency. Results at a single frequency were extracted from the broadband results and used to construct directivity plots for a selection of cases. These were then compared against directivity plots from equivalent single frequency cases. It was shown that the single frequency simulations are capable of accurately representing a given frequency from an equivalent broadband simulation. It was thus concluded that an estimate of the OASPL for a broadband source could be obtained by the incoherent summation of a set of single frequency results. Further, as it had been shown that the effect of non-uniform flow due to circulation on the scattering of a broadband source was negligible, these single frequency results could be obtained using a uniform flow assumption.

7.1.2 Quantification of the 2-D Assumption

The LEE investigations undertaken for this thesis were conducted in 2-D due to the computational expense of the corresponding 3-D simulations and the number of parameters that were investigated. There are two main differences between the the acoustic propagation in 2-D and 3-D. These are the geometrical spreading, which is cylindrical in 2-D and spherical in 3-D, and additional edge diffraction

effects in 3-D that might further influence the solution. In order to determine if the investigations undertaken in 2-D were representative of what would be observed in 3-D, additional simulations were undertaken in 3-D and compared to results obtained from 2-D simulations.

The symmetric NACA 0012 airfoil was chosen for the quantification of the 2-D assumption. It was assumed for the 3-D simulations that the airfoil was constant in cross-section with an infinite span so that wing tip effects were not present in either base flow or acoustic solutions. Thus, the base flow was constant in the spanwise direction. For the acoustic solution, non-reflecting boundary conditions were used at all six faces that bounded the computational domain to enforce the infinite span assumption. Simulations in both 2-D and 3-D were undertaken over both uniform and non-uniform base flows at $M_\infty = 0.2$ and $\alpha = 4°$. A source at 250 Hz was used for each simulation.

Values of $\mathrm{SPL}_{\text{non-uniform}} - \mathrm{SPL}_{\text{uniform}}$ were used throughout this thesis in order to quantify the effect of non-uniform flow due to circulation on the acoustic scattering. Therefore, these values were computed for the results in 2-D and in 3-D. It was seen that these values were in good agreement, despite the difference in geometrical spreading. It was also concluded that any additional edge diffraction effects in 3-D were negligible for these cases, and that the results observed in the 2-D investigations were representative of what would be observed in 3-D.

7.1.3 The Effect of an Alternative Source Location and Higher Mach Numbers

Having seen that in most cases representative of an airliner on approach that the difference in SPL between non-uniform and uniform base flows was small, it was of interest to determine if there were any configurations where it was comparatively large. Firstly, a higher Mach number of $M_\infty = 0.6$ was investigated using the NACA 0012 airfoil with a source at a single frequency in the same position as before. An angle of attack of 3° was used, which kept the local flow velocity subsonic in the non-uniform base flow. However, only a small difference was seen again between the directivities computed over non-uniform and uniform base flows.

The largest increase in local flow velocity in the non-uniform flow around a NACA 0012 airfoil with a positive angle of attack is seen over the top surface of the leading edge of the airfoil. This is on the opposite side of the airfoil from the source for all of the preceding investigations. Therefore, the single frequency source was

relocated above the airfoil, to determine if this region of higher flow velocity had a larger effect on the scattering of the source with this alternative source location. Although a source in this location is not representative of a landing gear noise source, it gives an insight into the possibility of mounting an engine above an airfoil in order to use the airfoil as an acoustic shield.

The effect of varying the Mach number in the range $0.2 \leq M_\infty \leq 0.6$ was investigated for the source in this location. With a free-stream Mach number of $M_\infty = 0.2$ and 0.3, again only a small difference in the directivities computed over non-uniform and uniform base flows was observed. However, larger differences were seen for $0.4 \leq M_\infty \leq 0.6$. These were attributed to the flow being transonic over the top surface of the leading edge of the airfoil in the non-uniform flow. In particular, at $M_\infty = 0.6$ the local flow velocity over the top surface of the leading edge of the airfoil was shown to be approximately $M_0 = 0.95$. It was seen that acoustic propagation was attenuated in this region, and differences in interference due to this were observed throughout the acoustic field. This led to a reduction in SPL of approximately 10 dB at the observers located upstream and in the direction of the ground.

7.1.4 The Frequency Content of Broadband Sources Scattered by a Lifting Wing

As discussed in Section 7.1.1, the input signal for the broadband source was constructed so as to give a PSD that was equal in power for a given range of frequencies at the observer radius in the free-field. This allowed the effect of installing the broadband source beneath a lifting wing on the PSD computed at the observers to easily be seen. Investigations were conducted using the NACA 0012 and RA16SC1 airfoils over non-uniform base flows. For a single-element airfoil, the major contributor to the obtained PSD was seen to be the distance of the source from the scattering surface.

The NACA 0012 airfoil was used to investigate the effect of varying angle of attack in the range $0° \leq \alpha \leq 8°$ with a fixed Mach number of $M_\infty = 0.2$, and the effect of varying the Mach number in the range $0.1 \leq M_\infty \leq 0.3$ with a fixed angle of attack of $\alpha = 5°$. It was seen that there was a negligible difference in the obtained PSD with varying angle of attack. There was a small difference in the obtained PSD with increasing Mach number. This was attributed to the convective effect of the flow effectively increasing the distance between the source and the airfoil

surface, which changes the frequencies where interference occurs. However, the major contributor was still concluded to be the distance of the source from the airfoil. The effect of varying flap and slat configuration was investigated using the RA16SC1 airfoil. Contour plots of PSD over frequency and observer angle showed that deployment of flap and slat had a large effect on the computed PSD. This was attributed to additional reflections from the flap cove, lower flap surface, and inside slat surface.

7.1.5 The Evaluation of BEM Flow Approximations for Landing Gear Noise Scattering Problems

Another of the aims of this thesis was to evaluate two existing BEM flow formulations for their suitability to model the scattering of landing gear noise sources. One formulation approximates the effect of a uniform flow using a Lorentz-type transform, and the other approximates the effect of a non-uniform potential flow using a transform proposed by Taylor [71]. Both methods reduce a convective wave equation to a regular Helmholtz equation through use of the respective transforms. This regular Helmholtz equation is then solved using standard BEM techniques. The formulations were evaluated in 2-D with comparison to the 2-D single frequency LEE solutions obtained for the investigations described in Section 7.1.1. It was assumed that the LEE solutions, which account for refraction through a non-uniform flow, were correct for the purpose of the evaluation.

In the non-uniform flow formulation, the acoustic pressure at an observer point is obtained by modifying the acoustic potential at that point, which is computed by the BEM, using the flow potential and its derivative at that point. A 2-D panel solver for multi-element airfoils was implemented in order to obtain the required flow potential at each observer for each case. In the derivation of the non-uniform flow formulation, terms of $O(M_\infty^2)$ are neglected. It was shown using a single-element airfoil that as the Mach number is increased with a fixed angle of attack, both flow formulations become less accurate with respect to the corresponding LEE solution. However, due to the neglecting of $O(M_\infty^2)$ terms, the non-uniform flow approximation becomes less accurate with increasing Mach number at a faster rate than the uniform flow approximation.

For a multi-element airfoil with a flap deployed at a high deflection angle, the reduction in flow velocity below the airfoil due to circulation is substantial. For the RA16SC1 airfoil with flap at 40° and a free-stream Mach number of $M_\infty = 0.2$,

the Mach number at the source location was approximately $M_0 = 0.13$. This large difference between the free-stream and local Mach number made the non-uniform flow approximation more accurate than the uniform flow approximation for this airfoil configuration. However, it cannot be concluded that the non-uniform flow formulation is generally better for an airfoil with deployed flap. If the free-stream velocity is high enough, the reduction in velocity below the airfoil might not be enough to make the non-uniform flow approximation more accurate than the uniform flow approximation. It was therefore concluded that the uniform flow approximation was generally a better choice for landing gear noise scattering predictions.

7.1.6 Coupling a Landing Gear Noise Source Model with a 3-D BEM Solver

The final aim of this thesis was to couple an existing landing gear noise model with a 3-D acoustic BEM solver. The landing gear noise model applies scaling laws to directional databases for isolated landing gear components in order to estimate far-field spectra for each component. The directional databases were acquired from CFD data coupled with an FWH solver. A particular landing gear configuration is specified from a selection of components, each with a given diameter, length, and rotation. The far-field spectra for all of the components are then summed to give an estimate of the total noise for the complete landing gear. Source installation effects can be included in the predictions. In order to do this, the reduction in flow velocity beneath the airfoil due to circulation is estimated using approximate values of the wing chord a and coefficient of lift C_L for the intended airfoil configuration.

In the current work, the far-field spectra for each landing gear configuration was integrated over octave bands. Two landing gear configurations were employed: an A320 MLG and an A320 NLG. The directivity obtained at each octave band centre frequency for each configuration was shown to be almost omni-directional up to 1000 Hz, which was expected following the discussion in Section 2.3. This allowed the noise from each landing gear to be represented by an omni-directional monopole for each octave band centre frequency. The strength of each source was chosen so as to match the average SPL of the directivity estimate for that landing gear configuration and frequency.

This coupling methodology was used to predict the SPL from installed landing gear noise sources on a 0.25 km^2 ground plane located 120 m below the nose of a

scattering aircraft geometry. The scattering geometry was chosen to be an A320-style aircraft, and the sources were located in the approximate location of each landing gear axle. Two configurations of the aircraft were chosen, which were flaps retracted and flaps deployed. This enabled the effect of flap deployment to be investigated. Following the results discussed in Section 7.1.5, the uniform flow BEM formulation was used for this investigation. A free-stream Mach number of $M_\infty = 0.2$ and angle of attack of $\alpha = 0°$ were used for both configurations to represent the typical approach conditions of a commercial airliner in high-lift configuration. Although physically unrealistic for the flap retracted configuration, keeping the flow parameters the same for both configurations allowed the geometrical effect of flap deployment to be investigated.

The geometrical effect of flap deployment was investigated using constant strength sources for each aircraft configuration. It was shown that the effect of flap deployment was to increase the SPL directly below and in the region immediately surrounding the aircraft. This was attributed to the additional flap surfaces reflecting a larger proportion of the incident wave from the MLG down towards these observers. It was shown that flap deployment does not have a significant effect on the scattering of the NLG sources, due to the comparatively large distance from the NLG source location to the flap surfaces. The source installation effect was then included in the predictions. It was shown that the SPL on the ground plane with flaps deployed is reduced by approximately 8 dB compared to the SPL with flaps retracted. This highlights the importance of including the source installation effect for installed landing gear noise predictions.

Finally, the effect of varying the position of the MLG sources was investigated at a single frequency. It was shown that the obtained SPL on the ground plane was sensitive to the source position. In particular, moving the source closer to the nacelle or flap showed additional shielding effects in the computed SPL. It was concluded that this is a drawback of the implemented methodology. Although an omni-directional monopole is capable of recreating the almost omni-directional far-field directivity of a landing gear, it does not recreate the non-compact acoustic source in the near field.

7.2 Future Work

There are a few areas of the current work that could be expanded upon with additional work in the future. These are summarised in the following sections.

7.2.1 Experimental Validation of Computational Methods

The computational methods employed throughout this thesis could be validated through experiments. There are examples in the literature of experiments that recreate a point source. Agarwal *et al.* [120] investigated the shielding effect of a flying wing airframe using a monopole source located above the geometry. Results from the experiments were used to validate a ray-tracing program that had been implemented for the investigation. In the experiments, a compression driver extended by a small diameter pipe was employed to simulate a monopole source. However, the experiments were conducted without flow, and so additional noise might be created by the pipe if a flow were required. Bahr *et al.* [121] investigated shear layer time-delay corrections for wind tunnel testing. They employed a non-intrusive method to simulate a monopole source, in which a plasma point source was created using a pulsed laser system.

7.2.2 Improving the Landing Gear Noise Source Model Coupling

One drawback of the implemented coupling methodology between the landing gear source model and the 3-D BEM solver has been noted, as discussed in Section 7.1.6. This is that the use of an omni-directional monopole allows the recreation of the almost omni-directional far-field directivity of a landing gear, but the point source does not recreate the realistic near-field non-compact acoustic source. A method developed by Vecherin *et al.* [117, 118] was also considered as an alternative for the coupling methodology. This method generates an equivalent source distribution that recreates a given far-field directivity pattern. A set of elementary configurations are constructed using point sources, each of which corresponding to a spherical harmonic. The elementary configurations are then linearly combined to reconstruct the required far-field directivity pattern.

This method was not chosen for the coupling implementation for two reasons. The authors noted that there will be errors in the source distribution if outliers exist in the target directivity, and there will be errors in the near-field if no phase information exists for the target directivity. Directivity estimates obtained from *SotonLGAP* do not contain phase information, and outliers can exist in the directivity estimates at higher frequencies. However, even if these issues could be overcome, one of the assumptions in the method is that the source distribution is compact. Therefore, a source distribution constructed using this method would

still not recreate a non-compact landing gear source in the near-field. A source distribution constructed using the method is also non-unique. If the method could be extended to construct a non-compact source distribution that is representative of a landing gear source in the near-field as well as the far-field, then landing gear source terms generated using this method might offer more accurate results for BEM scattering simulations than using a single monopole source.

7.2.3 Time-Domain BEM

Finally, recent advances for the time-domain BEM would enable further investigations into the scattering of landing gear noise sources by complex aircraft geometries. It was shown in Chapter 5 that results of single frequency simulations were in good agreement with a given frequency extracted from an equivalent broadband simulation. If a broadband source were used in a time-domain BEM simulation, all frequencies of interest would be computed simultaneously and the result for any required frequency could be extracted from the results. It was also discussed in Chapter 6 that in order to reduce the interference observed in SPL estimates from sources at discrete frequencies summed incoherently, a higher number of frequency bands should be used. This would require a larger number of simulations to be run. Using a broadband source in a time-domain BEM simulation would solve this issue, as interference would be greatly reduced.

Similar to the frequency-domain BEM, there were two major difficulties in the time-domain BEM: instability due to resonant frequencies, and computational cost [122]. A Burton-Miller type formulation was developed to achieve stability [123]. To reduce the computational cost, a FMM-style acceleration method was developed [124]. This reduced the computational cost from $O(N_t N^2)$ to $O(N_t N \log^2 N)$, where N is the total number of unknowns, and N_t is the total number of time steps. More recently, there have been further advances in the time-domain BEM specifically for aeroacoustic problems. Uniform flow approximation methods have been developed for arbitrary flow directions [122, 125], which would further enable the use of the time-domain BEM for landing gear noise scattering investigations.

Appendix

A LEE Simulation Data

This appendix lists data on each scattering LEE simulation undertaken for this thesis, including details of the grids used. All LEE simulations, including the computation of non-uniform base flows, were conducted on the high performance computing cluster *Iridis 4*. Each compute node of the cluster has dual 2.6 GHz Intel Sandybridge processors giving 16 cores per node with 64 GB of memory.

Table A.1: 2-D LEE scattering validation simulation.

Geometry	f (Hz)	Δt (s)	CFL	Number of cores	Time taken (hrs:mins:secs)
Cylinder	325	7.24×10^{-7}	0.417	128	00:11:52

Table A.2: Details of 2-D LEE airfoil grids. All lengths in m.

Configuration	Number of blocks	Number of nodes ($\times 10^5$)			Max Δx ($\times 10^{-2}$)
		125 Hz	250 Hz	500 Hz	
NACA 0012	97	2.09	2.13	2.21	4.5
RA16SC1	97	6.65	6.73	6.87	3.1
RA16SC1 with flap 20°	180	8.21	8.29	8.44	3.0
RA16SC1 with flap 40°	179	7.64	7.72	7.86	3.0
RA16SC1 with flap 40° plus slat	178	8.12	8.20	8.34	3.0

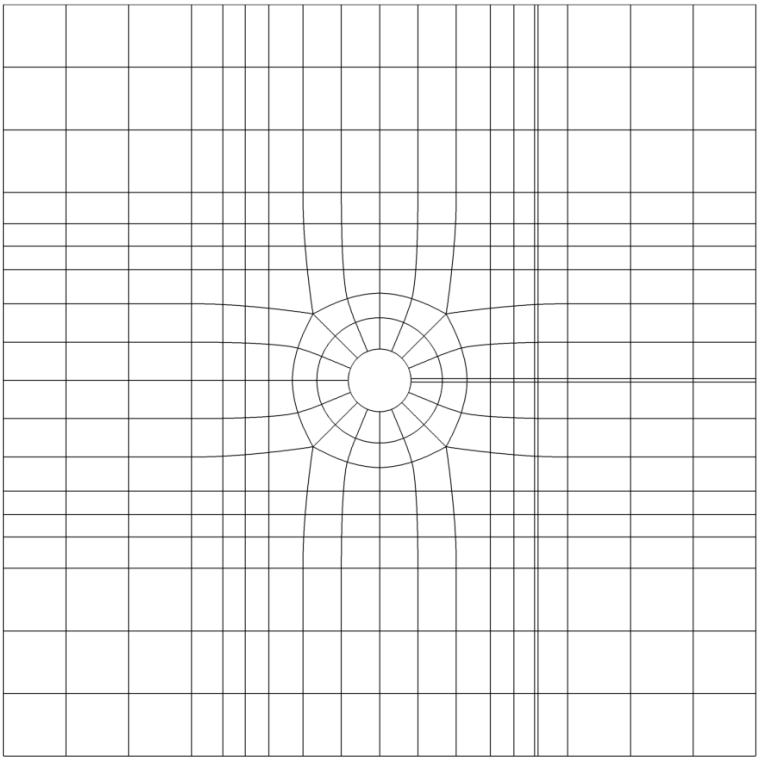

Figure A.1: Grid topology, circular cylinder.

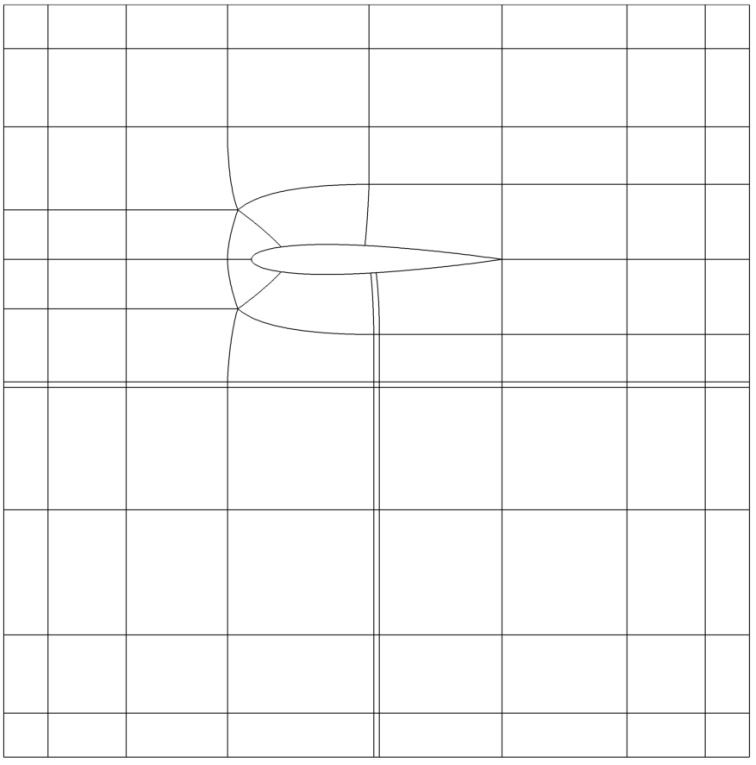

Figure A.2: Grid topology, NACA 0012 airfoil.

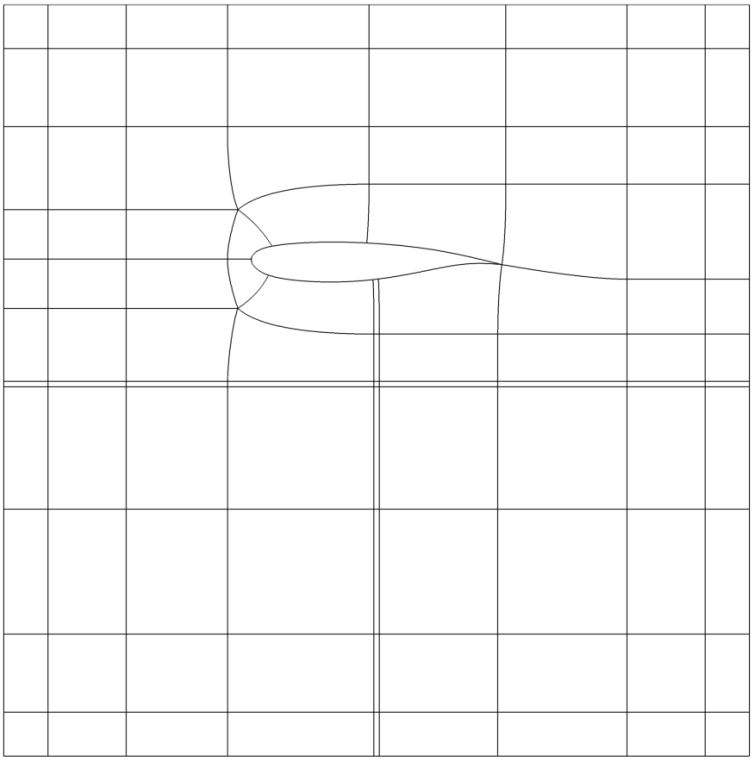

Figure A.3: Grid topology, RA16SC1 airfoil.

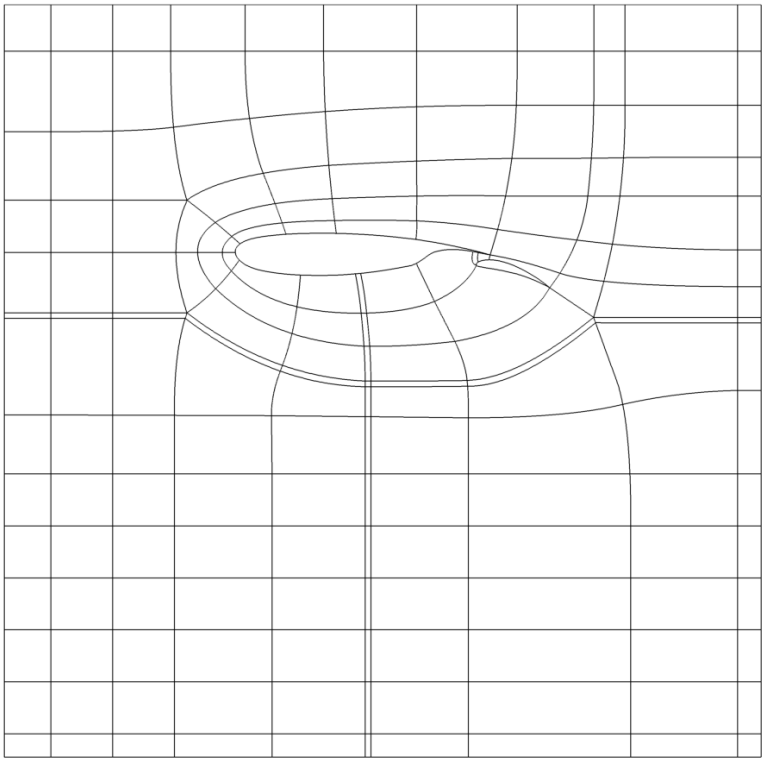

Figure A.4: Grid topology, RA16SC1 airfoil with flap 20°.

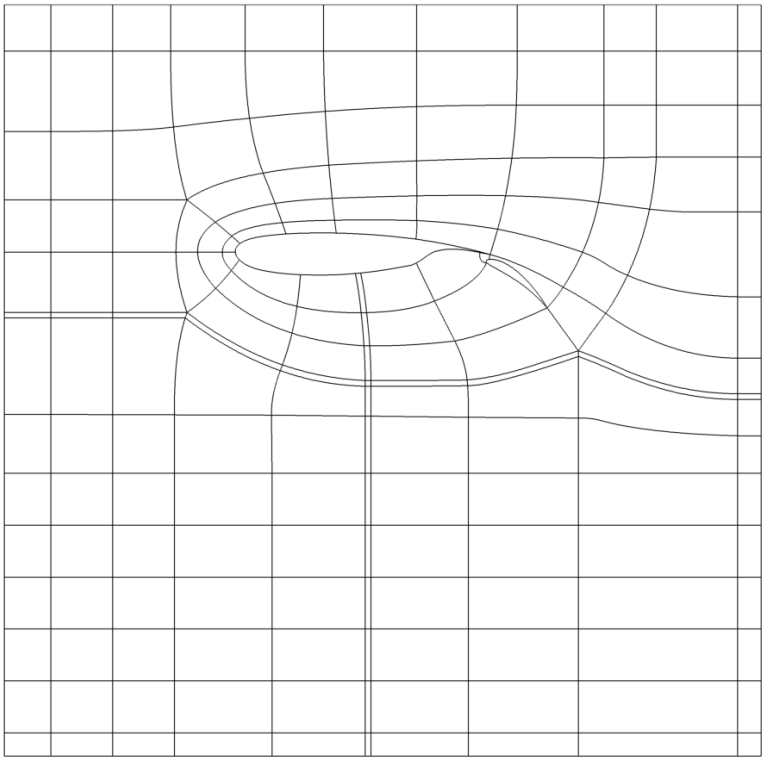

Figure A.5: Grid topology, RA16SC1 airfoil with flap 40°.

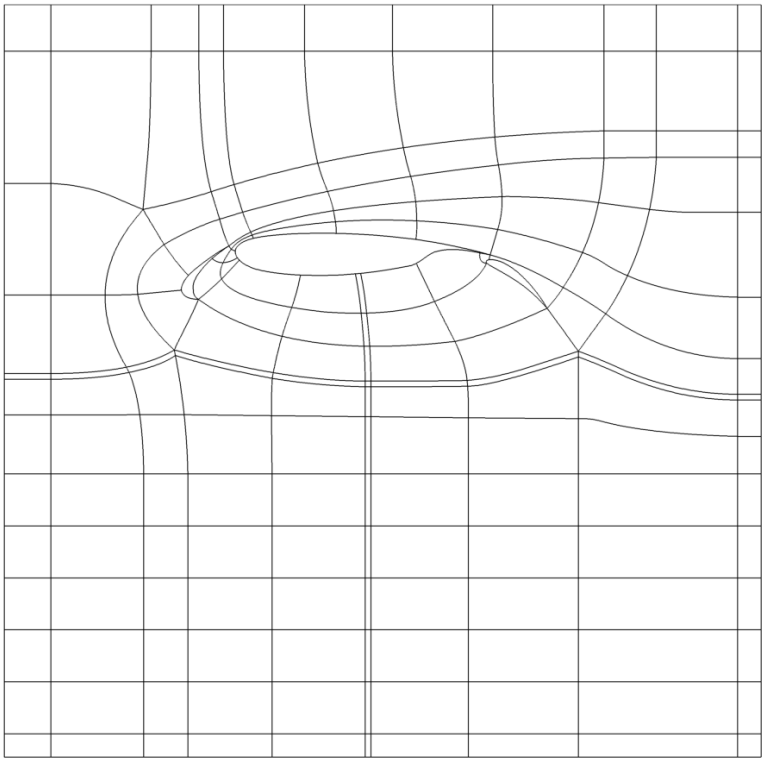

Figure A.6: Grid topology, RA16SC1 airfoil with flap 40° plus slat.

Table A.3: 2-D LEE single frequency simulations. Airfoil: N = NACA 0012, R = RA16SC1, R20 = RA16SC1 with flap 20°, R40 = RA16SC1 with flap 40°. Flow: NU = non-uniform, U = uniform.

Airfoil	f (Hz)	Flow	M_∞	α (°)	Δt (s)	CFL	Number of cores	Time taken (hrs:mins:secs)
N	125	-	0.0	-	8.42×10^{-6}	0.489	16	00:09:35
N	125	NU	0.1	5	8.42×10^{-6}	0.489	16	00:09:43
N	125	NU	0.15	5	8.42×10^{-6}	0.489	16	00:09:42
N	125	NU	0.2	0	8.42×10^{-6}	0.489	16	00:09:46
N	125	NU	0.2	1	8.42×10^{-6}	0.489	16	00:09:40
N	125	NU	0.2	2	8.42×10^{-6}	0.489	16	00:09:43
N	125	NU	0.2	3	8.42×10^{-6}	0.489	16	00:09:48
N	125	NU	0.2	4	8.42×10^{-6}	0.489	16	00:09:50
N	125	NU	0.2	5	8.42×10^{-6}	0.489	16	00:09:58
N	125	NU	0.2	6	8.42×10^{-6}	0.489	16	00:09:40
N	125	NU	0.2	7	8.42×10^{-6}	0.489	16	00:09:41
N	125	NU	0.2	8	8.42×10^{-6}	0.489	16	00:09:42
N	125	NU	0.25	5	8.42×10^{-6}	0.489	16	00:09:42
N	125	NU	0.3	5	8.42×10^{-6}	0.489	16	00:09:47
N	125	U	0.1	5	8.42×10^{-6}	0.489	16	00:09:35
N	125	U	0.15	5	8.42×10^{-6}	0.489	16	00:09:37
N	125	U	0.2	0	8.42×10^{-6}	0.489	16	00:09:36
N	125	U	0.2	1	8.42×10^{-6}	0.489	16	00:09:36
N	125	U	0.2	2	8.42×10^{-6}	0.489	16	00:09:35
N	125	U	0.2	3	8.42×10^{-6}	0.489	16	00:09:35
N	125	U	0.2	4	8.42×10^{-6}	0.489	16	00:09:36
N	125	U	0.2	5	8.42×10^{-6}	0.489	16	00:09:34
N	125	U	0.2	6	8.42×10^{-6}	0.489	16	00:09:37
N	125	U	0.2	7	8.42×10^{-6}	0.489	16	00:09:35
N	125	U	0.2	8	8.42×10^{-6}	0.489	16	00:09:41
N	125	U	0.25	5	8.42×10^{-6}	0.489	16	00:09:39
N	125	U	0.3	5	8.42×10^{-6}	0.489	16	00:09:35
N	250	-	0.0	-	6.67×10^{-6}	0.496	16	00:08:42

Table A.3: (continued)

Airfoil	f (Hz)	Flow	M_∞	α (°)	Δt (s)	CFL	Number of cores	Time taken (hrs:mins:secs)
N	250	NU	0.1	5	6.67×10^{-6}	0.496	16	00:08:51
N	250	NU	0.15	5	6.67×10^{-6}	0.496	16	00:08:54
N	250	NU	0.2	0	6.67×10^{-6}	0.496	16	00:08:57
N	250	NU	0.2	1	6.67×10^{-6}	0.496	16	00:08:57
N	250	NU	0.2	2	6.67×10^{-6}	0.496	16	00:08:51
N	250	NU	0.2	3	6.67×10^{-6}	0.496	16	00:08:55
N	250	NU	0.2	4	6.67×10^{-6}	0.496	16	00:08:54
N	250	NU	0.2	5	6.67×10^{-6}	0.496	16	00:09:03
N	250	NU	0.2	6	6.67×10^{-6}	0.496	16	00:08:51
N	250	NU	0.2	7	6.67×10^{-6}	0.496	16	00:08:52
N	250	NU	0.2	8	6.67×10^{-6}	0.496	16	00:08:51
N	250	NU	0.25	5	6.67×10^{-6}	0.496	16	00:08:52
N	250	NU	0.3	5	6.67×10^{-6}	0.496	16	00:08:51
N	250	U	0.1	5	6.67×10^{-6}	0.496	16	00:08:47
N	250	U	0.15	5	6.67×10^{-6}	0.496	16	00:08:48
N	250	U	0.2	0	6.67×10^{-6}	0.496	16	00:08:45
N	250	U	0.2	1	6.67×10^{-6}	0.496	16	00:08:45
N	250	U	0.2	2	6.67×10^{-6}	0.496	16	00:08:43
N	250	U	0.2	3	6.67×10^{-6}	0.496	16	00:08:44
N	250	U	0.2	4	6.67×10^{-6}	0.496	16	00:08:44
N	250	U	0.2	5	6.67×10^{-6}	0.496	16	00:08:46
N	250	U	0.2	6	6.67×10^{-6}	0.496	16	00:08:44
N	250	U	0.2	7	6.67×10^{-6}	0.496	16	00:08:43
N	250	U	0.2	8	6.67×10^{-6}	0.496	16	00:08:43
N	250	U	0.25	5	6.67×10^{-6}	0.496	16	00:08:48
N	250	U	0.3	5	6.67×10^{-6}	0.496	16	00:08:50
N	500	-	0.0	-	3.08×10^{-6}	0.483	16	00:16:01
N	500	NU	0.1	5	3.08×10^{-6}	0.483	16	00:16:11
N	500	NU	0.15	5	3.08×10^{-6}	0.483	16	00:16:12
N	500	NU	0.2	0	3.08×10^{-6}	0.483	16	00:16:08

Table A.3: (continued)

Airfoil	f (Hz)	Flow	M_∞	α (°)	Δt (s)	CFL	Number of cores	Time taken (hrs:mins:secs)
N	500	NU	0.2	1	3.08×10^{-6}	0.483	16	00:16:17
N	500	NU	0.2	2	3.08×10^{-6}	0.483	16	00:16:18
N	500	NU	0.2	3	3.08×10^{-6}	0.483	16	00:16:10
N	500	NU	0.2	4	3.08×10^{-6}	0.483	16	00:16:16
N	500	NU	0.2	5	3.08×10^{-6}	0.483	16	00:16:16
N	500	NU	0.2	6	3.08×10^{-6}	0.483	16	00:16:13
N	500	NU	0.2	7	3.08×10^{-6}	0.483	16	00:16:12
N	500	NU	0.2	8	3.08×10^{-6}	0.483	16	00:16:15
N	500	NU	0.25	5	3.08×10^{-6}	0.483	16	00:16:17
N	500	NU	0.3	5	3.08×10^{-6}	0.483	16	00:16:17
N	500	U	0.1	5	3.08×10^{-6}	0.483	16	00:16:01
N	500	U	0.15	5	3.08×10^{-6}	0.483	16	00:15:59
N	500	U	0.2	0	3.08×10^{-6}	0.483	16	00:16:02
N	500	U	0.2	1	3.08×10^{-6}	0.483	16	00:15:59
N	500	U	0.2	2	3.08×10^{-6}	0.483	16	00:16:01
N	500	U	0.2	3	3.08×10^{-6}	0.483	16	00:16:14
N	500	U	0.2	4	3.08×10^{-6}	0.483	16	00:15:59
N	500	U	0.2	5	3.08×10^{-6}	0.483	16	00:16:01
N	500	U	0.2	6	3.08×10^{-6}	0.483	16	00:16:00
N	500	U	0.2	7	3.08×10^{-6}	0.483	16	00:15:58
N	500	U	0.2	8	3.08×10^{-6}	0.483	16	00:15:58
N	500	U	0.25	5	3.08×10^{-6}	0.483	16	00:16:02
N	500	U	0.3	5	3.08×10^{-6}	0.483	16	00:15:55
R	125	-	0.0	-	7.62×10^{-7}	0.074	64	01:38:54
R	125	NU	0.2	0	7.62×10^{-7}	0.074	64	02:14:50
R	125	U	0.2	0	7.62×10^{-7}	0.074	64	02:22:13
R	250	-	0.0	-	7.62×10^{-7}	0.074	64	01:41:20
R	250	NU	0.2	0	7.62×10^{-7}	0.074	64	01:50:37
R	250	U	0.2	0	7.62×10^{-7}	0.074	64	01:52:26
R	500	-	0.0	-	7.62×10^{-7}	0.120	64	01:32:03

Table A.3: (continued)

Airfoil	f (Hz)	Flow	M_∞	α (°)	Δt (s)	CFL	Number of cores	Time taken (hrs:mins:secs)
R	500	NU	0.2	0	7.62×10^{-7}	0.120	64	01:37:51
R	500	U	0.2	0	7.62×10^{-7}	0.120	64	01:39:49
R20	125	-	0.0	-	7.62×10^{-7}	0.209	64	02:48:37
R20	125	NU	0.2	0	7.62×10^{-7}	0.209	64	02:48:43
R20	125	U	0.2	0	7.62×10^{-7}	0.209	64	02:49:22
R20	250	-	0.0	-	7.62×10^{-7}	0.209	64	01:58:23
R20	250	NU	0.2	0	7.62×10^{-7}	0.209	64	02:11:22
R20	250	U	0.2	0	7.62×10^{-7}	0.209	64	02:13:09
R20	500	-	0.0	-	7.62×10^{-7}	0.209	64	02:10:01
R20	500	NU	0.2	0	7.62×10^{-7}	0.209	64	02:10:55
R20	500	U	0.2	0	7.62×10^{-7}	0.209	64	02:17:55
R40	125	-	0.0	-	7.62×10^{-7}	0.285	64	02:05:20
R40	125	NU	0.2	0	7.62×10^{-7}	0.285	64	02:43:05
R40	125	U	0.2	0	7.62×10^{-7}	0.285	64	02:46:19
R40	250	-	0.0	-	7.62×10^{-7}	0.285	64	01:48:28
R40	250	NU	0.2	0	7.62×10^{-7}	0.285	64	02:25:02
R40	250	U	0.2	0	7.62×10^{-7}	0.285	64	02:26:33
R40	500	-	0.0	-	7.62×10^{-7}	0.285	64	01:43:11
R40	500	NU	0.2	0	7.62×10^{-7}	0.285	64	02:12:55
R40	500	U	0.2	0	7.62×10^{-7}	0.285	64	02:11:53

Table A.4: 2-D LEE single frequency simulations with a higher Mach number. Airfoil: N = NACA 0012. Flow: NU = non-uniform, U = uniform.

Airfoil	f (Hz)	Flow	M_∞	α (°)	Δt (s)	CFL	Number of cores	Time taken (hrs:mins:secs)
N	250	NU	0.6	3	6.67×10^{-6}	0.496	128	01:06:44
N	250	U	0.6	3	6.67×10^{-6}	0.496	128	01:05:37

Table A.5: 2-D LEE single frequency simulations with an alternative source location. Airfoil: N = NACA 0012. Flow: NU = non-uniform, U = uniform.

Airfoil	f (Hz)	Flow	M_∞	α (°)	Δt (s)	CFL	Number of cores	Time taken (hrs:mins:secs)
N	250	NU	0.2	3	6.67×10^{-6}	0.496	16	00:09:04
N	250	NU	0.3	3	6.67×10^{-6}	0.496	16	00:08:52
N	250	NU	0.4	3	6.67×10^{-6}	0.496	128	00:53:17
N	250	NU	0.5	3	6.67×10^{-6}	0.496	128	00:54:59
N	250	NU	0.6	3	6.67×10^{-6}	0.496	128	01:07:29
N	250	U	0.2	3	6.67×10^{-6}	0.496	16	00:08:52
N	250	U	0.3	3	6.67×10^{-6}	0.496	16	00:08:46
N	250	U	0.4	3	6.67×10^{-6}	0.496	128	00:51:39
N	250	U	0.5	3	6.67×10^{-6}	0.496	128	00:52:28
N	250	U	0.6	3	6.67×10^{-6}	0.496	128	01:04:35

Table A.6: 3-D LEE single frequency simulations. Airfoil: N = NACA 0012. Flow: NU = non-uniform, U = uniform.

Airfoil	f (Hz)	Flow	M_∞	α (°)	Δt (s)	CFL	Number of cores	Time taken (hrs:mins:secs)
N	250	NU	0.2	4	2.81×10^{-6}	0.493	400	56:41:09
N	250	U	0.2	4	2.81×10^{-6}	0.493	400	54:38:52

Table A.7: 2-D LEE broadband simulations. Airfoil: N = NACA 0012, R = RA16SC1, R20 = RA16SC1 with flap 20°, R40 = RA16SC1 with flap 40°, R40s = RA16SC1 with flap 40° plus slat. Flow: NU = non-uniform, U = uniform.

Airfoil	Flow	M_∞	α (°)	Δt (s)	CFL	Number of cores	Time taken (hrs:mins:secs)
N	NU	0.1	5	3.20×10^{-6}	0.503	64	06:14:16
N	NU	0.2	0	3.20×10^{-6}	0.503	64	06:40:28

Table A.7: (continued)

Airfoil	Flow	M_∞	α (°)	Δt (s)	CFL	Number of cores	Time taken (hrs:mins:secs)
N	NU	0.2	1	3.20×10^{-6}	0.503	64	06:06:21
N	NU	0.2	2	3.20×10^{-6}	0.503	64	06:39:44
N	NU	0.2	3	3.20×10^{-6}	0.503	64	06:28:51
N	NU	0.2	4	3.20×10^{-6}	0.503	64	06:32:43
N	NU	0.2	5	3.20×10^{-6}	0.503	64	06:35:48
N	NU	0.2	6	3.20×10^{-6}	0.503	64	06:58:34
N	NU	0.2	7	3.20×10^{-6}	0.503	64	07:16:05
N	NU	0.2	8	3.20×10^{-6}	0.503	64	06:59:37
N	NU	0.3	5	3.20×10^{-6}	0.503	64	06:06:35
N	U	0.1	5	3.20×10^{-6}	0.503	64	06:09:56
N	U	0.2	0	3.20×10^{-6}	0.503	64	06:54:56
N	U	0.2	1	3.20×10^{-6}	0.503	64	06:03:40
N	U	0.2	2	3.20×10^{-6}	0.503	64	06:58:57
N	U	0.2	3	3.20×10^{-6}	0.503	64	07:30:00
N	U	0.2	4	3.20×10^{-6}	0.503	64	06:38:24
N	U	0.2	5	3.20×10^{-6}	0.503	64	06:33:05
N	U	0.2	6	3.20×10^{-6}	0.503	64	06:46:41
N	U	0.2	7	3.20×10^{-6}	0.503	64	06:23:44
N	U	0.2	8	3.20×10^{-6}	0.503	64	06:32:29
N	U	0.3	5	3.20×10^{-6}	0.503	64	06:03:38
R	NU	0.2	0	3.20×10^{-6}	0.502	96	08:52:37
R	U	0.2	0	3.20×10^{-6}	0.502	96	08:39:03
R20	NU	0.2	0	1.60×10^{-6}	0.439	160	14:43:40
R20	U	0.2	0	1.60×10^{-6}	0.439	160	14:08:55
R40	NU	0.2	0	1.07×10^{-6}	0.400	176	19:10:05
R40	U	0.2	0	1.07×10^{-6}	0.400	176	17:43:34
R40s	NU	0.2	0	6.40×10^{-7}	0.425	176	35:22:31
R40s	U	0.2	0	6.40×10^{-7}	0.425	176	37:57:44

B BEM Simulation Data

This appendix lists data for all BEM simulations undertaken for this thesis, including details of the geometries and surface meshes used. All 2-D BEM and panel solver simulations were conducted on a desktop computer with an Intel Core i7-2600 3.4 GHz processor and 16 GB of memory running Ubuntu Linux 12.04 LTS. For each 2-D LEE simulation listed in Table A.3, an equivalent 2-D BEM solution was also conducted. A full list is omitted here. Each acoustic BEM simulation took at most 1 s to compute the acoustic pressure at each observer using a single core. Each panel solver simulation took at most 1 s to compute the flow potential and its derivative at each observer using a single core. The flow potential and its derivative are both required for the non-uniform flow BEM approximation. All 3-D BEM simulations were conducted on *Iridis 4*. In all that follows, Actipole is the name of the acoustic solver, Coucha is the name of the surface post-processor, and Proche is the name of the observer post-processor.

Table B.1: 3-D BEM scattering validation simulation. The acoustic pressure was obtained at two sets of observers using Proche: 1 = directivity radius, 2 = evaluation plane.

Geometry	f (Hz)	Number of cores			Time taken (hrs:mins:secs)		
		Actipole	Proche[1]	Proche[2]	Actipole	Proche[1]	Proche[2]
Sphere	325	16	16	16	00:01:57	00:00:17	00:01:24

Table B.2: 3-D BEM airfoil simulation.

Geometry	f (Hz)	Number of cores		Time taken (hrs:mins:secs)	
		Actipole	Proche	Actipole	Proche
NACA 0012	250	64	32	00:07:03	00:00:30

Table B.3: Details of 2-D boundary meshes for the BEM and panel solvers. All lengths in m.

Configuration	Number of boundary elements		Average element length ($\times 10^{-2}$)
	Main	Flap	
NACA 0012	260	-	4.0
RA16SC1	500	-	2.0
RA16SC1 with flap 20°	500	150	2.0
RA16SC1 with flap 40°	500	150	2.0

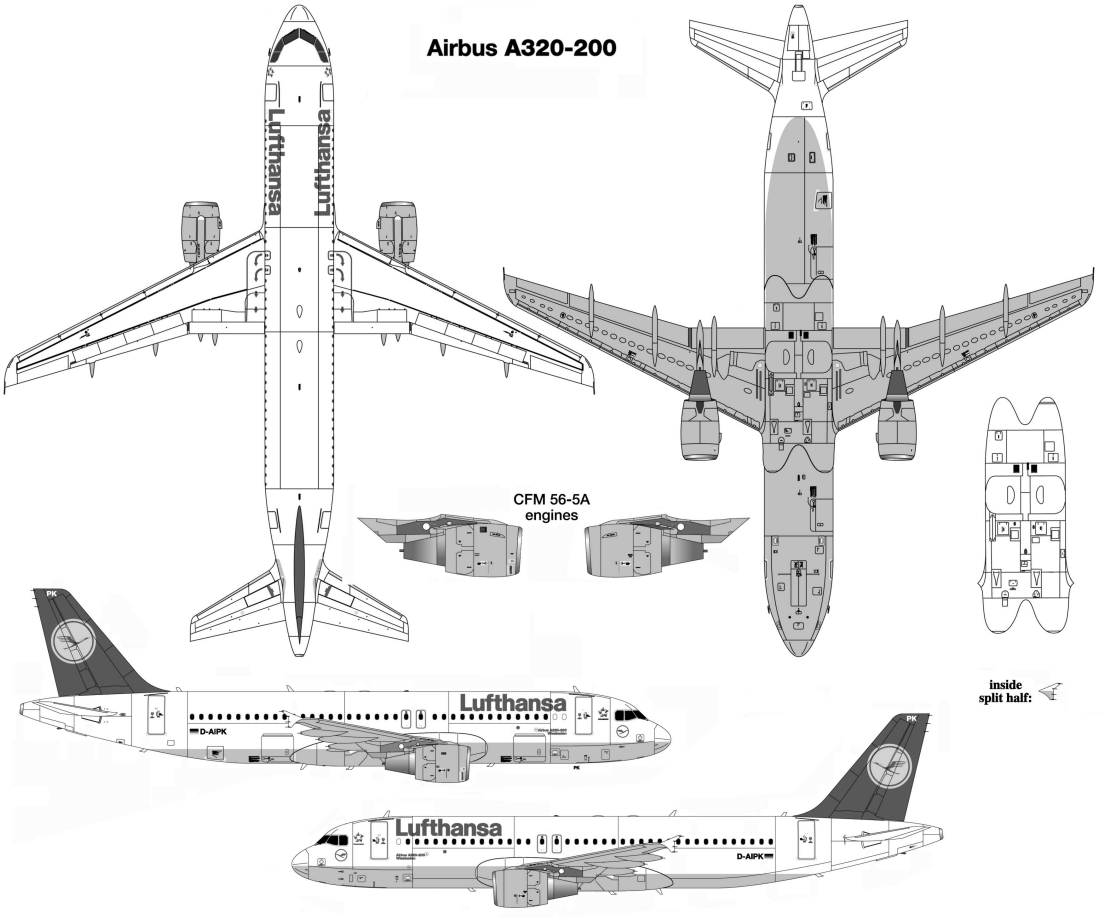

Figure B.1: Reference images used for the construction of the A320-style geometry. [Online] Available: http://drawingdatabase.com/airbus-a320-200/ [Accessed: 16th January 2015].

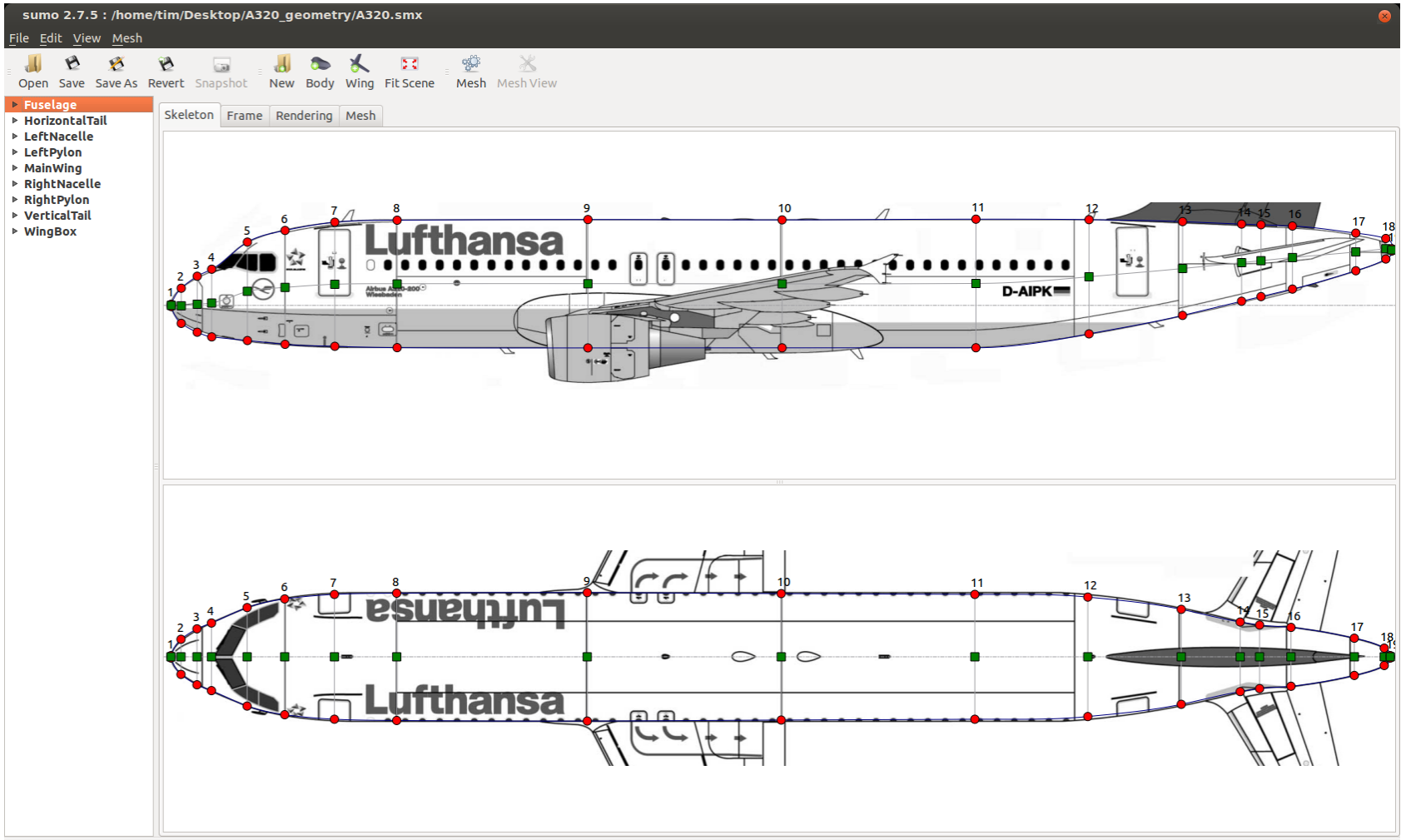

Figure B.2: Creating the A320-style fuselage surface using *Larosterna Sumo*.

Table B.4: Details of 3-D A320 boundary element meshes. FR = flaps retracted, FD = flaps deployed. All lengths in m.

	500 Hz		1000 Hz	
	FR	FD	FR	FD
Number of boundary elements ($\times 10^6$)	2.43	2.70	5.49	6.55
Number of points ($\times 10^6$)	1.22	1.35	2.74	3.28
Average Δx ($\times 10^{-2}$)	2.82	2.74	1.85	1.71
Maximum Δx ($\times 10^{-2}$)	7.79	7.79	4.45	4.45
Average number of elements per wavelength	19.68	20.25	14.92	16.02
Minimum number of elements per wavelength	8.52	8.52	7.49	7.49

Table B.5: 3-D BEM aircraft simulations. FR = flaps retracted, FD = flaps deployed.

Geometry	f (Hz)	Number of cores			Time taken (hrs:mins:secs)		
		Actipole	Coucha	Proche	Actipole	Coucha	Proche
FR	125	64	16	32	07:08:01	00:13:23	00:27:04
FR	250	64	16	32	07:12:52	00:13:57	00:29:12
FR	500	64	16	32	05:02:55	00:13:35	00:29:52
FR	1000	256	16	32	14:01:14	00:47:01	01:07:51
FD	125	64	16	32	09:12:48	00:14:31	00:28:08
FD	250	64	16	32	06:14:53	00:16:59	00:32:24
FD	500	64	16	32	08:24:26	00:15:58	00:33:34
FD	1000	256	16	32	24:43:01	01:04:18	01:20:00

Table B.6: 3-D BEM aircraft simulations with alternative source positions. All conducted with the flaps deployed geometry. XM1 = $x - 1\,\text{m}$, XP1 = $x + 1\,\text{m}$, ZP1 = $z + 1\,\text{m}$.

Sources	f (Hz)	Number of cores			Time taken (hrs:mins:secs)		
		Actipole	Coucha	Proche	Actipole	Coucha	Proche
XM1	500	64	16	32	07:20:56	00:14:14	00:32:26
XP1	500	64	16	32	07:20:29	00:14:29	00:33:07
ZP1	500	64	16	32	07:56:59	00:15:25	00:32:10

Table B.7: Airbus A320 MLG geometry input for *SotonLGAP*.

Strut	Type	Diameter	Length	U Ratio	Rx	Ry
Lower strut	1.00	0.231	1.085	1	11	5
Upper strut	3.31	0.231	0.853	1	11	5
Drag stay	3.32	0.085	0.853	1	11	5
Upper side stay	2.30	0.119	0.666	1	-26	3.4
Lower side stay	2.30	0.124	0.923	1	-26	3.4
Upper torque link	2.30	0.163	0.303	1	11	-48.1
Lower torque link	2.30	0.163	0.303	1	11	1.7
Lock stay	4.00	0.034	0.793	1	65.6	2.2
Axle	5.11	0.131	0.441	1	101	5
Wheel 1	7.31	1.284	0.476	1	101	5
Wheel 2	7.31	1.284	0.476	1	101	5
Brakes 1	7.41	0.510	0.308	1	101	6
Brakes 2	7.41	0.510	0.308	1	101	7
Lock actuator	2.45	0.045	0.6	1	-49	0
Wheel detail 1	7.51	1.284	0.4764	1	101	5
Wheel detail 2	7.51	1.284	0.4764	1	101	5
Door	8.00	0.9681	1	1	11	5

Table B.8: Airbus A320 NLG geometry input for *SotonLGAP*.

Strut	Type	Diameter	Length	U Ratio	Rx	Ry
Axle	5.11	0.11	0.275	1	90	0
Upper leg	1	0.1775	1.13	1	0	0
Lower leg	1	0.1375	0.595	1	0	0
Wheel 1	5.31	0.75	0.22	1	90	0
Wheel 2	5.31	0.75	0.22	1	90	0

Table B.9: Mean values of SPL and equivalent source strengths for A320 MLG and NLG from *SotonLGAP* estimate without installation effect.

Frequency (Hz)	MLG		NLG	
	Mean SPL (dB)	Q	Mean SPL (dB)	Q
62.5	100.005	35.564	90.754	12.259
125.0	110.127	114.047	104.662	60.795
250.0	112.297	146.426	106.272	73.172
500.0	116.281	231.639	103.007	50.245
1000.0	111.372	131.636	96.860	24.759
2000.0	109.795	109.781	89.597	10.730
4000.0	104.592	60.307	80.595	3.806

Table B.10: Mean values of SPL and equivalent source strengths for A320 MLG from *SotonLGAP* estimate with installation effect.

Frequency (Hz)	$C_L = 0.6$		$C_L = 2.5$	
	Mean SPL (dB)	Q	Mean SPL (dB)	Q
62.5	99.034	31.802	90.922	12.499
125.0	109.636	107.785	101.044	40.082
250.0	111.754	137.544	103.215	51.461
500.0	115.563	213.249	107.198	81.409
1000.0	113.877	175.641	102.290	46.263
2000.0	113.786	173.799	100.713	38.582
4000.0	114.201	182.314	95.509	21.195

C Guidance for *SotonLGAP* Subroutine to Generate *ACTIPOLE* Input Files

An additional subroutine was written for *SotonLGAP* that generates *ACTIPOLE* input files for a given run. Guidance on the use of this subroutine is provided in this appendix.

The additional variables required for *SotonLGAP* in the `input.xls` file in order to generate the *ACTIPOLE* input files are summarised in Table C.1. The source location relative to the geometry needs to be specified. Figure C.1 shows the coordinate system that should be used, and the location of a main landing gear source. The flow is assumed to be aligned with the x-axis, so the aircraft angle of attack should be taken into account by rotation of the geometry. For both the A340 and A320 landing gears, the source should be located 60 % of the overall gear length beneath the pressure surface of the wing. This was determined by calculating an average source strength averaged over the observer angles as a function of vertical distance along the landing gear length. The centroid was calculated to give the vertical location of an equivalent single source. The value was similar for both gears (59.5 % for A320 and 58.1 % for A340). Therefore the recommended vertical location of the landing gear source is 60 % of the overall gear length beneath the pressure surface of the wing along the axis of the cylindrical strut.

Table C.1: Additional variables in *SotonLGAP* input file `input.xls` that control *ACTIPOLE* output.

Input variable	Description
Output *ACTIPOLE* (0 = No; 1 = Yes)	Switch to output the input files required for *ACTIPOLE*
ACTIPOLE frequency bands	$1/N$ octave bands for *ACTIPOLE* output (e.g., 3 = one-third octave, 1 = octave, etc.)
Maximum frequency band for *ACTIPOLE* output	Maximum frequency to output for *ACTIPOLE*
ACTIPOLE source location relative to geometry (x, y, z)	Source location relative to the origin of the *ACTIPOLE* coordinate system shown in Figure C.1
ACTIPOLE geometry `.unv` file	Name of the `.d01` file obtained after running the *ANADEL* pre-processor

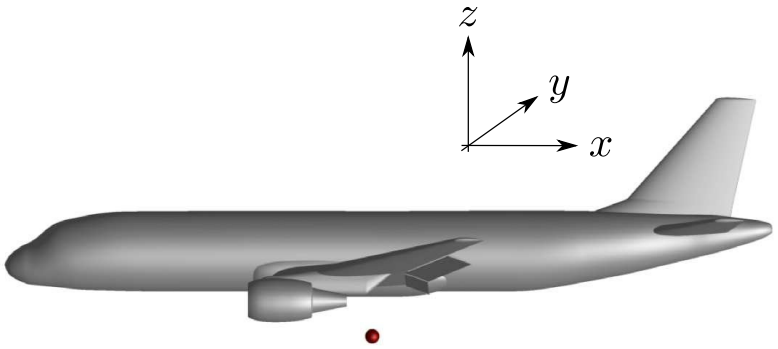

Figure C.1: Source location for *ACTIPOLE*. 60 % of the overall gear length beneath the pressure surface of the wing.

In *ACTIPOLE*, there are many options for specifying the position of the observers. One can list coordinates directly; specify regular 1-D, 2-D, or 3-D grids using min/max/increment arguments; or specify a `.unv` mesh file where the solution will be computed. The solution used in *SotonLGAP*, that allows the most flexibility, is to have a single file in the specified input directory in which the desired positions are specified in the format that is required in the generated `.p17` input files. The name of this file must be `ACTIPOLE_observer_locations.txt` and it must be located in the input directory along with `input.xls`, `geom.xls`, etc., for that run. The correct format to use is specified in the *ACTIPOLE* manual [66]. An example of the observer position file `ACTIPOLE_observer_locations.txt` is shown in Figure C.2. This example is of a 2-D grid, which was used to obtain the ground plane results shown in Section 6.5.

When specifying the observers in *SotonLGAP* to generate a landing gear source for *ACTIPOLE*, the region above the landing gear is as important as below the source, as this is the region where the source is incident to the aircraft surface. It is this incident field on the aircraft surface that is used to calculate the scattered field in the BEM. The scattered field is summed with the incident field to give the total field. The observer angle sweep should be over all 36 observers for the complete 360° at spacing of 10° as shown in Figure C.3.

```
2DGRID
-232.  -250.  -120.
 268.  -250.  -120.
-232.   250.  -120.
501 501
```

Figure C.2: Example contents of the *ACTIPOLE* observer position file `ACTIPOLE_observer_locations.txt` for a 2-D grid.

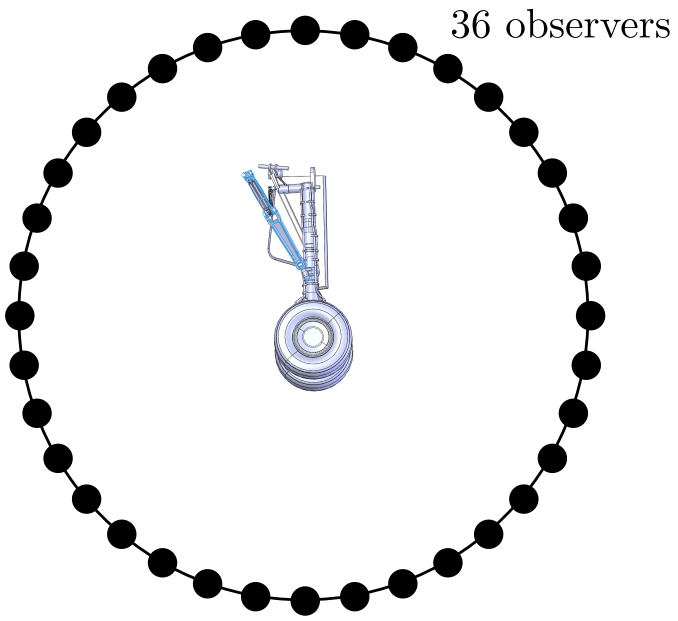

Figure C.3: Example of observers specified in *SotonLGAP* to generate landing gear sources for *ACTIPOLE*.

The *ACTIPOLE* output subroutine generates the following files:

- `.p01` input files for the *ACTIPOLE* solver for each frequency,
- `.p16` input files for the *COUCHA* surface post-processor for each frequency,
- `.p17` input files for the *PROCHE* observer post-processor for each frequency.

These generated files are placed in a folder named `Actipole_output_files` located in the specified run output directory. The folder also contains a summary of the output from the subroutine in `Actipole_output.csv` and a copy of the *SotonLGAP* input files for reference.

The landing gear source strength is represented as a single monopole to represent the approximately omni-directional landing gear directivity. The strength of the monopole Q is set to give the average SPL of the directivity obtained from *SotonLGAP* as shown in Figure C.3.

As an alternative, *ACTIPOLE*'s spherical wave formulation was investigated. In this case, a directivity pattern would be given as an input to the solver. However IMACS advised not to use this formulation with flow as it is inaccurate/unstable with flow. Another alternative considered to account for directivity was the use of spherical harmonics to construct an equivalent point-source distribution that reproduces a given directivity pattern in the far-field (Vecherin *et al.* [117, 118]). However this method introduces errors in the near-field if no phase information

exists for the directivity, as is the case for the predictions from *SotonLGAP*. Therefore, for the BEM solver, the landing gear sources are approximated to be omni-directional monopoles.

The calculation procedure in the subroutine is as follows. For each frequency, the obtained SPL at each observer shown in Figure C.3 is converted to p_{rms}. These values are then used to compute a mean value of p_{rms} for that frequency, which is then used to set the strength Q of the equivalent source. In order to find Q, the root mean square pressure is written in terms of the complex acoustic pressure using

$$p_{\text{rms}}(\mathbf{x}) = \frac{|p(\mathbf{x})|}{\sqrt{2}}. \tag{C.1}$$

Using the 3-D Green's function representation for the complex acoustic pressure $p(\mathbf{x})$, this can be written as

$$p_{\text{rms}}(\mathbf{x}) = \frac{Q|\exp(ikr)/(4\pi r)|}{\sqrt{2}}. \tag{C.2}$$

Equation (C.2) can be rearranged to find Q for a given frequency using the average value of p_{rms} computed using *SotonLGAP*. In this case, Q is real-valued due to using a single source, and the lack of phase information.

Equation (C.1) should be used when post-processing the results obtained using *COUCHA* or *PROCHE* in order to compute p_{rms}. This can then be used to compute the SPL.

D Additional 2-D LEE Simulation Examples

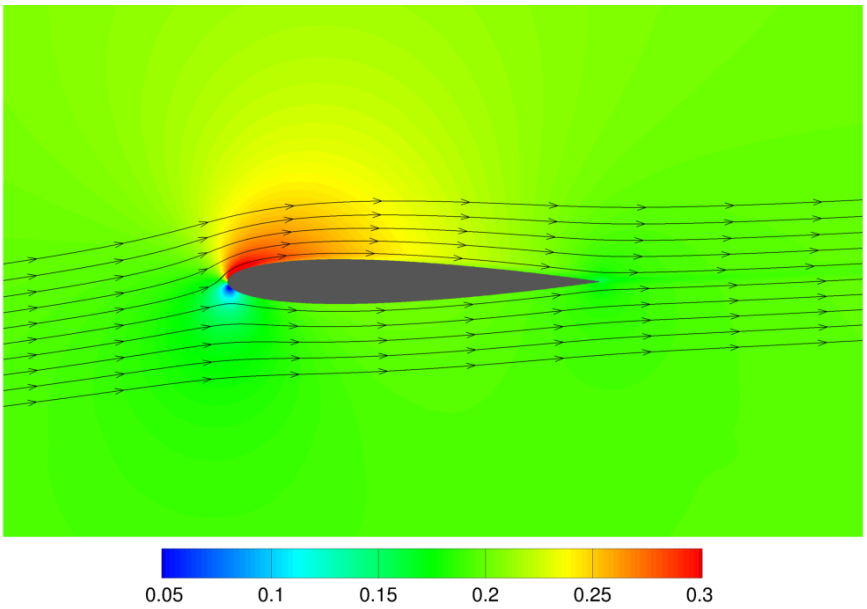

Figure D.1: Non-uniform base flow Mach number magnitude and streamlines, NACA 0012 airfoil, $\alpha = 5°$, $M_\infty = 0.2$.

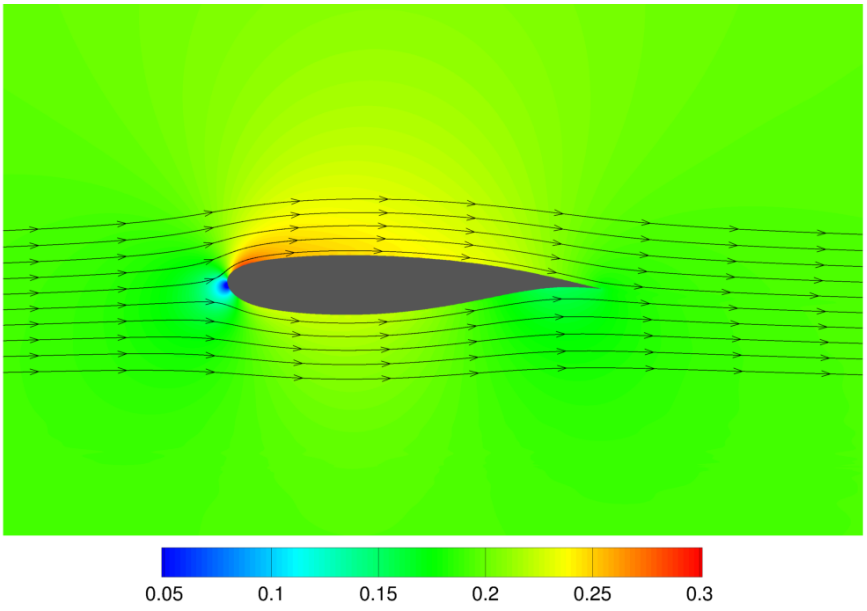

Figure D.2: Non-uniform base flow Mach number magnitude and streamlines, RA16SC1 airfoil, $\alpha = 0°$, $M_\infty = 0.2$.

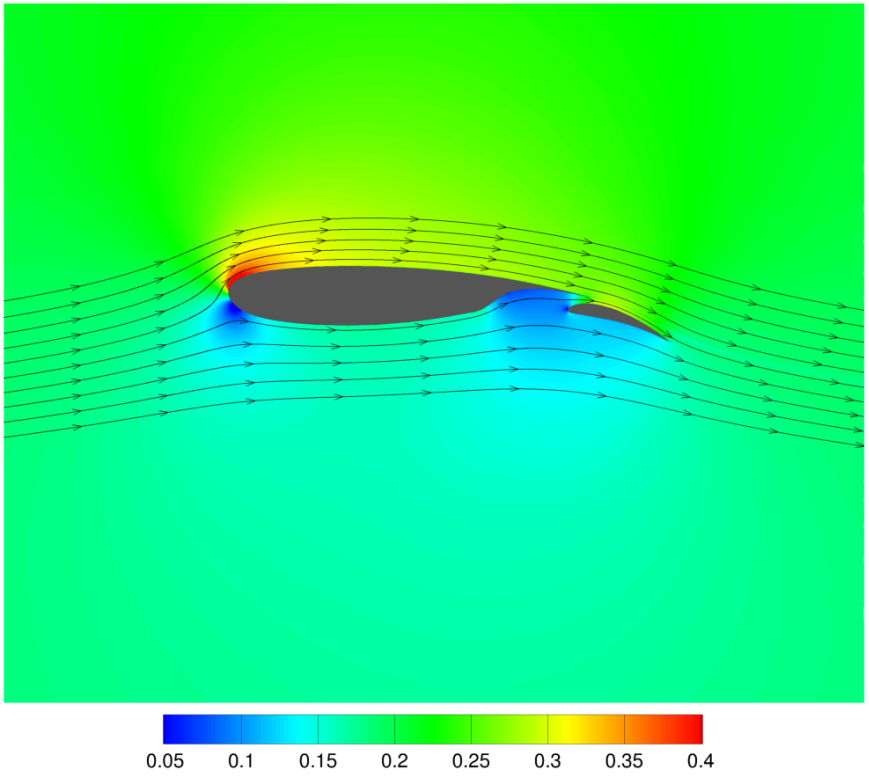

Figure D.3: Non-uniform base flow Mach number magnitude and streamlines, RA16SC1 airfoil with flap 20°, $\alpha = 0°$, $M_\infty = 0.2$.

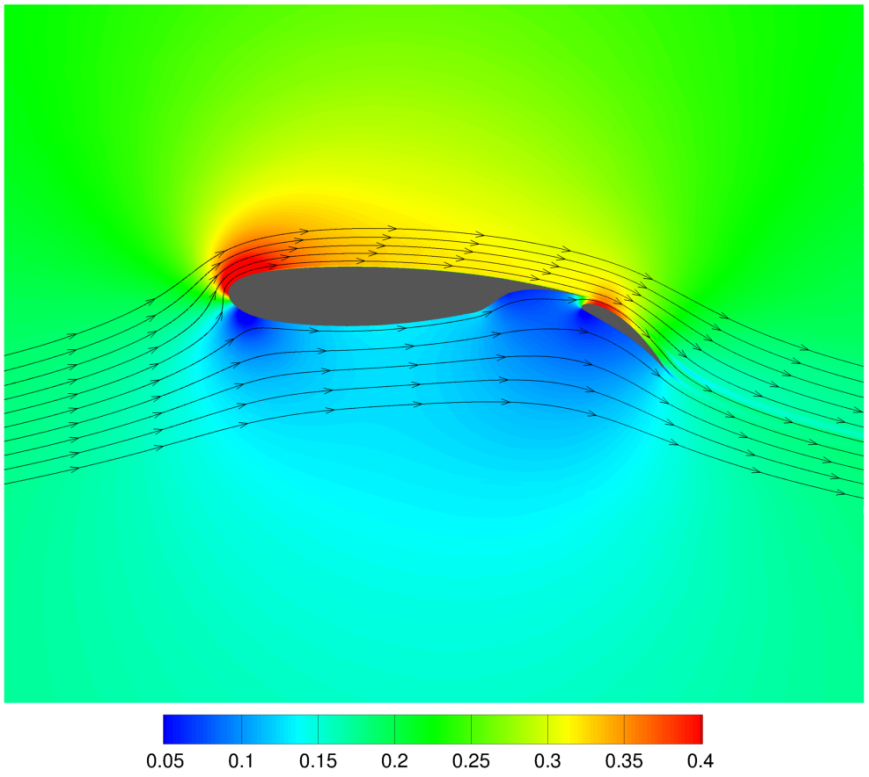

Figure D.4: Non-uniform base flow Mach number magnitude and streamlines, RA16SC1 airfoil with flap 40°, $\alpha = 0°$, $M_\infty = 0.2$.

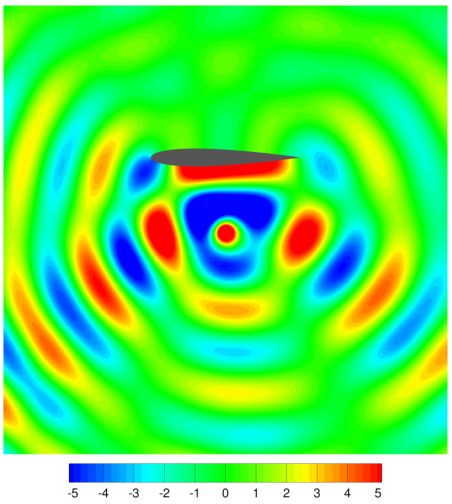

(a) Uniform $M_\infty = 0.1$.

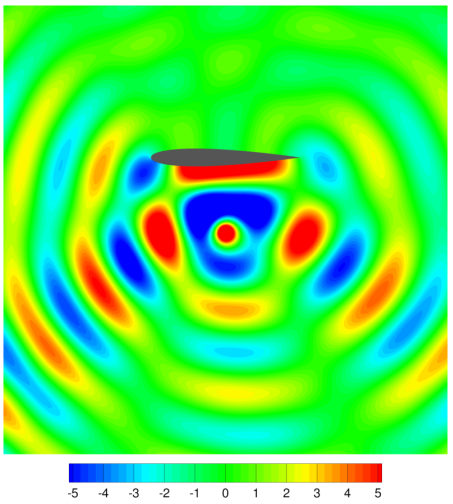

(b) Non-uniform $M_\infty = 0.1$.

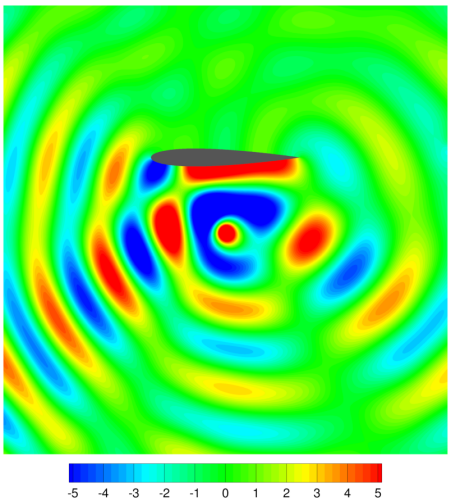

(c) Uniform $M_\infty = 0.2$.

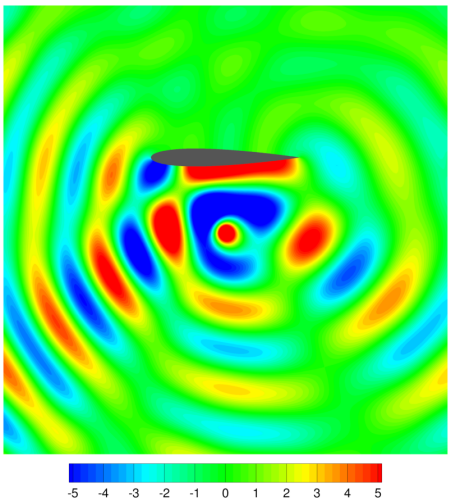

(d) Non-uniform $M_\infty = 0.2$.

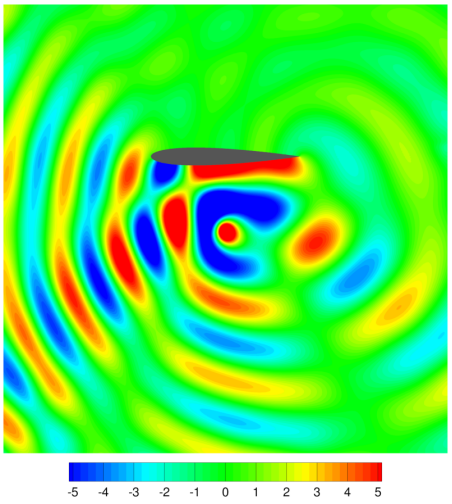

(e) Uniform $M_\infty = 0.3$.

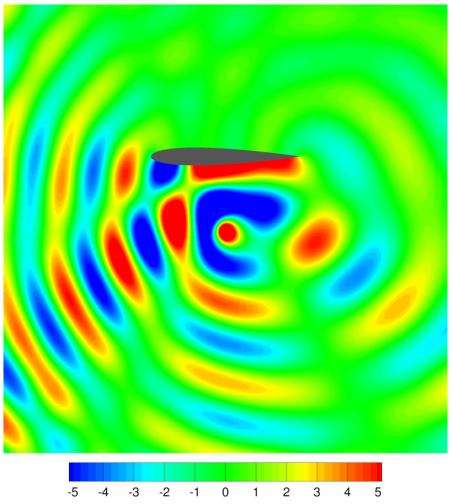

(f) Non-uniform $M_\infty = 0.3$.

Figure D.5: Acoustic pressure (Pa), NACA 0012, $\alpha = 5°$, 125 Hz.

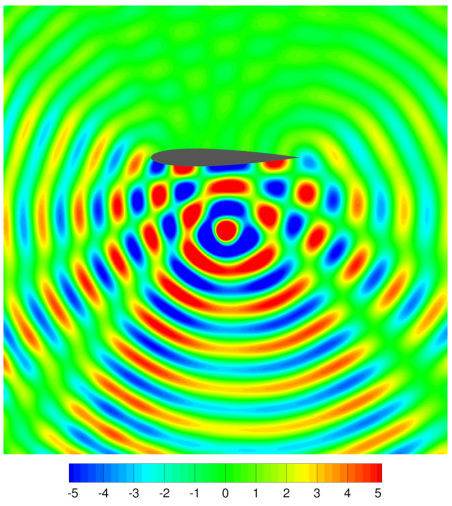

(a) Uniform $M_\infty = 0.1$.

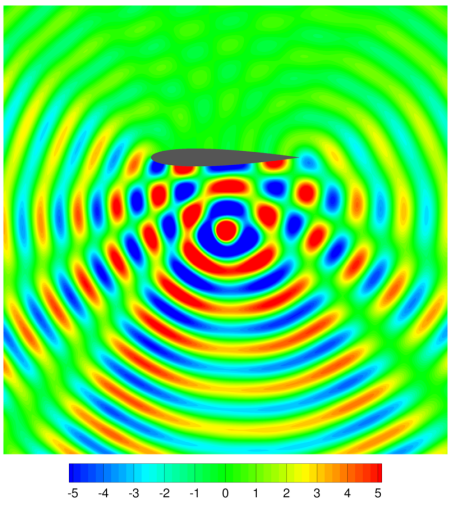

(b) Non-uniform $M_\infty = 0.1$.

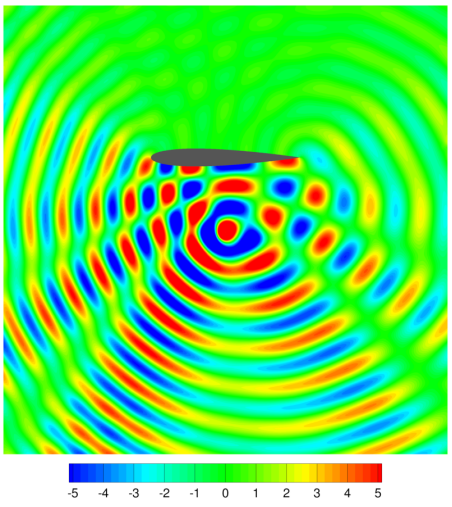

(c) Uniform $M_\infty = 0.2$.

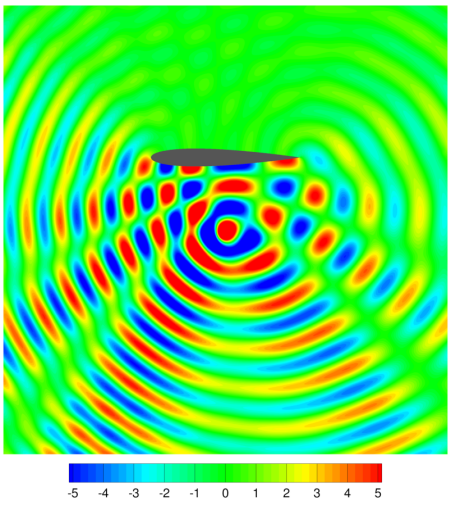

(d) Non-uniform $M_\infty = 0.2$.

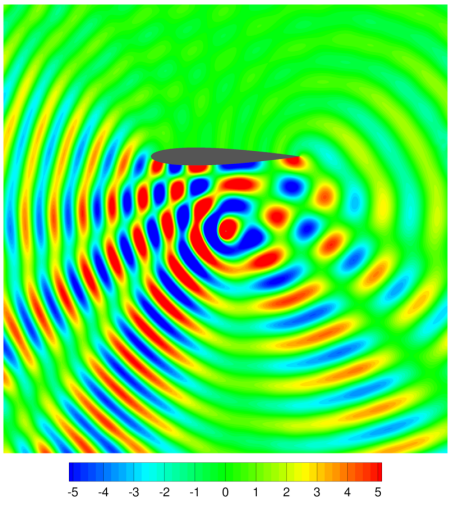

(e) Uniform $M_\infty = 0.3$.

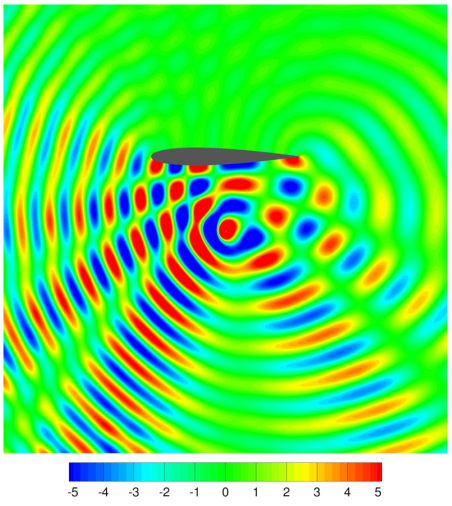

(f) Non-uniform $M_\infty = 0.3$.

Figure D.6: Acoustic pressure (Pa), NACA 0012, $\alpha = 5°$, 250 Hz.

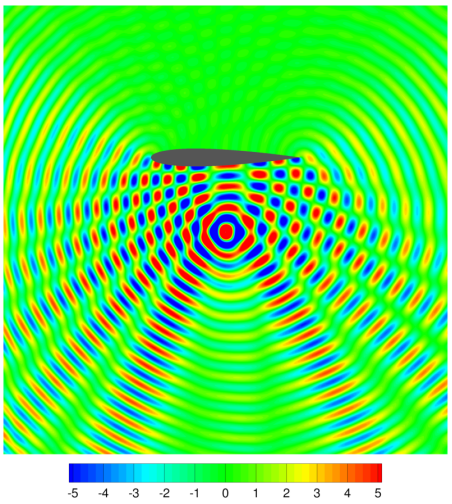

(a) Uniform $M_\infty = 0.1$.

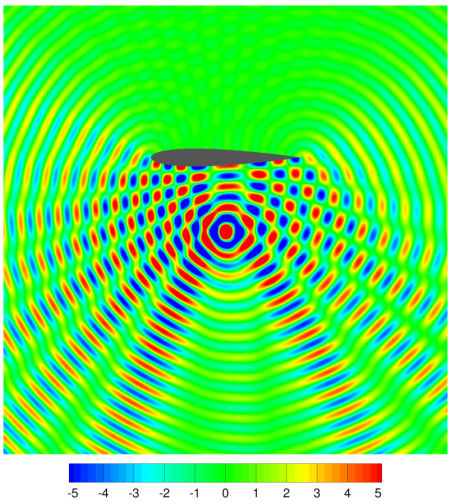

(b) Non-uniform $M_\infty = 0.1$.

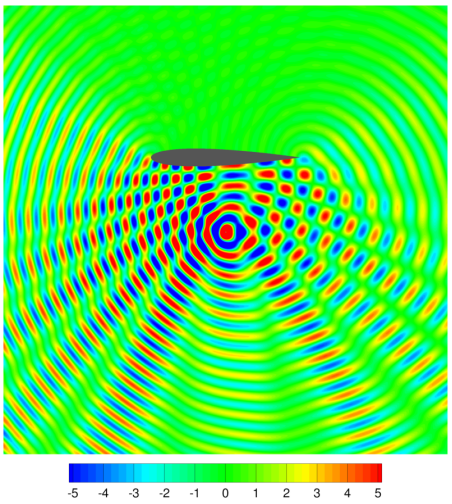

(c) Uniform $M_\infty = 0.2$.

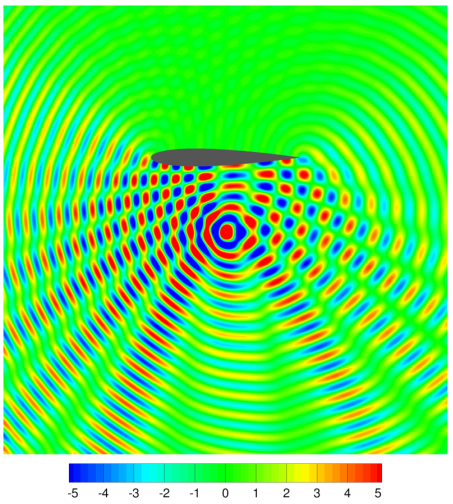

(d) Non-uniform $M_\infty = 0.2$.

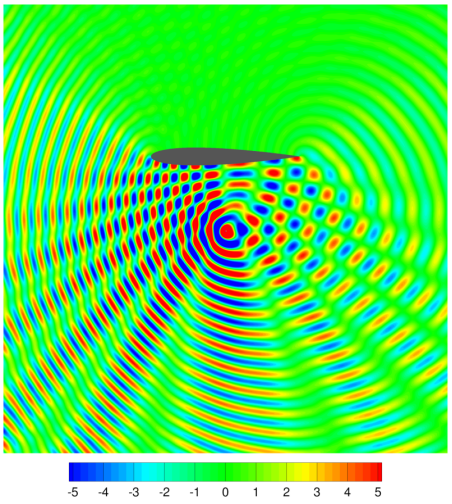

(e) Uniform $M_\infty = 0.3$.

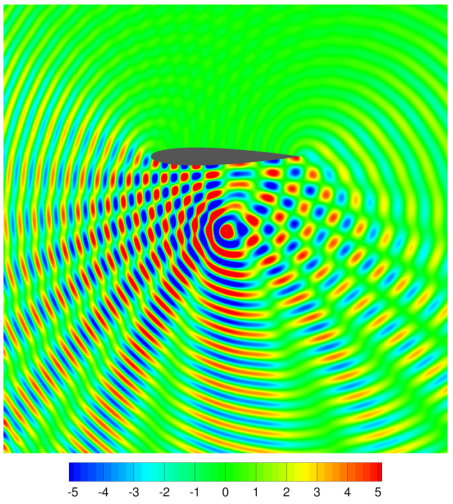

(f) Non-uniform $M_\infty = 0.3$.

Figure D.7: Acoustic pressure (Pa), NACA 0012, $\alpha = 5°$, 500 Hz.

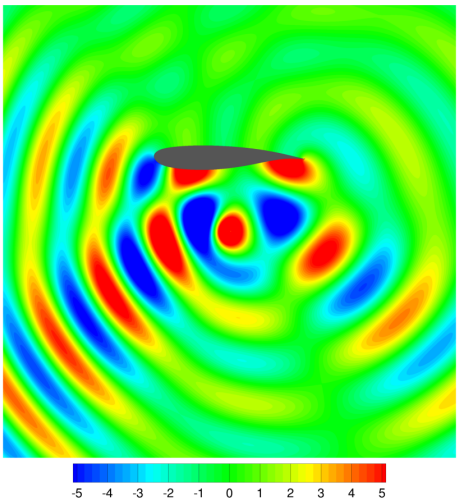

(a) Flap retracted, uniform $M_\infty = 0.2$.

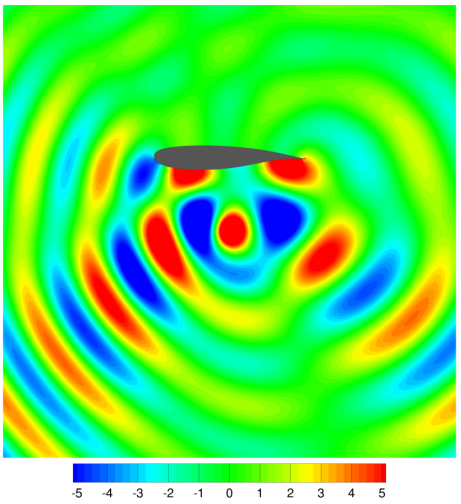

(b) Flap retracted, non-uniform $M_\infty = 0.2$.

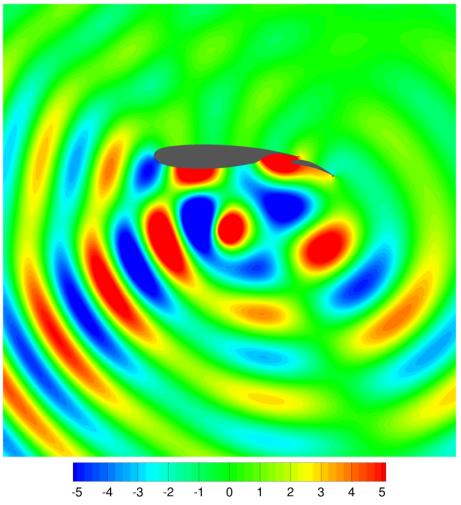

(c) Flap 20°, uniform $M_\infty = 0.2$.

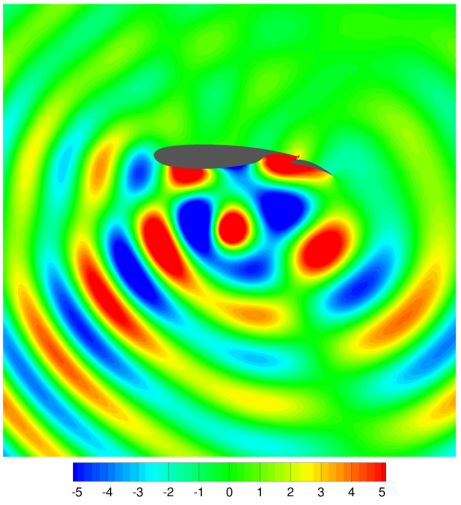

(d) Flap 20°, non-uniform $M_\infty = 0.2$.

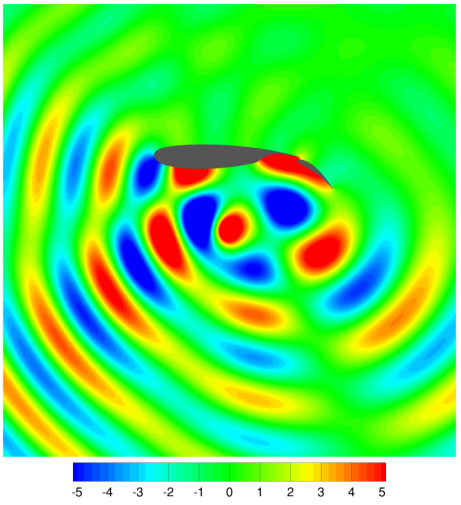

(e) Flap 40°, uniform $M_\infty = 0.2$.

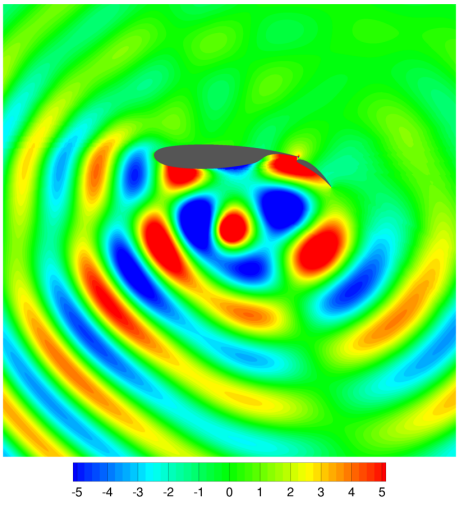

(f) Flap 40°, non-uniform $M_\infty = 0.2$.

Figure D.8: Acoustic pressure (Pa), RA16SC1, $\alpha = 0°$, 125 Hz.

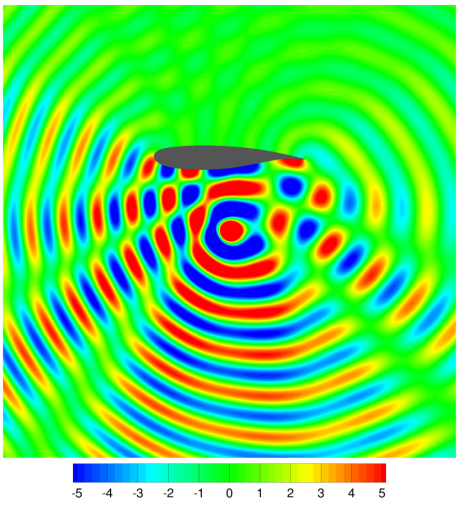

(a) Flap retracted, uniform $M_\infty = 0.2$.

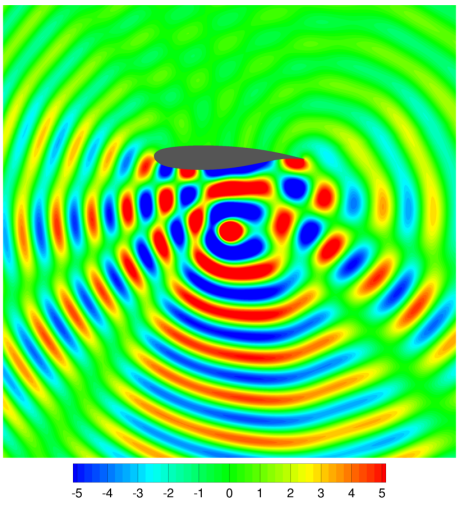

(b) Flap retracted, non-uniform $M_\infty = 0.2$.

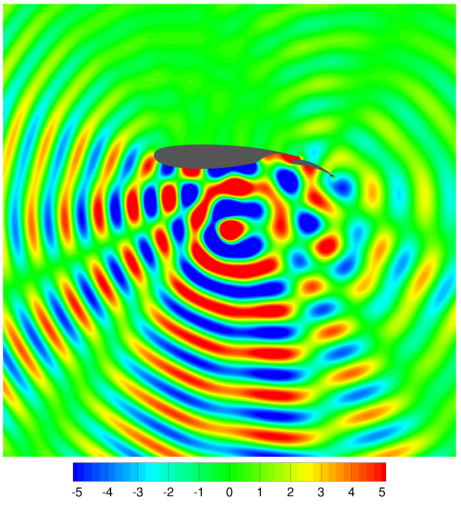

(c) Flap 20°, uniform $M_\infty = 0.2$.

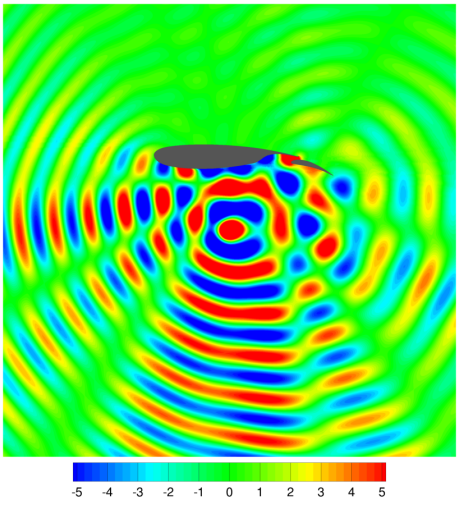

(d) Flap 20°, non-uniform $M_\infty = 0.2$.

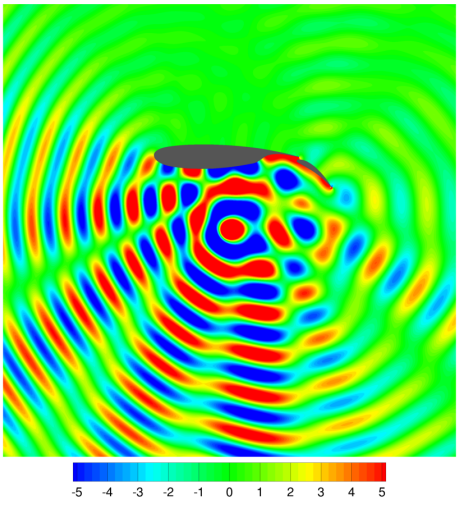

(e) Flap 40°, uniform $M_\infty = 0.2$.

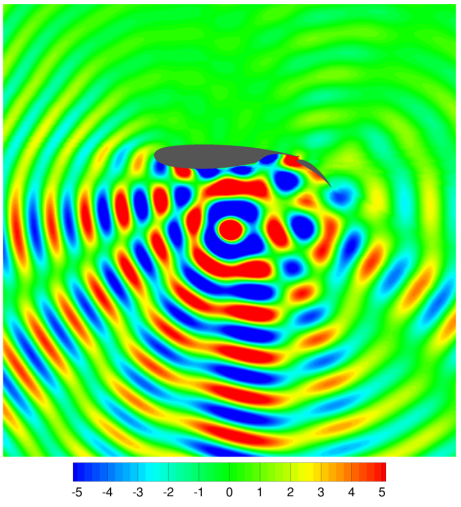

(f) Flap 40°, non-uniform $M_\infty = 0.2$.

Figure D.9: Acoustic pressure (Pa), RA16SC1, $\alpha = 0°$, 250 Hz.

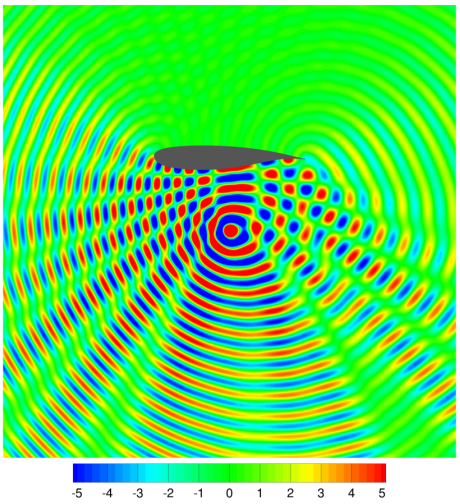

(a) Flap retracted, uniform $M_\infty = 0.2$.

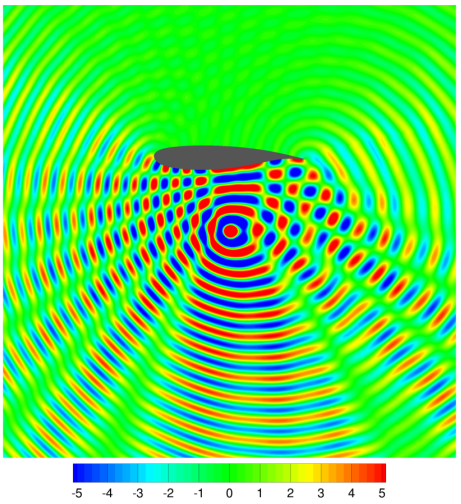

(b) Flap retracted, non-uniform $M_\infty = 0.2$.

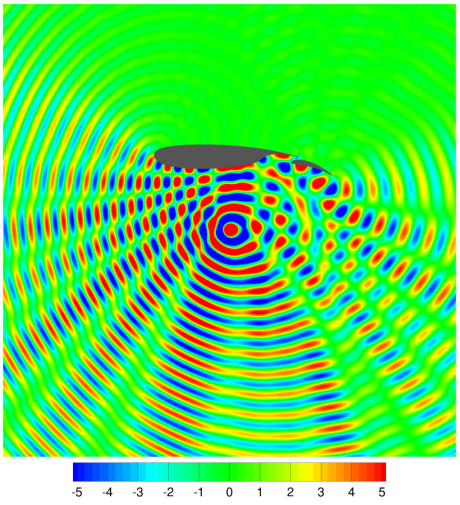

(c) Flap 20°, uniform $M_\infty = 0.2$.

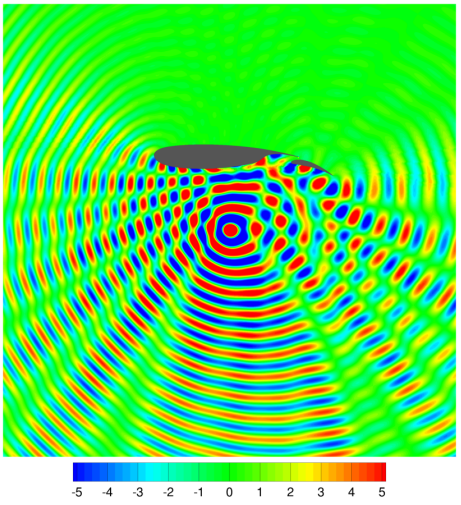

(d) Flap 20°, non-uniform $M_\infty = 0.2$.

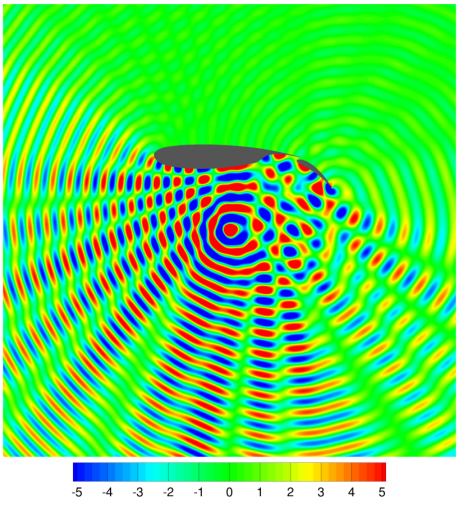

(e) Flap 40°, uniform $M_\infty = 0.2$.

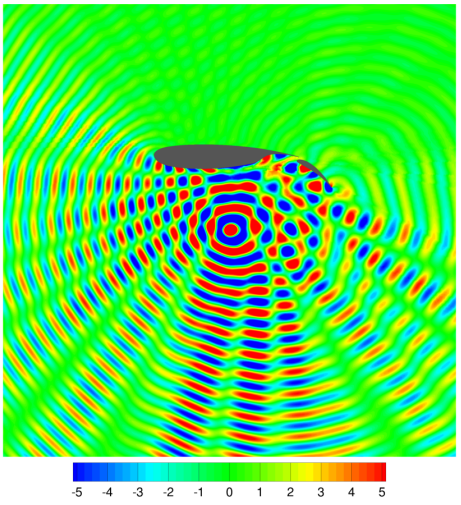

(f) Flap 40°, non-uniform $M_\infty = 0.2$.

Figure D.10: Acoustic pressure (Pa), RA16SC1, $\alpha = 0°$, 500 Hz.

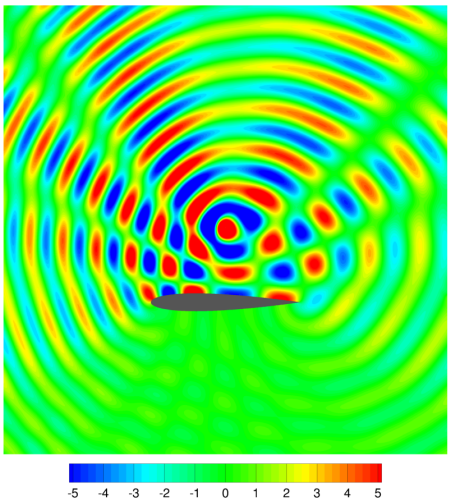

(a) Uniform $M_\infty = 0.2$.

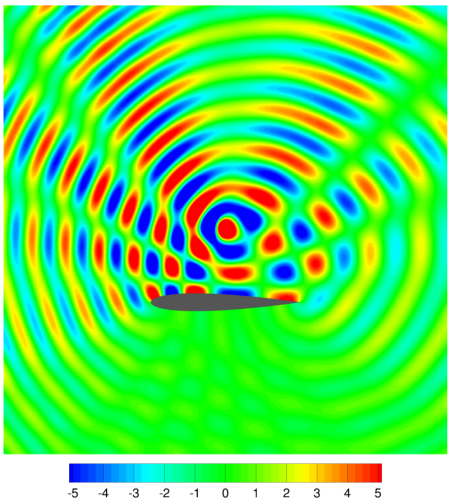

(b) Non-uniform $M_\infty = 0.2$.

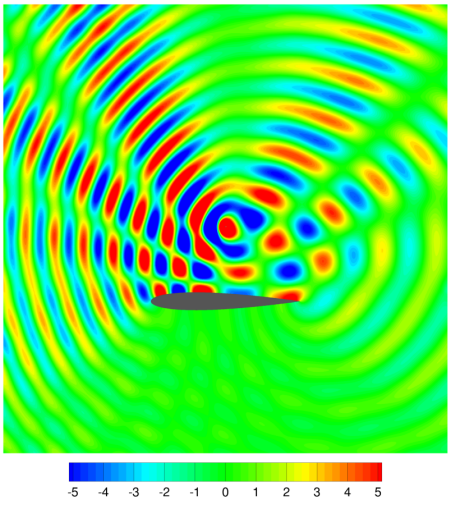

(c) Uniform $M_\infty = 0.3$.

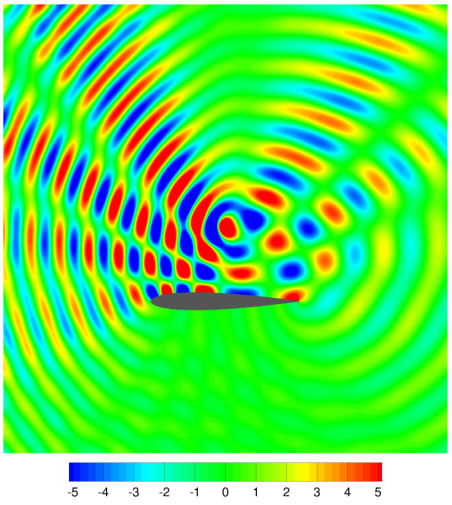

(d) Non-uniform $M_\infty = 0.3$.

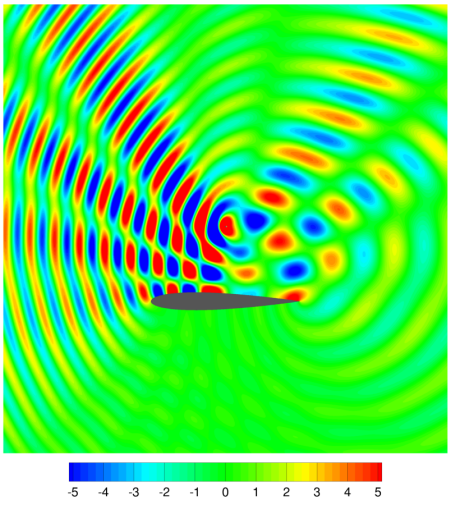

(e) Uniform $M_\infty = 0.4$.

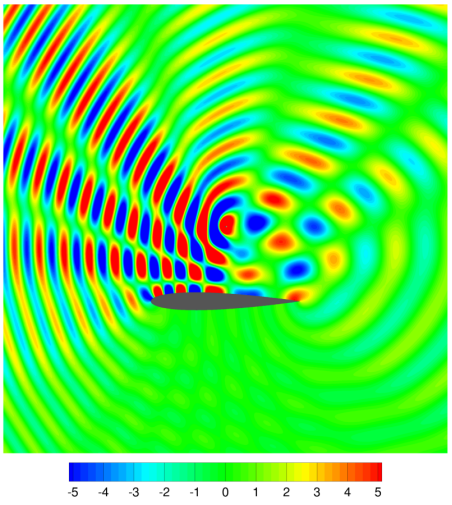

(f) Non-uniform $M_\infty = 0.4$.

Figure D.11: Acoustic pressure (Pa), NACA 0012, $\alpha = 3°$, 250 Hz.

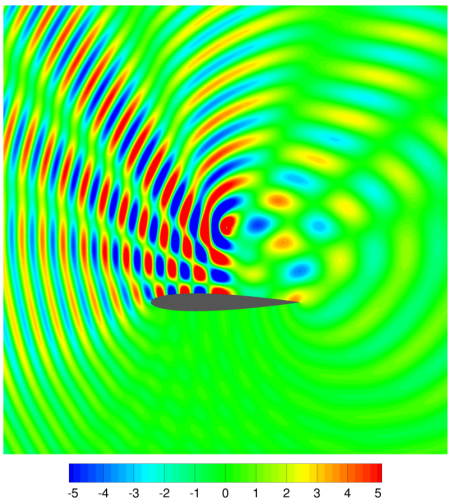

(g) Uniform $M_\infty = 0.5$.

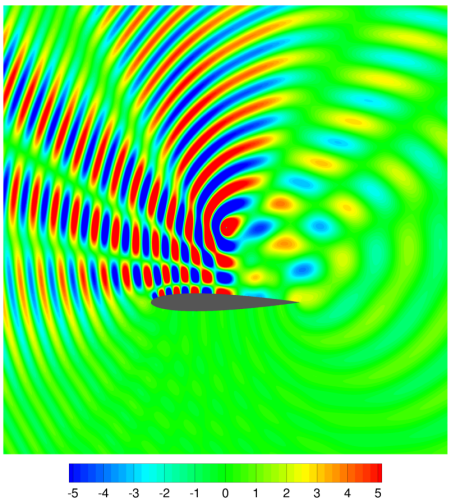

(h) Non-uniform $M_\infty = 0.5$.

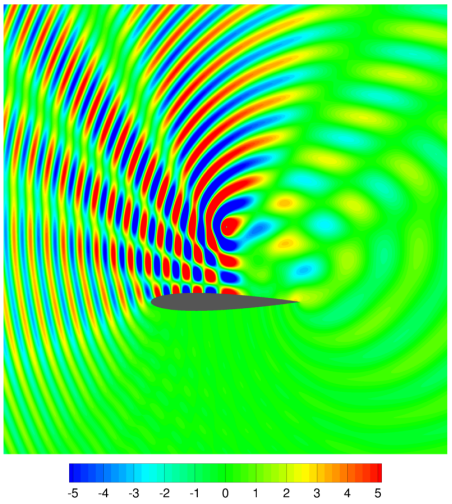

(i) Uniform $M_\infty = 0.6$.

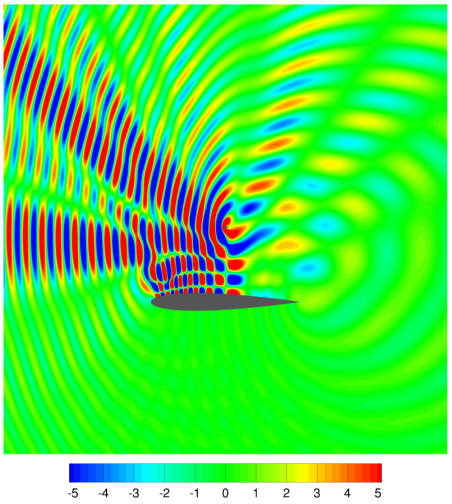

(j) Non-uniform $M_\infty = 0.6$.

Figure D.11: Acoustic pressure (Pa), NACA 0012, $\alpha = 3°$, 250 Hz (continued).

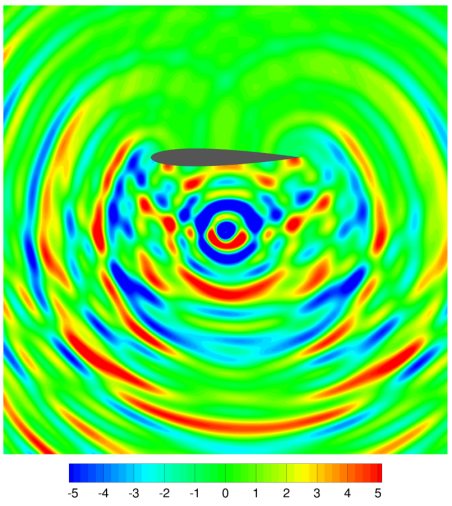

(a) Uniform $M_\infty = 0.1$.

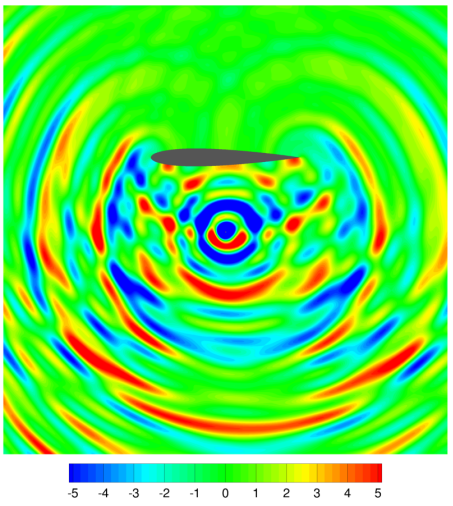

(b) Non-uniform $M_\infty = 0.1$.

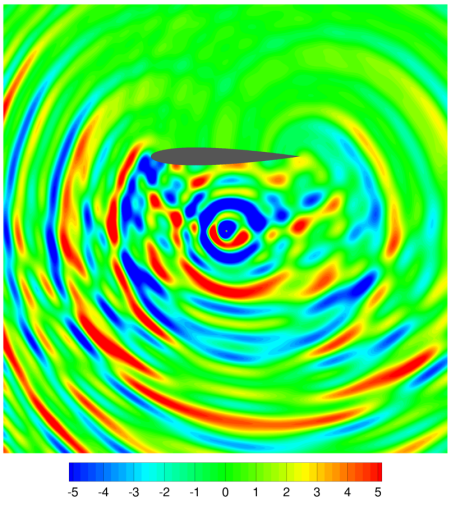

(c) Uniform $M_\infty = 0.2$.

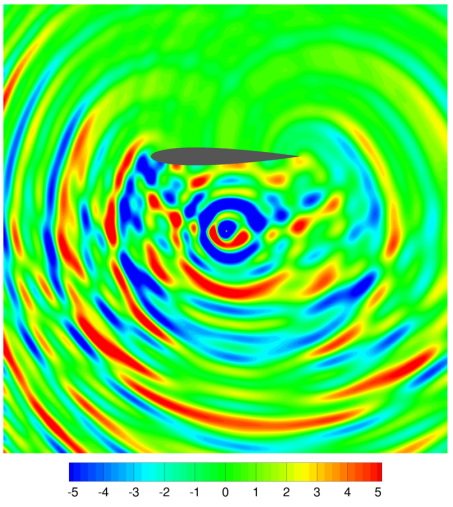

(d) Non-uniform $M_\infty = 0.2$.

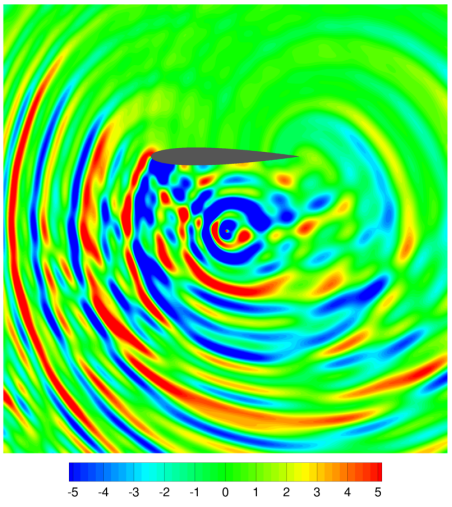

(e) Uniform $M_\infty = 0.3$.

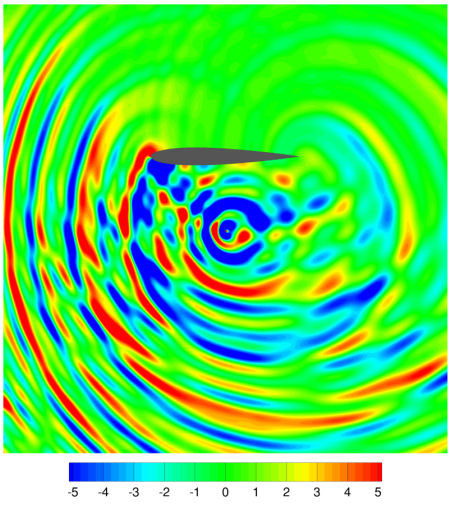

(f) Non-uniform $M_\infty = 0.3$.

Figure D.12: Acoustic pressure (Pa), NACA 0012, $\alpha = 5°$, broadband.

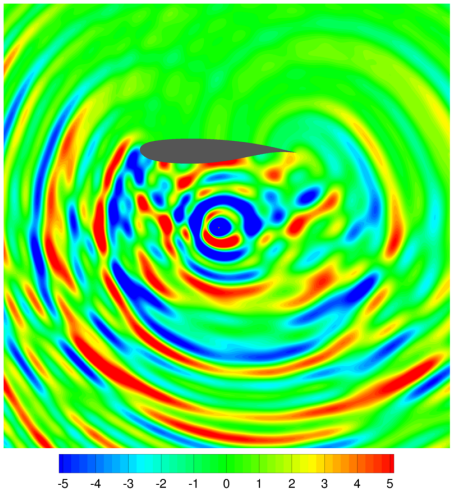

(a) Flap retracted, uniform $M_\infty = 0.2$.

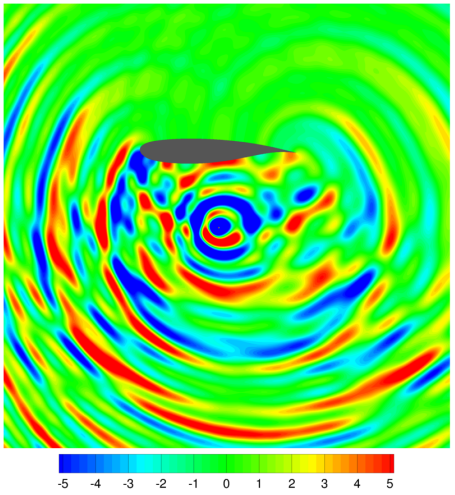

(b) Flap retracted, non-uniform $M_\infty = 0.2$.

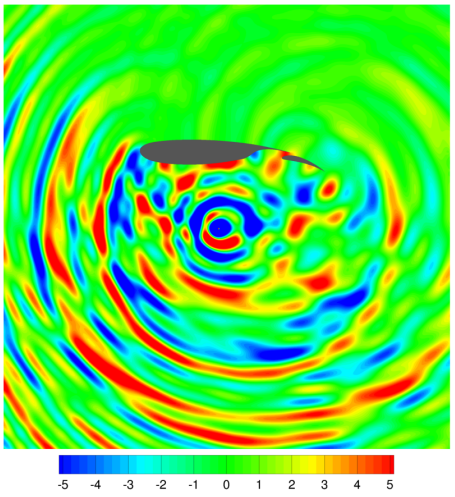

(c) Flap 20°, uniform $M_\infty = 0.2$.

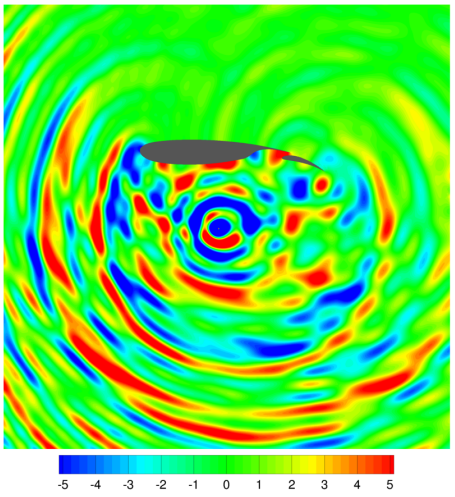

(d) Flap 20°, non-uniform $M_\infty = 0.2$.

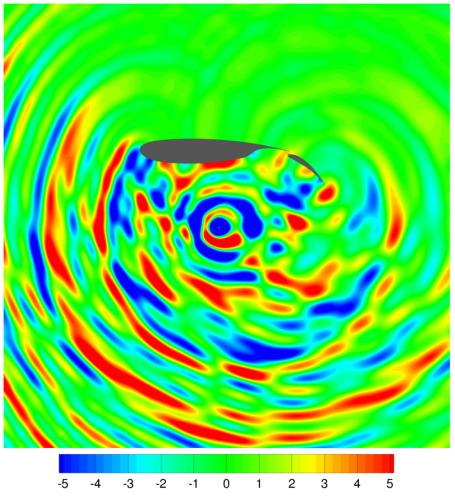

(e) Flap 40°, uniform $M_\infty = 0.2$.

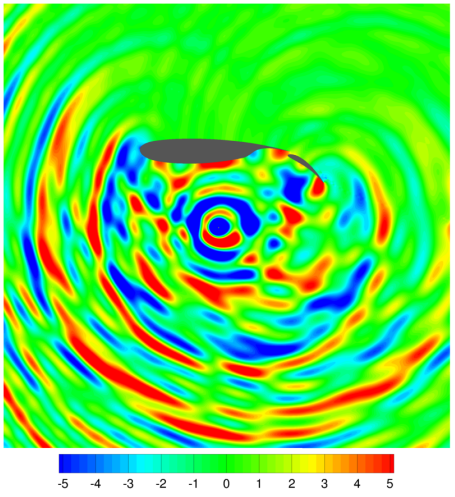

(f) Flap 40°, non-uniform $M_\infty = 0.2$.

Figure D.13: Acoustic pressure (Pa), RA16SC1, $\alpha = 0°$, broadband.

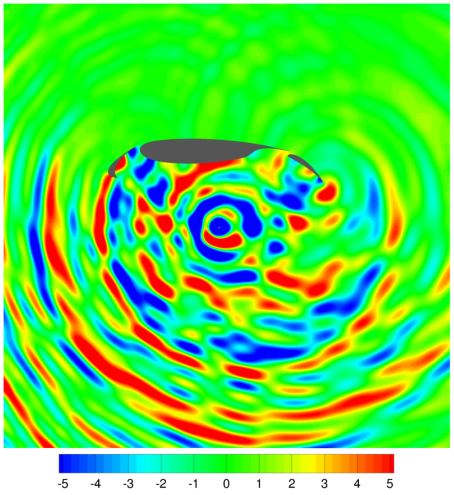

(g) Flap 40° plus slat, uniform $M_\infty = 0.2$.

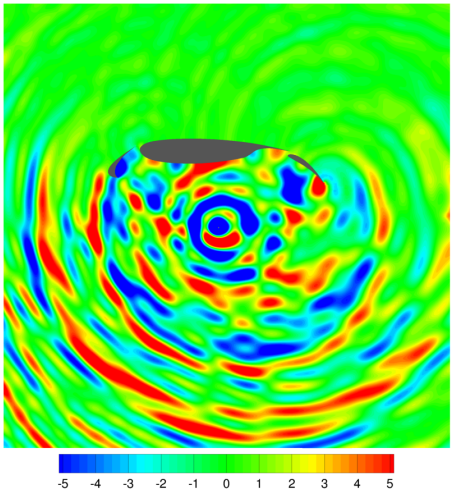

(h) Flap 40° plus slat, non-uniform $M_\infty = 0.2$.

Figure D.13: Acoustic pressure (Pa), RA16SC1, $\alpha = 0°$, broadband (continued).

References

[1] M. Basner, W. Babisch, A. Davis, M. Brink, C. Clark, S. Janssen, and S. Stansfeld, "Auditory and non-auditory effects of noise on health," *The Lancet*, vol. 383, pp. 1325–32, 2014.

[2] "European Aviation Environmental Report 2016," European Environment Agency, European Aviation Safety Agency and Eurocontrol, 2016.

[3] "Annex 16 to the Convention on International Civil Aviation: Volume 1 Aircraft Noise," 6th ed. International Civil Aviation Organization, 2011.

[4] R. J. Astley, "Propulsion System Noise: Turbomachinery," *Encyclopedia of Aerospace Engineering*, 2010.

[5] "Flightpath 2050: Europe's Vision for Aviation - Report of the High Level Group on Aviation Research," European Commision, 2011.

[6] W. Dobrzynski, "Almost 40 Years of Airframe Noise Reseach: What Did We Achieve?" *Journal of Aircraft*, vol. 47, no. 2, pp. 353–367, 2010.

[7] R. Merino-Martínez, M. Snellen, D. G. Simons, and L. Bertsch, "Analysis of landing gear noise during approach," in *Proceedings of the 22nd AIAA/CEAS Aeroacoustics Conference, Lyon, France, 30 May - 1 June 2016, AIAA-2016-2769*, 2016.

[8] W. M. Dobrzynski, "Airframe Noise: Landing Gear Noise," *Encyclopedia of Aerospace Engineering*, 2010.

[9] T. Heffernon, D. Angland, X. Zhang, and M. Smith, "The Effect of Flow Circulation on the Scattering of Landing Gear Noise," in *Proceedings of the 21st AIAA/CEAS Aeroacoustics Conference, Dallas, Texas, 22-26 June 2015, AIAA-2015-3257*, 2015.

[10] T. Heffernon, D. Angland, J. Gill, and X. Zhang, "A General Method to Specify a Broadband Monopole in the Time Domain with a Target Spectrum in Computational Aeroacoustics," *Journal of Computational Acoustics*, submitted, 2017.

[11] X. Zhang, "Aircraft noise and its nearfield propagation computations," *Acta Mechanica Sinica*, vol. 28, no. 4, pp. 960–977, 2012.

[12] R. H. Self, "Propeller Noise," *Encyclopedia of Aerospace Engineering*, 2010.

[13] E. Manoha, S. R. Redonnet, and S. Caro, "Computational Aeroacoustics," *Encyclopedia of Aerospace Engineering*, 2010.

[14] M. J. Lighthill, "On Sound Generated Aerodynamically. I. General Theory," *Proceedings of the Royal Society of London. Series A, Mathematical and Physical Sciences*, vol. 211, no. 1107, pp. 564–587, 1952.

[15] N. Curle, "The Influence of Solid Boundaries upon Aerodynamic Sound," *Proceedings of the Royal Society of London. Series A, Mathematical and Physical Sciences*, vol. 231, no. 1187, pp. 505–514, 1955.

[16] J. E. Ffowcs Williams and D. L. Hawkings, "Sound Generation by Turbulence and Surfaces in Arbitrary Motion," *Philosophical Transactions of the Royal Society of London. Series A, Mathematical and Physical Sciences*, vol. 264, pp. 321–342, 1969.

[17] W. R. Wolf and S. K. Lele, "Aeroacoustic Integrals Accelerated by Fast Multipole Method," *AIAA Journal*, vol. 49, no. 7, pp. 1466–1477, 2011.

[18] M. G. Smith and L. C. Chow, "Prediction Method for Aerodynamic Noise from Aircraft Landing Gear," in *Proceedings of the 4th AIAA/CEAS Aeroacoustics Conference, Toulouse, France, 2-4 June 1998, AIAA-98-2228*, 1998.

[19] M. G. Smith and L. C. Chow, "Validation of a Prediction model for Aerodynamic Noise from Aircraft Landing Gear," in *Proceedings of the 8th AIAA/CEAS Aeroacoustics Conference, Breckenridge, USA, 17-19 June 2002, AIAA-2002-2581*, 2002.

[20] Y. Guo, "A Semi-Empirical Model for Aircraft Landing Gear Noise Prediction," in *Proceedings of the 12th AIAA/CEAS Aeroacoustics Conference, Cambridge, Massachusetts, 8-10 May 2006, AIAA-2006-2627*, 2006.

[21] S. Marburg and B. Nolte, Eds., *Computational Acoustics of Noise Propagation in Fluids - Finite and Boundary Element Methods*. Springer, 2008.

[22] W. Béchara, C. Bailly, P. Lafon, and S. M. Candel, "Stochastic Approach to Noise Modeling for Free Turbulent Flows," *AIAA Journal*, vol. 32, no. 3, pp. 455–463, 1994.

[23] D. Casalino and M. Barbarino, "Stochastic Method for Airfoil Self-Noise Computation in Frequency Domain," *AIAA Journal*, vol. 49, no. 11, pp. 2453–2469, 2011.

[24] P. R. Spalart, M. L. Shur, M. Kh. Strelets, and A. K. Travin, "Initial noise predictions for rudimentary landing gear," *Journal of Sound and Vibration*, vol. 330, pp. 4180–4195, 2011.

[25] W. Liu, J. W. Kim, X. Zhang, D. Angland, and B. Caruelle, "Landing-gear noise prediction using high-order finite difference schemes," *Journal of Sound and Vibration*, vol. 332, pp. 3517–3534, 2013.

[26] W. R. Wolf and S. K. Lele, "Trailing-Edge Noise Predictions Using Compressible Large-Eddy Simulation and Acoustic Analogy," *AIAA Journal*, vol. 50, no. 11, pp. 2423–2434, 2012.

[27] D. Casalino, A. F. P. Ribeiro, E. Fares, and S. Nölting, "Lattice-Boltzmann Aeroacoustic Analysis of the LAGOON Landing-Gear Configuration," *AIAA Journal*, vol. 52, no. 6, pp. 1232–1248, 2014.

[28] D. Casalino, A. Hazir, and A. Mann, "Turbofan Broadband Noise Prediction using the Lattice Boltzmann Method," in *Proceedings of the 22nd AIAA/CEAS Aeroacoustics Conference, Lyon, France, 30 May - 1 June 2016, AIAA-2016-2945*, 2016.

[29] E. Fares, D. Casalino, and M. R. Khorrami, "Evaluation of Airframe Noise Reduction Concepts via Simulations Using a Lattice Boltzmann Approach," in *Proceedings of the 21st AIAA/CEAS Aeroacoustics Conference, Dallas, Texas, 22-26 June 2015, AIAA-2015-2988*, 2015.

[30] R. Hixon, "Prefactored Small-Stencil Compact Schemes," *Journal of Computational Physics*, vol. 165, no. 2, pp. 522–541, 2000.

[31] J. W. Kim, "Optimised boundary compact finite difference schemes for computational aeroacoustics," *Journal of Computational Physics*, vol. 225, pp. 995–1019, 2007.

[32] J. W. Kim and R. D. Sandberg, "Efficient parallel computing with a compact finite difference scheme," *Computers & Fluids*, vol. 58, pp. 70–87, 2012.

[33] J. W. Kim, "High-order compact filters with variable cut-off wavenumber and stable boundary treatment," *Computers & Fluids*, vol. 39, pp. 1168–1182, 2010.

[34] M. R. Visbal and D. V. Gaitonde, "High-Order Accurate Methods for Unsteady Vortical Flows on Curvilinear Meshes," in *Proceedings of the 36th AIAA Aerospace Sciences Meeting and Exhibit, Reno, NV, USA, 12-15 January 1998, AIAA-98-0131*, 1998.

[35] F. Hu, M. Y. Hussaini, and J. Manthey, "Low-Dissipation and Low-Dispersion Runge-Kutta Schemes for Computational Acoustics," *Journal of Computational Physics*, vol. 124, no. 1, pp. 177–191, 1996.

[36] J. Gill, R. Fattah, and X. Zhang, "Evaluation and Development of Non-Reflective Boundary Conditions for Aeroacoustic Simulations," in *Proceedings of the 21st AIAA/CEAS Aeroacoustics Conference, Dallas, Texas, 22-26 June 2015, AIAA-2015-2677*, 2015.

[37] S. K. Richards, X. Zhang, X. X. Chen, and P. A. Nelson, "The evaluation of non-reflecting boundary conditions for duct acoustic computation," *Journal of Sound and Vibration*, vol. 270, no. 3, pp. 539–557, 2004.

[38] C. Bogey, C. Bailly, and D. Juvé, "Computation of Flow Noise Using Source Terms in Linearized Eulers Equations," *AIAA Journal*, vol. 40, no. 2, pp. 235–243, 2002.

[39] R. Ewert and W. Schröder, "Acoustic perturbation equations based on flow decomposition via source filtering," *Journal of Computational Physics*, vol. 188, pp. 365–398, 2003.

[40] X. Zhang, X. Chen, J. Gill, and X. Huang, "Gradient Term Filtering for Stable Sound Propagation with Linearized Euler Equations," in *Proceedings of the 20th AIAA/CEAS Aeroacoustics Conference, Atlanta, GA, 16-20 June 2014, AIAA-2014-3306*, 2014.

[41] Y. Sun, S. Zhong, R. Fattah, X. Zhang, and X. Chen, "An evaluation of gradient term modification methods for linearized Euler equations," in *Proceedings of the 23rd International Congress on Sound & Vibration, Athens, Greece, 10-14 July 2016*, 2016.

[42] D. Casalino, "Finite Element Solutions of a Wave Equation for Sound Propagation in Sheared Flows," *AIAA Journal*, vol. 50, no. 1, pp. 37–45, 2012.

[43] P. Drage, B. Wiesler, P. van Beek, L. van Lier, R. Parchen, and P. Tibaut, "Prediction of noise radiation from basic configurations of landing gears by means of computational aeroacoustics," *Aerospace Science and Technology*, vol. 11, pp. 451–458, 2007.

[44] Z. Ma and X. Zhang, "Numerical Investigation of Broadband Slat Noise Attenuation with Acoustic Liner Treatment," *AIAA Journal*, vol. 47, no. 12, pp. 2812–2820, 2009.

[45] C. Bailly and D. Juvé, "Numerical Solution of Acoustic Propagation Problems Using Linearized Euler Equations," *AIAA Journal*, vol. 38, no. 1, pp. 22–29, 2000.

[46] S. Redonnet, E. Manoha, and P. Sagaut, "Numerical Simulation of Propagation of Small Perturbations interacting with Flows and Solid Bodies," in *Proceedings of the 7th AIAA/CEAS Aeroacoustics Conference, Maastricht, Netherlands, 28-30 May 2001, AIAA-2001-2223*, 2001.

[47] T. Padois, C. Prax, and V. Valeau, "Numerical validation of shear flow corrections for beamforming acoustic source localisation in open wind-tunnels," *Applied Acoustics*, vol. 74, pp. 591–601, 2013.

[48] H. Si, W. Shen, and W. Zhu, "Effect of non-uniform mean flow field on acoustic propagation problems in computational aeroacoustics," *Aerospace Science and Technology*, vol. 28, pp. 145–153, 2013.

[49] V. Clair and G. Gabard, "Numerical assessment of the scattering of acoustic waves by turbulent structures," in *Proceedings of the 21st AIAA/CEAS Aeroacoustics Conference, Dallas, Texas, 22-26 June 2015, AIAA-2015-2680*, 2015.

[50] J. Bin, M. Y. Hussaini, and S. Lee, "Broadband impedance boundary conditions for the simulation of sound propagation in the time domain," *Journal of the Acoustical Society of America*, vol. 125, no. 2, pp. 664–675, 2009.

[51] G. Reboul and C. Polacsek, "Toward Numerical Simulation of Fan Broadband Noise Aft Radiation from Aeroengines," *AIAA Journal*, vol. 48, no. 9, pp. 2038–2048, 2010.

[52] D. Dragna, P. Blanc-Benon, and F. Poisson, "Modeling of Broadband Moving Sources for Time-Domain Simulations of Outdoor Sound Propagation," *AIAA Journal*, vol. 52, no. 9, pp. 1928–1939, 2014.

[53] D. Angland and X. Zhang, "Installation Effects of Landing Gears," in *Proceedings of the 19th AIAA/CEAS Aeroacoustics Conference, Berlin, Germany, 27-29 May 2013, AIAA-2013-2138*, 2013.

[54] D. Casalino, M. Barbarino, and A. Visingardi, "Simulation of Helicopter Community Noise in Complex Urban Geometry," *AIAA Journal*, vol. 49, no. 8, pp. 1614–1624, 2011.

[55] S. Kirkup, *The Boundary Element Method in Acoustics*. [Online] Available: http://www.boundary-element-method.com/index.htm [Accessed: 19th March 2013], 2007.

[56] Y. J. Liu, S. Mukherjee, N. Nishimura, M. Schanz, W. Ye, A. Sutradhar, E. Pan, N. A. Dumont, A. Frangi, and A. Saez, "Recent Advances and Emerging Applications of the Boundary Element Method," *Applied Mechanics Reviews*, vol. 64, no. 3, p. 030802, 2011.

[57] Y. Liu, *Fast Multipole Boundary Element Method: Theory and Applications in Engineering*. Cambridge University Press, 2009.

[58] L. C. Wrobel, *The Boundary Element Method, Volume 1: Applications in Thermo-Fluids and Acoustics*. John Wiley & Sons, 2002.

[59] T. W. Wu, Ed., *Boundary Element Acoustics: Fundamentals and Computer Codes*. WIT Press, 2000.

[60] M. J. Crocker, Ed., *Handbook of Noise and Vibration Control*. John Wiley & Sons, 2007.

[61] N. Gumerov, R. Adelman, and R. Duraiswami, "Fast multipole accelerated indirect boundary elements for the Helmholtz equation," *Proceedings of Meetings on Acoustics*, vol. 19, 015097, 2013.

[62] S. T. Raveendra, N. Vlahopoulos, and A. Glaves, "An indirect boundary element formulation for multi-valued impedance simulation in structural acoustics," *Applied Mathematical Modelling*, vol. 22, pp. 379–393, 1998.

[63] A. J. Burton and G. F. Miller, "The Application of Integral Equation Methods to the Numerical Solution of Some Exterior Boundary-Value Problems," *Proceedings of the Royal Society of London. Series A, Mathematical and Physical Sciences*, vol. 323, no. 1553, pp. 201–210, 1971.

[64] S. Amini, "On the Choice of the Coupling Parameter in Boundary Integral Formulations of the Exterior Acoustic Problem," *Applicable Analysis*, vol. 35, pp. 75–92, 1990.

[65] H. A. Schenck, "Improved Integral Formulation for Acoustic Radiation Problems," *The Journal of the Acoustical Society of America*, vol. 44, no. 1, pp. 41–58, 1968.

[66] *ASERIS: ACTIPOLE V1.19.0 User Manual*, EADS Innovation Works, 2013.

[67] M. Ochmann, "The Source Simulation Technique for Acoustic Radiation Problems," *Acustica*, vol. 81, pp. 512–527, 1995.

[68] M. H. Dunn and A. F. Tinetti, "Aeroacoustic Scattering Via The Equivalent Source Method," in *Proceedings of the 10th AIAA/CEAS Aeroacoustics Conference, Manchester, UK, 10-12 May 2004, AIAA-2004-2937*, 2004.

[69] A. F. Tinetti and M. H. Dunn, "Aeroacoustic Noise Prediction Using the Fast Scattering Code," in *Proceedings of the 11th AIAA/CEAS Aeroacoustics Conference, Monterey, California, 23-25 May 2005, AIAA-2005-3061*, 2005.

[70] D. Papamoschou and S. Mayoral, "Modeling of Jet Noise Sources and their Diffraction with Uniform Flow," in *Proceedings of the 51st AIAA Aerospace Sciences Meeting, Grapevine, Texas, 7-10 January 2013, AIAA-2013-0326*, 2013.

[71] K. Taylor, "A transformation of the acoustic equation with implications for wind-tunnel and low-speed flight tests," *Proceedings of the Royal Society of London. Series A, Mathematical and Physical Sciences*, vol. 363, pp. 271–281, 1978.

[72] R. J. Astley and J. G. Bain, "A three-dimensional boundary element scheme for acoustic radiation in low mach number flows," *Journal of Sound and Vibration*, vol. 109, no. 3, pp. 445–465, 1986.

[73] T. W. Wu and L. Lee, "A Direct Boundary Integral Formulation For Acoustic Radiation In A Subsonic Uniform Flow," *Journal of Sound and Vibration*, vol. 175, no. 1, pp. 51–63, 1994.

[74] L. Lee, T. W. Wu, and P. Zhang, "A dual-reciprocity method for acoustic radiation in a subsonic non-uniform flow," *Engineering Analysis with Boundary Elements*, vol. 13, pp. 365–370, 1994.

[75] C. Clancy and H. J. Rice, "Acoustic Shielding in Low Mach Number Potential Flow Incorporating a Wake Model using BEM," in *Proceedings of the 15th AIAA/CEAS Aeroacoustics Conference, Manchester, UK, 11-13 May 2009, AIAA-2009-3174*, 2009.

[76] W. R. Wolf and S. K. Lele, "Fast acoustic scattering predictions with non-uniform potential flow effects," *Journal of the Brazilian Society of Mechanical Sciences and Engineering*, vol. 35, pp. 407–418, 2013.

[77] S. Mancini, R. J. Astley, S. Sinayoko, G. Gabard, and M. Tournour, "An integral formulation for wave propagation on weakly non-uniform potential flows," *Journal of Sound and Vibration*, vol. 385, pp. 184–201, 2016.

[78] S. Mancini, S. Sinayoko, R. J. Astley, G. Gabard, and M. Tournour, "Boundary element formulation for wave propagation in weakly non-uniform potential flows," in *Proceedings of the 22nd AIAA/CEAS Aeroacoustics Conference, Lyon, France, 30 May - 1 June 2016, AIAA-2016-2713*, 2016.

[79] X.-L. Zhao and T.-Z. Huang, "On the inverse of a general pentadiagonal matrix," *Applied Mathematics and Computation*, vol. 202, pp. 639–646, 2008.

[80] A. Brancati, M. H. Aliabadi, and I. Benedetti, "Hierarchical Adaptive Cross Approximation GMRES Technique for Solution of Acoustic Problems Using the Boundary Element Method," *CMES: Computer Modeling in Engineering & Sciences*, vol. 43, no. 2, pp. 149–172, 2009.

[81] H. Cheng, W. Y. Crutchfield, Z. Gimbutas, L. F. Greengard, J. F. Ethridge, J. Huang, V. Rokhlin, N. Yarvin, and J. Zhao, "A wideband fast multipole method for the Helmholtz equation in three dimensions," *Journal of Computational Physics*, vol. 216, pp. 300–325, 2006.

[82] Y. Saad and M. H. Schultz, "GMRES: A Generalized Minimal Residual Algorithm for Solving Nonsymmetric Linear Systems," *SIAM Journal on Scientific and Statistical Computing*, vol. 7, no. 3, pp. 856–869, 1986.

[83] N. A. Gumerov and R. Duraiswami, "A broadband fast multipole accelerated boundary element method for the three dimensional Helmholtz equation," *Journal of the Acoustical Society of America*, vol. 125, no. 1, pp. 191–205, 2009.

[84] W. Śmigaj, T. Betcke, S. Arridge, J. Phillips, and M. Schweiger, "Solving Boundary Integral Problems with BEM++," *ACM Transactions on Mathematical Software*, vol. 41, no. 2, article 6, 2015.

[85] V. Mallardo, M. H. Aliabadi, A. Brancati, and V. Marant, "An accelerated BEM for simulation of noise control in the aircraft cabin," *Aerospace Science and Technology*, vol. 23, pp. 418–428, 2012.

[86] Z. Y. Yan and X. W. Gao, "The development of the pFFT accelerated BEM for 3-D acoustic scattering problems based on the Burton and Miller's integral formulation," *Engineering Analysis with Boundary Elements*, vol. 37, pp. 409–418, 2013.

[87] A. Delnevo, S. Le Saint, G. Sylvand, and I. Terrasse, "Numerical Methods: Fast Multipole Method for Shielding Effects," in *Proceedings of the 11th AIAA/CEAS Aeroacoustics Conference, Monterey, California, 23-25 May 2005, AIAA-2005-2971*, 2005.

[88] E. Manoha, X. Juvigny, and F.-X. Roux, "Numerical Simulation of Aircraft Engine Installation Acoustic Effects," in *Proceedings of the 11th AIAA/CEAS Aeroacoustics Conference, Monterey, California, 23-25 May 2005, AIAA-2005-2920*, 2005.

[89] A. Agarwal and A. P. Dowling, "Low-Frequency Acoustic Shielding by the Silent Aircraft Airframe," *AIAA Journal*, vol. 45, no. 2, pp. 358–365, 2007.

[90] S. Redonnet, G. Desquesnes, E. Manoha, and C. Parzani, "Numerical Study of Acoustic Installation Effects with a Computational Aeroacoustics Method," *AIAA Journal*, vol. 48, pp. 929–937, 2010.

[91] W. R. Wolf and S. K. Lele, "Wideband fast multipole boundary element method: Application to acoustic scattering from aerodynamic bodies," *International Journal for Numerical Methods in Fluids*, vol. 67, pp. 2108–2129, 2011.

[92] Y. P. Guo, K. J. Yamamoto, and R. W. Stoker, "Experimental Study on Aircraft Landing Gear Noise," *Journal of Aircraft*, vol. 43, pp. 306–317, 2006.

[93] W. Dobrzynski, L. C. Chow, P. Guion, and D. Shiells, "A European study on landing gear airframe noise sources," in *Proceedings of the 6th AIAA/CEAS Aeroacoustics Conference, Lahaina, Hawaii, 12-14 June 2000, AIAA-2000-1971*, 2000.

[94] D. Casalino, A. F. P. Ribeiro, and E. Fares, "Facing rim cavities fluctuation modes," *Journal of Sound and Vibration*, vol. 333, pp. 2812–2830, 2014.

[95] M. Pott-Pollenske, W. Dobrzynski, H. Buchholz, S. Guérin, G. Saueressig, and U. Finke, "Airframe Noise Characteristics from Flyover Measurements and Predictions," in *Proceedings of the 12th AIAA/CEAS Aeroacoustics Conference, Cambridge, Massachusetts, 8-10 May 2006, AIAA-2006-2567*, 2006.

[96] Y. Guo, "Effects of Local Flow Variations on Landing Gear Noise Prediction and Analysis," *Journal of Aircraft*, vol. 47, no. 2, pp. 383–391, 2010.

[97] J. A. D. Carrilho and M. G. Smith, "Scattering of Landing Gear Noise by a Wing," in *Proceedings of the 14th AIAA/CEAS Aeroacoustics Conference, Vancouver, Canada, 5-7 May 2008, AIAA-2008-2965*, 2008.

[98] M. Smith, J. Carrilho, N. Molin, J.-F. Piet, and L. C. Chow, "Modelling landing gear noise with installation effects," in *Proceedings of the 13th AIAA/CEAS Aeroacoustics Conference, Rome, Italy, 21-23 May 2007, AIAA-2007-3472*, 2007.

[99] J. A. D. Carrilho and M. G. Smith, "The effect of a lifting wing on landing gear noise," in *Proceedings of the 16th AIAA/CEAS Aeroacoustics Conference, Stockholm, Sweden, 7-9 June 2010, AIAA-2010-3975*, 2010.

[100] S. Kirkup. ABEMFULL Open-Source Fortran 77 Code. [Online] Available: http://www.boundary-element-method.com/acoustics/manual/abem.htm [Accessed: 19th March 2013].

[101] P. J. Morris, "The scattering of sound from a spatially distributed axisymmetric cylindrical source by a circular cylinder," *Journal of the Acoustical Society of America*, vol. 97, no. 5, pp. 2651–2656, 1995.

[102] P. J. Morris, "Scattering of sound from a spatially distributed, spherically symmetric source by a sphere," *Journal of the Acoustical Society of America*, vol. 98, no. 6, pp. 3536–3539, 1995.

[103] E. L. Houghton and P. W. Carpenter, *Aerodynamics for Engineering Students*, 5th ed. Elsevier, 2003.

[104] XFOIL Subsonic Airfoil Development System Version 6.97. [Online] Available: http://web.mit.edu/drela/Public/web/xfoil/ [Accessed: 14th March 2014].

[105] A. D. Arnott, G. Schneider, K.-P. Neitzke, J. Agocs, A. Schröder, B. Sammler, and J. Kompenhans, "Detailed Characterisation, using PIV, of the Flow around an Airfoil in High-Lift Configuration," in *Proceedings of the EUROPIV 2 workshop held in Zaragoza, Spain, March 31 - April 1, 2003*, 2003.

[106] X. Zhang, X. X. Chen, C. L. Morfey, and P. A. Nelson, "Computation of Spinning Modal Radiation from an Unflanged Duct," *AIAA Journal*, vol. 42, no. 9, pp. 1975–1801, 2004.

[107] S. K. Richards, X. X. Chen, X. Huang, and X. Zhang, "Computation of fan noise radiation through an engine exhaust geometry with flow," *International Journal of Aeroacoustics*, vol. 6, no. 3, pp. 223–241, 2007.

[108] J. Gill, X. Zhang, and P. Joseph, "Symmetric airfoil geometry effects on leading edge noise," *Journal of the Acoustical Society of America*, vol. 134, no. 4, pp. 2669–2680, 2013.

[109] F. Gea-Aguilera, X. Zhang, X. Chen, J. Gill, and T. Nodé-Langlois, "Synthetic Turbulence Methods for Leading Edge Noise Predictions," in *Proceedings of the 21st AIAA/CEAS Aeroacoustics Conference, Dallas, Texas, 22-26 June 2015, AIAA-2015-2670*, 2015.

[110] I. H. Abbott and A. E. von Doenhoff, *Theory of Wing Sections*. Dover Publications, Inc., 1959.

[111] J. M. Nichols, C. C. Olson, J. V. Michalowicz, and F. Bucholtz, "A simple algorithm for generating spectrally colored, non-Gaussian signals," *Probabilistic Engineering Mechanics*, vol. 25, no. 3, pp. 315–322, 2010.

[112] P. D. Welch, "The Use of Fast Fourier Transform for the Estimation of Power Spectra: A Method Based on Time Averaging Over Short, Modified Periodograms," *IEEE Transactions on Audio and Electroacoustics*, vol. 15, no. 2, pp. 70–73, 1967.

[113] G. Gabard, "Noise Sources for Duct Acoustics Simulations: Broadband Noise and Tones," *AIAA Journal*, vol. 52, no. 9, pp. 1994–2006, 2014.

[114] Larosterna Sumo Aircraft Modeling & Surface Mesh Generation Software Version 2.7.5. [Online] Available: https://www.larosterna.com/sumo.html [Accessed: 12th January 2015].

[115] *A320 Aircraft Characteristics - Airport and Maintenance Planning Document*, Airbus S.A.S., Rev: May 01/15, 2015.

[116] D. Angland, *SotonLGAP Manual Version 1.6*, Airbus Noise Technology Centre, 2012.

[117] S. N. Vecherin, D. K. Wilson, and V. E. Ostashev, "Incorporating source directionality into outdoor sound propagation calculations," *Journal of the Acoustical Society of America*, vol. 130, no. 6, pp. 3608–3622, 2011.

[118] S. N. Vecherin, D. K. Wilson, and V. E. Ostashev, "Application of the equivalent source method to directional noise sources," *Noise Control Engineering Journal*, vol. 60, no. 2, pp. 137–147, 2012.

[119] D. A. Bies and C. H. Hansen, *Engineering Noise Control: Theory and practice*, 4th ed. Spon Press, 2009.

[120] A. Agarwal, A. P. Dowling, H.-C. Shin, and W. Graham, "Ray-Tracing Approach to Calculate Acoustic Shielding by a Flying Wing Airframe," *AIAA Journal*, vol. 45, no. 5, pp. 1080–1090, 2007.

[121] C. Bahr, N. S. Zawodny, T. Yardibi, F. Liu, D. Wetzel, B. Bertolucci, and L. Cattafesta, "Shear layer time-delay correction using a non-intrusive acoustic point source," *International Journal of Aeroacoustics*, vol. 10, no. 5&6, pp. 497–530, 2011.

[122] F. Q. Hu, "Further Development of a Time Domain Boundary Integral Equation Method for Aeroacoustic Scattering Computations," in *Proceedings of the 20th AIAA/CEAS Aeroacoustics Conference, Atlanta, GA, 16-20 June 2014, AIAA-2014-3194*, 2014.

[123] A. A. Ergin, B. Shanker, and E. Michielssen, "Analysis of transient wave scattering from rigid bodies using a Burton-Miller approach," *Journal of the Acoustical Society of America*, vol. 106, no. 5, pp. 2396–2404, 1999.

[124] A. A. Ergin, B. Shanker, and E. Michielssen, "Fast analysis of transient acoustic wave scattering from rigid bodies using the multilevel plane wave time domain algorithm," *Journal of the Acoustical Society of America*, vol. 107, no. 3, pp. 1168–1178, 2000.

[125] F. Q. Hu, M. E. Pizzo, and D. M. Nark, "On the Assessment of Acoustic Scattering and Shielding by Time Domain Boundary Integral Equation Solutions," in *Proceedings of the 22nd AIAA/CEAS Aeroacoustics Conference, Lyon, France, 30 May - 1 June 2016, AIAA-2016-2779*, 2016.